Doctoral Dissertation

Numerical Analysis of Seawater Intrusion into Groundwater System -An application to Liaodong Bay coastal plain, China-

Ding Fei

Graduate School for International Development and Cooperation
Hiroshima University

September 2012

Numerical Analysis of Seawater Intrusion into Groundwater System -An application to Liaodong Bay coastal plain, China-

Ding Fei

A Dissertation Submitted to
the Graduate School for International Development and Cooperation
of Hiroshima University in Partial Fulfillment
of the Requirement for the Degree of
Doctor of Engineering

July 2012

Abstract

In the latest decades, water resource stress and water environment are become seriously year by year which due to the contradiction between supply and demand of water resources become more and more seriously at all of the world. Optimal allocation of the limited water resources is an available method to solve this problem and it has become research hotspot. The local water resource conditions should be evaluated if we allocate the water resource. On the other hand, how to choice the best optimal allocation scheme is also very important.

At present, many coastal aquifers in the world experience an intensive seawater intrusion and it is one kind of water environment problem. In the Liaodong Bay coastal plain area, China, the seawater intrusion area is more than 4,000 m^2 with serious intrusion area of nearly 1,500 m^2. In this study, numerical models and coupling mode system have been constructed based on the Regional Environment Simulator (RES) and groundwater model which are used to analysis the mechanism of seawater intrusion and the groundwater resource conditions in Liaodong Bay coastal plain area, China. To study the atmosphere-ocean coupled model, a case study of typhoon Morakot has been done in this thesis. Meanwhile, evaluation system of scheme choice for optimal allocation of water resource is established and a case study in the north of Shen Yang city has been done in thesis.

The majors studied in this thesis are follows:

1) Numerical simulation of seawater intrusion in Liao Dng Bay coastal plain, China.

2) Numerical simulation of Typhoon Morakot.

3) Scheme choice for optimal allocation of water resources in the north of Shen Yang city.

The first part is construct numerical models and coupling mode system to simulate the seawater intrusion in Liaodong Bay coastal plain area, China. Four cases study has been done is respectively: 1) three vertical grid layers no consider tidal effect, 2) four vertical grid layers no consider tidal effect, 3) three vertical grid layers consider tidal effect, 4) four vertical grid layers consider tidal effect, meanwhile, using atmosphere–ocean-groundwater modeling system. The results show that four vertical grid layer in seawater intrusion simulation models can present the salt wedge very well and the tidal fluctuation has significant effects on the seawater intrusion. The prediction results showed that the maximum extent of seawater intrusion in Quaternary Layers was significantly faster than that in Neozonic Layers. The results also show that the atmosphere–ocean-groundwater modeling system can be used for seawater intrusion simulation. The modeling system can be used for precipitation, seawater level and seawater intrusion simulation, especially can be used for groundwater simulation in lack of data regions.

The second part is using atmosphere-ocean coupled model to analysis the unique track of typhoon Morakot and the extremely heavy rainfall in Taiwan. Typhoon Morakot formed early on 2 August, 2009. This storm system resulted in a new rainfall record of 2,777 mm at Alishan. Three kinds of case study have been done which are terrain cases, microphysics parameterization cases and bogus scheme cases, respectively. The results show that the sudden northward-turning track of Typhoon Morakot is effect of the large-scale monsoon surge and the subtropical high system changed moving direction. The energy exchange of Typhoons Morakot, Goni, and Etau and the Central Mountain Ridge of Taiwan are major reasons due to the extremely heavy rainfall in Taiwan. The Schultz mixed-phase scheme can simulate rainfall very well and the every six-hour bogus technique can improve results in all aspects, including the rainfall track , intensity and the seawater level of Typhoon Morakot.

The third part is construct the evaluation system of scheme choice for optimal allocation of water resources with using fuzzy language evaluation and the generalized induced ordered weighted averaging (GIOWA) operator. It chose the five constituents: investment (Yuan), daily water supplying (ton/day), fee of contaminated water disposal (Yuan), water conservation (fuzzy language), and development of economy (fuzzy language). And analytic hierarchy process (AHP) method is used to determine the weighting vector. A case study has been done using the evaluation system in the north of Shen Yang. The results show that the evaluation system is available.

The innovations in this thesis are follows:

1) It is the first time to deals with numerical model on seawater intrusion in Liaodong Bay coastal plain which is a quasi-three-dimensional variable-density numerical model and it considered groundwater density variable and seawater intrusion in Quaternary and Neozoic layers. Vertical grid layers and tidal effect on seawater intrusion have been done in this thesis.

2) It is the first time to develop an atmosphere–ocean-groundwater modeling system for seawater intrusion simulation, which especially can be used in the lack of precipitation and seawater level data regions area.

3) It is the first to construct a evaluation system of scheme choice for optimal allocation of water resources based on the fuzzy language evaluation and the generalized induced ordered weighted averaging (GIOWA) operator.

Acknowledgements

First of all, I would like to express my deep gratitude to my supervisor Prof. Takao Yamashita for his guidance, supervision and generous support for three years of my PH. D course study in Hiroshima University. I would also like to special thank for his proofreading and valuable comments of the draft manuscripts of my published articles and of this thesis. I would like to thank Prof. Haruyuki Yamamoto, Prof. Yasushi Higo, and for their guidance and valuable comments on this thesis. I would also like to thank the staffs and friends in Graduate School for International Development and Cooperation (IDEC), Hiroshima University for their support of research study and daily life, especially for all members of Environmental Simulator research group is greatly appreciated. I would also like to thank Dr. Han Soo Lee for his guidance for conducting simulation in parallel computer system and for the kind discussions during my PH. D study in IDEC, Hiroshima University. Thanks also goes to all Chinese students in Saijo for their warm support and help. I would like to thank to Prof. Jun Pan and his lab members in Shenyang Jianzhu University, China, who has guided and help me in the Environment engineering field for years which led me to continue my study abroad. I would like to acknowledgment to the supported by the scholarship of the Japanese Ministry of Education, Culture, Sports, Science and Technology (MEXT), and the Global Environmental Leaders Education Program in Hiroshima University funded by the MEXT, Japan. I owe great thanks to my family, my parents, my three bigger brothers，three sister-in-laws and nephews for their support and patience during the past several years of my life. Finally, I am really grateful to giant researchers who lend their shoulders for me to step on.

Table of Contents

List of Figures

List of Tables

Chapter 1

Introduction

Water is the source of life. Uses of water include agricultural, industrial, household, recreational and environmental activities. Virtually all of these human uses require fresh water.

As we know that, 97% of the water is salt water and only three percent is fresh water on the Earth. Over two thirds of freshwater is frozen in glaciers and polar ice caps (Gleick, 1996). The remaining unfrozen freshwater is found mainly as groundwater, with only a small fraction present above ground or in the air (http://www.greenfacts.org/en/water-resources/index.htm#2). Figure 1.1shows the distribution of the Earth's water.

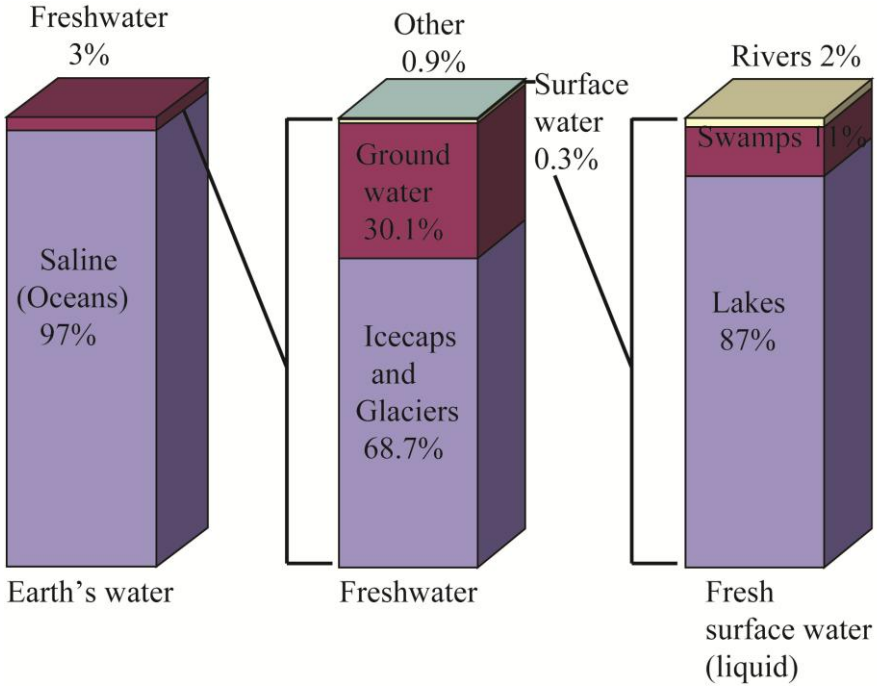

Figure 1. 1 Distribution of the Earth's water.

The water cycle, that is also known as the hydrologic cycle or H_2O cycle, describes the continuous movement of water on, above and below the surface of the Earth (see Figure 1.2). Water can change states among liquid, vapor, and solid at various places in the water cycle. The water moves from one reservoir to another, such as from the ocean to the atmosphere, from river to ocean, from atmosphere to land, or from ocean to groundwater, by the physical processes of evaporation, condensation, precipitation, infiltration, runoff, and subsurface flow. In so doing, the water goes through different phases: liquid, solid, and gas [web-1].

web-1: http://ga.water.usgs.gov/edu/watercycle.html

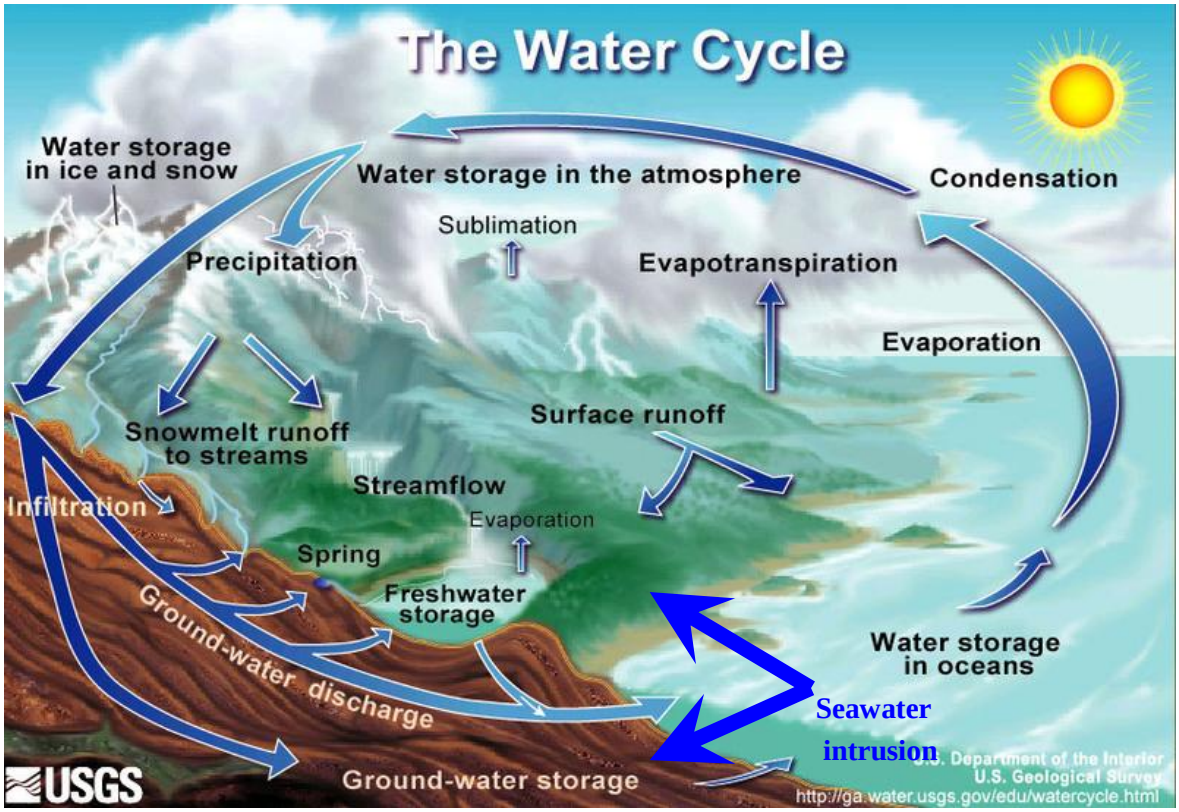

Figure 1. 2 The water cycle on the Earth (USGS)

1.1 Water Stress

The concept of water stress is relatively simple. According to the World Business Council for Sustainable Development, it applies to situations where there is not enough water for all uses, whether agricultural, industrial or domestic (WBCSD, 2005). Water stress is a worldwide problem. With increase of population, expansion of business activity, rapid urbanization, climate change, depletion of aquifers, pollution, water protection and temporal and spatial distribution imbalance, water stress problem has become serious year by year. And it will due to the following water resource environment problems, such as seawater intrusion, flood, extremely rainfall, groundwater depression, and so on.

Population growth:
In 2000, the world population was 6.2 billion. The world's population is likely to reach 9.1 billion by 2050 despite lower expected fertility rates. The United Nations Population Division says in its revised report for 2004 (UN, 2004). Most of the population increase in developing countries and the water demand will increase unless there are corresponding increases in water conservation and recycling which will suffer serious water stress (Foster, 2003).

In China, the population increased from 0.96 billion to 1.32 billion from 1978 to 2008[web-2]. China is the world's most populous country. China's population growth has been somewhat slowed by the one child policy, in effect since 1979. In spite of strict birth control, population growth continues and could reach 1.6 billion (UN, 1998) by the year 2050. This will lead to huge water stress in China.

web-2: http://wenku.baidu.com/view/1c4264d7c1c708a1284a4421.html

Expansion of business activity:
As we know that, the business activity ranging from industrialization to services such as tourism and entertainment continues to expand rapidly in all of the worlds. This expansion requires increased water services such as water supply and sanitation, which can lead to more stress on water resources (WBCSD, 2005). In China, the business activity has been increased very fast especially in some big cities such as Beijing, Shanghai and Guangzhou etc.

Rapid urbanization:
The human population has lived a rural lifestyle through most of history. The world's population, however, is quickly becoming urbanized as people migrate to the cities. The trend towards urbanization is accelerating in the latest decades. In 1950, less than 30% of the world's population lived in cities. This number grew to 47% in the year 2000 (2.8 billion people), and it is expected to grow to 60% by the year 2025. In the big city, the high density settlements are often highly polluted owing to the lack of urban services [web-3]. Urbanization requires significant investment in water infrastructure in order to deliver water to individuals and to process the concentrations of wastewater – both from individuals and from business (WBCSD, 2005).

web-3: http://www.globalchange.umich.edu/globalchange2/current/lectures/urban_gc/

In China, the level of urbanization was 22% in 1975, is 37% in 2006, and expected to reach 55% in 2025. The Chinese urban population is expected to increase five times during this period of 50 years (Varis and Vakkilainen, 2006). China's urban areas produced 35.1 km^3 of waste water in 1997. This is expected to grow to 650 km^3 by 2010, and 960 km^3 by 2030. The treatment level was 11% in 1997, and it is targeted to grow to 40% in 2010 (Oyang and Wang, 2000). All of these will lead to high water supply stress.

Climate change:
The IPCC's Fourth Assessment Report (2007) has concluded that observational records and climate projections provide ample evidence that water resources have the potential to be strongly impacted by climate change (World Bank, 2009). The climate change will lead to rising temperatures which will increase evaporation and lead to increases in precipitation, though there will be regional variations in rainfall. Both drought seasons and flood seasons may become more frequent in different regions at different times, and dramatic changes in snowfall and snow melt are expected in mountainous areas. There is now abundant evidence that increased hydrologic variability and change in climate has and will continue have a profound impact on the water sector through the hydrologic cycle, water availability, water demand, and water allocation at the global, regional, basin, and local levels (World Bank, 2009).

Climate change and its impacts on water resources and crop production is a major force with which China will have to cope in the twenty-first century. In China, the water resource is abundant in south and in north is dry. Many regions lie in transitional zones where water resources, and hence agricultural production, could be affected positively or negatively by changes in climate (Meehl, 2007; Piao et al., 2010). China has already experienced some devastating climate extremes in the past several decades (Editorial board, 2007). For example, the great flood of 1998 inundated $21x10^6$ hectares (21 Mha) of land and destroyed five million houses in the Yangtze basin, causing an economic loss of over

US$20 billion (Zong, 2000). In 2008, a series of winter storm events affected large portions of southern and central China from 25 January to 6 February. The systems affected most of the area with heavy snows, ice and cold temperatures causing extensive damage and transportation disruption for several thousand travelers. According to some media sources the storms were directly responsible for at least 129 deaths and causing an economic loss of over 1516.5 Chinese yuan (Xinhua News Agency,, 2008).

Depletion of aquifers:

Groundwater plays a fundamental role in shaping the economic and social health of many urban areas in the developing world. Due to its relatively low cost and generally high quality, groundwater has often been the preferred source for reticulated public water supplies and is widely exploited for private domestic and industrial uses. Urbanization and industrialization have a profound effect on urban groundwater resources, which are inextricably linked with land use and effluent and waste disposal practices in a complex fashion (Foster, 1998). A lot of countries, such as China, India, and the United States, are overpumping aquifers as they struggle to satisfy their growing water needs because of the more than half the world's people. (Lester Brown, 2010). Due to the expanding human population, competition for water is growing such that many of the worlds major aquifers are becoming depleted. This is due both for direct human consumption as well as agricultural irrigation by groundwater. Irrigation in dry areas such as northern China and India is supplied by groundwater, and is being extracted at an unsustainable rate. Cities that have experienced aquifer drops between 10 to 50 meters include Mexico City, Bangkok, Manila, Beijing, Madras and Shanghai (Foster, 1998).

A crisis is developing beneath China's thirsty farms and cities, but no one knows its full extent. With about 20% of the world's population but only about 5–7% of global freshwater resources, China draws heavily on groundwater. Groundwater is used to irrigate more than 40% of China's farmland, and for about 70% of the drinking water in the dry northern and northwestern regions. According to Opportunities and Challenges in the Chinese Groundwater Science, a 2009 report sponsored by China's National Natural Science Foundation and China Geological Survey (CGS), part of the Ministry of Land and Resources (MOLR), the past few decades have seen groundwater extraction increasing by about 2.5 billion cubic metres per year to meet these needs. Consequently, groundwater levels of the arid North China Plain have dropped as fast as 1 metre a year between 1974 and 2000, forcing people to dig hundreds of metres to access fresh water (http://www.nature.com/news/2010/100713/full/466308a.html). In Shenyang, China, the over-exploitation of groundwater by industry and agriculture, which are in a heated competition for water access. The government of Shenyang city must pay more than 300,000Yuan/year for the compensation of the damage caused by agriculture. Moreover, the over-exploitation of groundwater may also negatively impact water quality due to immersion and salty soil, which may be derived from the rise in the groundwater level related to the water storage in the Shi Fosi Reservoir (Ding, 2011).

Pollution and water protection:

Water pollution is the contamination of water bodies. If the pollutants are discharged directly or indirectly into water bodies without adequate treatment to remove harmful compounds, then water pollution occurs (Guha-Mazumdar et.al, 1997). The governments of numerous countries have striven to find solutions to reduce this problem. Many pollutants threaten water supplies, but the most widespread, especially in developing countries, is the discharge of raw sewage into natural waters. Sewage, sludge, garbage, and even toxic pollutants are all dumped into the water. Even if sewage is treated, problems

still arise. Treated sewage forms sludge, which may be placed in landfills, spread out on land, incinerated or dumped at sea (U.S. Senate, 1972).

The main sources of water pollution are: industrial (chemical, organic, and thermal wastes), municipal (largely sewage consisting of human wastes, other organic wastes, and detergents), and agricultural (animal wastes, pesticides, and fertilizers) (Brower et.al, 1990). In China, about one third of the industrial waste water and more than 90 percent of household sewage is released into rivers and lakes without being treated. In summer of 2011, the China government reported 43 percent of state-monitored rivers are so polluted, they're unsuitable for human contact. By one estimate one sixth of China's population is threatened by seriously polluted water. One study found that eight of 10 Chinese coastal cities discharge excessive amounts of sewage and pollutants into the sea, often near coastal resorts and sea farming areas. Water pollution is especially bad along the coastal manufacturing belt. Most of China's rural areas have no system in place to treat waste water (Jeffrey Hays, 2008). For the past several years, China has been affected with the water pollution crisis. Three examples of wastewater pollution crisis in China are the City of Tianjin, the Chao Lakes and Xian City (Kris Min, 1998).

In Shengyang city, if the concentrations of ferrous and manganese ion had not been taken into account, the groundwater quality from May to September, 2008 would have been considered good in 7.2% of total area, better in 76.6%, and bad in 16.2% of the total area using the comprehensive methods of water quality assessment in which an index ≤ 2.50 indicates good, and index between 2.50 and 4.25 is better, and an index between 4.25 and 7.20 is bad (Ding, 2011).

Temporal-spatial distribution imbalance:

The precipitation temporal and spatial distribution imbalance is a very important reason for shortage of water resources.

In China, precipitation decrease from the southeast to the northwest. The annual total of certain areas along the southeastern coast amounts to more than 2,000 mm. The Yangtze valley receives about 1,000 to 1,150 mm. Farther north, in the Huai River valley, the annual rainfall decreases to some 35 inches (880 mm). In the lower reaches of the Huang He, only 20 to 25 inches (500 to 650 mm) falls annually. The Northeast generally receives more precipitation than the North China Plain, with upwards of 40 or more inches falling in the Changbai Mountains (http://www.britannica.com/EBchecked/topic/111803/China). Figure 1.3 show the yearly precipitation of Wuhan (Yangtze valley) and Shenyang (Northern of China) from 1951 to 2009. It can obviously see that the precipitation of Wuhan is higher than Shenyang. Figure 1.4 show the monthly precipitation of Wuhan and Shenyang in 2004. It show that the rainfall is major from June to September. It show that the precipitation temporal and spatial distribution imbalance in China. Which lead to high water supply stress in China especially in the Northern of China area.

1.2 Optimal Allocation of Water Resources

From the above introduction, the available freshwater resource is limit on the earth. Along with the population growth, expansion of business activity, rapid urbanization, climate change, depletion of aquifers, pollution and water protection, and temporal and spatial distribution imbalance, the shortage of water resources and water pollution problems increasingly intensification. The contradiction between supply and demand of water

resources more and more seriously, which has become main restriction factors for social and economy sustainable development. There are two methods to solve this problem. The first method is save expenditure and establish water-saving society; the second method is to optimize the allocation of the limited water resources, (Sun, 2012).

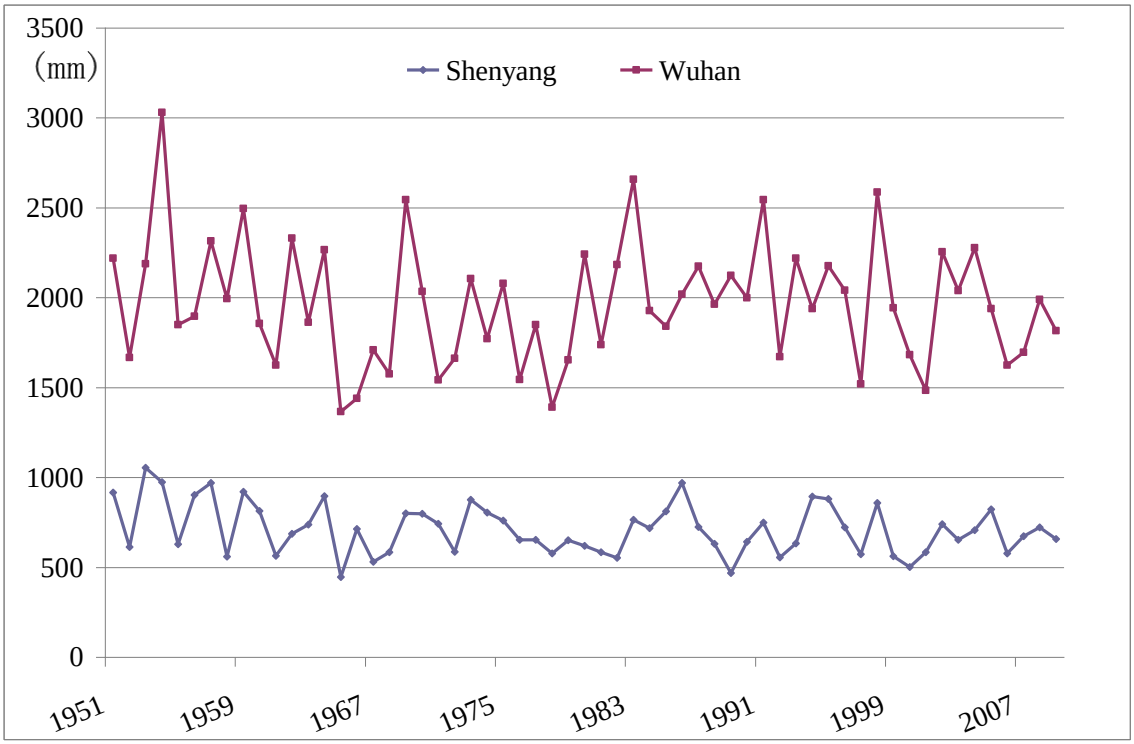

Figure 1. 3 Yearly precipitation of Wuhan and Shenyang from 1951 to 2009

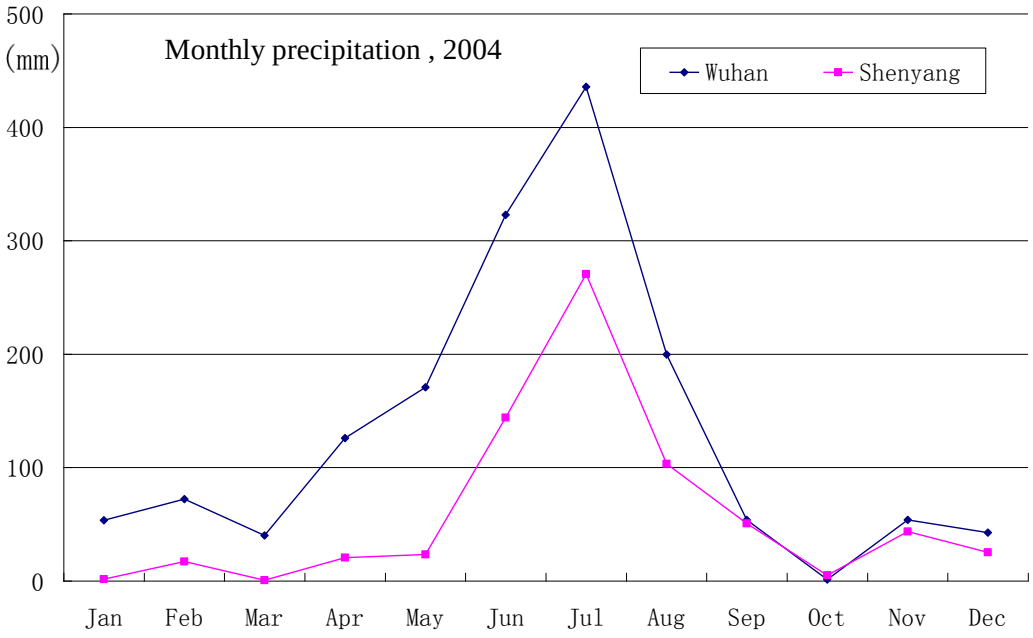

Figure 1. 4 Monthly precipitation of Wuhan and Shenyang in 2004

In the optimal allocation of water resources study, the very important things is how to choice the best optimal allocation scheme. As the scheme choice for optimal allocation of water resources (OAWR) is a fuzzy multi-attribute decision, an impact evaluated by the weight of each attribution should be considered. In the conventional method for decision, the maximum and the minimum arithmetic operators have usually been used. However, it often neglects too much important fuzzy language information. Therefore, further researches on the scientific evaluation system have to be conducted. Most multi-criteria decision analysis problems require neither strict "anding" (minimum) nor strict "oring" of the s-norm (maximum). For mutually exclusive and independent probabilities in the fault tree analysis, there are two extremes corresponding to multiplication (and-gate) and summation (or-gate). The appendix part will present a study on scheme choice for optimal allocation of water resources in the north of Shen Yang China, based on fuzzy language evaluation and the Generalized Induced Ordered Weighted Averaging (GIOWA) operator.

There are so many problems of water resources and environment in the north area of Shen Yang city, China (Figure 1.5). For the first example, cross-border and cross-years water issues in uneven quantity of the river water have been in the big dispute between the upstream and downstream communities in the watershed of the Liao river, the biggest river in Shen Yang city where a dry condition continues nearly five months.

The second example is the problem of an exceedance of the criterion in concentration of Fe and Mn ion in groundwater supply system. If the concentration of Fe and Mn ion was no accounted, the groundwater quality in Shen Yang city from May to September, 2008, was good in 7.2% of total area, better in 76.6%, bad in 16.2% of the total area using the comprehensive index methods of water quality assessment in which index $\leq$2.50 indicates good, index 2.50-4.25 better, index 4.25-7.20 bad (Water Resource Research Report of Shen Yang, China,2008).

The third example is an over-exploitation of groundwater caused by industrial and agricultural use which has heated a water access competition. Shen Yang city local government needs to pay more than 300,000Yuan/year for the compensation of the damage of agriculture. Moreover, over-exploitation of groundwater may cause another impact on water quality, that is immersion and salty soil which may be derived from groundwater level raising related to the water storage in the Shi Fosi reservoir resulting in its water table increase.

Most multi-criteria decision analysis problems require neither strict "anding" (minimum) nor strict "oring" of the s-norm (maximum). For mutually exclusive and independent probabilities in the fault tree analysis, there are two extremes corresponding to multiplication (and-gate) and summation (or-gate).

For generalizing the idea, Yager (1988) had introduced a new family of aggregation techniques named the ordered weighted average (OWA) operator, which form general mean type aggregators. The OWA operator could provide the flexibility in utilizing the range of "anding" or "oring", and to include the attitude of a decision maker in the aggregating process. Traditionally, in OWA, input criteria (sub-indices) are assumed to be equally important and OWA weight is assigned based on the ordinal position.

To deal with the criteria of varying importance in the aggregating process, Tora (1997) introduced the concept of weighted OWA (WOWA) operators, which initially assigns significance weights to the input values and then OWA aggregation is performed in a

regular way. Filev and Yager (1998) introduced induced OWA (IOWA) operator, unlike the OWA operator, which allows ordering by an inducing parameter that is associated with the input values.

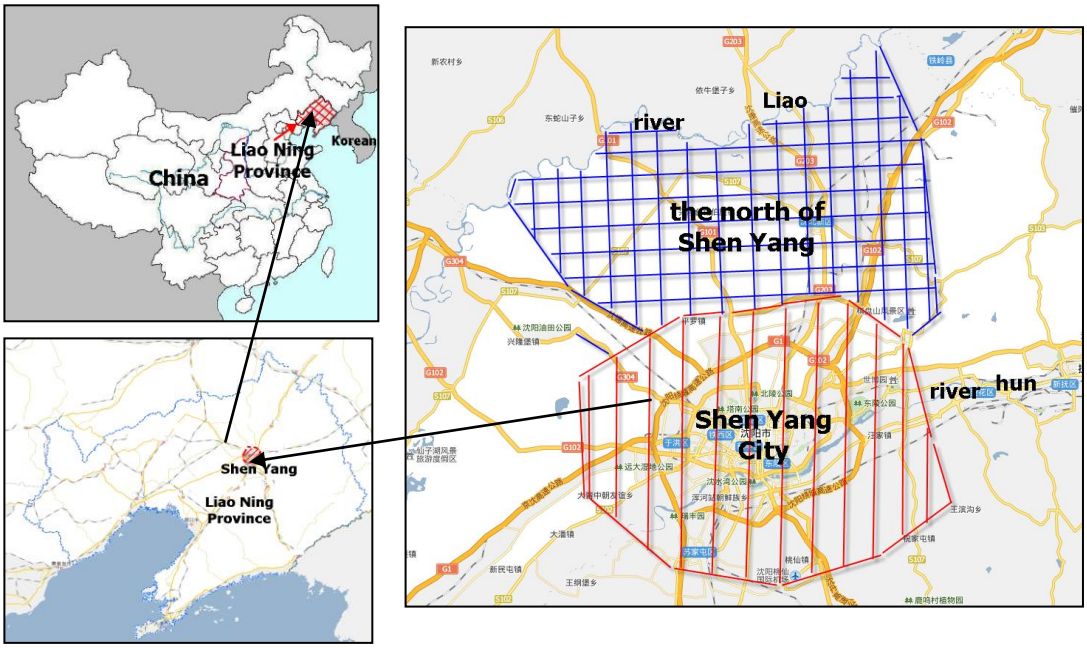

Figure 1. 5 Map of Shen Yang city and the north area of Shen Yang city, China.

The utility of the inducing parameter is only for ordering, and not in the aggregating process. Then Xu and Da (2002) proposed a generalized IOWA operator. Now, the GIOWA operator has been extensively used in many fields, such as selecting salt cavity gas storage site (Yang,2006), evaluation of environment quality (Bai,2005), effectiveness evaluation of vehicle maintenance equipment (Zhang,2009) and location decision of logistics center (Li, 2009), and so on.

Following the above processes development, the GIOWA operator has been extensively used in many fields. However, it has not yet been applied for the research on scheme choice for OAWR. In this study, evaluation system of scheme choice for optimal allocation of water resource is established based on the fuzzy language evaluation and the generalized induced ordered weighted averaging (GIOWA) operator. The evaluation system chose the five constituents: investment (Yuan), daily water supplying (ton/day), fee of contaminated water disposal (Yuan), water conservation (fuzzy language), and development of economy (fuzzy language). And analytic hierarchy process (AHP) method is used to determine the weighting vector. And then, a case study of the north of Shen Yang city was conducted. From the comprehensive judgment of the results estimated by the fuzzy language evaluation and GIOWA operator, it can be concluded that Scheme 1 is acceptable as a best choice in the schemes of optimal allocation of water resources (OAWR) in Shen Yang.

For the scheme 1, its total investment is 9.6 hundred million yuan, its total fee of contaminated water disposal is 0.83 hundred million yuan. These are not so much. Its daily water supplying is 91.02 ten thousand ton/day that is enough for the next 20 years daily water supplying in Shen Yang. Its water conservation and the development of economy are moderate. Then we can come to the conclusion that the Scheme 1 is acceptable to the

sustainable choice. The results show that the evaluation system is accurate. For more details can be found in appendix part.

1.3 Seawater Intrusion in Liaodong Bay Coastal Plain, China

In 2007, the State Oceanic Administration of People's Republic of China started monitoring seawater intrusion in China. The activity helped established the fact that seawater intrusion is in serious level condition particularly in Liaodong Bay area (Figure 2.9) where coverage of seawater intrusion area is more than 4,000 m^2 with serious intrusion area of nearly 1,500 m^2. The most remote region of seawater intrusion is 68 km far from the shore in Panjin City (Figure 1.6) [see web-4]. It is a significant task to make clear the seawater intrusion and to predict its extending area in Liaodong Bay coastal plain by numerical study.

web-4 http://www.soa.ov.cn/hyjww/zghybnew/tkb/webinfo/2008/01/1200912281939611.htm

Figure 1. 6 Seawater intrusion distribution of Liao Ning Province, China in 2007

1.4 Motivation and Objectives

In China, because of the huge population, the water resource stress is very serious especially in the beach city with serious seawater intrusion problem such as Liaodong Bay coastal plain area, Laizhou Bay and Beibu Bay.

In the process of water resource allocation study, not only the requirements of water quantities but also requirements of water quality are needed to consider. Thus, before allocating the water resource, the local water resource conditions should be evaluated

(Yang, 2008). To master the water resource condition in the Liaodong Bay coastal plain area, the seawater intrusion condition will be focused in this thesis by using the numerical simulation methods.

This thesis focuses on the following three points. The first point is constructing the evaluation system of scheme choice for OAWR in the north of Shen Yang, with using fuzzy language evaluation and the generalized induced ordered weighted averaging (GIOWA) operator. This is the first time to using the GIOWA operator in Scheme choice for OAWR. It chose the five constituents: investment (Yuan), daily water supplying (ton/day), fee of contaminated water disposal (Yuan), water conservation (fuzzy language), and development of economy (fuzzy language). And analytic hierarchy process (AHP) method is used to determine the weighting vector.

The second is deals with a quasi-three-dimensional variable-density model to study the seawater intrusion in Liaodong Bay coastal plain based on SEAWAT model. Meanwhile, the vertical grid effect and tidal effect case studies have been done in this thesis. Compare with previous studies, this study model improved in two parts. It considered groundwater density variable and seawater intrusion in Quaternary and Neozoic layers in Liaodong Bay coastal plain.

The third is the first time to construct an atmosphere–ocean-groundwater modeling system to study the seawater intrusion in the Liaodong Bay coastal plain. In the modeling system, the atmosphere model (MM5) and the ocean model (POM) is used to simulate the precipitation and seawater level, respectively while the SEAWAT model is used for groundwater model simulation. The modeling system can be used for precipitation, seawater level and seawater intrusion simulation. It especially can be used for groundwater simulation in lack of data regions. Two case of seawater intrusion and typhoon Morakot have been simulated using the modeling system in this thesis.

The objectives of this thesis is construct a improving model to analysis the seawater intrusion condition in Liaodong Bay coastal plain area, and construct an atmosphere–ocean-groundwater modeling system which can be used for precipitation, seawater level calculation and seawater intrusion simulation especially can be used for groundwater simulation in lack of data regions. On the other hand, the evaluation system of scheme choice for OAWR in the north of Shen Yang is established. This thesis study also can be used for future water resource allocation study.

1.5 Thesis Structure

This thesis consists of six chapters including the first chapter of introduction and scheme choice for OAWR in the north of Shen Yang. In chapter 2, the components model for atmosphere model (MM5), the ocean model (POM) in Regional Environment Simulator (RES), the groundwater model (SEAWAT) and the background of Liaodong Bay coastal plain are described. Chapter 3 presented numerical simulation of seawater intrusion in Liaodong Bay coastal plain, China using SEAWAT model. Three case studies (three and four vertical grid layer cases and tidal case) have been done to analysis the seawater intrusion condition and the vertical grid and tidal effect on seawater intrusion simulation.

Seawater intrusion process is one part of the hydrological cycle. To understand the atmosphere and ocean cycle, a case study about typhoon Morakot using atmosphere and ocean coupling model system is done in chapter 4. In this chapter, to investigate the

characteristics of Typhoon Morakot in terms of its extremely heavy rainfall, intensity and track, three kinds of numerical experiments (Microphysics scheme experiments, Terrain sensitivity experiments, Bogus scheme experiments) were performed in MM5 simulation and only Bogus scheme experiments in POM simulation. Chapter 5 describes the atmosphere–ocean-groundwater modeling system and using it to study the seawater intrusion in the Liaodong Bay coastal plain. The atmosphere model (MM5), the ocean model (POM) and the SEAWAT model are used in the modeling system. The results show that the atmosphere–ocean-groundwater modeling system provides a very reasonable result in seawater intrusion simulation. The modeling system also can be used for precipitation, seawater level calculation and seawater intrusion simulation and others groundwater simulation in lack of data regions. Finally, the concluding remarks of this thesis are presented in chapter 6. Thesis flowchart is shown in Figure 1.7.

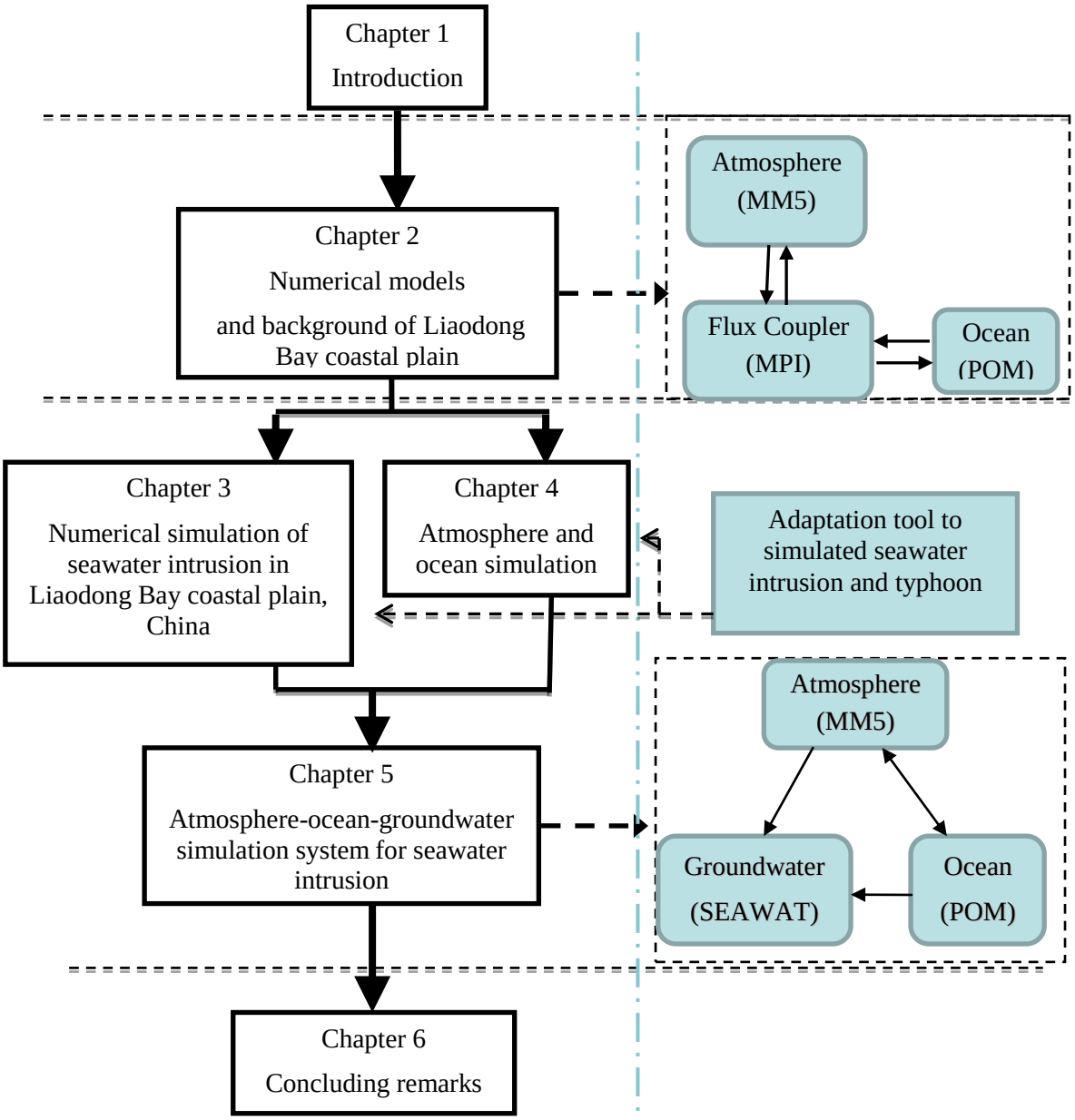

Figure 1. 7 Thesis structure

References

Bai, X.C., Ling, K., Guo, C.Z.: The Fuzzy Synthesizing Evaluation of City's Environmental Quality Based on GIOWA Operator: A Case of 13 Cities of Jiangsu province. *Chinese Journal of Population, Resources and Environment*, Vol.3 No.4:51-58, 2005.

Bates, B.C., Kundzewicz, Z.W., Wu, S. and Palutikof, J.P. Eds.: *Climate Change and Water*. Technical Paper of the Intergovernmental Panel on Climate Change, IPCC, Secretariat, Geneva, 210 pp, 2008.

Bordogna, G., Fedrizzi, M., Pasi, G.: A Linguistic Modeling of Consensus in Group Decision Making Based on OWA operators. IEEE Transactions on Systems, Man, and Cybernetics-Part A, 27:126-132, 1997.

Brower, J., Jerrold, Z., von Ende, C.: *Field and Laboratory Methods for General Ecology*. Wm.C. Brown Publishers, 1990.

Chan, H., et. al.: *China*. Encyclopædia Britannica. Encyclopædia Britannica Online. Encyclopædia Britannica Inc. (http://www.britannica.com/EBchecked/topic/111803/China), 2012.

Chinadaily.com.cn.: China says water pollution so severe that cities could lack safe supplies. June 7, 2005.

Ding, F., Yamashita, T., Lee, H. S. and Ping, J.: Scheme choice for optimal allocation of water resources based on fuzzy language evaluation and the generalized induced ordered weighted averaging operator, *Fuzzy Information and Engineering*, Volume 3, Number 2, 169-182, 2011.

European Environment Agency, *Europe's Environment: The Dobris Assessment*. Reports.eea.europa.eu. 1995-05-20. Retrieved 2009-03-12.

Filev, D., Yager, R.R.: On the issue of obtaining OWA operator weights. *Fuzzy sets and systems*, 94:157-169, 1998.

Foster, S., Lawrence, A., Morris, B.: *Groundwater in Urban Development: Assessing Management Needs and Formulating Policy Strategies*. Wds.worldbank.org, 1998.

Foster, S.S.D., Chilton, P.J.: Groundwater: the processes and global significance of aquifer degradation. Phil Trans R Soc Lond B., 258:1957–72, 2003.

Gleick, P. H.: *Water resources. In Encyclopedia of Climate and Weather*. ed. by S. H. Schneider, Oxford University Press, New York, vol. 2, pp.817-823, 1996.

Guha-Mazumdar, D.N, J. Das-Gupta, A. Santra, A. Pal, A. Ghose and S. Sarkar.: Non- Cancer Effects of Chronic Arsenicosis with Special Reference to Liver Damage. In: Abernathy, C.O., R. L. Calderon and W.R Chappell (Ed.), Arsenic: Exposure and Health Effects, Chapman and Hall, London, pp. 112-123, 1997.

IPCC: *Technical Paper on Climate Change and Water, IPCC Secretariat, Geneva*, Switzerland, 2008.

Kris, M.: Wastewater Pollution in China. (*http://www.dbc.uci.edu/~sustain/susco asts/krismin.html*), 1998.

Jeffrey, H.: Water pollution in China, (*http://factsanddetails.com/china.php?itemid=391&catid=10&subcatid=66*), 2008.

Lester, B., Brian, B., Galal, H.G.H., "Aquifer depletion". In: Encyclopedia of Earth. Eds. Cutler J. Cleveland (Washington, D.C.: Environmental Information Coalition, National Council for

Science and the Environment). [First published in the Encyclopedia of Earth January 23, 2010; Last revised Date March 22, 2011; Retrieved February 15, 2012. (*http://www.eoearth.org/article/Aquifer_depletion*)

Li, H., Chai, X.S., Wang, B.D.: Location Decision of Logistics Center Based on GIOWA Operator. *Technical and Method* (In Chinese), 28-7, 2009.

Meehl, G. A. et al. Global Climate Projections. In Climate Change 2007: *The Physical Science Basis. Contribution of Working Group I to the Fourth Assessment Report of the Intergovernmental Panel on Climate Change* (eds Solomon, S. et al.) (Cambridge University Press, 2007).

Piao, S., Ciais, P., Huang, Y., Shen, Z., Peng, S., Li, J., Zhou, L., et al.: The impacts of climate change on water resources and agriculture in China. *Nature*, 467 (7311), 43-51, 2010.

Schneider, Oxford University Press, New York, vol. 2, pp.817-823, 1996.

Sun, W. and Zeng, Z.: City optimal allocation of water resources research based on sustainable development. *Materials Research*, 449, 4028, 2012.

The New York Times.: As China Roars, Pollution Reaches Deadly Extremes. August 26, 2007.

Torra, V.: The weighted OWA Operator. *International Journal of Intelligent systems*, 12:153-166, 1997.

UN, 1998. *World Population 1998*. United Nations, New York

Un.org. *World population to reach 9.1 billion in 2050, UN projects*. 2005-02-24. Retrieved 2009-03-12.

United States Environmental Protection Agency (EPA). Washington, DC.: *The National Water Quality Inventory: Report to Congress for the 2002 Reporting Cycle – A Profile*. Fact Sheet No. EPA 841-F-07-003, October 2007.

U.S. Senate. *Marine Protection, Research and Sanctuaries Act of 1972*.

Vahid, A., Halla, M., Qaddmi, Eric, D., Sylvia, M.D., Alexander, V.D., Rafik, F.H., Gabrielle, P., Carolina, P., Michael, J., Brian, B.: *Water and Climate Change: Understanding the Risks and Making Climate-Smart Investment Decisions*. The World Bank, P. 174, 2009.

Varis, O., Vakkilainen, P.: *China's challenges to water resources management*. Agrifood Res. Report 68, pp.115–129, 2006.

"WBCSD *Water Facts & Trends*". http://www.unwater.org/downloads/Water_facts_and_trends.pdf August 2005. Reprint March 2006.

Xinhua News Agency: Harsh winter storms kill 107 people in China, February 13, 2008.

Xu, Z.S.: A Method Based on Fuzzy Linguistic assessments and Linguistic Ordered Weighted Averaging (OWA) Operator for Multi-attribute Group Decision-making Problems. *Systems Engineering* 20(5):79-82, 2002.

Xu, Z.S., Da, Q.: Multi-attribute Decision Making Based on Fuzzy Linguistic Assessments. *Journal of Southeast University* (Natural Science Edition), 32 (04):656-658, 2002.

Yager, R.R.: On ordered weighted averaging aggregation operators in multicriteria decision making. IEEE Transactions on Systems, Man , and Cybernetics 18:183-190, 1988.

Yang, L.L.: *Study on Water Resources Allocation Model Based on Water Environment Restoration*, PH. D thesis, (In Chinese), 2008.

Yang, Y., Xiao, C.Y., Tu, Y.: Salt Cavity Gas Storage Selecting Based On Fuzzy Language Evaluation and GIOWA Arithmetic Operators. *Fuzzy information and engineering*, 6:81-87, 2006.

Zhang, A.M., Zhang, C.R., Liu, Z.Y., Cai, Q.: Effectiveness Evaluation of Vehicle Maintenance Equipment Based on GIOWA Operator. *Ordnance Industry Automation* (In Chinese), 28-5, 2009.

Zong, Y. Q. and Chen, X. Q.: The 1998 flood on the Yangtze, China. *Nat. Hazards*, 22, 165–184, 2000.

Appendix:

1. Evaluation System of Scheme Choice for OAWR and Step of Evaluation System

1.1 GIOWA Operator

Definition 1

Let, $\hat{\mathbf{a}} = [a^L, a^M, a^U]$, where $0 < a^L < a^M < a^U$.

Then $\hat{a}$ is called a triangular number and is identified by its characteristic function (Van Laarhoven and Pedrycz, 1983).

$$\mathbf{U}_{\hat{a}} = \begin{cases} \dfrac{(x - a^L)}{(a^M - a^L)}, & a^L \le x \le a^M \\ \dfrac{(x - a^U)}{(a^M - a^U)}, & a^M \le x \le a^U \\ 0 & \text{others} \end{cases} \tag{A1}$$

For convenience, we give the following operational laws related to triangular fuzzy numbers.

1) $\hat{\mathbf{a}} + \hat{\mathbf{b}} = [a^L, a^M, a^U] + [b^L, b^M, b^U] = [a^L + b^L, a^M + b^M, a^U + b^U]$

2) $\lambda\hat{\mathbf{a}} = [\lambda a^L, \lambda a^M, \lambda a^U]$ where $\lambda > 0$

Definition 2

Let $\hat{\mathbf{a}} = [a^L, a^M, a^U]$, $\hat{\mathbf{b}} = [b^L, b^M, b^U]$.

If $a^L < b^L, a^M < b^M, a^U < b^U$ then it's said to be $\hat{\mathbf{a}} < \hat{\mathbf{b}}$.

Definition 3

$\mathbf{F}$ is called a induced ordered weighted averaging operator (IOWA), if

$$\mathbf{F}[\langle u_1, \alpha_1 \rangle, \cdots, \langle u_n, \alpha_n \rangle] = \sum_{j=1}^{n} \omega_j b_j \tag{A2}$$

where $\omega = [\omega_1, \cdots, \omega_n]^T$ is the associated weighting vector of $\mathbf{F}$,

$\omega_j \in [0,1] (j \in N)$, $\sum_{j=1}^{n} \omega_j = 1$, $\langle u_i, \alpha_i \rangle$ is called an OWA pair, b_j is the second component of the OWA pair having the j-th largest $u_i (i \in \{1,2,\cdots,6\})$ value. u_i is called the inducing component and α_i the numerical component (Yager, 1988; Filev and Yager,

1998; Bordogna, Fedrizzi and Pasi , 1997).

The IOWA operator with a more extensive meaning is the following:

Definition 4

g is called n dimension generalized IOWA operator (GIOWA operator) (Xu, 2002), if

$$\mathbf{g}[\langle \xi_1, \pi_1, \alpha_1 \rangle, \cdots, \langle \xi_n, \pi_n, \alpha_n \rangle] = \sum_{j=1}^{n} \omega_j b_j \qquad \text{(A3)}$$

where, vector $\omega = [\omega_1, \cdots, \omega_n]^T$ is the associated weighting vector of **g** , $\omega_j \in [0,1] (j \in \mathbf{N}), \quad \sum_{j=1}^{n} \omega_j = 1, \quad \langle \nu_i, u_i, \alpha_i \rangle \in \mathbf{\Phi} \times \mathbf{\Psi} \times \mathbf{\Theta}$ is three dimension pair, the first component ν_i shows an important level or characteristic of the second component u_i, that is the main body of the third component α_i, b_i is the third component that correspond to the j-th largest of $\nu_i (i \in \{1,2,\cdots,n\})$ value in three dimension pair, $\mathbf{\Phi}$, $\mathbf{\Psi}$ and $\mathbf{\Theta}$ are a set of the first, the second and the third component respectively in all three dimension pair. b_i can be obtained with the following method.

All three dimension pair are ordered according to the big or small of the first component $\nu_i (i \in \{1,2,\cdots,n\})$. b_i is the third component of the j-th ordered three dimension pair.

The radical trait of GIOWA operator is that there isn't any relation between $\langle \nu_i, u_i, \alpha_i \rangle$ and ω_i. That ω_i is only related to the i-th place in the assembled process. The element $\alpha_i (i \in \{1,2,\cdots,n\})$ weighted assembled isn't in accord with the big or small of oneself value and is based on $\nu_i (i \in \{1,2,\cdots,n\})$ value that corresponds with in $\langle \nu_i, u_i, \alpha_i \rangle$. u_i is the problem attribute generalized. ν_i is the important level and property of u_i ,such as weight, number, achievement, etc. u_i and ν_i are expressed with a language or a number. α_i is an attribute value generalized or the other quantity that indicates α_i. It is expressed with a number, for example, real number, interval number, triangular fuzzy number, etc.

Specially, if $\nu_i = \nu_j$, then α_i and α_j are averaged in the assembled process for three dimension pair $\langle \nu_i, u_i, \alpha_i \rangle$ and $\langle \nu_j, u_j, \alpha_j \rangle$. Three dimension pair $\left\langle \nu_i, u_i, \frac{\alpha_i + \alpha_j}{2} \right\rangle$ and $\left\langle \nu_j, u_j, \frac{\alpha_i + \alpha_j}{2} \right\rangle$ are gotten. The same method is used to solve the situation that the first component in three dimension pair of 3 or more than 3 is equal.

1.2 Group multiple attribute decision making based on GIOWA

The schemes choice of water resources's optimal allocation is a Group multiple attribute decision making problem. Every schemes of water resources's optimal allocation is regarded as the evaluated object. Let, **X**, **U** and **D** be an evaluated object set, an attribute set and an evaluating unit set. The evaluating unit $d_k \in \mathbf{D}$ gives the evaluated object

$x_i \in \mathbf{X}$ a fuzzy linguistic evaluating value $r_{ij}^{(k)}$ in the attribute $u_l \in \mathbf{U}$.The evaluating matrix $\mathbf{R_k} = \left| r_{ij}^{(k)} \right|$, $(r_{ij}^{(k)} \in \mathbf{S})$ is obtained, where **S** = [best, better, good, less good, generic, less bad, bad, worse, worst] is called the fuzzy linguistic scale (Xu and Da, 2002; Xu, 2002). The triangular fuzzy numbers corresponding to the above scale is as follows:

best =[0.8, 0.9, 1], better =[0.7, 0.8, 0.9], good =[0.6, 0.7, 0.8], less good =[0.5, 0.6, 0.7],

generic =[0.4, 0.5, 0.6], less bad =[0.3, 0.4, 0.5], bad =[0.2, 0.3, 0.4], worse =[0.1, 0.2, 0.3], worst = [0 , 0.1 , 0.2] ; where best>better>good>less good>generic>less bad>bad>worse>worst.

1.3 Evaluation system of scheme choice for OAWR

Based on the fuzzy linguistic evaluation and GIOWA operator, the evaluation system of scheme choice for OAWR is established:

Assuming that there are following two domains:

$$\mathbf{G} = [G_1, \cdots, G_m] \tag{A4}$$

$$\mathbf{S} = [S_1, \cdots, S_m] \tag{A5}$$

and **G** delegates "the multiple factors gathering" for syntheses evaluation, and **S** delegates "the comment gathering".

Syntheses evaluation mathematic model:

$$\mathbf{B} \times \mathbf{A} = \mathbf{C} \tag{A6}$$

Where **A** is $n \times n$ modules fuzzy matrix,

B -the fuzzy vector for scheme **G** , the gathering of weights of every evalution factor,

C -evaluation result, which is one of the fuzzy subclasses (fuzzy vector) on the domain **S** .

In fact, it is rather easy to evaluation a one factor thing. However if there are multiple factors in one thing, and we can get a evaluation result from one factor and get another evaluation result from another factor. Thus much real evaluation results will be obtained after synthesizing all factors.

The decision of the evaluating factors and weights:

According to the selecting principles of scheme choice for OAWR, it is thinking about economic and sustainable water supply in the paper.

For the economic aspect, it is contain investment, fee of contaminative water disposal, and development of economy. For the sustainable water supply aspect, it is contain daily water supplying and water conservation. Then, the syntheses evaluating factor gathering will be obtained:

$\mathbf{G}$ = [investment, daily water supplying, fee of contaminative water disposal, water conservation, development of economy]

Assuming that the weights are determined by some methods, (such as analytic hierarchy process method or the arithmetic average method), which was used in this stuy and the weights are unitary.

The decision of the comments gathering:

For the selecting of scheme choice for OAWR, the comment domain which has nine comments to one factor G_1 will be obtainded, where $\mathbf{S}$ = [best, better, good, less good, generic, less bad, bad, worse, worst] is called the fuzzy linguistic scale (Xu and Da, 2002; Xu, 2002). The triangular fuzzy numbers corresponding to the above scale are as follows: best = [0.8,0.9,1.0], better = [0.7,0.8,0.9], good = [0.6,0.7,0.8], less good = [0.5,0.6,0.7], generic = [0.4,0.5,0.6], less bad = [0.3,0.4,0.5], bad = [0.2,0.3,0.4], worse = [0.1,0.2,0.3], worst = [0,0.1,0.2] ; where best>better>good>less good>generic>less bad>bad >worse>worst.

One-factor evaluation system:

Based on the domain S, the one-factor evaluation matrix can be created, then can evaluate the candidate scheme based on fuzzy calculation to get the best scheme.

$$\mathbf{C} = [G_2, \cdots, G_5] \times \begin{vmatrix} x_{11} & x_{12} & \cdots & x_{15} \\ x_{21} & x_{22} & \cdots & x_{25} \\ \cdots & \cdots & \cdots & \cdots \\ x_{51} & x_{52} & \cdots & x_{55} \end{vmatrix} = [S_1, \cdots, S_5] \tag{A7}$$

1.4 The step of evaluation system

The specifics steps are as follows:

Let X as layout gathering, and let $\mathbf{G}$ as attribute gathering, and let $\mathbf{D}$ as the decision maker gathering.

Step 1 The decision maker. $d_k \in \mathbf{D}$ gives the fuzzy linguistic evaluating information $r_{ij}^{(k)}$ of the *i*-th evaluated object x_j in the attribute G_j. The evaluating matrix $\mathbf{R_k}$ is obtained.

Step 2 Use GIOWA operator g to assemble the *i*-rank fuzzy linguistic evaluating information in the evaluating matrix $\mathbf{R_k}$. The synthesizing evaluating value $\mathbf{r_i^{(k)}} (i \in N, k = 1,2,\cdots,t)$,

$$\mathbf{r_i^{(k)}} = \mathbf{g}[\langle r_{i1}^{(k)}, u_1, \hat{\alpha}_{i1}^{(k)} \rangle, \cdots, \langle r_{im}^{(k)}, u_m, \hat{\alpha}_{im}^{(k)} \rangle] = \sum \omega_l \hat{b}_{il}^{(k)} \tag{A8}$$

$r_{ij}^{(k)} \in \mathbf{S}$, $G_j \in \mathbf{G}$, $\hat{\alpha}_{ij}^{(k)}$ is the triangular fuzzy numbers corresponding to $\mathbf{r_{ij}^{(k)}}$, $\boldsymbol{\omega} = [\omega_1, \cdots, \omega_m]^T$ is the associated

weighting vector of **g**, $\omega_l \in [0,1]$, $\hat{b}_{il}^{(k)}$ is the third component of 3 dimension pair corresponding to the *l*-th largest element of $\mathbf{r_{ij}^{(k)}}$ ($j \in \{1,2,\cdots,m\}$).

Determine the weighting vector ω. In order to get the weighting vector objectively, we may use analytic hierarchy process （AHP） method to determine the weighting vector, $\boldsymbol{\omega} = [\omega_1, \cdots, \omega_m]^T$.

Step 3 Use $r_i^{(k)} (i \in N)$ to arrange an order and choice excellent about the scheme choice for OAWR. If the triangular fuzzy numbers corresponding to the water resources's optimal allocation of conceptual **A** and **B** are $[a_1, a_2, a_3]$ and $[b_1, b_2, b_3]$, $[a_1, a_2, a_3] > [b_1, b_2, b_3]>$, then the scheme **A** is better than scheme **B**.

2. A Case Study: Water resources allocation problem in Shen Yang

For the case of scheme choice for OAWR in the north of Shen Yang city, according to the level of socio-economic development and water conservation ability to determine the six daily water supplying schemes. See the Table 1.1. Evaluating scheme in the north area of Shen Yang . See the Figure 1.5.

Table 1. 1 The constitute of the six daily water supplying schemes

Development of economy	Water conservation	
	Moderation	Strengthen
High	Scheme Ⅴ	Scheme Ⅵ
Moderation	Scheme Ⅰ	Scheme Ⅱ
Low	Scheme Ⅲ	Scheme Ⅳ

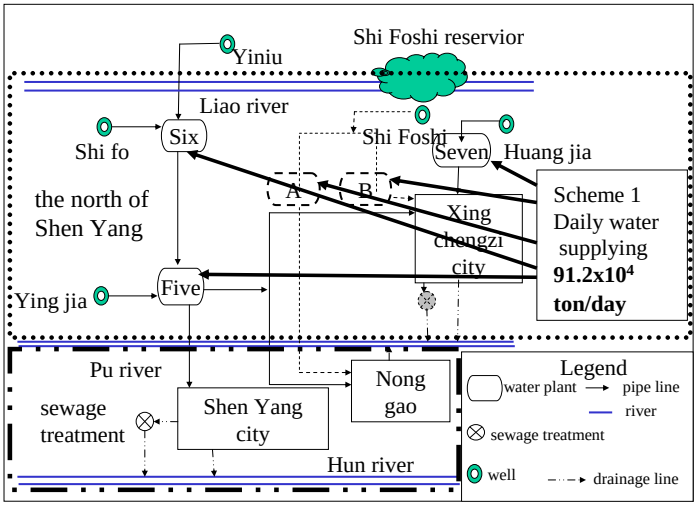

Figure 1. 8 Evaluating scheme in the north area of Shen Yang. The round dot line area is the north of Shen Yang, the long dash dot dot line area is Shen Yang city. The solid line means that is consist now, the dash line means that is planning construct.

There are six evaluating schemes $x_i (i = 1,2,\cdots,6)$ in the evaluation system and five attributes : investment (G_1), daily water supplying (G_2), fee of contaminative water disposal (G_3), water conservation (G_4) and development of economy (G_5).

Then the attributes can be obtained, the attributes are listed in Table 1.2. (based on the research project 'Controlling Mode of Water Supply System of Shi Foshi Reservoir and its Risk Analysis')

Table 1. 2 Attribute of optimal allocation of water resources (OAWR)

x_i \ G_j	Investment (10^8 yuan/yr)	Daily water supplying (10^4 ton/day)	Fee of contaminated water disposal (10^8 yuan/yr)	Water conservation	Eevelopment of economy
1	9.6	91.02	0.83	moderation	moderation
2	8.97	77.33	0.7	strengthen	moderation
3	6.8	63.8	0.58	moderation	low
4	6.01	54.15	0.49	strengthen	low
5	13.22	134.2	1.24	moderation	high
6	12.9	114.73	1.06	strengthen	high

(1) In this paper, we used analytic hierarchy process （AHP） method to determine the weighting vector $\boldsymbol{\omega}_1 = [0.04, 0.14, 0.08, 0.37, 0.37]^T$.

(2) Now, there are three experts $d_k, (k = 1,2,3)$ evaluate the six candidate schemes $x_1, x_2, x_3, x_4, x_5, x_6$, respectively through the factors gathering u_l one by one. Then we can get following fuzzy evaluating matrix $\mathbf{R_k}$, see Table 1.3-1.5.

Table 1. 3 Evaluating matrices by d_1

x_i \ G_j	Investment	Daily water supplying	Fee of contaminated water disposal	Water conservation	Development of economy
1	less good	less good	generic	less good	less good
2	good	good	less good	bad	less good
3	best	better	better	less good	bad
4	best	better	best	bad	bad
5	worse	worse	worst	less good	bad
6	bad	bad	worse	bad	bad

Table 1. 4 Evaluating matrices by d_2

G_j / x_i	Investment	Daily water supplying	Fee of contaminated water disposal	Water conservation	Development of economy
1	generic	less good	less bad	good	good
2	less good	better	generic	bad	good
3	better	better	better	good	bad
4	better	better	better	bad	bad
5	worst	worse	worst	good	bad
6	worse	bad	worse	bad	bad

Table 1. 5 Evaluating matrices by d_3

G_j / x_i	Investment	Daily water supplying	Fee of contaminated water disposal	Water conservation	Development of economy
1	less good	less good	less good	better	better
2	good	less good	less good	bad	better
3	better	good	better	better	bad
4	better	good	better	bad	bad
5	worse	bad	worse	better	bad
6	worse	bad	worse	bad	bad

Through GIOWA operator we can concentrate the fuzzy language evaluation information in the row of the evaluation matrix $\mathbf{R_k}$ and it will get the syntheses attribute evaluation $\mathbf{r_i^{(k)}}$ $(i = 1,2,3,4,5,6,\ k = 1,2,3)$ of the decision making layout x_i by expert d_k.

At first we may calculate the syntheses attribute evaluation information of every layout provided by expert d_1. Because of $r_{11}^{(1)}$ = less good, $r_{12}^{(1)}$ = less good, $r_{13}^{(1)}$ = generic, $r_{14}^{(1)}$ = less good, $r_{15}^{(1)}$ = less good. $r_{11}^{(1)} \sim r_{12}^{(1)} \sim r_{14}^{(1)} \sim r_{15}^{(1)} > r_{13}^{(1)}$. From the fuzzy language criterion in above content we know that the triangle fuzzy functions corresponding to $\mathbf{r_{ij}^{(1)}}$ $(j = 1,2,\cdots,5)$ are:

$$\mathbf{r_i^{(k)}} = \mathbf{g}[\langle r_{i1}^{(k)}, u_1, \bar{\alpha}_{i1}^{(k)} \rangle, \cdots, \langle r_{im}^{(k)}, u_m, \bar{\alpha}_{im}^{(k)} \rangle] = \sum \omega_l \bar{b}_{il}^{(k)}$$

$\bar{\alpha}_{11}^{(1)} = \bar{\alpha}_{12}^{(1)} = \bar{\alpha}_{14}^{(1)} = \bar{\alpha}_{15}^{(1)} = [0.5, 0.6, 0.7],\ \bar{\alpha}_{13}^{(1)} = [0.4, 0.5, 0.6],$

So,

$\hat{b}_{11}^{(1)} = \hat{b}_{12}^{(1)} = \hat{b}_{14}^{(1)} = \hat{b}_{15}^{(1)} = \hat{\alpha}_{11}^{(1)} = \hat{\alpha}_{12}^{(1)} = \hat{\alpha}_{14}^{(1)} = \hat{\alpha}_{15}^{(1)} = [0.5, 0.6, 0.7]$,

$\hat{b}_{13}^{(1)} = \hat{\alpha}_{13}^{(1)} = [0.4, 0.5, 0.6]$,

And we can get the below expression through GIOWA arithmetic operator g and the calculation principle of triangle fuzzy number:

$$\mathbf{r_1^{(1)}} = \mathbf{g}[\langle r_{11}^{(1)}, u_1, \hat{\alpha}_{11}^{(1)}\rangle, \langle r_{12}^{(1)}, u_2, \hat{\alpha}_{12}^{(1)}\rangle, \langle r_{13}^{(1)}, u_3, \hat{\alpha}_{13}^{(1)}\rangle, \langle r_{14}^{(1)}, u_4, \hat{\alpha}_{14}^{(1)}\rangle, \langle r_{15}^{(1)}, u5, \hat{\alpha}_{15}^{(1)}\rangle]$$

$$= \sum \omega_1 \hat{b}_{1l}^{(1)} = \begin{vmatrix} 0.04 & 0.14 & 0.08 & 0.37 & 0.37 \end{vmatrix} \times \begin{vmatrix} 0.5 & 0.6 & 0.7 \\ 0.5 & 0.6 & 0.7 \\ 0.5 & 0.6 & 0.7 \\ 0.5 & 0.6 & 0.7 \\ 0.4 & 0.5 & 0.6 \end{vmatrix} = [0.5, 0.6, 0.7]$$

Analogously we can get:

$$\mathbf{r_2^{(1)}} = \mathbf{g}[\langle r_{21}^{(1)}, u_1, \hat{\alpha}_{21}^{(1)}\rangle, \langle r_{22}^{(1)}, u_2, \hat{\alpha}_{22}^{(1)}\rangle, \langle r_{23}^{(1)}, u_3, \hat{\alpha}_{23}^{(1)}\rangle, \langle r_{24}^{(1)}, u_4, \hat{\alpha}_{24}^{(1)}\rangle, \langle r_{25}^{(1)}, u5, \hat{\alpha}_{25}^{(1)}\rangle]$$

$$= \sum \omega_1 \hat{b}_{2l}^{(1)} = \begin{vmatrix} 0.04 & 0.14 & 0.08 & 0.37 & 0.37 \end{vmatrix} \times \begin{vmatrix} 0.6 & 0.7 & 0.8 \\ 0.6 & 0.7 & 0.8 \\ 0.5 & 0.6 & 0.7 \\ 0.5 & 0.6 & 0.7 \\ 0.2 & 0.3 & 0.4 \end{vmatrix} = [0.4, 0.5, 0.6]$$

$$\mathbf{r_3^{(1)}} = \mathbf{g}[\langle r_{31}^{(1)}, u_1, \hat{\alpha}_{31}^{(1)}\rangle, \langle r_{32}^{(1)}, u_2, \hat{\alpha}_{32}^{(1)}\rangle, \langle r_{33}^{(1)}, u_3, \hat{\alpha}_{33}^{(1)}\rangle, \langle r_{34}^{(1)}, u_4, \hat{\alpha}_{34}^{(1)}\rangle, \langle r_{35}^{(1)}, u5, \hat{\alpha}_{35}^{(1)}\rangle]$$

$$= \sum \omega_1 \hat{b}_{3l}^{(1)} = \begin{vmatrix} 0.04 & 0.14 & 0.08 & 0.37 & 0.37 \end{vmatrix} \times \begin{vmatrix} 0.8 & 0.9 & 1.0 \\ 0.7 & 0.8 & 0.9 \\ 0.7 & 0.8 & 0.9 \\ 0.5 & 0.6 & 0.7 \\ 0.2 & 0.3 & 0.4 \end{vmatrix} = [0.4, 0.5, 0.6]$$

$$\mathbf{r_4^{(1)}} = \mathbf{g}[\langle r_{41}^{(1)}, u_1, \hat{\alpha}_{41}^{(1)}\rangle, \langle r_{42}^{(1)}, u_2, \hat{\alpha}_{42}^{(1)}\rangle, \langle r_{43}^{(1)}, u_3, \hat{\alpha}_{43}^{(1)}\rangle, \langle r_{44}^{(1)}, u_4, \hat{\alpha}_{44}^{(1)}\rangle, \langle r_{45}^{(1)}, u5, \hat{\alpha}_{45}^{(1)}\rangle]$$

$$= \sum \omega_1 \hat{b}_{4l}^{(1)} = \begin{vmatrix} 0.04 & 0.14 & 0.08 & 0.37 & 0.37 \end{vmatrix} \times \begin{vmatrix} 0.8 & 0.9 & 1.0 \\ 0.8 & 0.9 & 1.0 \\ 0.7 & 0.8 & 0.9 \\ 0.2 & 0.3 & 0.4 \\ 0.2 & 0.3 & 0.4 \end{vmatrix} = [0.4, 0.5, 0.6]$$

$$\mathbf{r_5^{(1)}} = \mathbf{g}[\langle r_{51}^{(1)}, u_1, \hat{\alpha}_{51}^{(1)}\rangle, \langle r_{52}^{(1)}, u_2, \hat{\alpha}_{52}^{(1)}\rangle, \langle r_{53}^{(1)}, u_3, \hat{\alpha}_{53}^{(1)}\rangle, \langle r_{54}^{(1)}, u_4, \hat{\alpha}_{54}^{(1)}\rangle, \langle r_{55}^{(1)}, u5, \hat{\alpha}_{55}^{(1)}\rangle]$$

$$= \sum \omega_1 \hat{b}_{5l}^{(1)} = \begin{vmatrix} 0.04 & 0.14 & 0.08 & 0.37 & 0.37 \end{vmatrix} \times \begin{vmatrix} 0.5 & 0.6 & 0.7 \\ 0.2 & 0.3 & 0.4 \\ 0.1 & 0.2 & 0.3 \\ 0.1 & 0.2 & 0.3 \\ 0 & 0.1 & 0.2 \end{vmatrix} = [0.1, 0.2, 0.3]$$

$$\mathbf{r_6^{(1)}} = \mathbf{g}[\langle r_{61}^{(1)}, u_1, \hat{\alpha}_{61}^{(1)}\rangle, \langle r_{62}^{(1)}, u_2, \hat{\alpha}_{62}^{(1)}\rangle, \langle r_{63}^{(1)}, u_3, \hat{\alpha}_{63}^{(1)}\rangle, \langle r_{64}^{(1)}, u_4, \hat{\alpha}_{64}^{(1)}\rangle, \langle r_{65}^{(1)}, u5, \hat{\alpha}_{65}^{(1)}\rangle]$$

$$= \sum \omega_l \hat{b}_{6l}^{(1)} = \begin{vmatrix} 0.04 & 0.14 & 0.08 & 0.37 & 0.37 \end{vmatrix} \times \begin{vmatrix} 0.2 & 0.3 & 0.4 \\ 0.2 & 0.3 & 0.4 \\ 0.2 & 0.3 & 0.4 \\ 0.2 & 0.3 & 0.4 \\ 0.1 & 0.2 & 0.3 \end{vmatrix} = [0.2, 0.3, 0.4]$$

In the same way we can get the syntheses evaluation information of d_2 and d_3.

$\mathbf{r_1^{(2)}} = [0.4, 0.5, 0.6]$, $\mathbf{r_2^{(2)}} = [0.4, 0.5, 0.6]$, $\mathbf{r_3^{(2)}} = [0.4, 0.5, 0.6]$, $\mathbf{r_4^{(2)}} = [0.3, 0.4, 0.5]$,

$\mathbf{r_5^{(2)}} = [0.1, 0.2, 0.3]$, $\mathbf{r_6^{(2)}} = [0.2, 0.3, 0.4]$

$\mathbf{r_1^{(3)}} = [0.5, 0.6, 0.7]$, $\mathbf{r_2^{(3)}} = [0.4, 0.5, 0.6]$, $\mathbf{r_3^{(3)}} = [0.5, 0.6, 0.7]$, $\mathbf{r_4^{(3)}} = [0.3, 0.4, 0.5]$,

$\mathbf{r_5^{(3)}} = [0.1, 0.2, 0.3]$, $\mathbf{r_6^{(3)}} = [0.1, 0.2, 0.3]$

(3) Finally, we can concentrate the syntheses attribute evaluation $\mathbf{r_i^{(k)}}$ ($k = 1,2,3$) of the layout x_i provided by the three experts through GIOWA arithmetic operator g'. If $\boldsymbol{\omega}_2 = [0.3, 0.4, 0.3]^{\mathrm{T}}$, then it get the colony syntheses attribute evaluation $\mathbf{r_i}$ ($i = 1,2,3,4,5,6$) of decision making layout x_i:

$$\mathbf{r_1} = \mathbf{g}'[\langle r_1^{(1)}, d_1, \hat{\alpha}_1^{(1)}\rangle, \langle r_1^{(2)}, d_2, \hat{\alpha}_1^{(2)}\rangle, \langle r_1^{(3)}, d_3, \hat{\alpha}_1^{(3)}\rangle]$$

$$= \sum \omega_2 \hat{b}_{1l}^{(1)} = \begin{vmatrix} 0.3 & 0.4 & 0.3 \end{vmatrix} \times \begin{vmatrix} 0.6 & 0.7 & 0.8 \\ 0.5 & 0.6 & 0.7 \\ 0.4 & 0.5 & 0.6 \end{vmatrix} = [0.5, 0.6, 0.7]$$

$$\mathbf{r_2} = \mathbf{g}'[\langle r_2^{(1)}, d_1, \hat{\alpha}_2^{(1)}\rangle, \langle r_2^{(2)}, d_2, \hat{\alpha}_2^{(2)}\rangle, \langle r_2^{(3)}, d_3, \hat{\alpha}_2^{(3)}\rangle]$$

$$= \sum \omega_2 \hat{b}_{2l}^{(1)} = \begin{vmatrix} 0.3 & 0.4 & 0.3 \end{vmatrix} \times \begin{vmatrix} 0.4 & 0.5 & 0.6 \\ 0.4 & 0.5 & 0.6 \\ 0.4 & 0.5 & 0.6 \end{vmatrix} = [0.4, 0.5, 0.6]$$

$$\mathbf{r_3} = \mathbf{g}'[\langle r_3^{(1)}, d_1, \hat{\alpha}_3^{(1)}\rangle, \langle r_3^{(2)}, d_2, \hat{\alpha}_3^{(2)}\rangle, \langle r_3^{(3)}, d_3, \hat{\alpha}_3^{(3)}\rangle]$$

$$= \sum \omega_2 \hat{b}_{3l}^{(1)} = \begin{vmatrix} 0.3 & 0.4 & 0.3 \end{vmatrix} \times \begin{vmatrix} 0.5 & 0.6 & 0.7 \\ 0.4 & 0.5 & 0.6 \\ 0.4 & 0.5 & 0.6 \end{vmatrix} = [0.4,0.5,0.6]$$

$$\mathbf{r_4} = \mathbf{g}'[\langle r_4^{(1)}, d_1, \hat{\alpha}_4^{(1)}\rangle, \langle r_4^{(2)}, d_2, \hat{\alpha}_4^{(2)}\rangle, \langle r_4^{(3)}, d_3, \hat{\alpha}_4^{(3)}\rangle]$$

$$= \sum \omega_2 \hat{b}_{4l}^{(1)} = \begin{vmatrix} 0.3 & 0.4 & 0.3 \end{vmatrix} \times \begin{vmatrix} 0.4 & 0.5 & 0.6 \\ 0.3 & 0.4 & 0.5 \\ 0.3 & 0.4 & 0.5 \end{vmatrix} = [0.3,0.4,0.5]$$

$$\mathbf{r_5} = \mathbf{g}'[\langle r_5^{(1)}, d_1, \hat{\alpha}_5^{(1)} \rangle, \langle r_5^{(2)}, d_2, \hat{\alpha}_5^{(2)} \rangle, \langle r_5^{(3)}, d_3, \hat{\alpha}_5^{(3)} \rangle]$$

$$= \sum \omega_2 \hat{b}_{5l}^{(1)} = \begin{vmatrix} 0.3 & 0.4 & 0.3 \end{vmatrix} \times \begin{vmatrix} 0.1 & 0.2 & 0.3 \\ 0.1 & 0.2 & 0.3 \\ 0.1 & 0.2 & 0.3 \end{vmatrix} = [0.1, 0.2, 0.3]$$

$$\mathbf{r_6} = \mathbf{g}'[\langle r_6^{(1)}, d_1, \hat{\alpha}_6^{(1)} \rangle, \langle r_6^{(2)}, d_2, \hat{\alpha}_6^{(2)} \rangle, \langle r_6^{(3)}, d_3, \hat{\alpha}_6^{(3)} \rangle]$$

$$= \sum \omega_2 \hat{b}_{6l}^{(1)} = \begin{vmatrix} 0.3 & 0.4 & 0.3 \end{vmatrix} \times \begin{vmatrix} 0.2 & 0.3 & 0.4 \\ 0.2 & 0.3 & 0.4 \\ 0.1 & 0.2 & 0.3 \end{vmatrix} = [0.2, 0.3, 0.4]$$

(4) Ordering the candidate sites through $\mathbf{r_i}$ ($i = 1,2,3,4,5,6$) ,

$$\mathbf{r}_1 > \mathbf{r}_2 \approx \mathbf{r}_3 > \mathbf{r}_4 > \mathbf{r_6} > \mathbf{r}_5$$

So, we get

$$x_1 > x_2 \approx x_3 > x_4 > x_6 > x_5$$

Therefore, the best scheme is x_1.

From the Table 2, it is obviously to find that investment of Schemes 3 and 4 are much more than that of Scheme 1. However, the development of economy of Schemes 3 and 4 are so low that it is not acceptable for the economic situation in Shen Yang. Investment of Schemes 3 and 4 are bigger than that of Scheme 1. On the other hand, economic development of Schemes 3 and 4 indicate quite quick progress. It may cause the crisis of the scheme from the economic point of view. As the investment of Scheme 1 is not so much, the development of economy will be moderate that is considered to be agreeable as the sustainable choice. From the comprehensive judgment of the results estimated by the fuzzy language evaluation and GIOWA operator, it can be concluded that Scheme 1 is acceptable as a best choice in the schemes of optimal allocation of water resources (OAWR) in Shen Yang.

For the scheme 1, its total investment is 9.6 hundred million yuan, its total fee of contaminated water disposal is 0.83 hundred million yuan. These are not so much. Its daily water supplying is 91.02 ten thousand ton/day that is enough for the next 20 years daily water supplying in Shen Yang. Its water conservation and the development of economy are moderate. Then we can come to the conclusion that the Scheme 1 is acceptable to the sustainable choice.

3. Discussions and Conclusions

The group multi-attribute decision making problems have been widespread in practical use. The scheme choice for OAWR is one of them. In this study, using fuzzy language evaluation and the generalized induced ordered weighted averaging (GIOWA) operator, the evaluation system of Scheme choice for OAWR was established. It chose the five constituents: investment (Yuan), daily water supplying (ton/day), fee of contaminated water disposal (Yuan), water conservation (fuzzy language), and development of economy (fuzzy language). And analytic hierarchy process (AHP) method is used to determine the weighting vector. A case study was conducted to check its applicability. The result showed

that the evaluation system of the scheme choice for OAWR was feasible and useful.

In this research, the alternate water supply source and reliability of water supply are not considered. It is better to add a factor of reliability about water supply in the syntheses evaluating factor gathering. It is also better to think of the total investment to the alternate water supply sources. Finally it should be noted that the method used in this study still needs the improvement in getting the better weighting vector, and how to get a reasonable weighting vector and how improve these issues are very important. And these are the focus study in the future.

Chapter 2

Numerical Models and Background of Liaodong Bay Coastal Plain

2.1 Introduction

Seawater intrusion is the movement of saline water into freshwater aquifers. Normally, it is caused by ground-water pumping from coastal wells. Seawater intrusion can also occur as the result of a natural process like a storm surge from a hurricane. Seawater intrusion process is one part of water cycle. Thus, in this study, we simulate the seawater intrusion based on the groundwater model (SEAWAT code) and considered the atmosphere-ocean interaction. Atmospheric–ocean coupled model is introduced as part of Regional Environment Simulator (RES) to simulate the precipitation and seawater level. The basic equation of these sub-models will introduce for understanding the dynamic of each models.

2.2 Regional Environment Simulator (RES)

The Regional Environment Simulator (RES) is a coupled system of numerical simulation modules for Meteorology, Physical Oceanography, Land Surface Vegetation, Hydrology, Estuary and Coastal Dynamics and Urban Environment, which is mainly made use of natural environmental assessment against human activities the numerical model system. The RES combined three simulation parts such as atmosphere-ocean interactions, atmosphere-land surface interactions, and coastal-estuarine circulation. The model used in RES to represent the atmospheric circulation is Pennsylvania State University and National Center for Atmospheric Research Fifth Generation Meso-scale Model (PSU/NCAR-MM5; Grell et al. 1996). The land surface is represented by the detailed multi-layer land surface model (SOLVEG; Nagai 2002). Basins hydrology and water quality is represented by Hydrology Simulation Program- Fortran (HSPF, Bicknell et al. 1997). The ocean waves are represented by the third-generation ocean wind-wave model of NOAA, WW3 (WW3; Tolman 2002) and Simulating Waves Nearshore (SWAN), and the ocean currents are represented by the Princeton Ocean Model (POM; Mellor 2004). Additional models that can extend the RES application field include estuary circulation model, coastal models, dynamic vegetation model, and urban air quality model. The system configuration of RES is briefly explained as follows, (Figure 2.1).

In this study, the governing equations and model concepts of atmospheric model (MM5) and ocean circulation Model (POM) of RES are described as follow.

2.2.1 Atmospheric Model: MM5

The MM5 model (MM5; Grell *et al*., 1996) was developed by the Pennsylvania State University/ National Center for Atmospheric Research (PSU/ NCAR) mesoscale model and is used in RES. MM5 is non-hydrostatic model designed to simulate or predict

mesoscale and regional-scale for meteorological conditions in huge areas such as convective systems, fronts, monsoons, hurricanes, cyclones, tropical storms, land-sea breezes, mountain-valley circulations and urban heat islands. A multiple nest-grid is included in MM5 model that can support up 10 domains of arbitrary horizontal resolution at few kilometer scale and coarser outer domains ranging about 200 km. The MM5 used a terrain-following non-dimensional pressure or sigma-*p* on 23 levels amd a four-dimensional data-assimilation capability to keep the model closed to the true condition from the errors and the gaps in the initial analysis and deficiencies in model physics. The horizontal grid used Arakawa-Lamb B-staggering of the velocity variables with respect to the scalars and more physics options. The governing equations and the parameterization of physical processes in MM5 are mentioned in the following sections.

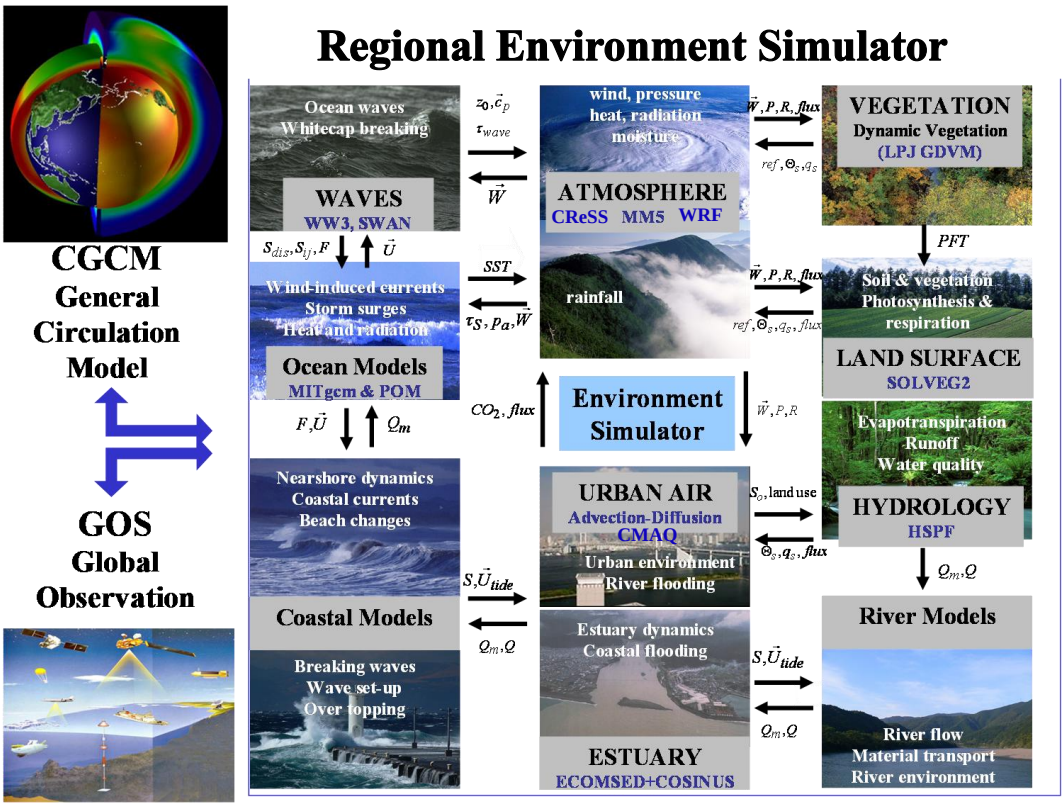

Figure 2. 1 System configuration of RES (Yamashita *et al.*, 2007)

Basic equations

According Grell *et al.* (1995), in the MM5 model, the non-hydrostatic equations in terms of Cartesian-sigma coordinate (x, y, σ) without consideration of the Earth's curvature can be written in the system equations (Eqs. 2.1 to 2.8). So far as the sigma coordinate and the derivatives with respect to (x, y, σ), refer the under mentioned Eqs.(2.9)-(2.13) in POM model.

For the non-hydrostatic pressure p':

$$\frac{\partial p'}{\partial t} + \mathbf{v}\cdot\nabla p' = \rho_0 g w - \gamma p \nabla\cdot\mathbf{v} + \frac{\gamma p}{T}\left(\frac{\dot{Q}}{c_p} + \frac{T_0}{\theta_0} D_\theta\right) \tag{2.1}$$

Momentum (x-component) with velocity u:

$$\frac{\partial u}{\partial t}+\mathbf{v}\cdot\nabla u=-\frac{1}{\rho}\left(\frac{\partial p'}{\partial x}-\frac{\sigma}{p^*}\frac{\partial p^*}{\partial x}\frac{\partial p'}{\partial \sigma}\right)+fv+D_u \tag{2.2}$$

Momentum (y-component) with velocity v:

$$\frac{\partial u}{\partial t}v+\mathbf{v}\cdot\nabla v=-\frac{1}{\rho}\left(\frac{\partial p'}{\partial y}-\frac{\sigma}{p^*}\frac{\partial p^*}{\partial y}\frac{\partial p'}{\partial \sigma}\right)-fu+D_v \tag{2.3}$$

Momentum (z-component) with velocity w:

$$\frac{\partial w}{\partial t}+\mathbf{v}\cdot\nabla w=\frac{\rho_0}{\rho}\frac{g}{p^*}\frac{\partial p'}{\partial \sigma}-\frac{g}{\gamma}\frac{p'}{p}+g\frac{p_0}{p}\frac{T'}{T_0}-\frac{gR_d}{c_p}\frac{p'}{p}+D_w \tag{2.4}$$

Thermodynamics with temperature T:

$$\frac{\partial T}{\partial t}+\mathbf{v}\cdot\nabla T=\frac{1}{\rho c_p}\left(\frac{\partial p'}{\partial t}+\mathbf{v}\cdot\nabla p'-\rho_0 g w\right)+\frac{\dot{Q}}{c_p}+\frac{T_0}{\theta_0}D_w \tag{2.5}$$

where ρ, θ, $\dot{Q}$ and D_* are the density, potential temperature, heating rate due to diabatic processes and subgrid-scale eddy viscous terms for each equation, respectively. The constants g, f, R_d, c_p and γ are acceleration due to gravity, Coriolis parameter, gas constant of dry air, heat capacity of constant pressure of air and ratio of heat capacity for air constant pressure to constant volume.

Advection terms can be addressed as

$$\mathbf{v}\cdot\nabla A=u\frac{\partial A}{\partial x}+v\frac{\partial A}{\partial y}+\dot{\sigma}\frac{\partial A}{\partial \sigma} \tag{2.6}$$

where $\dot{\sigma}$ can be addressed as

$$\dot{\sigma}=-\frac{\rho_0 g}{p^*}w-\frac{\sigma}{p^*}\frac{\partial p^*}{\partial x}u-\frac{\sigma}{p^*}\frac{\partial p^*}{\partial y}v \tag{2.7}$$

Divergence term can be expanded in the terrain following coordinates as

$$\nabla\cdot\mathbf{v}=\frac{\partial u}{\partial x}-\frac{\sigma}{p^*}\frac{\partial p^*}{\partial x}\frac{\partial u}{\partial \sigma}+\frac{\partial v}{\partial y}-\frac{\sigma}{p^*}\frac{\partial p^*}{\partial y}\frac{\partial v}{\partial \sigma}-\frac{\rho_0 g}{p^*}\frac{\partial w}{\partial \sigma} \tag{2.8}$$

Physical Processes in MM5

In MM5 model, the physical mechanisms such as cumulus parameterizations (ICUPA), planetary boundary layer (PBL) schemes, explicit moisture schemes, atmospheric radiation schemes and surface schemes are described together the advection and various source and sink terms. Table 2.1 shows the available physics schemes in MM5 model such as cumulus, explicit moisture, radiation, land surface and PBL schemes. Figure 2.2 through 2.6 show the simple illustrations of cumulus scheme, PBL processes, microphysics

processes, atmospheric radiation processes and surface processes, respectively. Then, the last figure (Figure 2.7) presents the direct interactions of physics parameterizations (refer to Grell et al., 1996 for more details).

Table 2. 1 Physics parameterizations in the MM5 model

Physics Schemes	References
Cumulus schemes	
Anthes-Kuo scheme	
Grell scheme	Grell *et al*. (1996)
Arakawa-Schubert scheme	Grell *et al*. (1996)
Fritsch-Chappell scheme	Fritsch and Chappell (1980)
Kain-Fritsch scheme	Kain and Fritsch (1993)
Betts-Miller scheme	Betts and Miller (1986, 1993)
Kain-Fritsch 2 scheme	Kain (2002)
Shallow cumulus scheme	
Planetary boundary layer (PBL) and diffusion schemes	
Bulk PBL scheme	
Blackadar PBl scheme	
Burk-Thompson PBL scheme	Burk and Thompson (1989)
ETA PBL scheme	Janjic (1989, 1994)
MRF PBL scheme	Hong and Pan (1996)
Gayno-Seaman PBL scheme	Ballard *et al*. (1991); Shafran *et al*. (2000)
Pleim-Chang PBL Scheme	Pleim and Chang (1992)
Moist vertical diffusion	
Thermal roughness length	
Horizontal diffusion	Zangel (2002)
Explicit moisture schemes	
Dry scheme	
Stable precipitation scheme	
Warm rain scheme	
Dudhia simple ice scheme	
Mixed phase (Reisner 1) scheme	Reisner *et al*. (1998)
Goddard microphysics scheme	Lin *et al*. (1983); Tao *et al*. (1989, 1993)
Reisner graupel (Reisner 2) scheme	
Schultz microphysics scheme	Schultz (1995)
Radiation schemes	
Simple cooling scheme	
Surface radiation scheme	
Cloud-radiation scheme	
CCM2 radiation scheme	Hack et al. (1993)
RRTM longwave scheme	Mlawer et al. (1997)
Surface schemes	
Force/ restore (Blakadar) scheme	
Five-Layer Soil model	Dudhia (1996)
Noah Land-Surface Model	Chen and Dudhia (2001)
Pleim-Xiu Land-Surface Model	Xiu and Pleim (2000)
Bucket Soil Moisture Model	
Snow Cover Model	

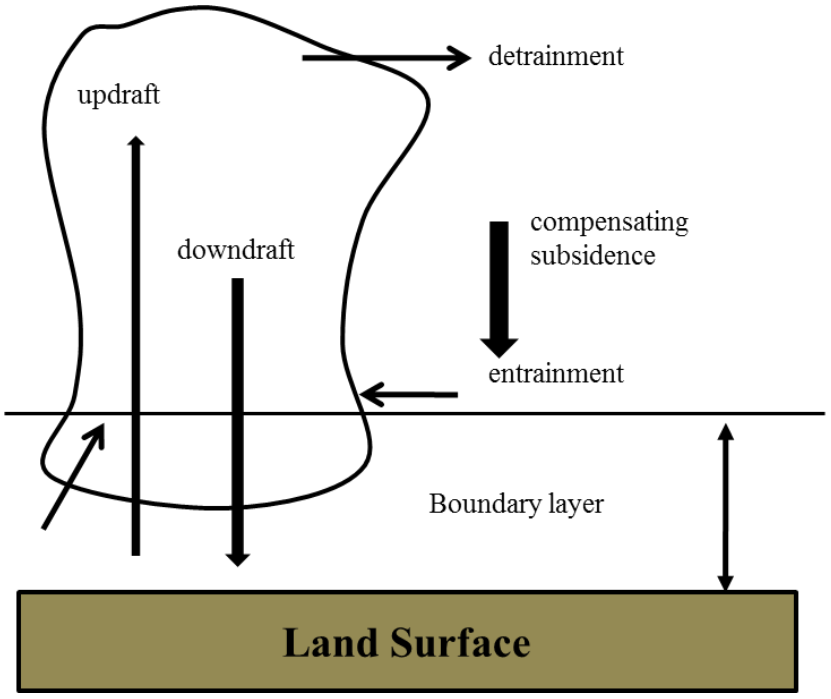

Figure 2. 2 Illustration of cumulus processes in MM5

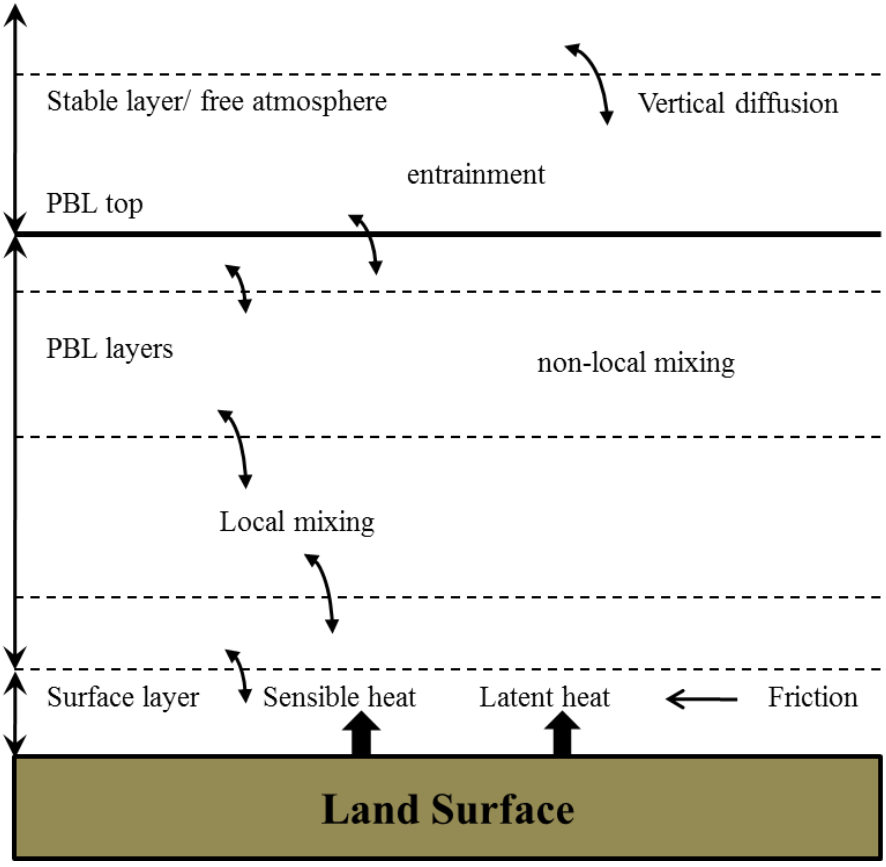

Figure 2. 3 Illustration of PBL processes in MM5

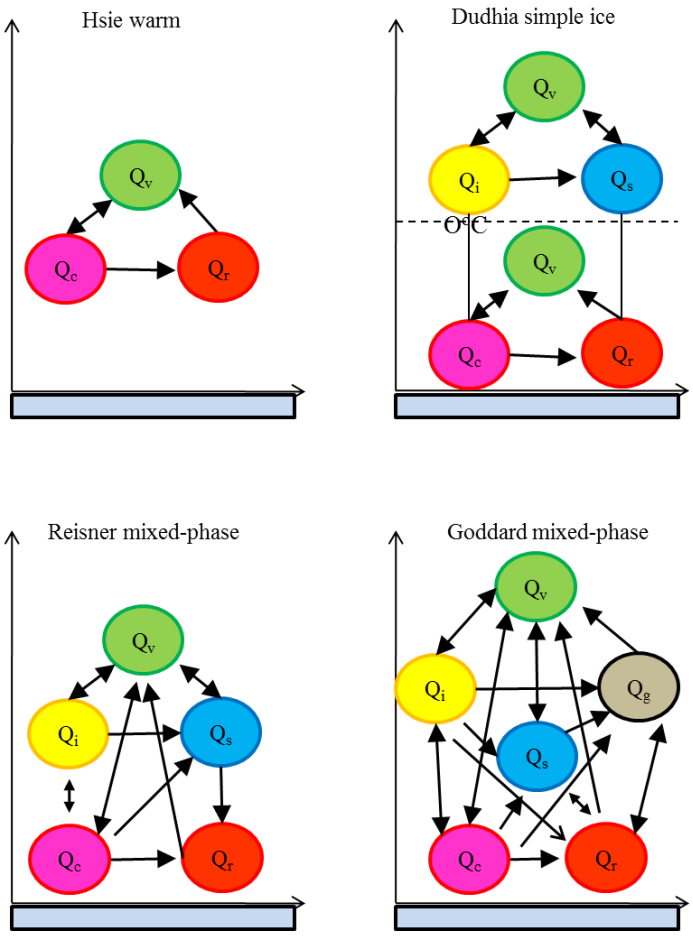

Figure 2. 4 Illustration of microphysics processes in MM5 model

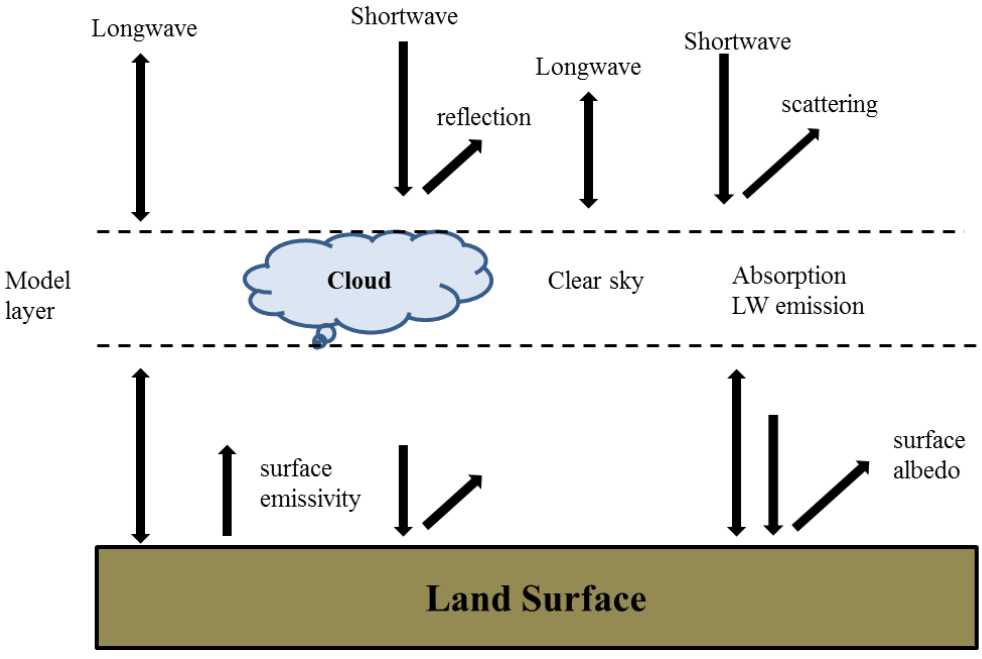

Figure 2. 5 Illustration of radiation processes in MM5 model

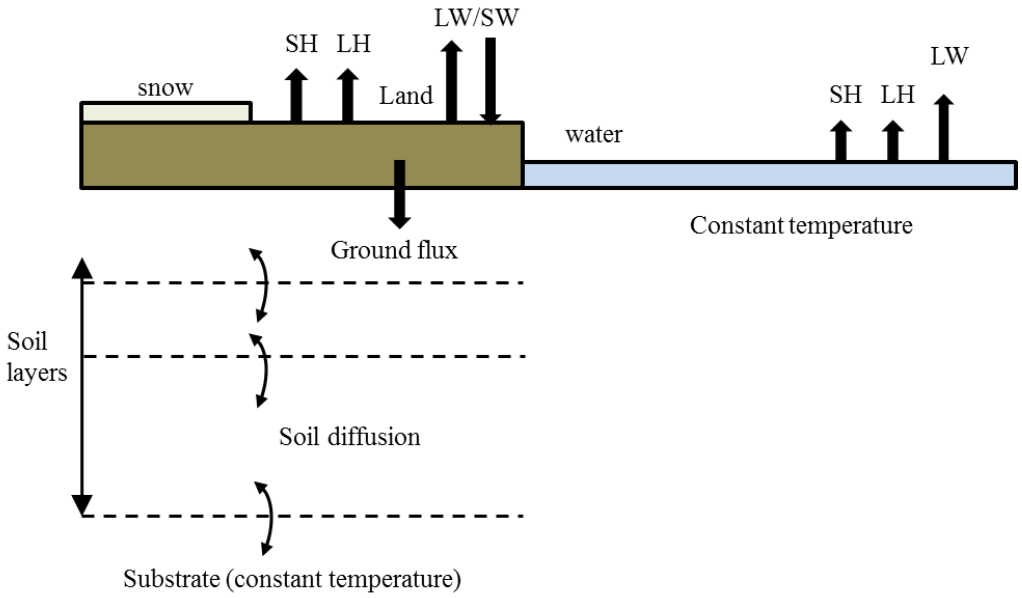

Figure 2. 6 Illustration of surface processes in MM5 model

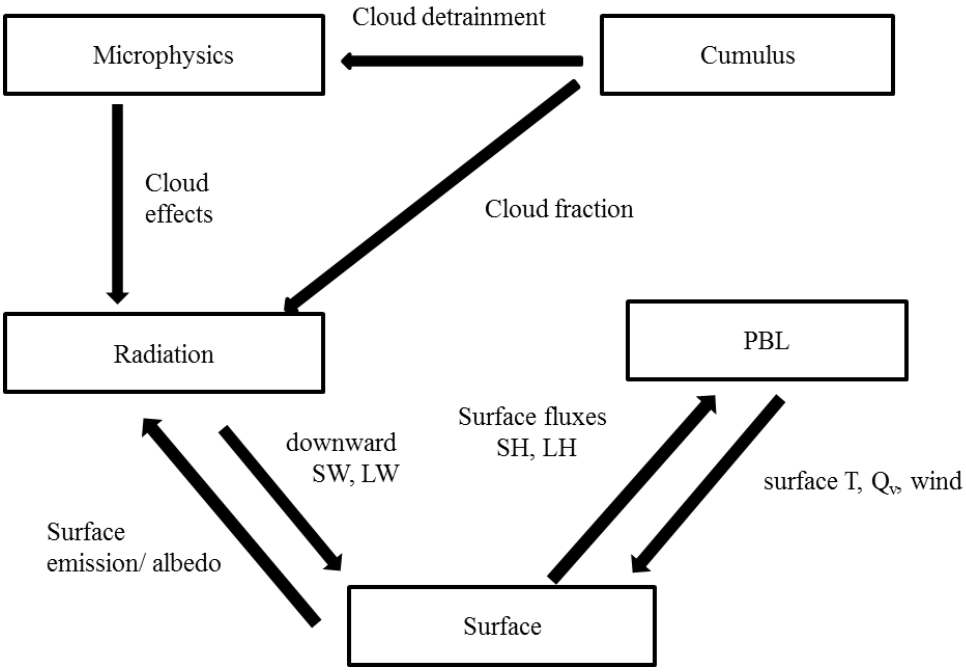

Figure 2. 7 Direct interactions of parameterizations in MM5 model

2.2.2 Ocean Circulation Model: POM

The POM model is developed in Princeton University and applied to many oceanographic problems. POM is three-dimensional coastal ocean model, incorporating a turbulence model to provide a realistic parameterization of vertical mixing processes. The prognostic variables are the three components of velocity, free surface elevation, temperature, salinity, turbulent kinetic energy and turbulent length scale. The momentum equations are non-

linear and incorporate a variable Coriolis parameter. The main features of POM model can be summarized as follow (Mellor, 2004).

1) It contains an imbedded second moment turbulence closure model to estimate vertical mixing coefficients.
2) It is a sigma coordinate model that the vertical coordinate is scaled on water depth.
3) The horizontal grid uses curvilinear orthogonal coordinates and the Arakawa C grid differencing scheme.
4) The horizontal time differencing is explicit whereas the vertical differencing is implicit. The latter eliminates time constraints for the vertical coordinate and permits the use of fine vertical resolution in the surface and bottom boundary layers.
5) POM model has a free surface boundary and a split time step in two different modes. The external mode is two-dimensional and uses a short time step based on the CFL condition and the external wave speed. On the other hand, the internal mode is three-dimensional and uses a long time step based on the CFL condition and the internal wave speed.
6) The complete thermodynamics is implemented.

Governing equations of POM

POM model is based on hydrostatic primitive equations in bottom following sigma coordinate. The relation between the Cartesian and sigma coordinate is based on the transformation:

$$\sigma = \frac{z - \eta(x,y,t)}{D}; \qquad D \equiv H(x,y) + \eta(x,y,t) \tag{2.9}$$

where $H(x,y)$ is bottom topography and $\eta(x,y,t)$ is the surface elevation. Here the simple derivation of governing equations in sigma coordinate is a follows;

Let $\phi(x,y,z,t) = \phi'(x,y,z,t)$ and then the partial derivation of ϕ using the chain rule become

$$\frac{\partial \phi}{\partial x} = \frac{\partial \phi'}{\partial x} + \frac{\partial \phi'}{\partial \sigma}\frac{\partial \sigma}{\partial x} = \frac{\partial \phi'}{\partial x} - \frac{\partial \phi^*}{\partial \sigma}\frac{1}{D}\left(\frac{\partial \eta}{\partial x} + \sigma\frac{\partial D}{\partial x}\right) \tag{2.10}$$

$$\frac{\partial \phi}{\partial y} = \frac{\partial \phi'}{\partial y} + \frac{\partial \phi'}{\partial \sigma}\frac{\partial \sigma}{\partial y} = \frac{\partial \phi'}{\partial y} - \frac{\partial \phi^*}{\partial \sigma}\frac{1}{D}\left(\frac{\partial \eta}{\partial y} + \sigma\frac{\partial D}{\partial y}\right) \tag{2.11}$$

$$\frac{\partial \phi}{\partial z} = \frac{1}{D}\frac{\partial \phi'}{\partial \sigma} \tag{2.12}$$

$$\frac{\partial \phi}{\partial t} = \frac{\partial \phi'}{\partial t} + \frac{\partial \phi'}{\partial \sigma}\frac{\partial \sigma}{\partial t} = \frac{\partial \phi'}{\partial t} - \frac{\partial \phi^*}{\partial \sigma}\frac{1}{D}\left(\frac{\partial \eta}{\partial t} + \sigma\frac{\partial D}{\partial t}\right) \tag{2.13}$$

Now, the continuity equation $\nabla.\mathbf{v} = 0$ in conventional Cartesian coordinate is

$$\frac{\partial u}{\partial x}+\frac{\partial v}{\partial y}+\frac{\partial w}{\partial z}=0 \tag{2.14}$$

substituting (2.10), (2.11), (2.12) into continuity equation (2.14) become

$$\frac{\partial u}{\partial x}-\frac{\partial u}{\partial \sigma}\frac{1}{D}\left(\frac{\partial \eta}{\partial x}+\sigma\frac{\partial D}{\partial x}\right)+\frac{\partial v}{\partial y}-\frac{\partial v}{\partial \sigma}\frac{1}{D}\left(\frac{\partial \eta}{\partial y}+\sigma\frac{\partial D}{\partial y}\right)+\frac{1}{D}\frac{\partial w}{\partial \sigma}=0 \tag{2.15}$$

using the relation of Cartesian vertical velocity to sigma velocity;

$$w=\dot{\sigma}+u\left(\frac{\partial \eta}{\partial x}+\sigma\frac{\partial D}{\partial x}\right)+v(\left(\frac{\partial \eta}{\partial y}+\sigma\frac{\partial D}{\partial y}\right)+\frac{\partial \eta}{\partial t}+\sigma\frac{\partial D}{\partial t} \tag{2.16}$$

where $\dot{\sigma}$ is the vertical velocity in sigma coordinates, gives

$$\frac{\partial u}{\partial x}-\frac{\partial u}{\partial \sigma}\left(\frac{\partial \eta}{\partial x}+\sigma\frac{\partial D}{\partial x}\right)+\frac{\partial v}{\partial y}-\frac{\partial v}{\partial \sigma}\left(\frac{\partial \eta}{\partial y}+\sigma\frac{\partial D}{\partial y}\right)$$

$$+\frac{\partial \dot{\sigma}}{\partial \sigma}-\frac{\partial u}{\partial \sigma}\left(\frac{\partial \eta}{\partial x}+\sigma\frac{\partial D}{\partial x}\right)+\frac{\partial uD}{\partial x}-\frac{\partial v}{\partial \sigma}\left(\frac{\partial \eta}{\partial y}+\sigma\frac{\partial D}{\partial y}\right)+\frac{\partial vD}{\partial y}+\frac{\partial \eta}{\partial t}=0 \tag{2.17}$$

that can be simplified as

$$\frac{\partial uD}{\partial x}+\frac{\partial vD}{\partial y}+\frac{\partial \dot{\sigma}}{\partial \sigma}+\frac{\partial \eta}{\partial t}=0 \tag{2.18}$$

since $D_t=\partial\eta/\partial t$

After applying the same procedure to momentum, temperature and salinity equations, the governing equations the model solves are described in the below.

The momentum equation

$$\frac{\partial uD}{\partial t}+\frac{\partial u^2D}{\partial x}+\frac{\partial uvD}{\partial y}+\frac{\partial u\dot{\sigma}}{\partial \sigma}=$$

$$fvD-gD\frac{\partial \eta}{\partial x}-\frac{gD^2}{\rho_r}\int_\sigma^0[\frac{\partial p'}{\partial x}-\frac{\sigma'}{D}\frac{\partial D}{\partial x}\frac{\partial p'}{\partial \sigma'}]\partial\sigma'+\frac{\partial}{\partial \sigma}[\frac{K_M}{D}\frac{\partial u}{\partial \sigma}]+F_x \tag{2.19}$$

$$\frac{\partial vD}{\partial t}+\frac{\partial uvD}{\partial x}+\frac{\partial v^2D}{\partial y}+\frac{\partial v\dot{\sigma}}{\partial \sigma}=$$

$$fuD-gD\frac{\partial \eta}{\partial y}-\frac{gD^2}{\rho_r}\int_\sigma^0[\frac{\partial p'}{\partial y}-\frac{\sigma'}{D}\frac{\partial D}{\partial y}\frac{\partial \rho'}{\partial \sigma'}]\partial\sigma'+\frac{\partial}{\partial \sigma}[\frac{K_M}{D}\frac{\partial v}{\partial \sigma}]+F_y \tag{2.20}$$

where ρ_r is the reference density, ρ' is the in situ density, g is the gravitational acceleration, K_M is the vertical kinematic viscosity and f is the latitudinal variation of the Coriolis parameter.

Temperature and salinity equations

$$\frac{\partial TD}{\partial t}+\frac{\partial TuD}{\partial x}+\frac{\partial TvD}{\partial y}+\frac{\partial T\dot{\sigma}}{\partial \sigma}=\frac{\partial}{\partial \sigma}[\frac{K_H}{D}\frac{\partial T}{\partial \sigma}]+F_T-\frac{\partial R}{\partial z} \tag{2.21}$$

$$\frac{\partial SD}{\partial t}+\frac{\partial SuD}{\partial x}+\frac{\partial SvD}{\partial y}+\frac{\partial S\dot{\sigma}}{\partial \sigma}=\frac{\partial}{\partial \sigma}[\frac{K_H}{D}\frac{\partial S}{\partial \sigma}]+F_S \tag{2.22}$$

where T and S are the temperature and salinity, K_H is the vertical eddy diffusivity of turbulent momentum mixing and *R* is the radiation flux.

The turbulent equations

In POM model, Mellor-Yamada turbulence closure model (Mellow and Yamada, 1982) is incorporated to calculate for the turbulent diffusion of momentum, heat and salt. The vertical mixing coefficients K_M , K_H are obtained by appealing to a second order turbulence closure model which characterized the turbulence by equations of turbulence kinetic energy q^2 and turbulence kinetic energy length scale l

$$\frac{\partial q^2 D}{\partial t}+\frac{\partial uq^2 D}{\partial x}+\frac{\partial vq^2 D}{\partial x}+\frac{\partial \dot{\sigma} q^2}{\partial \sigma}=$$

$$\frac{\partial}{\partial \sigma}[\frac{K_q}{D}\frac{\partial q^2}{\partial \sigma}]+\frac{2K_M}{D}[(\frac{\partial u}{\partial \sigma})^2+(\frac{\partial vu}{\partial \sigma})^2]+\frac{2g}{\rho_o}K_H\frac{\partial \tilde{\rho}}{\partial \sigma}-\frac{2Dq^3}{B_1 l}+F_q \tag{2.23}$$

$$\frac{\partial q^2 lD}{\partial t}+\frac{\partial uq^2 lD}{\partial x}+\frac{\partial vq^2 lD}{\partial x}+\frac{\partial \dot{\sigma} q^2 l}{\partial \sigma}=$$

$$\frac{\partial}{\partial \sigma}[\frac{K_q}{D}\frac{\partial q^2 l}{\partial \sigma}]+E_1 l[\frac{2K_M}{D}((\frac{\partial u}{\partial \sigma})^2+(\frac{\partial vu}{\partial \sigma})^2)+E_3 K_H\frac{\partial \tilde{\rho}}{\partial \sigma}]-\frac{Dq^3}{B_1}\tilde{W}+F_l \tag{2.24}$$

The horizontal viscosity and diffusion terms in the momentum equations are defined as:

$$F_x \equiv \frac{\partial}{\partial x}(H\tau_{xx})+\frac{\partial}{\partial y}(H\tau_{xy}) \tag{2.25}$$

$$F_y \equiv \frac{\partial}{\partial x}(H\tau_{xy}) + \frac{\partial}{\partial y}(H\tau_{yy}) \tag{2.26}$$

where,

$$\tau_{xx} = 2A_M \frac{\partial u}{\partial x}, \tau_{xy} = \tau_{yx} = 2A_M \left(\frac{\partial u}{\partial y} + \frac{\partial v}{\partial y} \right), \tau_{yy} = 2A_M \frac{\partial v}{\partial y} \tag{2.27}$$

Also,

$$F_\phi \equiv \frac{\partial}{\partial x}(Hq_x) + \frac{\partial}{\partial y}(Hq_y) \tag{2.28}$$

where,

$$q_x = A_H \frac{\partial \phi}{\partial x}, q_y = A_H \frac{\partial \phi}{\partial y} \tag{2.29}$$

where $F_{x'}, F_{y'}, F_T, F_S, F_q$ are the horizontal viscosity and diffusion terms and $\tilde{W}$ is the wall proximity function. ϕ represents the *T*, *S*, q^2 or $q^2 l$.

The equations governing the dynamics of coastal circulation contain fast moving external gravity waves and slow moving internal gravity waves. The surface gravity waves are obtained in the 2D external mode by the vertically integrating equations for continuity and momentum equations where the thermodynamic properties are invariant in time. On the other hand, the 3D internal mode is governed by the hydrostatic primitive equation as described in Eq. 2.19 to Eq. 2.24.

2.3 Seawater Intrusion Simulation Models

2.3.1 Background of seawater intrusion simulation study

Seawater intrusion is the movement of ocean water into fresh groundwater due to the natural processes or human activities. As the economy developed, water demand increases and over-exploitation of groundwater occurs, especially, in many coastal regions. It has disturbed the established balance between fresh water and seawater, causing extensive seawater intrusion into groundwater.

A number of mathematical and numerical models have been used to predict the location and movement of the seawater intrusion. Depending on the method of treating the interface for simulation, these models can be grouped into two broad categories: sharp interface and variable density models where a wide interface zone separates the two fluids (Langevin et al., 2006; Bobba, 1993; Kopsiaftis et al., 2009). The sharp interface assumption can be applied only under certain the conditions when the width of the transition zone is relatively small compared with the thickness of the aquifer.

The phenomenon of freshwater underlain by saltwater is quite a complex one. Fresh water and salt water are miscible fluids, and a transition zone always exists between them in coastal aquifers (Bear, 1979). In reality the two fluids are separated by a transition zone with a continuous upward gradient of salt concentration from saltwater below to uncontaminated above (Bobba, 1993). The transition zone will move landwards when seawater intrusion occurs. The variable density model that accounts for the effects of hydrodynamic dispersion may be more practical as it provides more details concerning the transition zone (Langevin et al., 2006). Therefore, most of the simulation codes have been developed based on the variable density theory. Several computer codes that can be used to simulate density-dependent groundwater flow have been developed (Sorek, 1999). In the last decade, there were several density-dependent simulation codes developed based on the commonly-used groundwater model (Lin et al., 2009) MODFLOW which was developed by the U.S. Geological Survey (Harbaugh et al., 2000; Mcdonald and Harbaugh, 1998). The major commonly-used MODFLOW-based computer codes are SEAWAT (Guo and Bennett, 1998; Guo and Langevin, 2002; Langevin et al., 2003), MOCDENS3D (Oude Essink, 1998), MODHMS (Harbaugh et al., 2000; Mcdonald and Harbaugh, 1998) and the Sea Water Intrusion Package for MODFLOW (Bakker and Schaars, 2003). All these codes can been applied to case studies and have been documented and tested with variable-density benchmark problems. A summary of these four codes was reviewed by Langevin *et al.* (2004).

A number of case studies on seawater intrusion based on variable density theory in coastal area have been done. Andersen *et al.* (1988) used a finite element model SWICHA (Huyakorn *et al*., 1987) to simulate salt-water intrusion in Hallandale, located on the east coast of Florida. A numerical model on saltwater intrusion in the unconfined coastal aquifer of Ravenna (Italy) was made by Giambastiani *et al.* (2007) with the MOCDENS3D code. El-Bihery (2009) numerically simulated seawater intrusion of Quaternary aquifer in Ras Sudr, Egypt by using MODFLOW code and SEAWAT. Lin *et al.* (2009) used SEAWAT code to solve a variable-density groundwater flow and miscible salt transport numerical model to investigate the extent of seawater intrusion in the Gulf coast aquifers of Alabama, USA. Kopsiaftis *et al.* (2009) constructed a quasi-three-dimensional variable density transport model about unconfined aquifer located in the central part of Thira Island (Santorini) solved iteratively using software package FEFLOW. Bhosale (2002) used SUTRA (Voss, 1984) model to simulation of seawater intrusion in Ernakulam coast.

The FEFLOW, SUTRA, and SEAWAT have been applied on a variety of real-world and analytical problems. SUTRA (Saturated-Unsaturated Transport) employs a two-dimensional finite-element approximation of the governing equations in space and an implicit finite-difference approximation in time and is suitable for simulation of a vertical section of an aquifer that is subject to seawater intrusion. On the other hand, FEFLOW is a finite-element package for simulating 3D and 2D fluid density-coupled flow, contaminant mass (salinity) and heat transport occurring in the subsurface. It evaluates the impact of seawater intrusion caused by groundwater pumping and/or mining activities along coastal regions (Bhosale and Kumar, 2002). The SEAWAT program is a coupled version of MODFLOW and MT3DMS designed to simulate three dimensional finite-difference, variable-density and saturated ground-water flow. Flexible equations were added to the program to allow fluid density to be calculated as a function of one or more MT3DMS species (Langevin *et al.*, 2002). While FEFLOW and SEAWAT allow transport for more than one solute, as is required for simulation of contaminant migration in the variable density flows of coastal aquifers, SEAWAT is the more readily available of these codes,

being available free of charge from the U.S. Geological Survey free of charge (U.S. Geological Survey, 2004) (Guo and langevin, 2002; Evans, 2005).

2.3.2 SEAWAT model

The SEAWAT code is a useful tool for simulating various types of variable-density fluid flow through complex geometries and geological settings, including seawater intrusion in coastal aquifers, submarine groundwater discharge, brine transport, and groundwater flow near salt domes (Lin et al., 2009). The fundamental concept of this code is to combine the two commonly-used groundwater flow and solute transport modeling programs of MODFLOW (Harbaugh et al., 2000) and MT3DMS (Zheng and Wang, 1999). These were combined into a single program that solves the basic equations for density-dependent groundwater flow and solute-transport.

The governing equation for density-dependent groundwater flow in terms of freshwater head, which is solved by MODFLOW routines in the SEAWAT code (Guo and Langevin, 2002; Lin, 2009) is as follows:

$$\begin{aligned}&\frac{\partial}{\partial\alpha}\left\{\rho K_{f\alpha}\left[\frac{\partial h_f}{\partial\alpha}+\frac{\rho-\rho_f}{\rho_f}\frac{\partial Z}{\partial\alpha}\right]\right\}+\frac{\partial}{\partial\beta}\left\{\rho K_{f\beta}\left[\frac{\partial h_f}{\partial\beta}+\frac{\rho-\rho_f}{\rho_f}\frac{\partial Z}{\partial\beta}\right]\right\}\\&+\frac{\partial}{\partial\gamma}\left\{\rho K_{f\gamma}\left[\frac{\partial h_f}{\partial\gamma}+\frac{\rho-\rho_f}{\rho_f}\frac{\partial Z}{\partial\gamma}\right]\right\}=\rho S_f\frac{\partial h_f}{\partial t}+\theta\frac{\partial\rho}{\partial C}\frac{\partial C}{\partial t}-\bar{\rho}q_s\end{aligned} \tag{2.30}$$

where α, β, γ are orthogonal coordinate axes, aligned with the principal directions of permeability; $K_{f\alpha}$, $K_{f\beta}$, $K_{f\gamma}$, are equivalent freshwater hydraulic conductivities in the three coordinate directions, respectively [LT^{-1}]; ρ is the fluid density [ML^{-3}]; ρ_f is the density of freshwater [ML^{-3}]; h_f is the equivalent freshwater head [L]; Z is the elevation above datum of the center of a model cell [L]; S_f is the equivalent freshwater specific storage [L^{-1}]; θ is effective porosity [dimensionless]; C is the solute concentration [ML^{-3}]; $\bar{\rho}$ is the density of water entering from a source or leaving through a sink [ML^{-3}]; q_s is the volumetric flow rate of sources or sinks per unit volume of aquifer [T^{-1}]; and t is time [T].

The solute-transport governing equation of SEAWAT code utilizes MT3DMS routines (Zheng and Wang, 1999) are as follows:

$$\frac{\partial C}{\partial t}=\nabla\cdot(D\cdot\nabla C)-\nabla\cdot(\bar{\upsilon}C)-\frac{q_s}{\theta}C_s+\sum_{k=1}^{N}R_k \tag{2.31}$$

where D is the hydrodynamic dispersion coefficient [L^2T^{-1}]; $\bar{\upsilon}$ is the fluid velocity [LT^{-1}]; C_s is the solute concentration of water entering from sources or leaving through sinks [ML^{-3}]; and $R_k(k=1,...,N)$ is the rate of solute production or decay in reaction k of N different reactions [$ML^{-3}T^{-1}$].

For a coupled variable-density flow and solute-transport simulation, fluid density is assumed to be a function only of solute concentration; the effects of pressure and

temperature on fluid density are ignored (Langevin et al., 2003). A linear equation of state is used by the SEAWAT code to convert solute concentration to fluid density (Guo and Langevin, 2002; Langevin et al., 2007):

$$\rho = \rho_f + \frac{\partial \rho}{\partial C} C \tag{2.32}$$

where $\partial p / \partial C$ is the slope of the equation. The value for $\partial p / \partial C$ is entered by the user and depends on the units used for the simulation. For example, if meters and kilograms are used for the simulation, $\partial p / \partial C$ is set to a value of 0.7143, which approximately equals the change in fluid density divided by the change in solute concentration for freshwater and seawater. For more details on SEAWAT, refer to its user's manual (Guo and Langevin, 2002).

2.4 Background of Liaodong Bay Coastal Plain

2.4.1 Site description

The Liaodong Bay coastal plain is located in the south of Liao Ning province, China. The major study area is Panjing city and a part of Yingkou city, Jinzhou City and Haicheng city as shown in Figure 2.8. This area is rich in surface water, but the rainfall runoff has been decreasing year by year and water quality has been degraded. About 50% of the city water and 100% industrial water depend on the groundwater in this area (Bian and Tang, 2006).

The average annual temperature is 8.4 ℃. The average maximum temperature is 23.8 ℃ in the summer and -9.7 ℃ in winter respectively. The average annual rainfall is 647.4 mm/year. Most of the rainfall occurs in the summer from June to September, about 63% of the annual precipitation. The average annual evaporation is 1,568.6 mm/year.

The study area is located in the central and southern Liaodong Bay coastal Plain. The terrain is flat and the north area is higher than the south area. The northern elevation is from 5 to 7 m and most of the southern part is below 5 m. The terrain sloping from northeast to southwest and the average hydraulic gradient is 0.02 ‰.

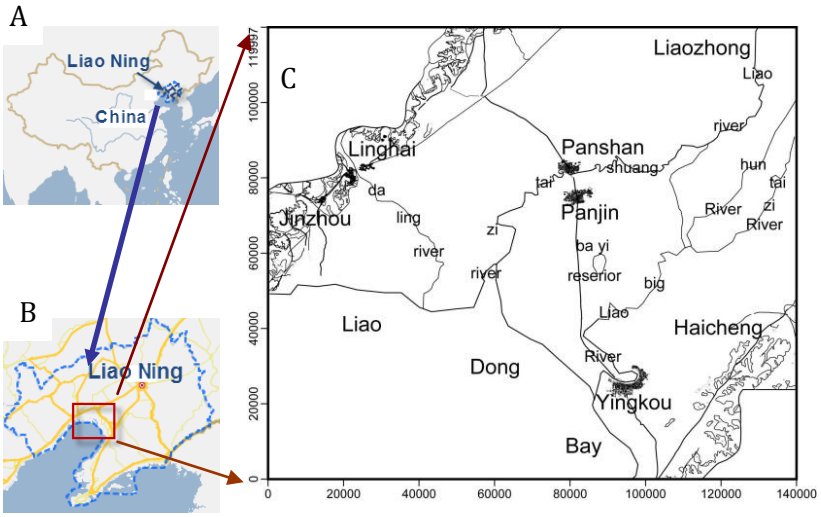

Figure 2. 8 A: Location of Liaodong Bay coastal plain, China. B: blue line indicates Liao Ning and red line the study area. C : the simulation domain. (unit in meter)

2.4.2 Stratigraphy

The subsurface stratigraphy of the study area consists of sedimentary rocks ranging from the Cenozoic to Holocene in age. There are two stratigraphies in the Quaternary stratigraphy and Neozoic stratigraphy in the study area. The generally east–west cross-section was constructed in the area (Figure 2.9) based on the geologic information as well as geologic data from a few drilled wells.

The Quaternary stratigraphy

In the study area, the Quaternary stratigraphy development was essentially complete with thickness ranges from 65 to 400 m (Bian and Tang, 2006; Li, 2005; Wang et al., 2992; Xue, 2005). The Quaternary stratigraphy from top to bottom developed in the ages of Holocene, upper Pleistocene, middle Pleistocene and lower Pleistocene, and the corresponding genetic types of deposits are alluvium-marine, alluvium, alluvium-diluvium, and diluvium. Quaternary stratigraphy from the new to the old is described as follows :

1) Holocene stratigraphy (Q_{4p}). It is Alluvium-marine. The underlying layer is Pleistocene alluvium with thickness between 10 and 15 m. It consists of a yellowish brown to grayish brown Middle-fine to fine sand, clay and silt. At piedmont alluvial-pluvial fan, the major portion consists of sand and gravel with thickness between 10 to 170 mm and quartz based mineral composition.

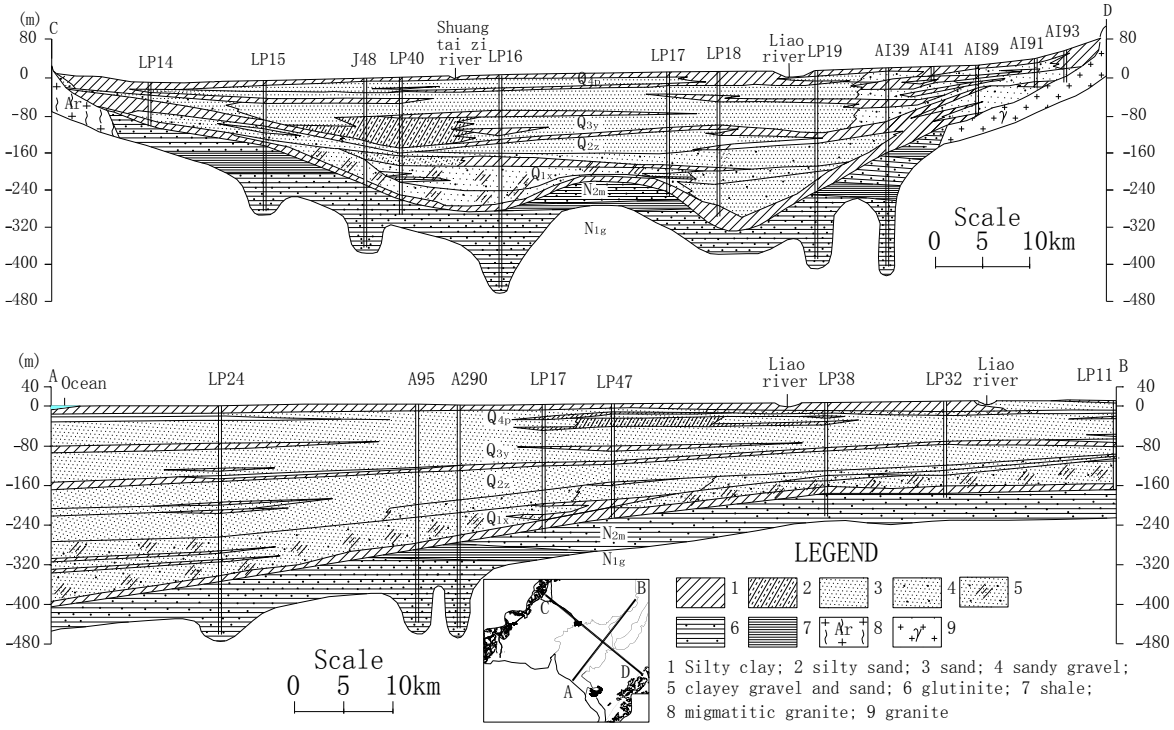

Figure 2. 9 Geologic cross-sections of the study area

2) Upper Pleistocene stratigraphy (Q_{3y}). The Upper Pleistocene stratigraphy underlies the Holocene sediments and overlies the Middle Pleistocene alluvial sediments. It is between 50 and 60 m thick. Lithology is mainly fine sand or sub-clay in the coarse sand lens sub-folder and the color is gray, gray and yellow, and taupe. The plasticity of sub-clay is strong loam, and iron disseminated widely. Fine sand or coarse sand is good sorted

rounded, mainly consist of quartz, feldspar and so on. There is stable sub-clay layer at the top of Upper Pleistocene layer.

3) Middle Pleistocene stratigraphy (Q_{2z}). The Middle Pleistocene stratigraphy underlies the Upper Pleistocene alluvium sediments on the system and has a thickness between 40 and 50 m thick. Lithology is mainly coarse sand, fine sand and clay sub sandwich. The color is gray, grayish yellow or gray-green. Fine sand, coarse sand sorting rounded is normal, the main mineral composition of quartz and feldspar. Sand distribution is more continuous while sub-clay layers are discontinuous. There is no recognizable divides between Upper Pleistocene layer and Middle Pleistocene layer.

4) Lower Pleistocene stratigraphy (Q_{1x}). The lower Pleistocene stratigraphy underlies the Middle Pleistocene alluvium sediments and has a thickness of more than 20 m. Lithology is gravel mixed sub-clay and there are thin layers of sub-clay in some area. There is stable sub-clay layer at the top and bottom of lower Pleistocene layer. The color is gray, gray and yellow, dark gray.

In summary, the Quaternary sedimentary rhythm in the study area is clear and cyclic. The Holocene, upper Pleistocene and middle Pleistocene deposits have two or more cycles. Because of the tectonic movement, the middle Pleistocene deposit in this area extended toward further northwest than the lower Pleistocene deposit and the Holocene deposit extended further toward northwest than the middle Pleistocene deposit. This is the overlap of the stacking features.

The Neogene stratigraphy

The Neogene stratigraphy consists of upper Neozoic stratigraphy and lower Neozoic stratigraphy. The upper Neozoic sedimentary is thicker and is divided into Minghuazhen group (N_{2m}) and Guantao group (N_{1g}) formations. There are volcanic and volcaniclastic rocks with the foot and fluvial-lacustrine clastic deposits. The fault is well-developed and sedimentation distribution is not uniform. Under the function of different sedimentation, there are seven high-angle normal faults and the separation is 10 to 145 m. These faults broke thrust the Minghua and Guantao formation (Bian and Tang, 2006; Li, 2005; Wang et al., 1992; Xue, 2005).

1) Minghuazhen stratigraphy (N_{2m})

The Minghuazhen group is a lacustrine sediment divided into two belts. The top belt of the Minghuazhen group formation forms a white sandrock from semi-coarse to semi-fine particle, conglomerate with sand and sandrock with gravel. The particles were sorted well, gravel diameter is 0.5 - 20 mm, which became slender from north to south. The bottom belt of the Minghuazhen group is gray green, yellow brown development bedding and plant detritus is composed of mudrock, conglomerate with sand. The mudrock is attributed in the upper apex and partial deletion with thickness from 4 to 8 m. The embedded depth of the formation is between 100 to 400 m with shallow portion from bilateral east-west to middle and deeper part from northeast to southwest (Bian and Tang, 2006).

2) Guantao stratigraphy (N_{1g})

Guantao stratigraphy lies under the Minghuazhen group Formation with a set of coarse clastic fluvial facies deposits, lithology single, gray-white, light gray green conglomerate

with boulders, small conglomerate, pebbly sandstone, sandstone mudstone, there are the gray green mudstone, muddy silt layer or lens. Gravel diameter is generally 3 - 10mm. The particles are sorted poor. The embedded depth of the formation is between 350 to 1200 m with shallow portion from bilateral east-west to middle and deeper portion from northeast to southwest. The thickness of the formation is generally 50 - 370 m with thicker and deeper layer from bilateral east-west to middle and from northeast to southwest. In the eastern and western of study area, the Guantao stratigraphy is missing.

The lower Neozoic is located below the upper Neozoic. The upper part forms Dongying group formation (E_d) lithology which mainly consists mainly of white, light gray sandstone and glutenite, variegated mudstone. Its thickness is 200 - 1600m. The bottom layer is Shahejie group formation (E_s) which has a complex lithology.

2.4.3 Hydrogeology

Due to the high degree of variability and lateral discontinuity within the geologic units, aquifer zones are determined upon their hydrogeologic characteristics. Hydrogeologic units, utilized as groundwater sources in the study area, are described in Table 2.2.

Major groundwater source occurrences are in the Quaternary layer with unconsolidated rock porosity and in the upper Neozoic clastic rocks layer with the fracture - the pores, in study area. The regional groundwater flow is mainly from north to the Liaodong Bay Sea, from west and east mountain area to the middle plan area.

Quaternary pore water

The Quaternary loosened deposits generally cover the whole study area. Its maximum thickness reaches to 370 m. The major recharge of groundwater is vertical infiltration and the major discharge is evaporation and artificial pumping.

At the east and west sloping piedmont in the study area, groundwater mainly exists in alluvium and alluvium-diluvium sand, gravel, sandy gravel and sandy gravel mixed soil pores.

The thickness of its aquifer ranges from 70 to 160 m with hydraulic conductivity between 20 to 115 m/day and groundwater depth from 3 to l0 m. The potential water source per well is 7,000 m^3/day in this rich water resource region. In the alluvial plains on the northern study area, the main occurrence of groundwater occurs in the fine sand of marine red, medium-fine sand, gravel, sand and gravel mixed soil pores. The aquifer has a thickness which ranges from 150 to 280 m, a hydraulic conductivity between l2 to 20 m/day, a groundwater depth from l to 4 m, and a potential water source per well of 5,000 m^3/day.

Salt water is generally distributed in the mid-south coastal plain where the groundwater mainly exists in alluvium-marine silt, fine sand, fine sand, sand and gravel pores. In this water resource generic region, the thickness of the aquifer ranges from 70 to 360 m, the hydraulic conductivity is 8 to 14 m/day, the groundwater depth is 0.5 to 3 m, and the potential water source per well is 100 to 1,000 m^3/day.

Table 2. 2 Hydrogeologic units

Hydrogeologic unit		**Unit character**	
Aquifer zone	Geologic interval units	Lithologic	Hydrologic
A1 (Quaternary)	Holocene (alluvium-marine)	Sand, yellowish brown to grayish brown, Middle-fine to fine sand, clay and silt.	Sand and gravel in unit comprise major aquifers. The upper aquifers is unconfined aquifer and the lower aquifers are generally semiconfined. At east, west and northern of the study area is major freshwater, Potential soure of 5,000 to 7,000 m^3/day of water per well. Salt water general distribute in the mid-south coastal plain. Potential soure of 100 to 1,000 m^3/day of water per well.
	Upper Pleistocene (alluvium)	Sand, gray, gray and yellow, taupe, fine sand or sub-clay in the coarse sand lens sub-folder, There is stable sub-clay layer at the top it.	
A2 (Quaternary)	Middle Pleistocene (Alluvium-Diluvium)	Sand, gray, grayish yellow or gray-green, coarse sand, fine sand and clay sub sandwich. sub-clay layers are discontinuous.	
	Lower Pleistocene (Diluvium.)	Sand, gray, gray and yellow, dark gray, gravel mixed sub-clay. There is stable sub-clay layer at the top and bottom of lower Pleistocene layer.	
A3 (Upper Neozonic)	Minghuazhen group	Mudstone and argillaceous siltstone. It is impermeable layer.	The thickness is more than 3 m.
A4 (Upper Neozonic)	Minghuazhen group (lacustrine sediment)	The top belt is the white sandrock from semi-coarse to semi-fine particle, conglomerate with sand and sandrock with gravel.The bottom belt is gray green, yellow brown development bedding and plant detritus is composed of mudrock, conglomerate with sand.	Sandstone and pebbly sandstone in unit comprise major aquifers. The aquifers are generally confined. Potential soure of 33.4 to 4,689 m^3/day of water per well.
A5 (Upper Neozonic)	Guantao group (coarse clastic fluvial facies deposits)	gray-white, light gray green conglomerate with boulders, small conglomerate, pebbly sandstone, sandstone mudstone, there are the gray green mudstone, muddy silt layer or lens.	Sandstone and conglomerate in unit comprise major aquifers. The aquifers are generally confined. Potential soure of 273 to 4992 m^3/day of water per well.

The upper Neozoic pore-crack ground water

The upper Neozoic water is divided into Minhuazhen group and Guantao group. Fresh water exists in medium-grained sandrock and conglomerate accumulated in river and lakes.

1) Minhuazhen group groundwater:

The major recharge of groundwater in Minhuazhen group comes from the rainfall runoff of adjacent aquifer, the vertical infiltration of groundwater in the Quaternary layer, and the lateral recharge in an old foundation base. The natural flow field of groundwater reflected the runoff flows slowly from east and west bilaterally and north to southwest. In exploiting condition, the groundwater flow direction is changed and the all surrounding groundwater is collected into the center. In natural condition, the groundwater discharges itself to southwest and the artificial withdrawal is only the discharge way.

Minhuazhen group groundwater consists of freshwater region and salt water region. Saline water is divided into three zones, namely, whole saline water zone, the upper saline, and the lower fresh water zone. The whole saline water zone is distributed in the middle of the saline water zone. Its chlorine concentration is more than 1,000 mg/l. The upper saline and the lower fresh water zone is distributed around the whole saline water zone, where is the transition belt of the saline and fresh water as shown in the Fig. 10B. Its chlorine concentration is more than 250 mg/l. Minghuazhen group salt water occurs in the river and lake facies, paludal facies of siltstone, fine sandstone, fine sandstone, coarse sandstone and pebbly sandstone layer, and the water depth ranges from 230 to 450 m,

Minhuazhen group freshwater mainly occurs in fluvial facies, river and lake facies stratum of coarse sandstone, sandstone, pebbly sandstone and conglomerate. Its roof depth ranges from 100 to 990 m, and the aquifer thickness is between l0 to 900 m.

2) Guantao group groundwater:

A major Guantao group groundwater occurrence is in the fluvial facies deposits, pebbly sandstone, conglomerate, fine conglomerate, and conglomerate boulder with a small amount of pores and cracks. The rock cementation is poor and its aquifer thickness ranges from 14 to 350 m. Groundwater level is generally -5 to -40 m. The confined aquifer has a hydraulic conductivity of 0.8 to 9.2 m/day and the potential water yield per well is 273 to 4992 m^3/day.

2.4.4 Likely causes of seawater intrusion

The first cause is the natural seawater intrusion in the layers of primary sedimentary of marine bed. There exists the several periods of seawater intrusion into Liaodong Bay coastal plain due to earth crust uplift and down-welling since the Neozoic. After the occurrence of the seawater intrusion, in each period a large amount of marine sediment deposited. This is the major cause of salt water intrusion into Liaodong Bay coastal plain in which some original salt water is retained.

The second cause is anthropogenic one. The increasing population subsequently caused the excessive exploitation of groundwater which damaged the water balance of salt water and freshwater, resulting in the increase of seawater intrusion. In Ying Kou City and Jing Zhou City, due to an excessive exploitation of groundwater, the groundwater level has continued

to decline, particularly in the region of Ying Kou City where the freshwater table has reached below sea level in the funnel region.

In Liaodong Bay coastal plain, there were three steps of large-scale transgression of layers since the Quaternary period. The first is the Pan Shan transgression layer in mid-Holocene with thickness from 8 to 34 m. The second is the Pioneer transgression layer in lower Pleistocene with thickness from 44.6 to 79.1 m. The third is the Water resource transgression layer in middle Pleistocene with thickness from 89.2 to 161.8 m. All of the ground water contains salt water in the Quaternary layer in the south of Pan Shan area.

For the salt water in Neozoic period, according to the analysis of the environment of salt water occurrence media, underground salt water distribution, water chemistry and environmental isotope characteristics, it was found out that the original underground salt water of Minghuazhen group is from precipitation, and its origin has no connection with the sea water. The salt water of Minghuazhen group was sealed off from the residual of lake water after its evaporation in the continental deposition environment (Li, 2005).

2.5 Summary

The Regional Environment Simulator (RES) and its components that represent meteorological condition and oceanic condition are represented with focusing on both governing equations and model concepts. Meteorological part is being modeled by MM5 with appropriate physics and FDDA applied. On the other hand, ocean current and circulations are described by POM. Background of seawater intrusion simulation study and the governing equations of SEAWAT code are represented.

Background of Liaodong Bay coastal plain such as stratigraphy, hydrogeology, seawater intrusion distribution of Liao Ning Province, China and its likely causes of seawater intrusion are also represented in this chapter.

REFERENCES

Andersen, P. F., Mercer, J. W., and White, J. H. O.: Numerical modeling of salt-water intrusion at Hallandale, Florida. *Ground Water*, Vol. 26 (5), pp. 619–630, 1988.

Bakker, M., and Schaars, F.: *The sea water intrusion (SWI) package manual*, version 0.2, University of Georgia, Athens, 2003.

Ballard, S.P., Golding, B.W. and Smith, R.N.: Mesoscale model experiment forecasts of the Haar of northeast Scotland. *Mon. Wea. Rev*., 119, 2107-2123, 1991.

Battjes, J.A. and Janssen, J.P.F.M.: Energy loss and set-up due to breaking of random waves. *Proc. 16th Inter. Conf. Coastal Engineering*, ASCE, 569-587, 1978.

Bear, J.: *Hydraulics of groundwater*. New York, McGraw-Hill, 1979.

Betts, A.K. and Miller, M.J.: *The Betts-Miller scheme. The representation of cumulus convection in numerical models*, Emanuel, K.A. and Raymond, D.J., Eds. Amer. Meteor. Soc., 246 pp, 1993.

Bhosale, D. and Kumar, C.: Simulation of Seawater Intrusion in Ernakulam Coast. proceeding of International Conference on Hydrology and Watershed Management, Hyderabad, pp. 390-399, 2002.

Bian, J. M., and Tang, J.: Groundwater resources optimal allocation countermeasures in the liaohe oil field area. Proceedings of the 34th Congress of International Association of Hydrogeologists, Bejing,China, October 9-13, 2006.

Bicknell, B.R., Imhoff, J.C., Kittle, J.L.: *Hydrological Simulation Program Fortran, User's manual for version 11*: U.S. Environmental Protection Agency, National Exposure Research Laboratory, Athens, Ga., EPA/600/R-97/080, 755 p, 1997.

Bobba, A.G.: Mathematical models for saltwater intrusion in coastal aquifers. *Water Resources Management*, Vol. 7: pp. 3–37, 1993.

Bouws, E. and Komen, G.J.: On the balance between growth and dissipation in an extreme depth-limited wind sea in the southern North Sea. *J. Phys. Ocean.*, 13, 1653, 1983.

Burk, S.D. and Thompson, W.T.: A vertically nested regional numerical prediction model with second-order closure physics. *Mon. Wea. Rev*., 117, 2305-2324, 1989.

Chalikov, D.V. and Belevich, M.Y.: One-dimensional theory of the wave boundary layer. *Bound. Layer Meteor*., 63, 65-96, 1993.

Charnock, H.: Wind stress on a water surface. *Quarterly Journal of Royal Meteorological Society*, 81, pp. 639-640, 1955.

Dudhia, J.: *A multi-layer soil temperature model for MM5*. Preprints, The Sixth PSU/ NCAR Mesoscale Model User's Workshop, 22-24 July 1996, Boulder, Colorado, 49-50, 1996.

El-Bihery, M. A.: Groundwater flow modeling of Quaternary aquifer Ras Sudr, Egypt. *Environmental Geology*, Vol. 58, pp. 1095–1105, 2009.

Evans, M.: *Nutrient Discharge to Cockburn Sound from a Subterranean Mixing Zone: a Comparison of Transport and Reaction Timescales*. Honours thesis, University of Western Australia, p.83, 2005.

Fritsch, J.M. and Chappell, C.F.: Numerical prediction of convectively driven mesoscale pressure systems. Part I: Convective parameterization. *J. Atmos. Sci*., 37, 1722-1733, 1980.

Grell, G.A., Dudhia, J. and Stauffer, D.R.: *A description of the fifth-generation Penn State/ NCAR mesoscale model (MM5)*. NCAR Technical Note, NCAR/ TN-398+STR, 117 pp, 1995.

Giambastiani, B. M. S., Antonellini, M., Oude Essink, G. H. P., and Stuurman, R. J.: Saltwater intrusion in the unconfined coastal aquifer of Ravenna (Italy): A numerical model. *Journal of Hydrology*, Vol. 340, pp. 91-104, 2007.

Guo, W., and Bennett, G. D.: Simulation of saline/fresh water flows using MODFLOW. Proceedings of MODFLOW '98 conference at the international ground water modeling center, Colorado School of Mines, Golden, Colorado, vol 1, pp. 267–274, 1998a.

Guo, W. X., and Langevin, C. D.: *User's guide to SEAWAT: a computer program for the simulation of three-dimensional variable-density ground-water flow*. USGS Techniques of Water Resources Investigations, Book 6, chap A7, p. 77, 2002.

Hack, J.J., Boville, B.A., Briegleb, B.P., *et al*.: Parameterization of moist convection in the NCAR Community Climate Model (CCM2). *J. Geophys. Res*., 99, 20785-20813, 1993.

Harbaugh, A. W., Banta, E. R., Hill, M. C., and McDonald, M. G.: *MODFLOW- 2000, the U.S. Geological Survey Modular Ground-Water Model—User Guide to Modularization Concepts and the Ground-Water Flow Processes*. U.S. Geological Survey Open- File Report 00-92, 121p, 2000.

Hong, S.Y. and Pan, H.L.: Non-local boundary layer certical diffusion in a medium-range forecast model. *Mon. Wea. Rev*., 124, 2322-2339, 1996.

Huyakorn, P. S., Andersen, P. F., Mercer, J. W., and White, J. H. O.: Saltwater intrusion in aquifers: Development and testing of a three-dimensional finite element model. *Water Resource Research*, Vol. 23(2): 293–312, 1987.

HydroGeoLogic Inc.: *MODHMS—MODFLOW-Based Hydrologic Modeling System: Documentation and User's Guide*, Herndon, Virginia, 2002.

Kain, J.S. and Fritsch, J.M.: *Convective parameterization for mesoscale models: The Kain-Fritsch scheme.* The representation of cumulus convection in numerical models, Emanuel, K.A. and Raymond, D.J., Eds. Amer. Meteor. Soc., 246 pp, 1993.

Kim, K.: *Coastal ocean model with consideration of meterological-oceanographic mesoscale interaction*. PhD dissertation, Kyoto University, Japan, 2005.

Komwn, G.J., Hasselmann, S. and Hasselmann, K,: On the existance of a fully developed wind-sea spectrum. *J. Phys. Oceanogr*., 14, 1271-1285, 1984.

Kopsiaftis, G., Mantoglou, A., and Giannoulopoulos, P.: Variable density coastal aquifer models with application to an aquifer on Thira Island. *Desalination*, Vol. 237, pp. 65–80, 2009.

Langevin, C. D., Shoemaker, W. B., and Guo, W.: *MODFLOW-2000, the U.S. Geological Survey Modular Ground-Water Model—Documentation of the SEAWAT-2000 version with the variabledensity flow process (VDF) and the integrated MT3DMS Transport Process (IMT)*. USGS Open-File Report 03-426, 2003.

Langevin, C. D., Oude Essink, G. H. P., Panday, S., Bakker, M., Prommer, H., Swain, E. D., Jones, W., Beach, M., and Barcelo, M.: *MODFLOW based tools for simulation of variable-density groundwater flow*. In: Cheng A, Ouazar D (eds) Coastal aquifer management: monitoring, modeling, and case studies, Lewis Publishers, Boca Raton, pp. 49–76, 2004.

Langevin, C. D., and Guo, W. X.: MODFLOW/MT3DMS–Based Simulation of Variable-Density Ground Water Flow and Transport. *Ground water*, Vol. 44, No. 3, pp. 339–351, 2006.

Langevin, C.D., Thorne, D.T., Jr., Dausman, A.M., Sukop, M.C., and Guo, W. X.: *SEAWAT Version 4: A Computer Program for Simulation of Multi-Species Solute and Heat Transport*. U.S. Geological Survey Techniques and Methods Book 6, Chapter A22, 39 p, 2007.

Li, Y. M.: *Groundwater quality simulation and forecast in liaohe oil field*, (in chinese). Msc Thesis, Jiling University, 86 p, 2005.

Lin, J., Snodsmith, J. B., Zheng, C. M., and Wu, J. F.: A modeling study of seawater intrusion in Alabama Gulf Coast, USA. *Environmental Geology*, 57: pp. 119–130, 2009.

Lin, Y.L., Farley, F.D. and Orville, H.D.: Bulk parameterization of the snow field of the cloud model. *J. Climate Appl. Meteor*., 22, 1065-1092, 1983.

Mao, X., Enot, P., Barry, D.A., Li, L., Binley, A., and Jeng, D. S.: Tidal influence on behaviour of a coastal aquifer adjacent to a low-relief estuary. *Journal of Hydrology*, 327, pp. 110-127, 2006.

Marshall, J., Adcroft, A., Hill, C., Perelman, L. and Heisey, C.: A finite-volume, incompressible navier-stokes model for studies of the ocean on parallel computers. *J. Geophys. Res*., 102(C3), 5753-5766, 1997a.

Marshall, J., Hill, C., Perelman, L. and Adcroft, A.: Hydrostatic, quasi-hydrostatic and non-hydrostatic ocean modeling. *J. Geophys. Res*., 102(C3), 5733-5752, 1997b.

McDonald, M. G., and Harbaugh, A. W.: *A modular three-dimensional finite-difference ground-water flow model*. U.S. Geological Survey Techniques of Water Resources Investigations, Book 6, chap A1, 588p, 1988.

Mellor, G.L. and Yamada, T.: Development of a turbulence closure model for geophysical fluid problems. *Rev. Geophys. Space Phys*., 20, 851-875, 1982.

Mellor, G.L.: *Uses guide for a three-dimensional, primitive equation, numerical ocean model*. 56 pp, 2004.

Ministry of Health of the Heople's Republic of China, *Standards for drinking water quality*, (in chinese). GB 5749-2006, p. 9, 2006.

Nagai, H.: Validation and sensitivity analysis of new atmosphere-soil-vegetation model. *Journal of Applied Meteorology*, 41, 160-176, 2002.

Nagai, H.: Validation and sensitivity analysis of a new atmosphere-soil-vegetation model. Part II: Impacts on in-canopy latent heat flux over a winter wheat field determined by detailed calculation of canopy radiation transmission and stomatal resistance. *Journal of Applied Meteorology*, 42, 434-451, 2003.

Nagai, H.: Incorporation of CO2 exchange processes into a multilayer atmosphere-soil-vegetation model. *Journal of Applied Meteorology*, 44, 1574-1592, 2005.

Oude Essink, G. H. P.: MOC3D adapted to simulate 3D densitydependent groundwater flow. Proceedings of MODFLOW '98 conference at the international ground water modeling center, Colorado School of Mines, Golden, Colorado, vol 1, pp. 291–300, 1998.

Pierson, W.J. and Moskowitz, L.: A proposed spectral for fully developed wind seas based on the similarity theory of A.A. Kitaigorodskii. *J. Geophys. Res*., 69, 5181-5190, 1964.

Pleim, J.E., and Chang, J.S.: A non-local closure model for vertical mixing in the convective boundary layer. *Atm.. Env*., 26A, 965-981, 1992.

Reisner, J., Rasmussen, R.M. and Bruintjes, R.T.: Explicit forecasting of supercooled liquid water in winter storms using the MM5 mesoscale model. *Quart. J. Roy. Meteo. Soc*., 124B, 1071-1107, 1998.

Schultz, P.: An explicit Cloud Physics Parameterization for Operational Numerical Weather Prediction. *Mon. Wea. Rev*., 123(1), 3331-3343, 1995.

Snyder, R.L., Dobson, F.W., Elliot, J.A. and Long, R.B.: Array measurements of atmospheric pressure fluctuations above surface gravity waves. *J. Fluid Mech*., 102, 1-59, 1981.

Sorek, S., and Pinder, G. F.: *Survey of computer codes and case histories. In: Bear J et al (ed) Seawater intrusion in coastal aquifers: concepts, methods, and practices*. Kluwer Academic Publishers, Dordrecht, pp. 399–461, 1999.

Tao, W.K. and Simpson, J.: The Goddard Cumulus Ensemble Model. Part I: Model Description. *Terrestrial, Atmospheric and Oceanic Sciences*, 4, 19-54, 1993.

Tao, W.K., Simpson, J. and McCumber, M.: An ice-water saturation adjustment. *Mon. Wea. Rev*., 117, 231-235, 1989.

Tolman, H.L. and Chalikov, D.V.: Source terms in a third-generation wind-wave model. *J. Phys. Oceanogr*., 26, 2497-2518, 1996.

Tolman, H.L.: *User manual and system documentation of Wave Watch III version 2.22*, TN-No 222, NCEP MMAB, 133 pp, 2002.

Trenberth, K. E., Dai, A., Rasmussen, R.M. and Parsons, D.B.: The changing character of precipitation. *Bull. Am. Meteorol. Soc*., 84, 1205– 1217, 2003.

Voss, C.: SUTRA: *A Finite-Element Simulation Model for Saturated-Unsaturated Fluid-Density-Dependent Ground-Water Flow With Energy Transport or Chemically-Reactive Single-Species Solute Transport*. Water Resources Investigation Report 84-4369, U.S. Geological Survey, 1984.

Wang, W. D., Zhang, G. X., and Li, B. L.: *Report on Groundwater Management Simulation in Panjin City, Liaoning Province*, (in chinese). Liaoning hydrogeology and engineering geology exploration, 1992.

Wells, N., Goddard, S. and Hayes, M.J.: A self-calibrating Palmer Drought Severity Index. *J. Clim.*, **17**, 2335–2351, 2004.

Xue, X. D.: *The research of the simulation with prediction of the groundwater level and the rational utilization of the water resource in panjin area*, (in chinese). Msc Thesis, Jiling University, 91p, 2005.

Yamashita, T., Kim, K., Lee, H.S., and Haggag, M.: Environment Simulator: Contribution to Coastal Engineering Problems (in Japanese). *Annual Journal of Coastal Engineering*, JSCE, 54, 1301-1305, 2007.

Yamashita, T.: Regional Environment Simulator and Its Applications to Environmental Impact Assessment. Presented in ISWREP, 2011.

Yamazawa, H and Nagai, H.: Development of one-dimensional atmosphere-bare soil model (in Japanese), *Japan Atomic Energy Research Institute Rep*., 97-140, 56 pp, 1997.

Zheng, C. M. and Wang, P. P.: *MT3DMS: Documentation and User's Guide*. Contract Report SERDP-99-1, U.S. Army Engineer Research and Development Center, Vicksburg, MS, 1999.

Chapter 3

Numerical Simulation of Seawater Intrusion in Liaodong Bay Coastal Plain by SEAWAT Model

3.1 Introduction

Seawater intrusion is the movement of seawater into fresh groundwater due to the natural processes or human activities [web-1]. As the economy developed, water demand increases and over-exploitation of groundwater occurs, especially, in many coastal regions. It has disturbed the established balance between fresh water and seawater, causing extensive seawater intrusion into groundwater.

web-1 http://www.lenntech.com/groundwater/seawater-intrusions.htm

In 2007, the State Oceanic Administration of People's Republic of China started monitoring seawater intrusion in China. The activity helped established the fact that seawater intrusion is in serious level condition particularly in Liaodong Bay area (Figure. 3.1) where coverage of seawater intrusion area is more than 4,000 m^2 with serious intrusion area of nearly 1,500 m^2. The most remote region of seawater intrusion is 68 km far from the shore in Pan Jin City [web-2].

Web-2 http://www.soa.gov.cn/hyjww/zghybnew/tkb/webinfo/2008/01/1200912281939611.htm

It is significant task to make clear the seawater intrusion and to predict its extending area in Liaodong Bay coastal plain by numerical study. Li (2005) employed the software of Visual MODFLOW for the first time to study numerical seawater intrusion in the upper Neozoic layer of the Liaohe Oil Field which is located in the south of the lower Liaohe Plain. Xue (2005) conducted the simulation of groundwater level in the upper Neozoic using Visual MODFLOW in Pan Jin area. For seawater intrusion problem, spatial variations in fluid density can markedly affect ground water flow patterns (Langevin et al., 2006). In previous model studies (Li, 2005; Xue, 2005) of Liaodong Bay coastal plain area, they used Visual MODFLOW software to calculate the quasi-three-dimensional flows which have not considered groundwater density variable and Quarternary layer salt water effect.

This study deals with numerical model on seawater intrusion in Liaodong Bay coastal plain based on SEAWAT which is a quasi-three-dimensional variable-density numerical code. This simulation considers both the groundwater layers of Quaternary and upper Neozoic. On the other hand, to analysis the vertical grid effect on the seawater intrusion simulation, two case studies have been done in this study. The three and four vertical grid layer was used in case 1 and 2, respectively. Compare with previous studies, this two model improved in two parts. It considered groundwater density variable and seawater intrusion in Quaternary and Neozoic layers. The total simulation period is 55 months from October 2004 to April 2009. After the model calibration by using the observation data in April

2009, the calibrated model was used to predict the extent of seawater intrusion for 40 years to come assuming the same conditions in 2004.

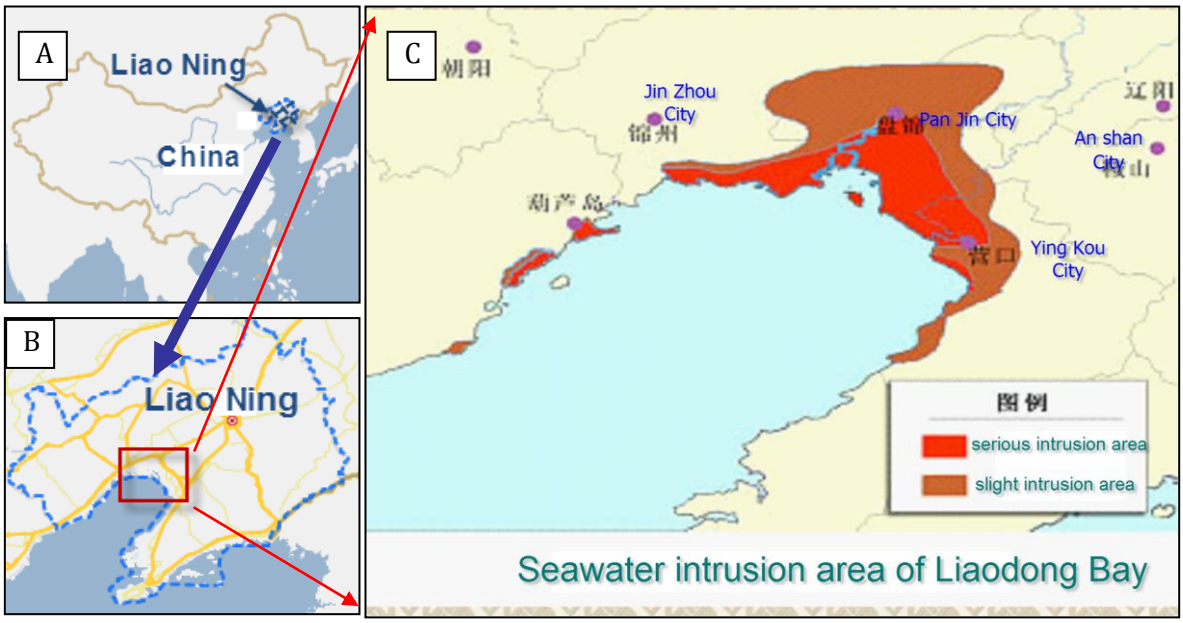

Figure 3. 1 A: location of Liao Ning Province, China. B: Liaodong bay coastal plain (red square). C: seawater intrusion distribution

3.2 Simulation Code

There is several simulation codes can be used in seawater intrusion simulation. In this study, the SEAWAT code capable of simulating quasi-three-dimensional variable-density groundwater flow in porous media was used to simulate the seawater intrusion into the coastal aquifers in Liaodong Bay coastal plain. The fundamental concept of this code is to combine the two commonly-used groundwater flow and solute transport modeling programs of MODFLOW (Harbaugh et al., 2000) and MT3DMS (Zheng andWang, 1999). For more background of simulation codes can be found in chapter 2.3.

3.3 Case 1 Study: Three vertical grid layer without tidal effect

3.3.1 Model discretization

In the plan view, the model grid consists of the grid system of 60 columns and 60 rows with uniform spacing of 2.0km (WE-direction) and 2.33 km (NS-direction), respectively (Figure 3.2).

In the vertical direction, the model grid consists of three layers representing the hydrostratigraphy of Liaodong Bay coastal plain (Figure 3.3 and 3.4). Layer-1 corresponds to the Quaternary (A1) aquifer. Layer-2 represents the Minhuazhen group (A2) aquifer that is a confining layer. Layer-C1 is an aquitard existing between A1 and A2 aquifers, which is also the confining bed between two aquifers (A1 and A2).

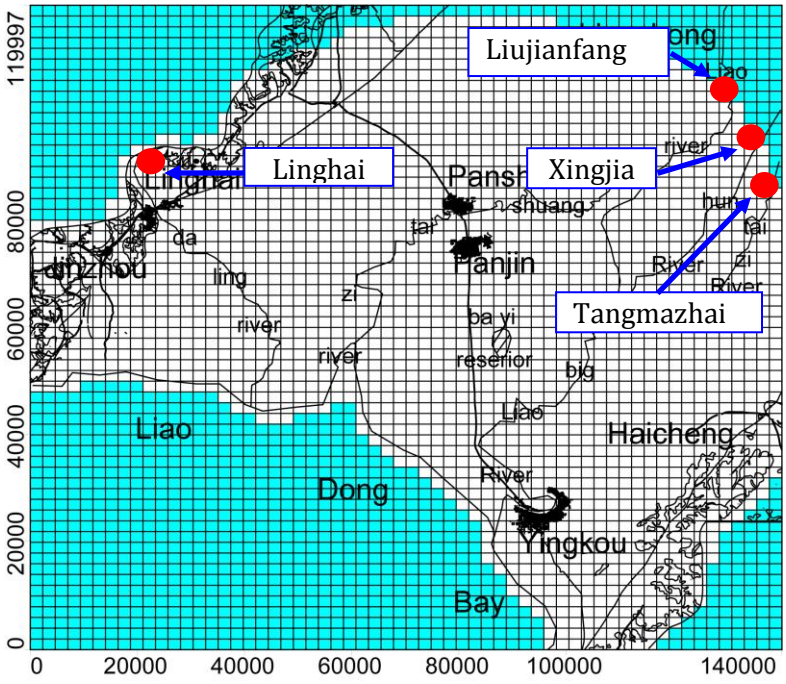

Figure 3. 2 Plan view of spatial discretization for the numerical model (unit in meter) showing the inactive area (green color) and the active area (white color).

In this model, two bottom boundaries of A1 and A2 are set by the informations from Guantao group aquifer and lower Neozoic aquifer. Model layer thicknesses are determined by the occurrence of sand and clay layers documented in well driller's reports archived by the Liao Ning hydrogeology and engineering geology exploration institute (Wang et al., 1992).

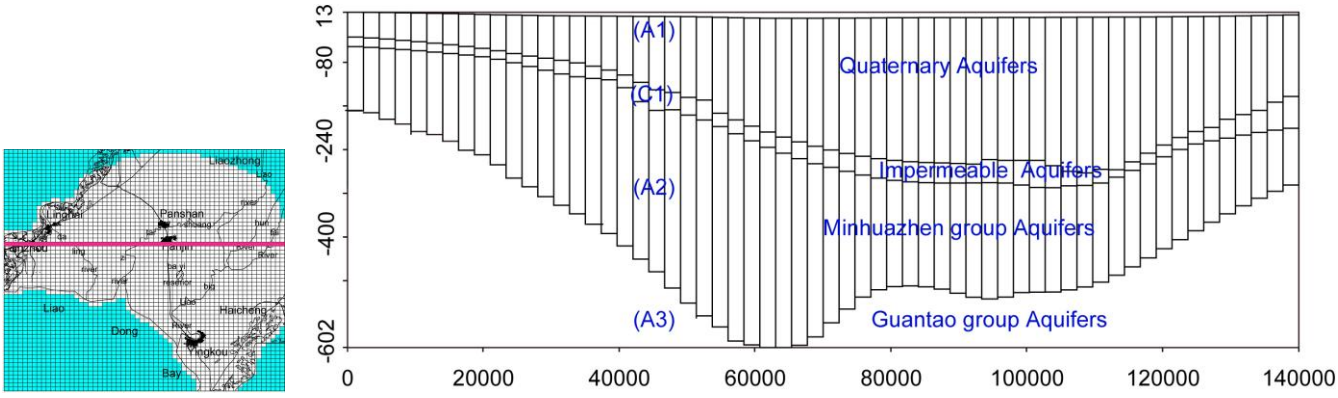

Figure 3. 3 The west to east cross-section showing the hydrogeologic units and vertical spatial discretization of the study area with all units in meter.

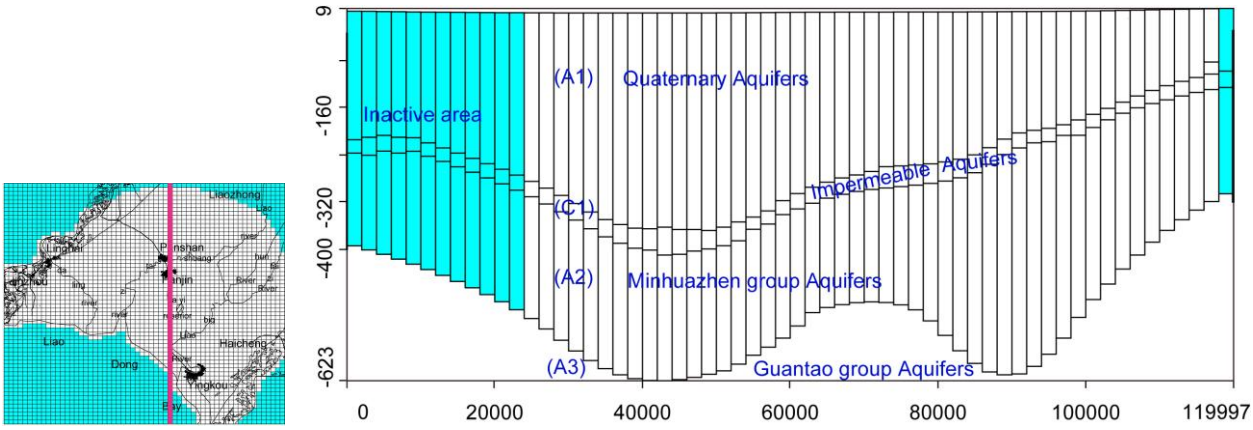

Figure 3. 4 The south to north cross-section showing the hydrogeologic units and vertical spatial discretization of the study area with all units in meter.

A total of 55 stress periods, from October 2004 to April 2009, is used in the model simulation with time step of 1 month.

3.3.2 Hydrogeological parameters

The zoning map of the hydraulic conductivity was created using the data determined by pumping tests that were conducted at the time of well completion. It was recorded in well driller's logs. All hydraulic conductivities are shown by averaged values in each zone. Considering the size of zone, model's hydraulic conductivities were adjusted during model calibration. Hydraulic conductivity of the aquitards is determined to be 4.32×10^{-3}m/day in Layers C1 and assumed to be constant inside the whole aquitard. For all the layers, the vertical hydraulic conductivity is assumed to be 10% of the horizontal hydraulic conductivity. Representative properties of the study area (Table 3.1) were assigned to the model cells.

Streams and rivers are specified with the river package of the SEAWAT code. Width, depth, and river stage and salt concentration of river water are determined from topographic maps. Recharge is applied to the most active upper layer. Monthly precipitation data was obtained from the China Meteorological Data Sharing Service System. From annual evapotranspiration data, an averaged evapotranspiration rate was calculated as 4.298×10^{-4}m/day.

The effective porosity is set to be 0.15 to 0.25 as an initial guess. The longitudinal dispersivity is set to be 10 to 40 m in the flow system based on the injecting tests conducted at the time of well completion (from the well driller's logs). The ratio of horizontal transverse dispersivity to the longitudinal dispersivity is assumed to be 0.1. On the other hand, the ratio of the vertical transverse dispersivity to the longitudinal dispersivity is assumed to be 0.01. As needed, these values should be adjusted during the model calibration.

Table 3. 1 Input parameters for the model and simulation strategies for this study

Parameter	**Layer A1**	**Layer C1**	**Layer A2**
Hydraulic conductivity (Kx, m/d)	40～80	0.000432	4～10
Hydraulic conductivity (Ky, m/d)	40～80	0.000432	4～10
Hydraulic conductivity (Kz, m/d)	4～8	0.000013	0.4～1
Total porosity	0.23～0.3	0.000017	0.3
Effective porosity	0.15～0.25	0.000015	0.15
Specific storage	0.00018 ～ 0.00022	0.00001	0.0001 ～ 0.0002
Specific yield	0.18～0.22	0.001	0.15～0.23
Longitudinal dispersivity (m)	10～40	0.0027	10～35
Horizontal/Longitudinal dispersivity	0.1	0.1	0.1
Vertical/Longitudinal dispersivity	0.01	0.01	0.01
Molecular diffusion (m^2/s)	1.0×10^{-9}	1.0×10^{-9}	1.0×10^{-9}
Freshwater density (kg/m^3)	1000	1000	1000
Seawater density (kg/m^3)	1025	1025	1025
Constant head (m)	2		
Recharge concentration (mg/L)	0		
Constant head concentration (mg/L)	7000～12000	6500	
Initial Concentration	Based on observation data		
Recharge	Based on observation data		

3.3.3 Boundary and initial conditions

Since the model is set up to simulate the seawater intrusion into the coastal aquifers, both groundwater flow and solute transport processes have to be simultaneously involved. Then boundary conditions for these two processes are required. For the flow computation, the boundary conditions are specified by hydraulic head at everywhere apart from the Layers-1 which was set by the no-flow boundaries at the northwestern and southeastern mountain edges. The specified hydraulic head values are either 2m (the mean sea level) or interpolated values from the measured water heads along the boundaries. For the flow computation, the boundary conditions (Figure. 3.5) were set as constant head boundary with crimson line in Layer A1 (Figure. 3.5a) which was set by the no-flow boundaries (Fig. 3.5a, pink line) at the northwestern and southeastern mountain edges. The blue color line is river boundary.

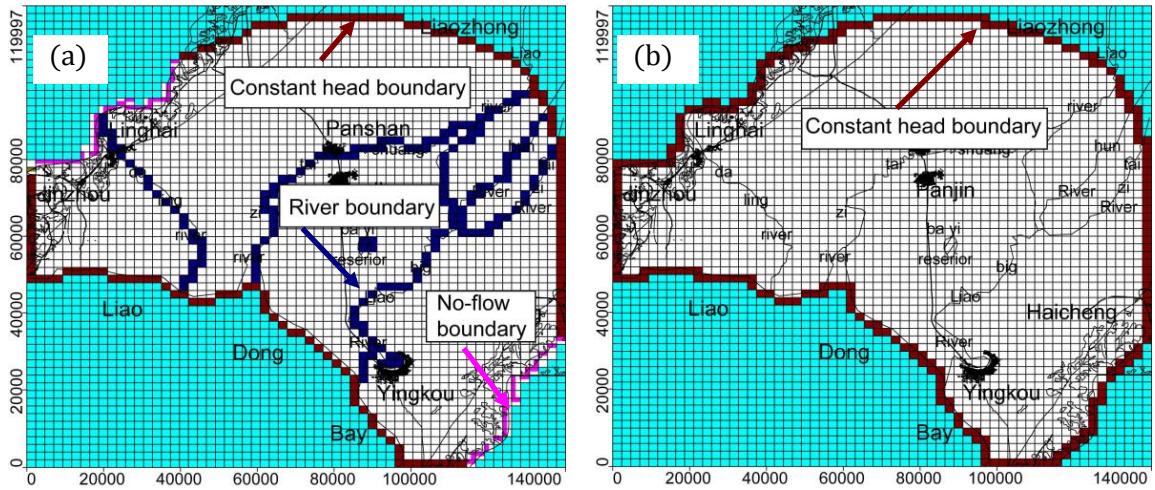

Figure 3. 5 Flow boundary conditions for each layer of the numerical model (unit in meter): a Layers A1, and b Layers A2.

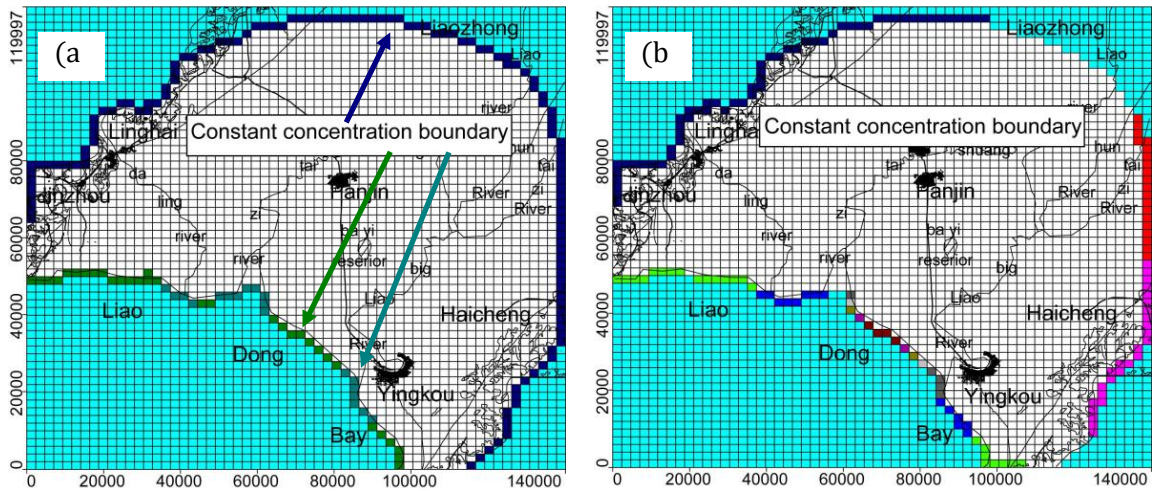

Figure 3. 6 Transport boundary conditions for each layer of the numerical model (unit in meter): a Layers A1, and b Layers A2.

The concentration level of Total Dissolved Solids (TDS), Sodium (Na) and Chloride concentration (Cl) are normally used as verifiable indicators for seawater intrusion.

However, due to the lack of data on TDS and Na, chloride concentration is considered as the simulated component in this study for the solute transport computation. In addition, seawater intrusion can be observed if at any specific location in the aquifer the chloride concentration rises above 0.25 kg/m^3 as set forth by the Ministry of health. (SDWQ, 2006). For the solute transport computation, chloride is the simulated component. The chloride concentration in seawater is approximately 12 kg/m^3. In both Layer-1 and Layer-2, the boundary conditions are set by the specified concentration (Figure. 3.6). As the A1 aquifer is in contact with the surface water, chloride concentration along the coast is specified 12 kg/m^3, and 7 kg/m^3 in the river mouth area where mixing of freshwater with seawater is considered. On the other boundary the chloride concentration value is set to be 0.05 kg/m^3. Through the computation, these boundary conditions are assumed to be same values as the chloride concentration in 2004.

3.3.4 Model calibration

The model calibration is conducted through a trial-and-error approach by adjusting the zonation and values of two key parameters, i.e., hydraulic conductivities and effective porosity. The hydraulic head value is computed by SEAWAT until it matches the observed value with a satisfactory level. However, due to the scarcity of observed chloride concentrations, no attempt is made to adjust several transport parameters including dispersivities and recharge rates. These values remain same as initial assigned value. Furthermore, because of the lack of continuously monitored hydraulic head data, the model is only calibrated against the observed hydraulic heads at the end of simulation. During calibration, a total of 18 observed hydraulic head values measured in April of 2009 are used. All the observation well locations are shown in Fig. 3.14.Model calibration is stopped when a reasonable match between the observed and calculated heads is achieved.

Figure 3.7 shows that an overall correlation coefficient of 0.983, a mean error of 0.862 m and a root mean square value of 0.955 m are obtained by the model calibration. This is indicating a reasonably good match between the observed and calculated heads. Residuals between the observed and calculated heads are also listed in Table 3.2. After model calibration, the resulting horizontal hydraulic conductivity for Layers-1 and -2 ranges from 3 to 80 m/day, while the resulting effective porosity from 0.14 to 0.3. It is noteworthy that the model calibration of this study is of preliminary nature due to the limited number and duration of the observation data. Therefore, additional model calibration should be attempted when more field data become available in future.

The simulated extent of seawater intrusion into the aquifer Layers-1 and -2 in April 2009 is depicted in Figure 3.8. Compared with that in October 2004, the extent of seawater intrusion was expanded, indicating that further seawater intrusion occurred from October 2004 to April 2009. As shown in Figure 3.8, seawater intrusion in Layer-1 is considerably faster than that in Layers-2 during the 55 months. Note that at any specific location of the aquifer, when the chloride concentration rises above 0.25 kg/m^3, the limit for freshwater use set by the data of Ministry of Health (GB-5748, 2006). This location is considered to have been affected by seawater intrusion.

Table 3. 2 Observed and calculated heads with residuals at 18 observation points

Well ID	X-Model	Y-Model	Observed heads(m)	Calculated head(m)	Residuals (m)
1	117348.5	75583.85	2.8	3.498236	0.698236
2	107162	27707.29	4.1	2.913963	-1.18604
3	93919.55	59896.63	2.4	2.283095	-0.11691
4	96160.58	107569.5	3.5	4.328045	0.828045
5	70490.6	97586.69	3.7	2.787997	-0.912
6	64989.89	85770.35	2.4	2.290782	-0.10922
7	41968.39	73342.82	2.6	3.149929	0.549929
8	44820.61	85159.16	3.7	3.049591	-0.65041
9	31170.7	60304.1	2.5	3.739237	1.239237
10	129164.9	78843.53	-3.7	-2.90949	0.790515
11	105735.9	66823.46	-7.3	-8.85499	-1.55499
12	104106.1	79658.45	-6.5	-7.07436	-0.57436
13	95549.39	99216.53	-6.8	-5.58358	1.216425
14	70083.14	86177.81	-6.5	-7.27422	-0.77422
15	58877.98	80065.91	-9	-7.67393	1.326071
16	46246.72	65397.35	-8.3	-7.09574	1.204257
17	89844.95	38301.25	-6.6	-7.01338	-0.41338
18	91882.25	53988.46	-7.4	-8.77951	-1.37951

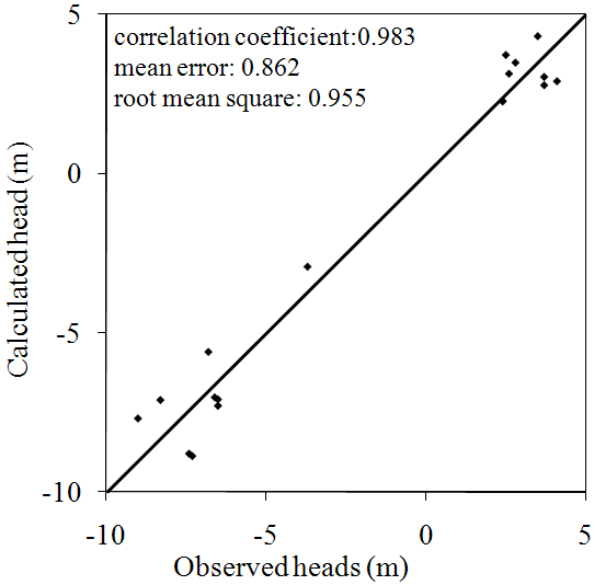

Figure 3. 7 Scatter diagram that shows good fit between the boserved an calculated heads for computation in April 2009.

3.3.5 Simulation of seawater intrusion

Prediction of the extent of seawater intrusion in coastal aquifers in Liaodong Bay coastal plain 40 years to come after April 2009 is carried out by running the calibrated computation 40-year forwards with all the conditions assumed to remain the same as those in October 2004. The predicted extents of seawater intrusion in Layers-1 and -2 are in Figure 3.8, that shows the further seawater intrusion occurrence even if all the hydrogeological conditions remain same as those in October 2004.

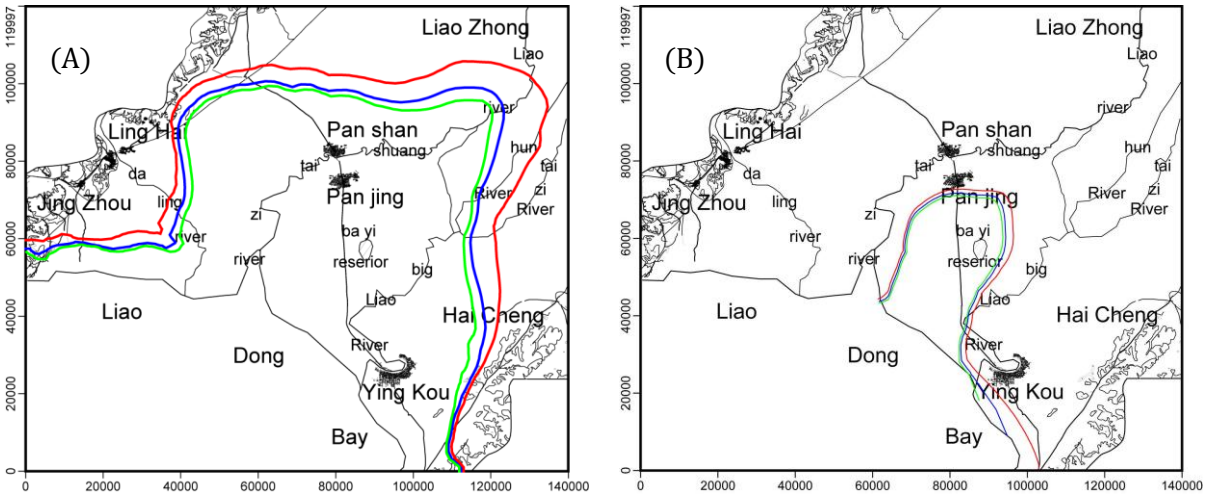

Figure 3. 8 Simulated extent of seawater intrusion for (A) Layer- 1 and (B) Layer-2 in April 2009 shown by a dashed blue line. Extent of seawater intrusion in October 2004 shown by a dashed green line. Predicted extent of seawater intrusion by April 2049 shown by a dashed red line.

Figure 3.8A shows that the maximum extent of seawater intrusion in Quaternary layer will increase 7 km toward northwest in research area. In the southwest and northeast area, the extent of seawater intrusion becomes smaller than other area. Compared with the Figure

3.8A and 3.8B, it can be found that the seawater intrusion in Layer-1 becomes significantly faster than that in Layer- 2.

In prediction model, all the conditions assumed to remain same as those in October 2004. With the continuous population increase, the demand for groundwater pumping will increase. It can be expected the actual extent of seawater intrusion in future will be more severe than the model prediction.

3.3.6 Summary and conclusions

In order to predicted the extent of seawater intrusion in future and provide useful information for the protection of groundwater resources, a quasi-three-dimensional numerical model of density-dependent groundwater flow and miscible salt transport was developed and assessed the future condition of seawater intrusion in the study area. The developed model incorporated regional geologic, geographic, and hydrogeological features. The model input parameters were determined from analysis of well logs, well driller's reports, and pumping tests. SEAWAT code was employed in the numerical study for the coupled density-dependent flow system, which was a combined version of the two commonly used groundwater flow and solute transport computational programs, MODFLOW and MT3DMS.

Due to the scarcity of the observed chloride concentrations and continuously monitored head data, the model was only calibrated against the observed hydraulic heads in April 2009. During calibration, a total of 18 observed hydraulic head values were used. The results showed that the observed and calculated hydraulic heads matched well. However, additional calibration was necessary when more data became available in future.

After calibrated the model, the extent of seawater intrusion in the study area was computed for 40 years after April 2009 under the assumption that all the conditions remained same as those in October 2004. The result showed that the maximum extent of seawater intrusion in Quaternary layer increased 7 km in the northwest of research area. In the southwest and northeast area, the extent of seawater intrusion increased smaller than other area. The seawater intrusion in Quaternary layer was significantly faster than that in upper Neozoic Layer. As a continuous increase in population, the demand for groundwater pumping might be intensified. Then it can be expected the actual extent of seawater intrusion in future might be more severe than the model prediction. So it is very important to protect the freshwater aquifers from salt water contamination in the study area.

This study constructed a new numerical model that can analyze and predict the extent of seawater intrusion in Liaodong Bay coastal plain that contents Quaternary and Neozoic layers. The three vertical grid layer was used in case study. The main numerical code employed in the new modeling was SEAWAT that can serve as an effective tool for simulating variable-density flow and transport under complex geometries and geological settings. This computational code may provide valuable information for the study of seawater intrusion in other coastal aquifers under similar hydrogeological conditions.

3.4 Case 2 study: Four vertical grid layer without tidal effect

To analysis the vertical grid effect on the seawater intrusion simulation, two case studies (case 1 and 2) have been done in this study. The three and four vertical grid layer was used

in case 1 and 2, respectively. This part will present the results of four vertical grid layer case.

3.4.1 Model discretization

In the plan view, the model grid consists of the grid system of 60 columns and 60 rows with uniform spacing of 2.0 km (NS-direction) and 2.33 km (WE-direction), respectively (Fig. 3.9).

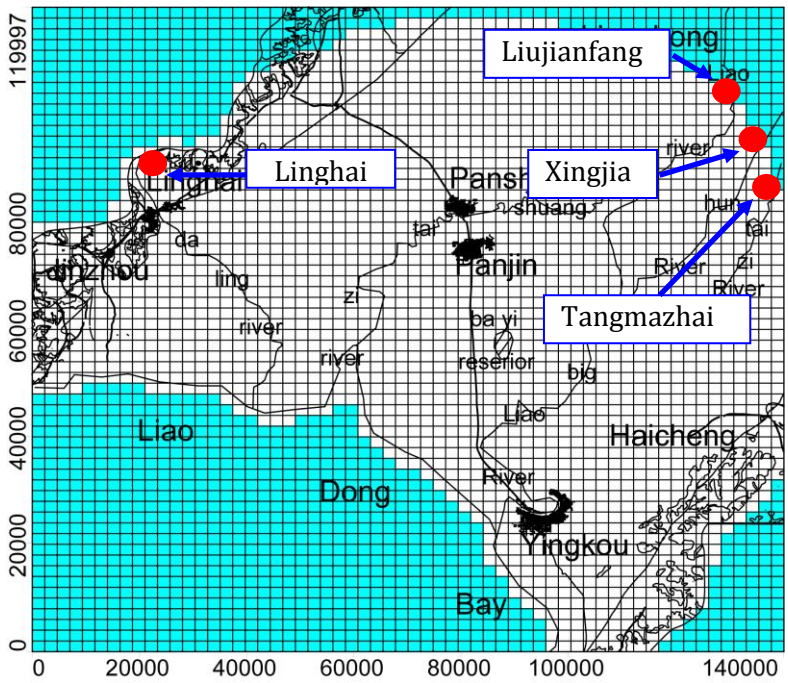

Figure 3. 9 Plan view of spatial discretization for the numerical model (unit in meter) showing the inactive area (green color) and the active area (white color).

In the vertical direction, the model grid consists of four layers representing the hydro-stratigraphy of Liaodong Bay coastal plain (see Fig. 3.10 and Fig. 3.11). The right figure is the cross-section passing through Liaodong Bay coast plain showing hydrogeologic units and vertical view of spatial discretization for the quasi-three-dimensional numerical model. For the left map, the red line shows the location of the cross-section, the green color area is the inactive area and the white color area represents the active area.

Layer-1 corresponds to the Holocene (Q_{4p}) and Upper Pleistocene (Q_{3y}) Quaternary aquifers (A1). Layer-2 corresponds to the Middle Pleistocene (Q_{2z}) and Lower Pleistocene (Q_{1x}) Quaternary aquifers (A1). Layer-3 represents the Minhuazhen group (A4) aquifer that is a confining layer. Layer-A3 is an existing aquitard between A2 and A4 aquifer which is also the confining bed between two aquifers (A2 and A4). In this model, the bottom boundary (A5) of A4 is set by the informations from Guantao group aquifer and lower Neozoic aquifer (A1-A5 showing table 1). Model layer thicknesses are determined by the occurrence of sand and clay layers documented in well driller's reports archived by the Liao Ning hydrogeology and engineering geology exploration institute (Wang et al., 1992).

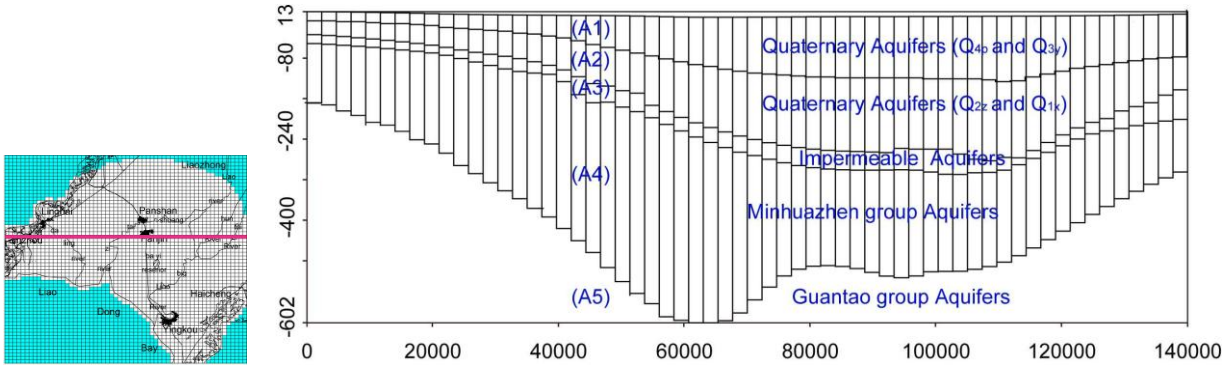

Figure 3. 10 The west to east cross-section showing the hydrogeologic units and vertical spatial discretization of the study area with all units in meter.

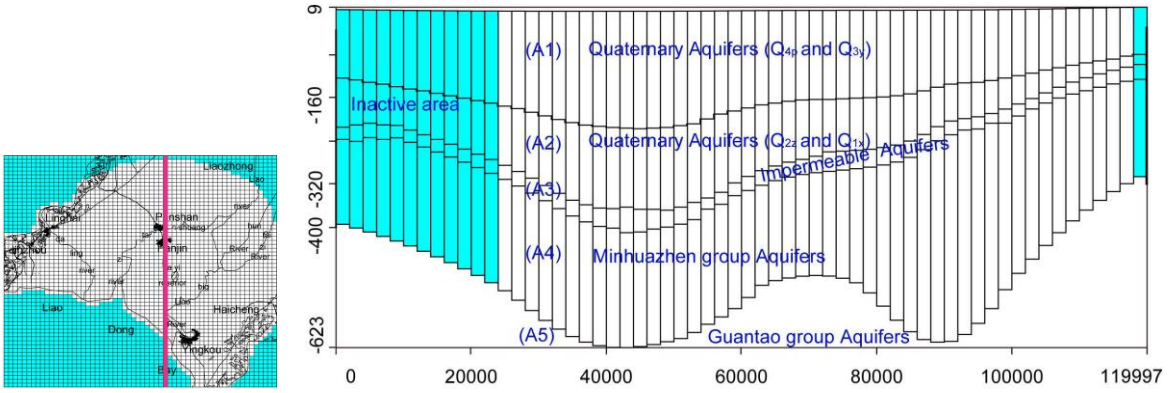

Figure 3. 11 The south to north cross-section showing the hydrogeologic units and vertical spatial discretization of the study area with all units in meter.

A cross-section of the model from west to east is shown in Fig. 3.10 while Fig. 3.11 depicts a south to north trending cross-section of the Liaodong Bay coastal plan. On both figures, units of distance and elevation are measured in meters, and the red line represents the location of the cross-section while the green and the white color areas refer to the inactive and active areas, respectively.

A total of 55 stress periods, from October 2004 to April 2009, is used in the model simulation with time step of 1 month.

3.4.2 Hydrogeological parameters

The zoning map of the hydraulic conductivity was created using the data determined by pumping tests conducted at the time of well completion and recorded in well driller's logs. All hydraulic conductivities are used with averaged values in each zone. Considering the size of zone, model's hydraulic conductivities were adjusted during model calibration.

Representative properties of the study area (Table 3.3) were assigned to the model cells. Hydraulic conductivity of the aquitards was determined to be 4.32×10^{-4} m/day in Layers A3 and assumed to be constant inside the whole aquitard. For all the layers, the vertical hydraulic conductivity was assumed to be 10% of the horizontal hydraulic conductivity.

Table 3. 3 Input parameters for the model and simulation strategies for this study

Parameter	Layer A1	Layer A2	Layer A3	Layer A4
Hydraulic conductivity (Kx, m/d)	40～75	25～55	0.000432	4～10
Hydraulic conductivity (Ky, m/d)	40～75	25～55	0.000432	4～10
Hydraulic conductivity (Kz, m/d)	4～7.5	2.5～5.5	0.000013	0.4～1
Total porosity	0.23～0.3	0.23～0.3	0.000017	0.3
Effective porosity	0.15～0.25	0.15～0.25	0.000015	0.15
Specific storage	0.00018～0.00022	0.00018～0.00022	0.00001	0.0001～0.0002
Specific yield	0.18～0.22	0.18～0.22	0.001	0.15～0.23
Longitudinal dispersivity (m)	10～40	10～40	0.0027	10～35
Horizontal/Longitudinal dispersivity	0.1	0.1	0.1	0.1
Vertical/Longitudinal dispersivity	0.01	0.01	0.01	0.01
Molecular diffusion (m^2/s)	1.0×10^{-9}	1.0×10^{-9}	1.0×10^{-9}	1.0×10^{-9}
Freshwater density (kg/m^3)	1000	1000	1000	1000
Seawater density (kg/m^3)	1025	1025	1025	1025
Constant head (m)	2			
Recharge concentration (mg/L)	0			
Constant head concentration (mg/L)	7000～12000	6500	6500	
Initial Concentration	Based on observation data			
Recharge	Based on observation data			

Recharge was applied to the most active upper layer. Monthly precipitation data was obtained from the China Meteorological Data Sharing Service System. From annual

evapotranspiration data, an averaged evapotranspiration rate was calculated as 4.298×10^{-4} m/day.

The effective porosity was set at 0.15 to 0.25 as an initial guess. The longitudinal dispersivity was set at 10 to 40 m in the flow system based on the injecting tests conducted at the time of well completion (from the well driller's logs). The ratio of horizontal transverse dispersivity to the longitudinal dispersivity was assumed to be 0.1. On the other hand, the ratio of the vertical transverse dispersivity to the longitudinal dispersivity was assumed to be 0.01. As needed, these values were adjusted during the model calibration.

3.4.3 Boundary and initial conditions

Since the model was set up to simulate the seawater intrusion into the coastal aquifers, both groundwater flow and solute transport processes were simultaneously involved with consideration of the boundary conditions. For the flow computation, the boundary conditions (Figure. 12) were set as constant head boundary with crimson line in Layer A1 (Figure. 12a) which was set by the no-flow boundaries (Figure. 12a, pink line) at the northwestern and southeastern mountain edges. The blue color line is river boundary. The specified hydraulic head values either 2 m (the mean sea level) or interpolated values from the measured water heads along the boundaries. The flow boundaries of layer A2 and A4 was set as constant head boundary according to the observe data in October 2004. The green color area is the inactive area and the white color area represents the active area.

Streams and rivers (Fig. 12a, blue line) were specified with the river package of the SEAWAT code. Width, depth, and river stage of river water were determined from the observed data in Linghai, Liujianfang, Tangmazhai and Xingjia stations (Fig. 3.9) while the width, depth and river stage at the river mouth are determined from topographic maps. Based on the stations observed data and river mouth data, each part of river width, depth, and river stage was then interpolated.

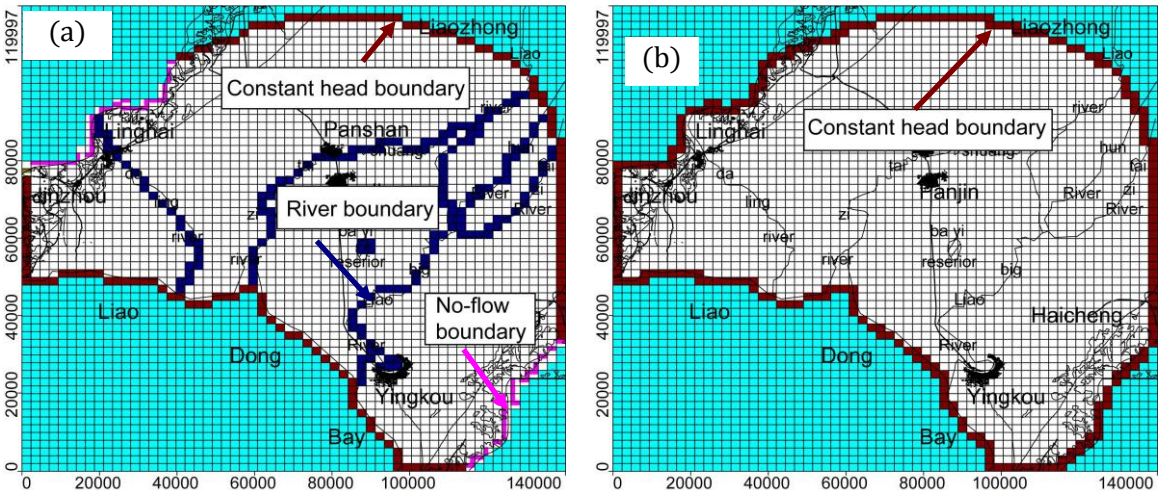

Figure 3. 12 Flow boundary conditions for each layer of the numerical model (unit in meter): a Layers A1, and b Layers A2 and A4.

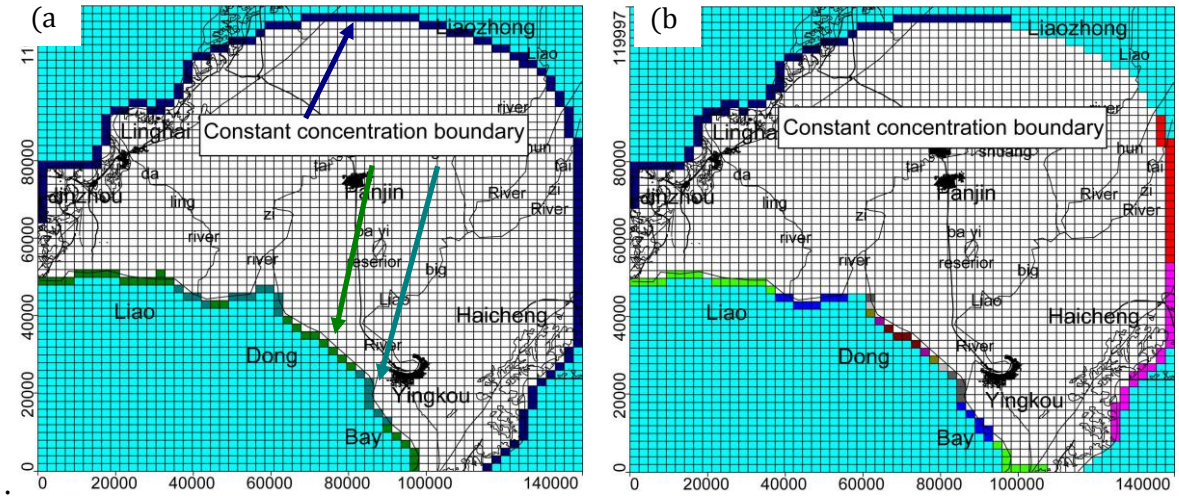

Figure 3. 13 Transport boundary conditions for each layer of the numerical model (unit in meter): a Layers A1, and b Layers A2 and A4.

In this case study, the chloride concentration is also considered as the simulated component for the solute transport computation. In addition, seawater intrusion can be observed if at any specific location in the aquifer the chloride concentration rises above 0.25 kg/m^3 as set forth by the Ministry of health. (SDWQ, 2006). The chloride concentration in seawater is approximately 12 kg/m^3. In the Layer A1, A2 and Layer A4, the boundary conditions are set as the Constant concentration boundary (Fig. 3.13). As the A1 aquifer is in contact with the surface water, chloride concentration along the coast was specified at 12 kg/m^3 (Fig. 3.13a, lightblue line), and 7 kg/m^3 (Fig. 3.13a, green line) in the river mouth area where mixing of freshwater with seawater was considered. Chloride concentration along the coast was set as 6.5 kg/m^3 in the A2 aquifer. Salt concentration of river water was determined from the observed data in Linghai, Liujianfang, Tangmazhai and Xingjia stations (see Fig. 3.9). And each part river chloride concentration can be interpolated between the stations observed data and river mouth data. On the other boundary the chloride concentration value was set at 0.05 kg/m^3. Throughout the computation, values of the chloride concentration in October 2004 were assumed constant at the boundary conditions. The green color area is the inactive area and the white color area represents the active area.

3.4.4 Model calibration

The model calibration method and steps is almost same as case 1 studies. The model calibration was conducted through a trial-and-error approach by adjusting the zonation and values of the two key parameters, i.e., hydraulic conductivities and effective porosity. The hydraulic head value was computed using SEAWAT until it matches the observed value with a satisfactory level. During calibration, a total of 18 observed hydraulic head values measured in April 2009 were used. All the observation well locations are shown in Fig. 3.14. Model calibration was stopped when a reasonable match between the observed and calculated heads is achieved.

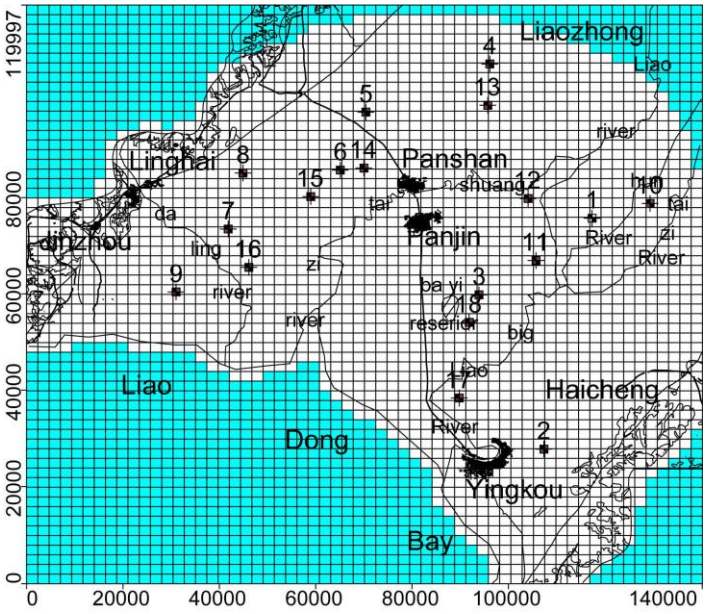

Figure 3. 14 Location of head observation wells (black dot points) used in model calibration (unit in meter).

Figure 3.15 shows that an overall correlation coefficient of 0.982, a mean error of 0.886 m and a root mean square error value of 0.987 m are obtained by the model calibration. This indicates a reasonably good match between the observed and calculated heads. Residuals between the observed and calculated heads are also listed in Table 3.4. After model calibration, the resulting horizontal hydraulic conductivity for Layers A1, A2 and A4 ranges from 3 to 80 m/day, while the resulting effective porosity from 0.14 to 0.3. It is noteworthy that the model calibration of this study is of preliminary nature due to the limited number and duration of the observation data. Additional model calibration shall be attempted when more field data become available in the future.

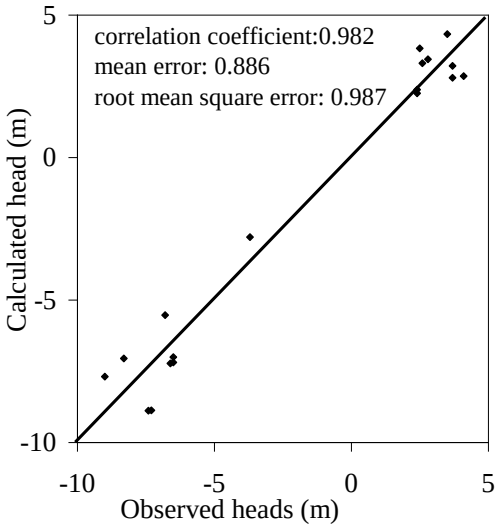

Figure 3. 15 Scatter diagram showing the relationship between the observed and calculated heads in April 2009.

Table 3. 4 Observed and calculated heads with residuals at 18 observation points

Well ID	X-Model	Y-Model	Observed heads(m)	Calculated head(m)	Residuals (m)
1	117348.5	75583.85	2.8	3.449896	0.649896
2	107162	27707.29	4.1	2.848223	-1.25178
3	93919.55	59896.63	2.4	2.25253	-0.14747
4	96160.58	107569.5	3.5	4.329527	0.829527
5	70490.6	97586.69	3.7	2.791774	-0.90823
6	64989.89	85770.35	2.4	2.372885	-0.02712
7	41968.39	73342.82	2.6	3.311563	0.711563
8	44820.61	85159.16	3.7	3.208998	-0.491
9	31170.7	60304.1	2.5	3.822999	1.322999
10	129164.9	78843.53	-3.7	-2.79269	0.907314
11	105735.9	66823.46	-7.3	-8.87193	-1.57193
12	104106.1	79658.45	-6.5	-7.00136	-0.50136
13	95549.39	99216.53	-6.8	-5.52821	1.271788
14	70083.14	86177.81	-6.5	-7.1932	-0.6932
15	58877.98	80065.91	-9	-7.69063	1.309371
16	46246.72	65397.35	-8.3	-7.05188	1.24812
17	89844.95	38301.25	-6.6	-7.23111	-0.63111
18	91882.25	53988.46	-7.4	-8.88264	-1.48264

The simulated extent of seawater intrusion into the aquifer Layers A1, A2 and A4 in April 2009 is depicted in Figure. 3.16. Compared with that in October 2004, the extent of seawater intrusion was expanded, indicating that further seawater intrusion occurred from October 2004 to April 2009. As shown in Figure. 3.16, seawater intrusion in LayerA2 is considerably faster than that in Layers A1and A3 in April 2009.

3.4.5 Results of seawater intrusion and discussions

Prediction of the extent of seawater intrusion in coastal aquifers in Liaodong Bay coastal plain 40 years to come after April 2009 was carried out by running the calibrated computation 40-year forwards with all the conditions assumed to remain the same as those in 2004.

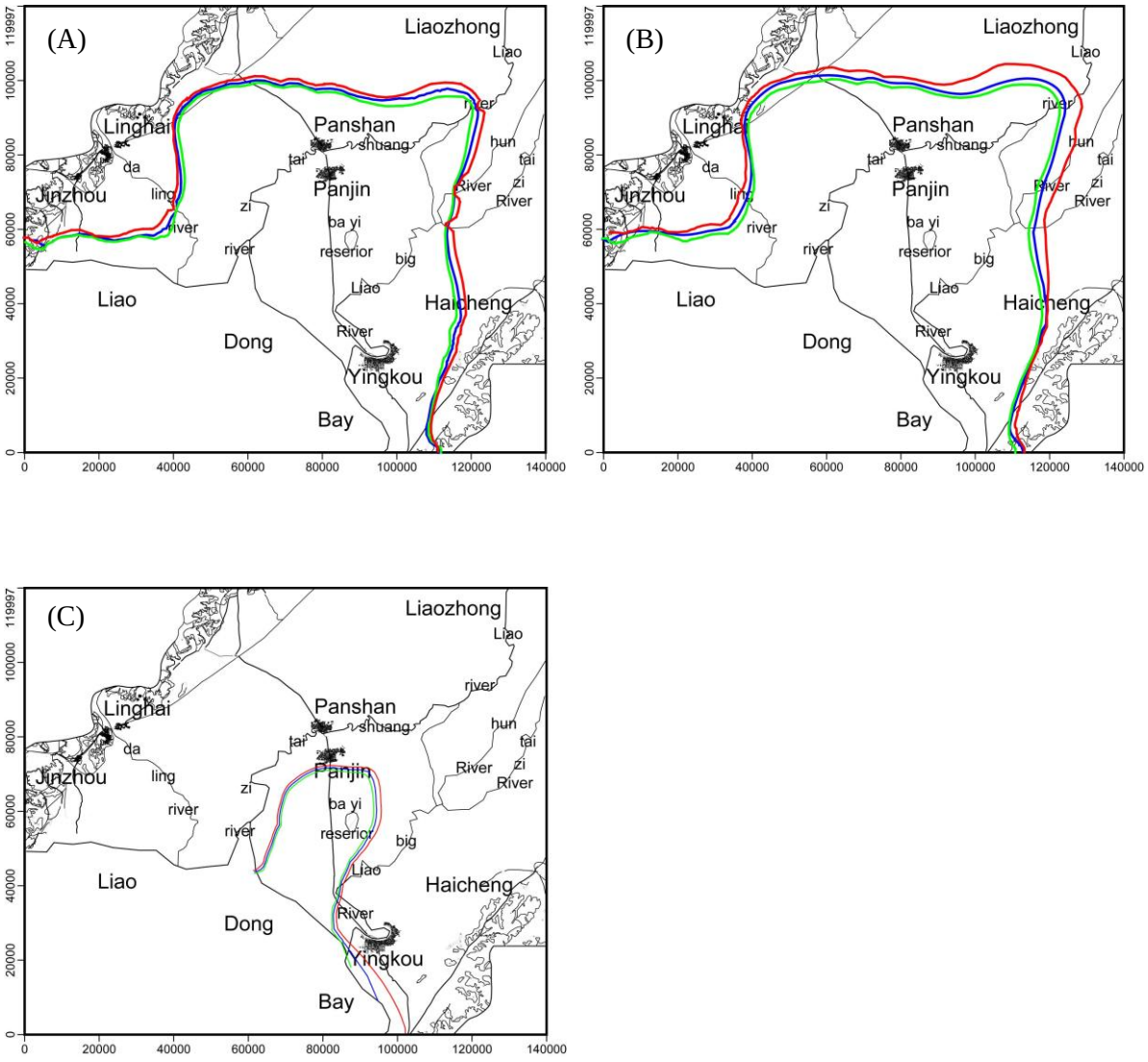

Figure 3. 16 The extent of seawater intrusion for (A) Layer A1, (B) Layer A2 and (C) Layer A4 in October 2004 (dashed green line), April 2009 (dashed blue line), and April 2049 (dashed red line).

The predicted extents of seawater intrusion in Layers A1, A2 and A4 (Figure. 3.16) shows the further seawater intrusion occurrence even if all the hydrogeological conditions remained constant. Figure 3.16(A) shows that the maximum extent of seawater intrusion in Layers A1 will increase 4.3 km and Layers A2 will increase 6.2 km toward north in

research area. In the southwest and northeast area, the extent of seawater intrusion becomes smaller than in the other area. Compared with the Figure. 3.16(A), 3.16(B) and 3.16(C), it can be described that the seawater intrusion in Layer A2 becomes significantly faster than that in Layer A1 and A3. Figure 3.16(C) shows that the maximum extent of seawater intrusion in Minghuazhen group layer will increase 2.8 km toward northwest in research area, the highest velocity of seawater intrusion is 62.2 m/yr in Minghuazhen group aquifer of this study. The results of Li (2005) show that in Minghuazhen group aquifer, the average seawater intrusion velocity is 3.066 m/yr, the velocity of high seawater intrusion area is between 18.7 and 364.3 m/yr. In Guantao group aquifer, the chloride concentration slightly defers from Li's results (2005). In this model, Guantao group aquifer is setting as bottom boundary.

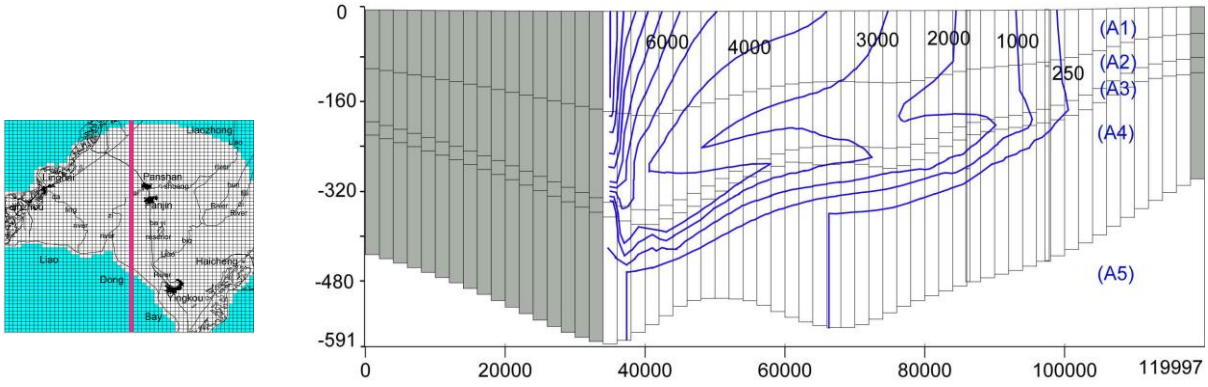

Figure 3. 17 The vertical distribution of chloride concentration in April 2049 along the south to north cross-section with unit in g/m^3.

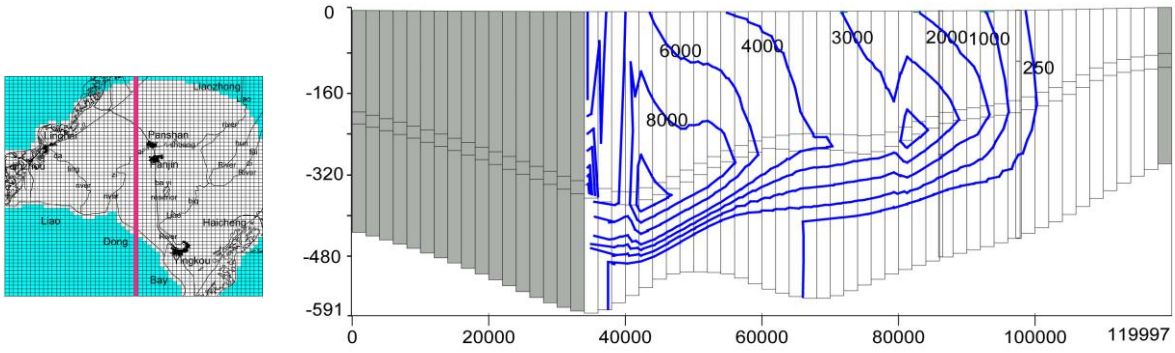

Figure 3. 18 The vertical distribution of chloride concentration in April 2049 along the south to north cross-section with unit in g/m^3.

The predicted vertical distribution of chloride concentration in April 2049 of case 1 (three vertical grid layer) is shown in Figure. 3.18. For the left and right map, the green color area is the inactive area and the white color area is the active area. For the left map, the red line on the left map shows the location of the cross-section. Compare the Figure 3.17 and Figure 3.18, the results show that case 1and case 2 can present the salt wedge at the bottom of the aquifer (quaternary aquifer). But in case1, it can not present the salt wedge at the top of the aquifer (quaternary aquifer) and it can be present very well in case 2. Thus, it can be advised to using more vertical grid layer in seawater intrusion simulation models if data

enough. In this study, duo to the lack of data, just try to do the three and four layers case study. It need to be improved in the future study if can get the data.

In the prediction model, all the conditions are assumed to remain same as those in October 2004. With the continuous population increase, the demand for groundwater pumping will increase. It can be expected the actual extent of seawater intrusion in future will be more severe than the model prediction.

In this study, a quasi-three-dimensional model was constructed to simulate and predict the seawater intrusion in Liaodong Bay coastal plain. To obtain a more realistic result, it is better to construct a three-dimensional model and using time series data to calibrate the model. For seawater intrusion, three-dimensional observation network for long-term observation is lacking in the study area. It is necessary to set up such observation network in this area. In addition, because of the lack of terrain data on the beach, this study considered ocean boundary as vertical beach slope. Ataie-Ashtiani *et el* (1999) has done research to analysis the effect of the vertical beach slope and the sloping beach in seawater intrusion in unconfined aquifers. The results shows that in the steady-state case, for the vertical beach slope the sea water has intruded a little further inland than for the sloping beach case. In the further research, it is better to use vertical beach slope ocean boundary as the model ocean boundary.

This study did not consider the tidal effect on seawater intrusion and the effects of fluid viscosity variations which are most commonly caused by temperature variations (Langevin et al., 2007). The results of Ataie-Ashtiani *et al*. (1999) showed that the tidal activity forces the seawater to intrude further inland and it also creates a thicker interface than would occur without tidal effects in unconfined aquifers. The tidal and temperature variation effects on seawater intrusion will be emphasized in the further research.

In this model, to save the hard disk and calculation time, the plan model grid consists of the grid system of 60 columns and 60 rows with uniform spacing of 2.0 km (NS-direction) and 2.33 km (WE-direction), respectively. If using smaller grid size or if non-uniform grid is used (e.g. smaller grid size near the shore and larger at land side), it might affect the chloride concentration results at near shore area but the trend of seawater intrusion might be almost the same. It is necessary to try the smaller grid size and non-uniform grid size case in future study to analysis the grid size effect on seawater intrusion simulation.

3.4.6 Summary and conclusions

Groundwater is the important source of water in Liaodong Bay coastal plain in Liao Ning, China, where 50% of the domestic water and the whole industrial water depend on the groundwater (Bian and Tang, 2006). Therefore, it is imperative to protect groundwater from seawater intrusion in this area.

To predict the extent of seawater intrusion in future and provide useful information for the protection of groundwater resources, a quasi-three-dimensional numerical model of density-dependent groundwater flow and miscible salt transport was developed and assessed the future condition of seawater intrusion in the study area. The developed model incorporated regional geologic, geographic, and hydrogeological features. The model input parameters were determined from analysis of well logs, well driller's reports, and pumping tests. SEAWAT code was employed in the numerical study for the coupled density-dependent flow system, which was a combined version of the two commonly used

groundwater flow and solute transport computational programs, MODFLOW and MT3DMS. The prediction results showed that the maximum extent of seawater intrusion in Layers A1 will increase 4.3 km and Layers A2 will increase 6.2 km toward north in research area. In the southwest and northeast area, the extent of seawater intrusion increased smaller than other area. The seawater intrusion in Layer A2 was significantly faster than that in other two Layers.

3.5 Case 3 study: Three vertical grid layer with tidal effect of seawater intrusion

3.5.1 Introduction

A number of mathematical and numerical models have been used to predict the location and movement of the seawater intrusion. It has introduced in chapter 2.3. Usually, regional groundwater flow and contaminant transport studies in the vicinity of the coastal zone assume that the coastal boundary water level is equivalent to the mean sea level and that tidal- and wave induced variations have negligible effect (Ataie-Ashtiani et al., 2001). However, the tidal fluctuation is also effect on the seawater intrusion. Dominick et al. (1971) used an implicit finite-difference numerical solution of the Boussinesq equation to simulate beach water-table response to tidal forcing. Their model was for a beach with a vertical face and, as shall be demonstrated, this produces substantial differences from the real case of a sloping beach when predicting water tables and discharges. Ataie-Ashtiani et al. (1999a) using the SUTRA model (Voss, 1984) to study the effect of tidal oscillations on seawater intrusion in coastal aquifers based on the dispersed interface theory. It was noted that the effect can be significant on near-shore groundwater hydrodynamics and salt-water intrusion, especially for a low-relief beach.

Mao et al. (2006) studied tidal influence on behaviour using SEAWAT-2000 in Ardeer, Scotland. The results show that groundwater dynamics, salt-water intrusion and chemical transport in a coastal aquifer are influenced by tidal fluctuations. Based on monitor data, Zhou et al (2006) used mathematic model to analysis tidal effects of groundwater levels in the coastal aquifers near Beihai, China. The results show that fluctuation in the tide-induced groundwater levels follows the tide and the tide can affect the groundwater levels at observation wells as far as about 4,200 and 3,300 m in the southern and northern coasts in Beihai. In Liaodong Bay coastal plain, Li (2005) and Xue (2005) using Visual MODFLOW to seawater intrusion and groundwater level in the upper Neozoic layer. However, they did not consider the seawater intrusion into the Quaternary layer, groundwater density variable and tidal effect.

This study deals with numerical simulation on the seawater intrusion in the Liaodong Bay coastal plain based on the case 1 study of chapter 3. The numerical code used is SEAWAT that is three-dimensional and density variable. In the simulation, as groundwater layers, the Quaternary layer and the upper Neozoic layer were considered. The total simulation period is 55 months from October 2004 to April 2009. Then, the model calibration was done using the observed data in April 2009. After which, this model was used to predict the extent of seawater intrusion in Liaodong Bay coastal plain 40 years after April 2009 considering with and without tidal effects. Finally, compare the results between with and without tidal case. Tide data was imposed with observed sea level data at the Ying Kou tidal station.

3.5.2 Model setup

To analysis the tidal effect on the seawater intrusion simulation, two case (excluding tidal case 1 and including tidal case 3) studies have been done in this chapter. For the including tidal case 3, the calibration model of case 1 is used for prediction the extents of seawater intrusion from April, 2009 to April, 2049, and the all parameter, boundary and initial conditions are same as the April, 2009's, except the ocean seawater level boundary using the observed tidal data of Yingkou station in 2004. The observed tidal data of Yingkou station show in the figure 3.19 (the observed tidal data got from the website of http://www.myfishing.org/index.php?option=com_content&task=view&id=81&Itemid=60). The numerical code used is SEAWAT. In the simulation, as groundwater layers, the Quaternary layer and the upper Neozoic layer were considered. The total simulation period is 55 months from October 2004 to April 2009. Then, the model calibration was done using the observed data in April 2009. After which, this model was used to predict the extent of seawater intrusion in Liaodong Bay coastal plain 40 years after April 2009 considering with and without tidal effects. Finally, compare the results between with and without tidal case.

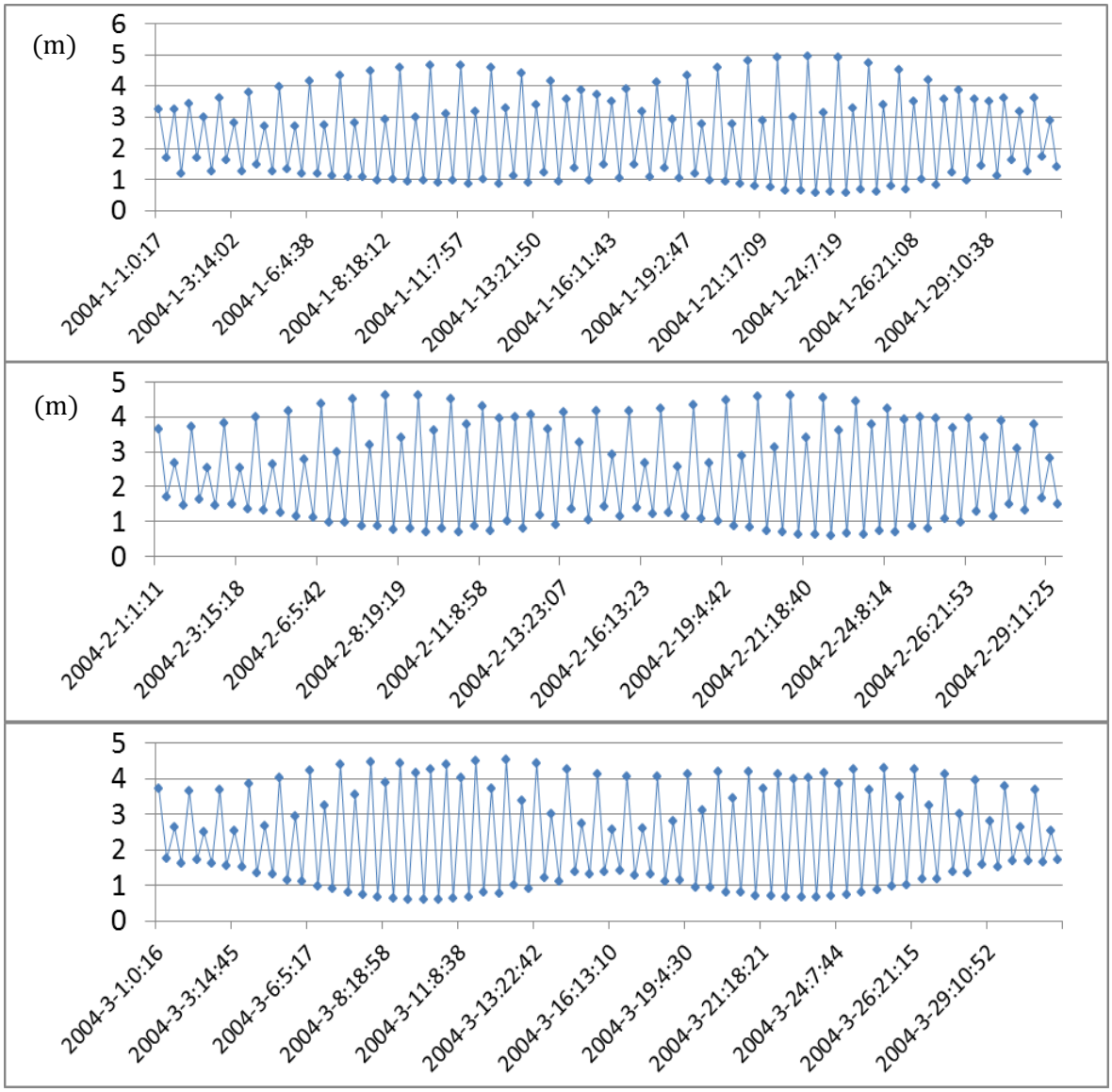

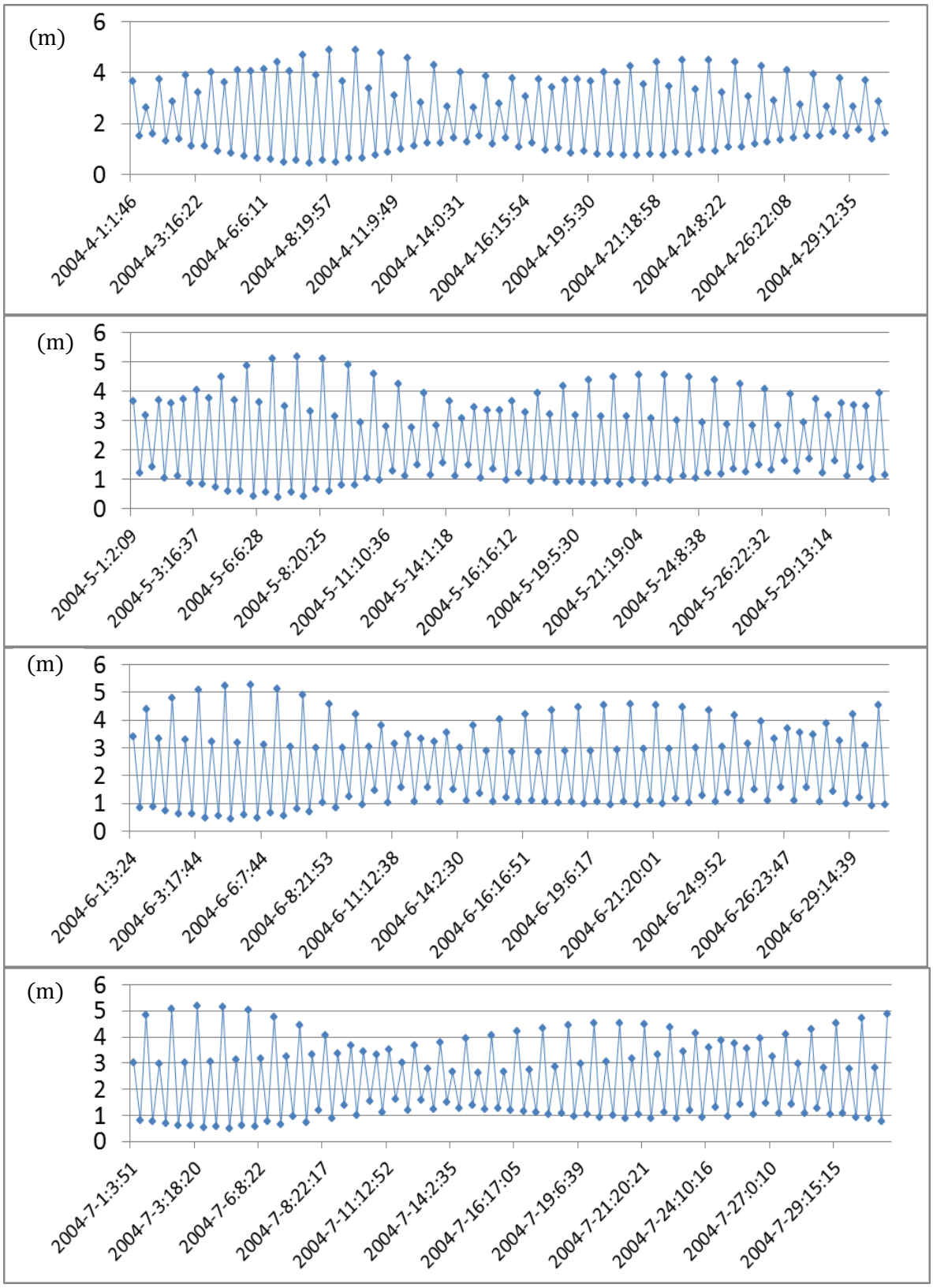
(m)
6
4
2
0
2004-4-1:1:46
2004-4-3:16:22
2004-4-6:6:11
2004-4-8:19:57
2004-4-11:9:49
2004-4-14:0:31
2004-4-16:15:54
2004-4-19:5:30
2004-4-21:18:58
2004-4-24:8:22
2004-4-26:22:08
2004-4-29:12:35
(m)
6
5
4
3
2
1
0
2004-5-1:2:09
2004-5-3:16:37
2004-5-6:6:28
2004-5-8:20:25
2004-5-11:10:36
2004-5-14:1:18
2004-5-16:16:12
2004-5-19:5:30
2004-5-21:19:04
2004-5-24:8:38
2004-5-26:22:32
2004-5-29:13:14
(m)
6
5
4
3
2
1
0
2004-6-1:3:24
2004-6-3:17:44
2004-6-6:7:44
2004-6-8:21:53
2004-6-11:12:38
2004-6-14:2:30
2004-6-16:16:51
2004-6-19:6:17
2004-6-21:20:01
2004-6-24:9:52
2004-6-26:23:47
2004-6-29:14:39
(m)
6
5
4
3
2
1
0
2004-7-1:3:51
2004-7-3:18:20
2004-7-6:8:22
2004-7-8:22:17
2004-7-11:12:52
2004-7-14:2:35
2004-7-16:17:05
2004-7-19:6:39
2004-7-21:20:21
2004-7-24:10:16
2004-7-27:0:10
2004-7-29:15:15

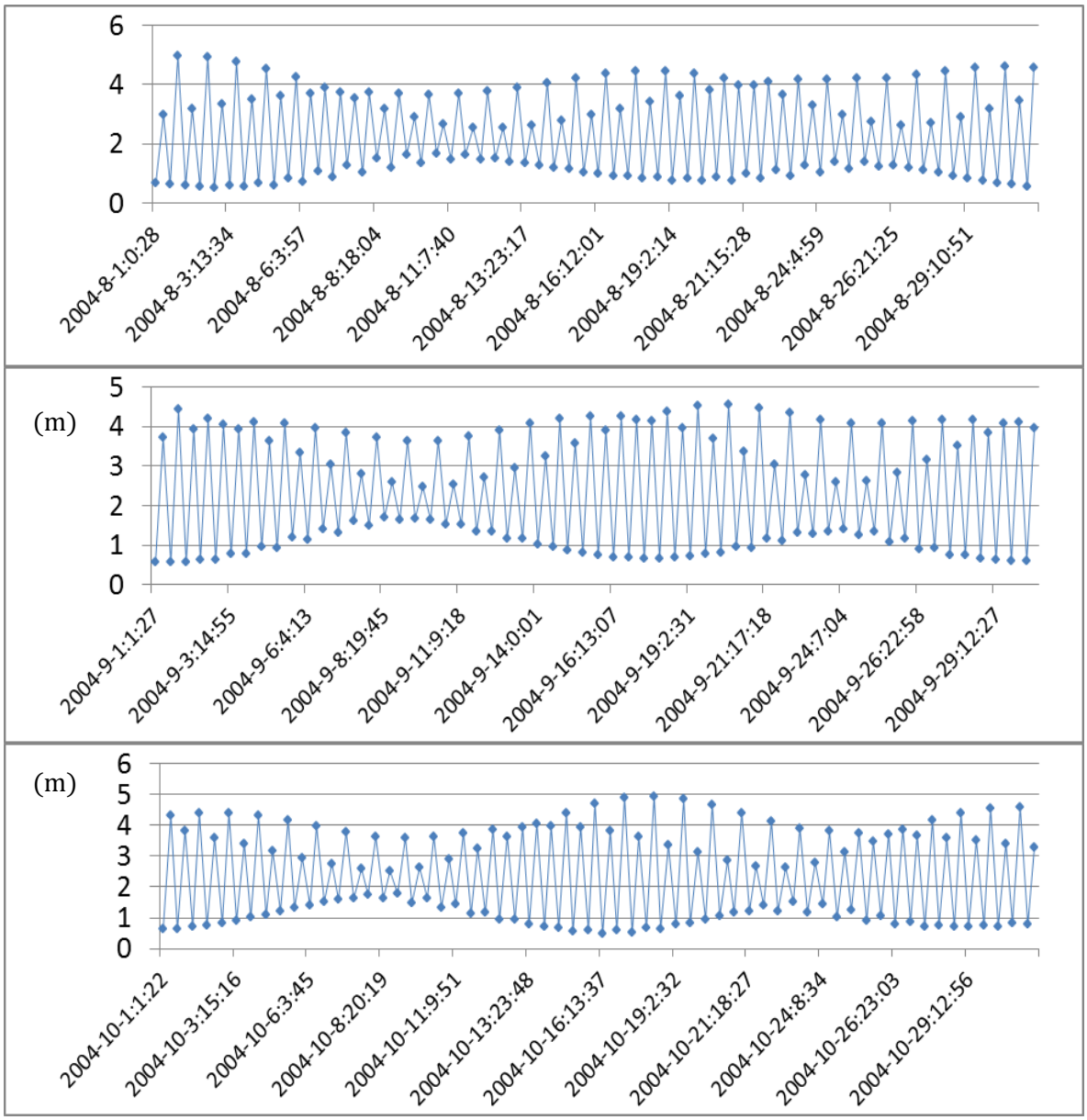
6
4
2
0
2004-8-1:0:28
2004-8-3:13:34
2004-8-6:3:57
2004-8-8:18:04
2004-8-11:7:40
2004-8-13:23:17
2004-8-16:12:01
2004-8-19:2:14
2004-8-21:15:28
2004-8-24:4:59
2004-8-26:21:25
2004-8-29:10:51
(m)
5
4
3
2
1
0
2004-9-1:1:27
2004-9-3:14:55
2004-9-6:4:13
2004-9-8:19:45
2004-9-11:9:18
2004-9-14:0:01
2004-9-16:13:07
2004-9-19:2:31
2004-9-21:17:18
2004-9-24:7:04
2004-9-26:22:58
2004-9-29:12:27
(m)
6
5
4
3
2
1
0
2004-10-1:1:22
2004-10-3:15:16
2004-10-6:3:45
2004-10-8:20:19
2004-10-11:9:51
2004-10-13:23:48
2004-10-16:13:37
2004-10-19:2:32
2004-10-21:18:27
2004-10-24:8:34
2004-10-26:23:03
2004-10-29:12:56

(m)

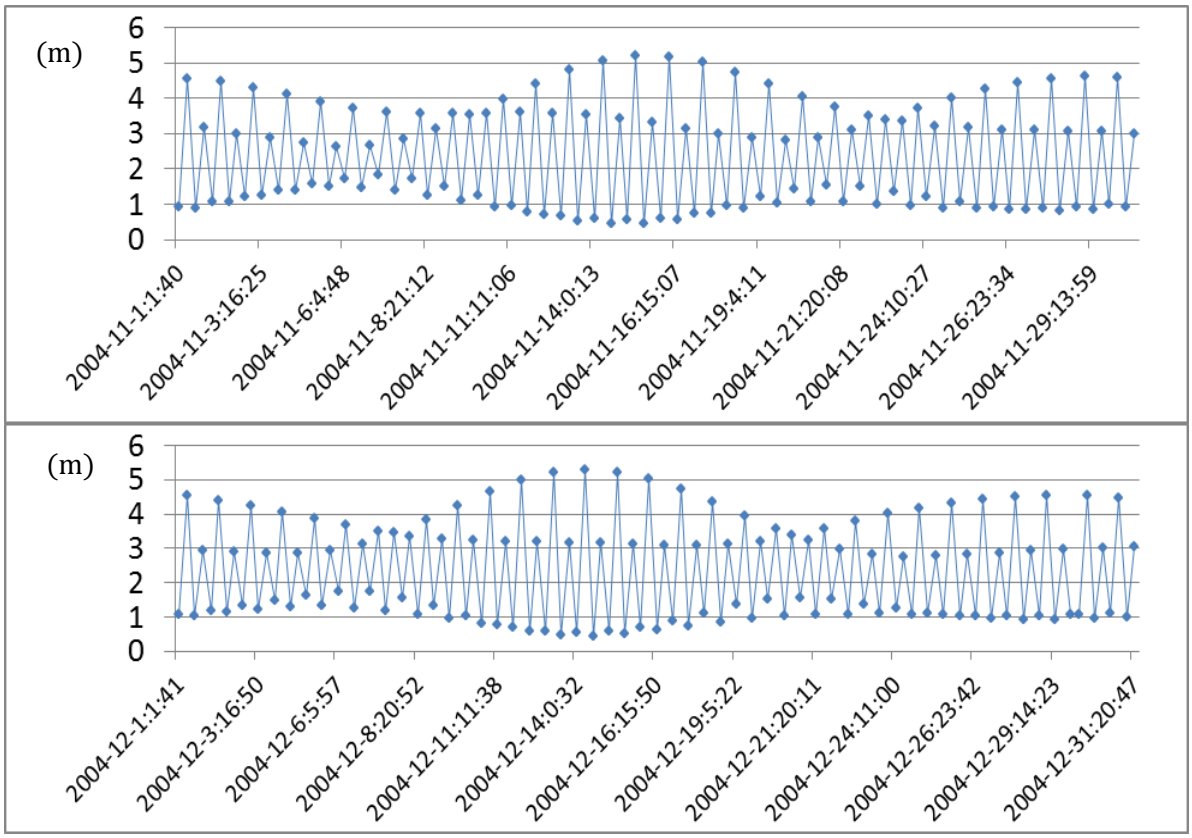

Figure 3. 19 The observation seawater level of Yingkou station from January to December, 2004. (unit in m)

3.5.3 Prediction of seawater intrusion

The model calibration was conducted by the simulation between 2004 (initial condition) and 2009 (calibration by observed data) with tuning conductivity, porosity. Using this calibrated model, prediction was conducted for 40 years from April, 2009 to April, 2049. Figure 3.20 indicates the processes of calibration and prediction computations.

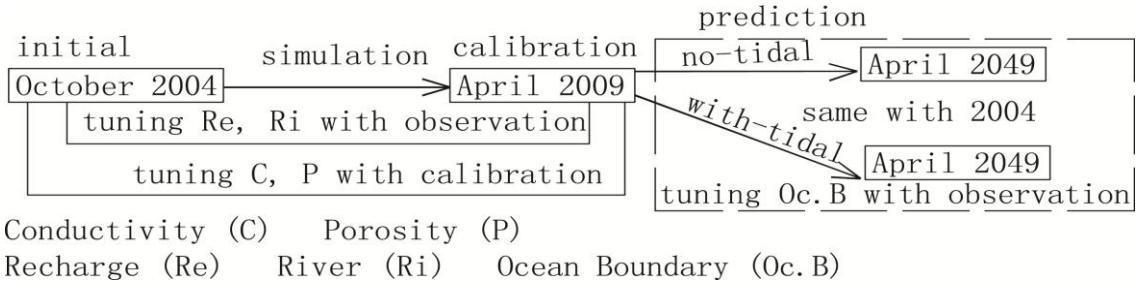

Figure 3. 20 Processes of calibration and prediction computations

Excluding tidal effect: case 1

Excluding the tidal effect, computation of the extent of seawater intrusion into the inland aquifers in Liaodong Bay coastal plain was conducted for 40 years from April, 2009 to April, 2049 using calibrated model.

The predicted extents of seawater intrusion in Layer-A1 (Quaternary layer) and Layer-A3 are shown in Figure 3.21 which depicts further seawater intrusion. Figure 3.21 (A) depicts

that the maximum extent of seawater intrusion in Layer-A1 sprawls about 7 km in the northwest direction and the extent of seawater intrusion in the southwest and northeast area is quite small. It also shows that the seawater intrusion in Layer-A1 is significantly faster than that in Layer-A3.

Including tidal effect: case 3

The same computation as in the case of 1 was conducted but this time with consideration of the tidal changes at the coastal boundary.

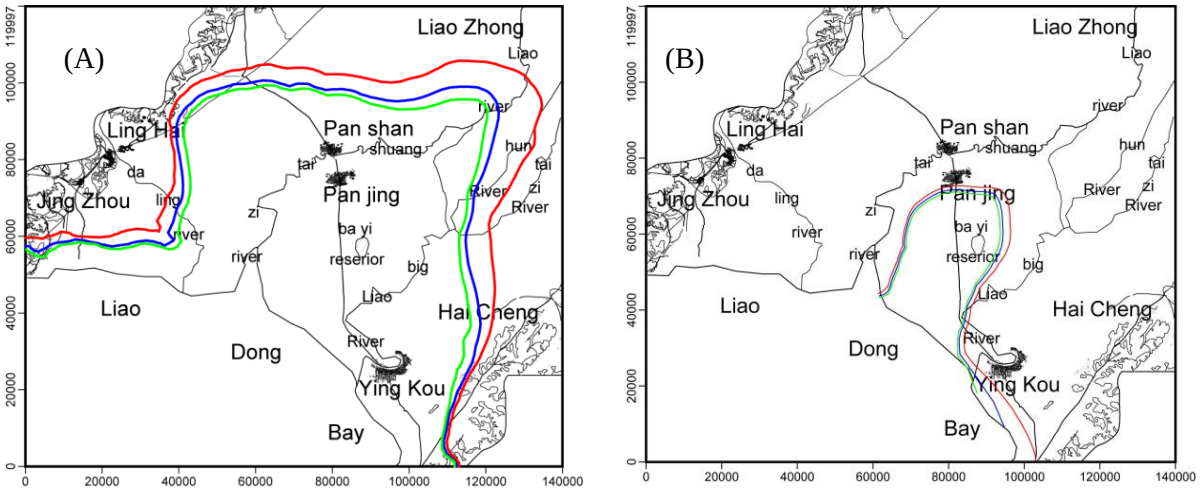

Figure 3. 21 Computed seawater intrusion limit in the case of tide effect excluded (case 1). (A) Layer-1 and (B) Layer-3. Blue line shows the simulated seawater intrusion limit in April 2009, green line in October 2004, and red line in April 2049.

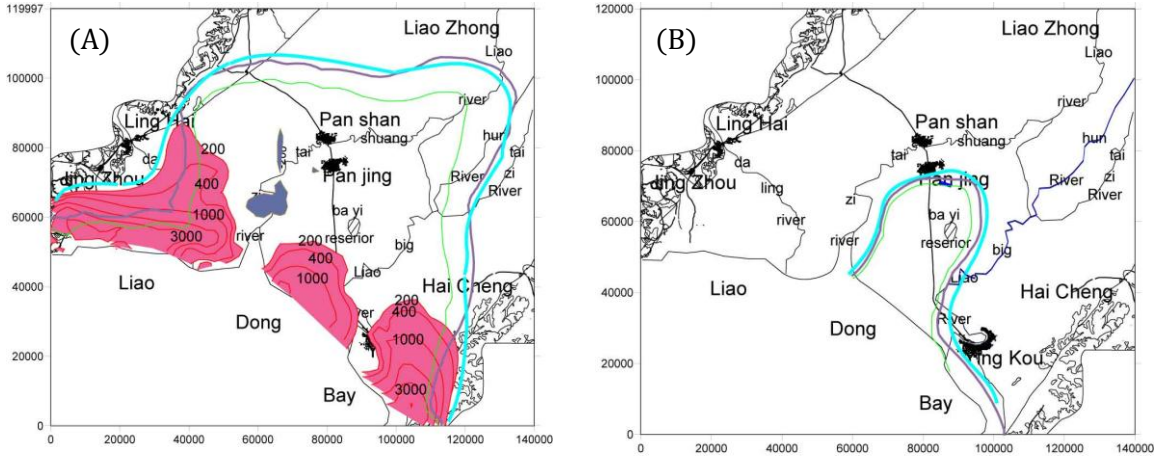

Figure 3. 22 Computed seawater intrusion limit in the case of tide effect included (case 3). (A) Layer- 1 and (B) Layer-3. Blue line shows the simulated seawater intrusion limit in April 2049, green line in October 2004. The purple line indicates the limit of case 1 (tide excluded) in April 2049. The area shaded in red and numeric in Layer-1 (A) show the chloride concentration difference between case 3 (tide included) and case 1 (tide excluded).

In Figure 3.22A, the area shaded in red and the associated numbers of Layer-A1 express the effect of tide to the extent of seawater intrusion, that is the difference of case 3 and case 1 (case 3 - case 1 for chloride concentration in April 2049). The difference of seawater

intrusion area between case 1 and case 3 is nearly 10 km (Figure 3.22A) at the southwest and southeast areas in Layer-1, while it is almost 3 km in Layer-A3 (Figure 3.22B). In addition, it can be seen that on the coastal area tidal effect affects nearly 20 km far from the coastal boundary of the Layer-1 (Figure 3.22A). The chlorine content in case 3 (including tide) is higher than that of case 1 (excluding tide).

3.5.4 Summary and conclusions

This study conducted a three-dimensional numerical simulation of density-dependent groundwater flow and miscible salt transport using SEAWAT code to assess the tidal effect on seawater intrusion in the Liaodong Bay coastal plain. Two cases of computations, that is, tide exclusion and tide inclusion were considered. The results showed that the chlorine content from tide computation experiment is higher than that from the tide exclusion computation experiment, specifically at point 20 km far from the sea boundary area of the Quaternary layer in April 2049. Compared with the tide exclusion computation experiment results, the seawater intrusion area from tide computation experiment increased nearly 10 km at the southwest and southeast of study area in the Quaternary layer and 3km in the Minhuazhen group layer. In conclusion, this study shows that the tidal fluctuation has significant effects on the seawater intrusion. Therefore, it is necessary to consider tidal effect for simulation of seawater intrusion in the coastal plane.

3.6 Conclusions

The prediction results of the three case studies showed that the maximum extent of seawater intrusion in Quaternary Layers was significantly faster than that in Neozonic Layers. As a continuous increase in population, the demand for groundwater pumping might be intensified. Then it can be expected the actual extent of seawater intrusion in future might be more severe than the model prediction. So it is very important to protect the freshwater aquifers from salt water contamination in the study area.

Due to the scarcity of the observed chloride concentrations and continuously monitored head data, the two models were only calibrated against the observed hydraulic heads in April 2009. During calibration, a total of 18 observed hydraulic head values were used. The results showed that the observed and calculated hydraulic heads matched well. However, additional calibration was necessary after more data became available in the future.

To protect the groundwater resources in the coastal aquifers of this study area from the seawater intrusion, regional water resources assessment and optimal allocation study should be done. Meantime, it is recommended that some protection schemes, such as operational controls (e.g., pumping and well-construction restrictions) and engineering works (e.g., artificial recharge schemes and cut-off wall schemes), should be established based on the regional water resources assessment and optimal allocation study. Specifically, it is necessary to reduce pumping groundwater in Minghuazhen group aquifer.

REFERENCES

Abd-Elhamid, H.F. and Javadi, A.A.: A density-dependant finite element model for analysis of saltwater intrusion in coastal aquifers. *Journal of Hydrology*, Vol. 401, pp. 259 - 271, 2011.

Andersen, P. F., Mercer, J. W. and White, J. H. O.: Numerical modeling of salt-water intrusion at Hallandale, Florida. *Ground Water*, Vol. 26 (5), pp. 619–630, 1988.

Arlai, P., Koch, M., and Koontanakulvong, S.: Modeling flow and transport for sustainable yield estimation of groundwater resources in the Bangkok aquifer system. EGU General Assembly 2006, Vienna, Austria, 2006.

Arlai, P., Koch M., Koontanakulvong, S. ,and Weerapol, B.: Numerical Modeling as a Tool to Investigate the Feasibility of Artificial Recharge to Prevent Possible Saltwater Intrusion into the Bangkok Coastal Aquifers System. Proceedings of Groundwater Hydraulics in omplex Environments, Toulouse, France, 2006.

Arlai, P., Koch ,M. ,and Koontanakulvong, S.: Statistical and Stochastic Approaches to Assess Reasonable Calibrated Parameters in a Complex Multi-Aquifer System. Proceedings of CMWR XVI-Computational Methods in Water Resources, Copenhagen, Denmar, 2006.

Arlai, P., Koch, M. ,and Koontanakulvong, S. Numerical.: Investigation of the Cradle of Saline Contamination and Effective Remediation Schemes for Amending Saline Water Pollution Problem in the Bangkok Coastal Aquifers System. 3rd APHW Conference, Bangkok, 2006.

Ataie-Ashtiani, B., Volker, R.E., and Lockington, D.A.: Tidal effects on sea water intrusion in unconfined aquifers. *Journal of Hydrology*, Vol. 216, pp. 17–31, 1999.

Ataie-Ashtiani, B., Volker, R.E., and Lockington, D.A.: Tidal effects on groundwater dynamics in unconfined aquifers. *Journal of Hydrological processes*, 15, 655–669, 2001.

Bakker, M., and Schaars, F.: *The sea water intrusion (SWI) package manual*, version 0.2, University of Georgia, Athens, 2003.

Bear, J.: *Hydraulics of groundwater*, New York, McGraw-Hill, 1979.

Bhosale, D. and Kumar, C.: Simulation of Seawater Intrusion in Ernakulam Coast. proceeding of International Conference on Hydrology and Watershed Management, Hyderabad, pp. 390-399, 2002.

Bian, J. M., and Tang, J.: Groundwater resources optimal allocation countermeasures in the liaohe oil field area. Proceedings of the 34th Congress of International Association of Hydrogeologists, Bejing, China, October 9-13, 2006.

Bobba, A.G.: Mathematical models for saltwater intrusion in coastal aquifers. *Water Resources Management*, Vol. 7: pp. 3–37, 1993.

Dominick TF, Wilkins B, Roberts H.: Mathematical model for beach groundwater fluctuations. *Water Resources Research*, 7, 1971.

El-Bihery, M. A.: Groundwater flow modeling of Quaternary aquifer Ras Sudr, Egypt. *Environmental Geology*, Vol. 58, pp. 1095–1105, 2009.

Evans, M.: *Nutrient Discharge to Cockburn Sound from a Subterranean Mixing Zone: a Comparison of Transport and Reaction Timescales*, Honours thesis, University of Western Australia, p.83, 2005.

Giambastiani, B. M. S., Antonellini, M., Oude Essink, G. H. P., and Stuurman, R. J.: Saltwater intrusion in the unconfined coastal aquifer of Ravenna (Italy): A numerical model. *Journal of Hydrology*, Vol. 340, pp. 91-104, 2007.

Guo, W., and Bennett, G. D.: *Simulation of saline/fresh water flows using MODFLOW*. Proceedings of MODFLOW '98 conference at the international ground water modeling center, Colorado School of Mines, Golden, Colorado, vol 1, pp. 267–274, 1998.

Guo, W. X., and Langevin, C. D.: *User's guide to SEAWAT: a computer program for the simulation of three-dimensional variable-density ground-water flow*. USGS Techniques of Water Resources Investigations. Book 6, chap A7, p. 77, 2002.

Harbaugh, A. W., Banta, E. R., Hill, M. C., and McDonald, M. G.: *MODFLOW- 2000, the U.S. Geological Survey Modular Ground-Water Model—User Guide to Modularization Concepts and the Ground-Water Flow Processes*. U.S. Geological Survey Open- File Report 00-92, 121p, 2000.

Huyakorn, P. S., Andersen, P. F., Mercer, J. W., and White, J. H. O.: Saltwater intrusion in aquifers: Development and testing of a three-dimensional finite element model. *Water Resource Research*, Vol. 23(2): 293–312, 1987.

HydroGeoLogic Inc.: *MODHMS—MODFLOW-Based Hydrologic Modeling System: Documentation and User's Guide*, Herndon, Virginia, 2002.

Kopsiaftis, G., Mantoglou, A., and Giannoulopoulos, P.: Variable density coastal aquifer models with application to an aquifer on Thira Islan. *Desalination*, Vol. 237, pp. 65–80, 2009.

Langevin, C. D., Shoemaker, W. B., and Guo, W.: *MODFLOW-2000, the U.S. Geological Survey Modular Ground-Water Model—Documentation of the SEAWAT-2000 version with the variabledensity flow process (VDF) and the integrated MT3DMS Transport Process (IMT)*. USGS Open-File Report 03-426, 2003.

Langevin, C. D., Oude Essink, G. H. P., Panday, S., Bakker, M., Prommer, H., Swain, E. D., Jones, W., Beach, M., and Barcelo, M.: *MODFLOW based tools for simulation of variable-density groundwater flow*. In: Cheng A, Ouazar D (eds) Coastal aquifer management: monitoring, modeling, and case studies, Lewis Publishers, Boca Raton, pp. 49–76, 2004.

Langevin, C. D., and Guo, W. X.: MODFLOW/MT3DMS–Based Simulation of Variable-Density Ground Water Flow and Transport. *Ground water*, Vol. 44, No. 3, pp. 339–351, 2006.

Langevin, C.D., Thorne, D.T., Jr., Dausman, A.M., Sukop, M.C., and Guo, W. X.: *SEAWAT Version 4: A Computer Program for Simulation of Multi-Species Solute and Heat Transport*. U.S. Geological Survey Techniques and Methods Book 6, Chapter A22, 39 p, 2007.

Li, Y. M.: *Groundwater quality simulation and forecast in liaohe oil field* (in chinese). Msc Thesis, Jiling University, 86 p, 2005.

Lin, J., Snodsmith, J. B., Zheng, C. M., and Wu, J. F.: A modeling study of seawater intrusion in Alabama Gulf Coast, USA. *Environmental Geology*, 57: pp. 119–130, 2009.

Mao, X., Enot, P., Barry, D.A., Li, L., Binley, A., and Jeng, D. S.: Tidal influence on behaviour of a coastal aquifer adjacent to a low-relief estuary. *Journal of Hydrology*, 327, pp. 110-127, 2006.

McDonald, M. G., and Harbaugh, A. W.: *A modular three-dimensional finite-difference ground-water flow model*, U.S. Geological Survey Techniques of Water Resources Investigations, Book 6, chap A1, 588p, 1988.

Ministry of Health of the Heople's Republic of China, *Standards for drinking water quality*, GB 5749-2006, p. 9, 2006.

Oude Essink, G. H. P.: MOC3D adapted to simulate 3D densitydependent groundwater flow. Proceedings of MODFLOW '98 conference at the international ground water modeling center, Colorado School of Mines, Golden, Colorado, vol 1, pp. 291–300, 1998.

Oude Essink, G. H. P.: Saltwater Intrusion in 3D Large-Scale Aquifers: A Dutch Case. Phys. *Chem. Earth* (B), Vol. 26, No. 4, pp. 337-344, 200l.

Sorek, S., and Pinder, G. F.: *Survey of computer codes and case histories*. In: Bear J et al (ed) Seawater intrusion in coastal aquifers: concepts, methods, and practices, Kluwer Academic Publishers, Dordrecht, pp. 399–461, 1999.

Voss, C.: *SUTRA: A Finite-Element Simulation Model for Saturated-Unsaturated Fluid-Density-Dependent Ground-Water Flow With Energy Transport or Chemically-Reactive Single-Species Solute Transport*. Water Resources Investigation Report 84-4369, U.S. Geological Survey, 1984.

Wang, W. D., Zhang, G. X., and Li, B. L.: *Report on Groundwater Management Simulation in Panjin City, Liaoning Province*, (in chinese). Liaoning hydrogeology and engineering geology exploration, 1992.

Xue, X. D.: *The research of the simulation with prediction of the groundwater level and the rational utilization of the water resource in panjin area*, (in chinese). Msc Thesis, Jiling University, 91p, 2005.

Zheng, C. M. and Wang, P. P.: *MT3DMS: Documentation and User's Guide*. Contract Report SERDP-99-1, U.S. Army Engineer Research and Development Center, Vicksburg, MS, 1999.

Chapter 4

Atmosphere and Ocean Simulation

Precipitation, evaporation, freezing and melting and condensation are all part of the hydrological cycle-a never ending global process of water circulation from clouds to land, to the ocean, and back to the clouds. This cycling of water is intimately linked with energy exchanges among the atmosphere, ocean, and land that determine the Earth's climate and cause much of natural climate variability [web-1]. Seawater intrusion process is one part of the hydrological cycle. Therefore, it is necessary to study the seawater intrusion based on the hydrological cycle. To understand the atmosphere and ocean cycle and provide the atmospheric and oceanic disturbance parameters induced by typhoon, a case study about typhoon Morakot is done in this chapter.

web-1: http://science.nasa.gov/earth-science/ oceanography/ocean-earth-system/ocean-water-cycle/

4.1 Introduction

Tropical cyclones (TCs) are one of the most intense weather hazards of all meteorological phenomena that form over the tropical oceans and seas. Typhoons in the west Pacific Ocean, where Taiwan Island is located, are equivalent to hurricanes on the west US coast, which are generated due to the warmer seas of the west Pacific Ocean and south-westerly monsoons in the South China Sea (SCS) (Pan et al., 2010). The island of Taiwan is roughly 200 km wide and 400 km long. This land mass is centred at 23.58°N, 121.8°E and is frequently located along the routes of typhoons in the western North Pacific (WNP). Typically, three to four typhoons make landfall in Taiwan each year, causing loss of life and property damage (Hsiao et al., 2009). The direct threats that a TC pose toward human life and property mainly come from its destructive winds and heavy rainfall, as well as debris flows caused by continuous heavy rainfall.

From 3 to 11 August, 2009, Typhoon Morakot caused significant loss of life and property in Taiwan. Morakot was the most damaging typhoon to make landfall in Taiwan in the last half century. As of 18 September, 2009, the National Disaster Prevention and Protection Commission (NDPPC) in Taiwan has reported 639 identified and 62 unidentified deaths; 58 persons have been reported missing. An economic loss of over US $3 billion has been incurred. The slow moving storm also caused widespread damage in China, leaving eight people dead and causing $1.4 billion (USD) in damages. Nearly 2,000 homes were destroyed in the country and 136,000 more were reported to have sustained damage. The storm also caused severe flooding in the northern Philippines that killed 26 people. Therefore, it is important to research that enables a timely forecast of typhoon tracks and rainfall amounts.

There are several studies relating to tropical cyclones (TCs) simulation. Surface fluxes of latent and sensible heat play a vital role in the development and maintenance of TCs (Bayers, 1944). The favourable conditions for the formation of TC have been known for some time and it requires a preexisting disturbance of sufficient amplitude such that air-sea

interaction can occur (Riehl, 1948; Gray, 1968; McBride and Zehr, 1981). Performance of a numerical model in TC forecast depends on how good the convection is parameterized in the model. Cumulus convection, surface fluxes of heat, moisture, momentum, vertical mixing in the PBL, radiative heating and cooling also play important roles in the development of TCs (Anthes, 1982).

The importance of microphysical schemes (MS) within TCs has been recognized for a long time (Yang and Houze 1995,), Yang and Houze (1995) indicated that the simulated rainfall amount, distribution, and internal mesoscale structure were highly sensitive to the hydrometeor types and MS implemented in the model. Wang (2002) further indicated that the detailed cloud structures of an idealized TC were quite different with various MS, although the intensification rate and final intensity were not very sensitive to the details of cloud microphysics parameterizations. Although there are now several MS available to use in numerical models, a systematic comparison of MS in a TC simulation is still important for typhoon forecasting over the Taiwan area.

The bogus scheme was first developed to improve the numerical simulation of TCs in a mesoscale model (Low-Nam and Davis, 2001). There are some experiments to used bogus scheme in Typhoon simulation (Pu and Braun 2001, Kwon et al. 2002, Lee et al. 2010). It is important to analysis the role of bogus scheme for the simulation of Typhoon Morakot with the extreme heavy rainfall.

In general, the TC-related rainfall distribution depends greatly on the internal structure of the TC. For example, the size of the eyewall determines to first order the location of the maximum rain rate (Lonfat et al., 2004). Asymmetry in the eyewall convection and mesoscale convective systems embedded in the TC are also important factors. For Taiwan, two other factors influence the local TC-related rainfall to a large extent and cause significant difficulties in forecasting these events: (1) the topographical effect of the Central Mountain Range (CMR). The CMR in Taiwan, which has an average height of about 3 km, may greatly modify TC tracks (Yeh and Elsberry, 1993a; b) and impact rainfall distribution (Wu and Kuo, 1999; Chiao and Lin, 2003; Jian and Wu, 2008); (2) the interaction of the approaching TC with the Asian monsoon system. This may also lead to a rainfall pattern that deviates substantially from the TC rainfall climatology (Ge et al., 2010).

Ge et al. (2010) used the Advanced Research Weather Research and Forecasting model (WRF-ARW) to analysis what causes the extremely heavy rainfall during Typhoon Morakot. It suggested the critical role of the CMR for Morakot in their numerical experiments at 3-km resolution. Their control case resulted in a maximum rainfall total of more than 1800 mm. It is insufficient for this unprecedented rainfall of the 2,777 mm maximum. Here, we apply a non-hydrostatic mesoscale model, MM5, with 3 km resolution to simulate the total rainfall (more than 2,400 mm maximum) more closer to the observed than that of Ge et al. (2010) . To examine the topographic effect, he just conducted one experiment (TOP100), in which the topography over Taiwan Island is set to be 100 m if the elevation is higher than this value. It is very important to do a systematic experiments with different elevation of Taiwan Island to analysis the role of CMR for typhoon forecasting over the Taiwan area.

In this study, we performed a number of numerical experiments using a non-hydrostatic mesoscale model, MM5, to investigate the possible reasons for the unique track of Typhoon Morakot and the extremely heavy rainfall produced during its landfall in Taiwan.

In particular, the effects of the terrain, microphysics parameterization and bogus scheme application were examined.

The primitive-equation ocean model, POM (Mellor, 2004), for the ocean. The Princeton Ocean Model (POM), a simple-to-run yet powerful ocean modeling code that is able to simulate a wide-range of problems: circulation and mixing processes in rivers, estuaries, shelf and slope, lakes, semi-enclosed seas and open and global ocean. POM is a sigma coordinate, free surface ocean model with embedded turbulence and wave sub-models, and wet-dry capability.

4.2 Synoptic Background of Typhoon

Typhoon Morakot was the deadliest typhoon to impact Taiwan in recorded history. It formed early on 2 August, 2009 and was an unnamed tropical depression at that time. During the course of the day the depression gradually developed. Late on 3 August, this depression was upgraded to a tropical storm and assigned the name Morakot by the Japan Meteorological Agency (JMA). The large storm system gradually intensified as it tracked westward towards Taiwan. By 5 August, the JMA and Joint Typhoon Warning Center (JTWC) upgraded Morakot to a typhoon. The barometric pressure of the typhoon steadily decreased owing to its size. However, its maximum winds increased only slightly. Early on 7 August, the storm attained its peak intensity with winds of 150 km/h (41.7 m/s 10-m sustained) and lowest central pressure of 945 hPa according to the JMA. Morakot weakened slightly before making landfall at Hualian in the eastern part of Taiwan later that day (at 23:00 UTC 7 August). At this point it was classified as a medium strong typhoon (Category 2 TC on the Saffir-Simpson scale). This storm system resulted in a new rainfall record of 2777 mm at Alishan (Mount Ali; previous rainfall record of 1,736 mm was set by Typhoon Herb in 1996). The path of Morakot, its satellite images with clouds and the observed accumulated rainfall from 6 to 10 August, 2009 are shown in Figures 4.1, 4.2 and 4.3, respectively. The typhoon passed through the central and northern parts of Taiwan and left at Taoyuan, on the western coast. Torrential rains were primarily concentrated in the south. Thus, the most heavily damaged areas were in this southern region. Roughly 24 hours later, the storm emerged back over water into the Taiwan Strait and weakened to a severe tropical storm before making landfall in China on 9 August. The storm gradually weakened as it continued to slowly track inland. The remnants of the typhoon eventually dissipated on 11 August (Figure 4.4).

In the west of Morakot, tropical storm Goni formed at SCS before Typhoon Morakot formed. This storm system then strengthened and made landfall at Guangdong province in China on the night of 4 August. Subsequently, the storm dissipated over land until it strengthened again to the tropical storm level and moved into the Beibu Gulf.

Another tropical storm, named Etau, originated on 5 August and moved to the northwest, strengthening into a tropical storm. By 9 August, the centre of circulation for this storm became more defined as convection wrapped around it. Around 12:00 UTC, the JMA upgraded the depression to a tropical storm and gave it the name Etau. On 10 August, the system re-curved toward the east around the western periphery of the subtropical ridge. Etau also became slightly disorganized at this point, as it began to interact with the baroclinic zone near Japan on 7 August.

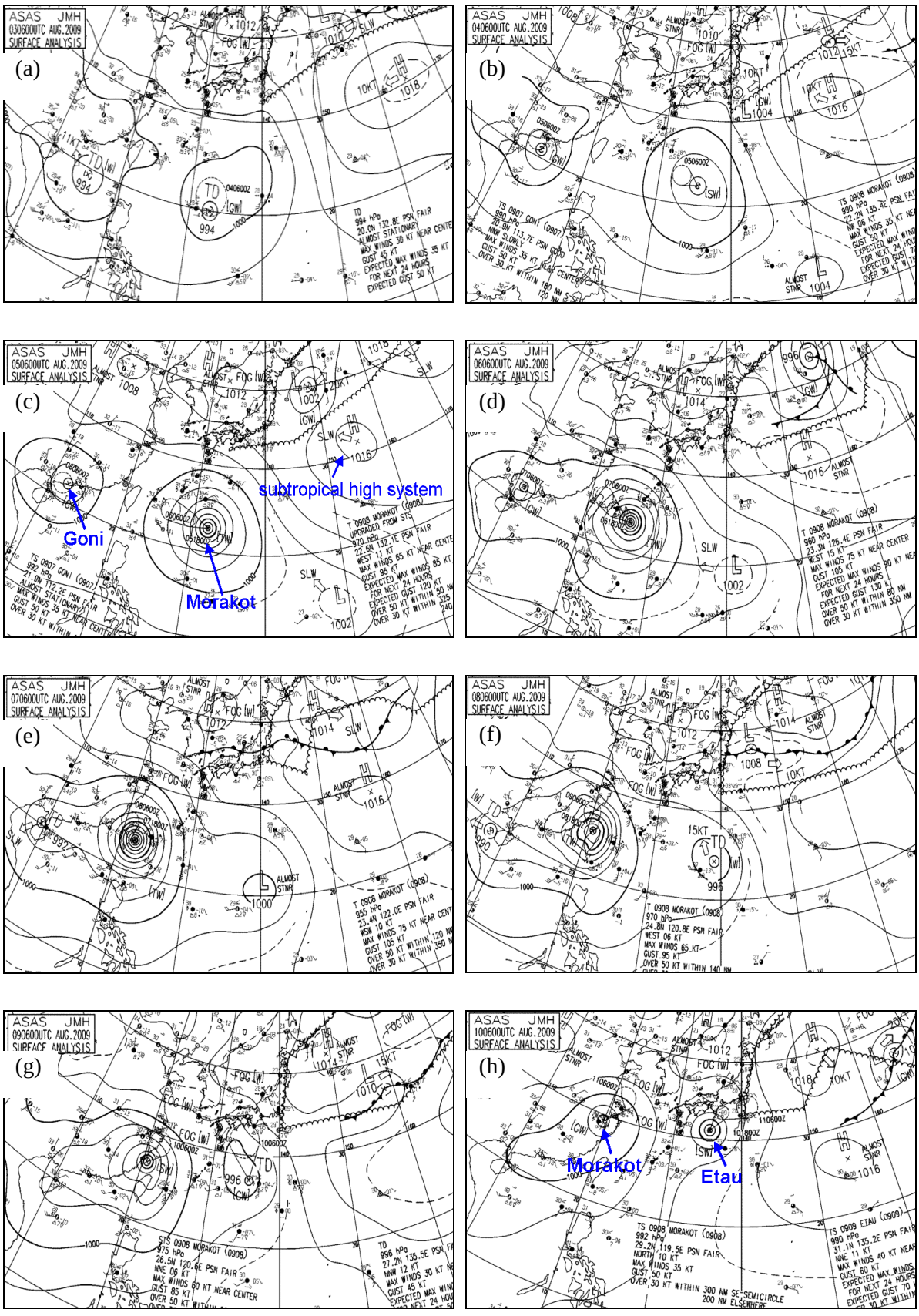

Figure 4. 1 Weather charts for one-day increments from 06:00 UTC 3 to 06:00 UTC 10 August 2009 showing the Typhoons Goni, Morakot, and Etau together with the subtropical high system [from Japan Meteorological Agency (JMA)

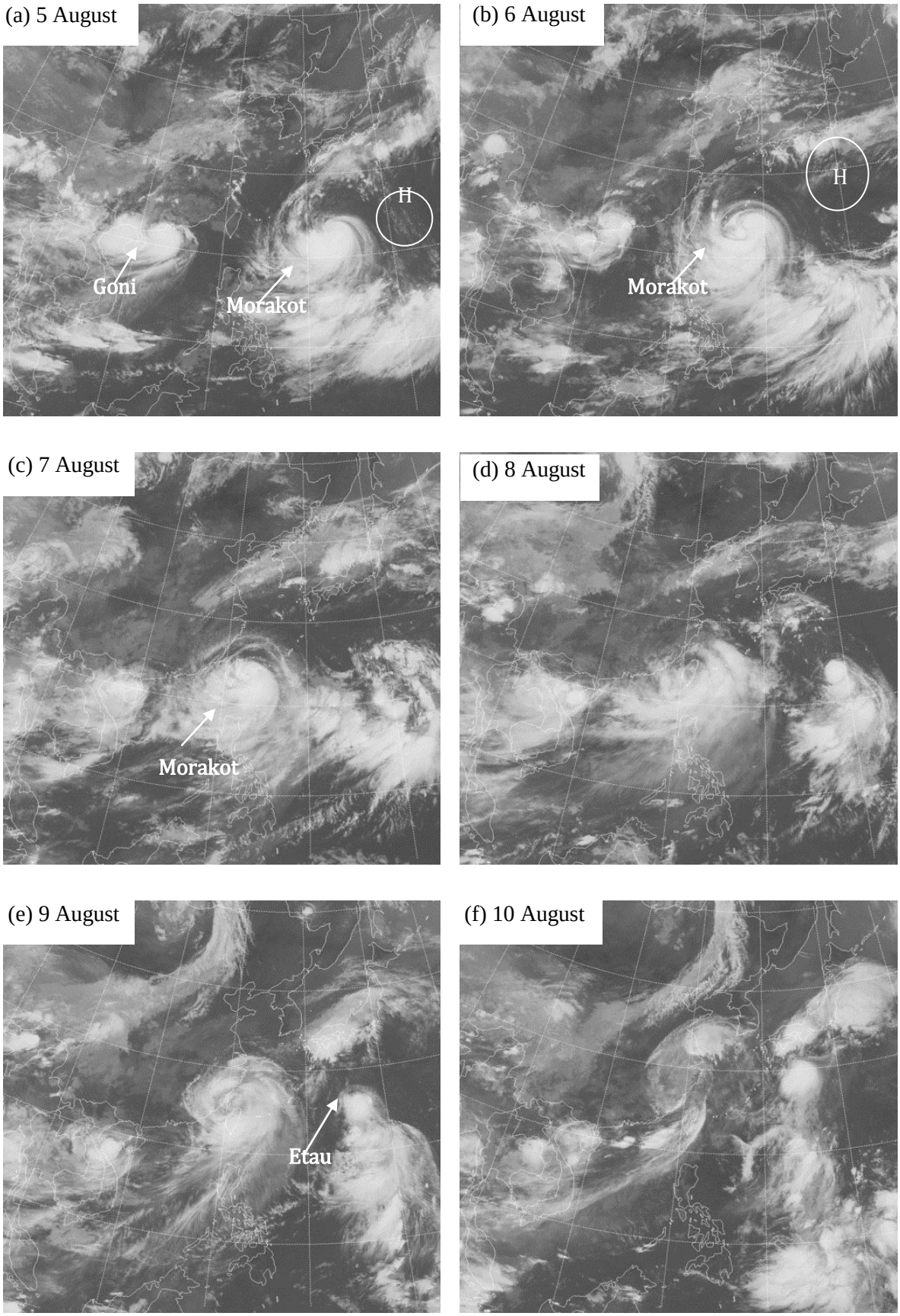

Figure 4. 2 Infrared satellite images for one-day increments from 08:30 UTC 5 to 08:30 UTC 10 August 2009 from the Central Weather Bureau (CWB), Taiwan

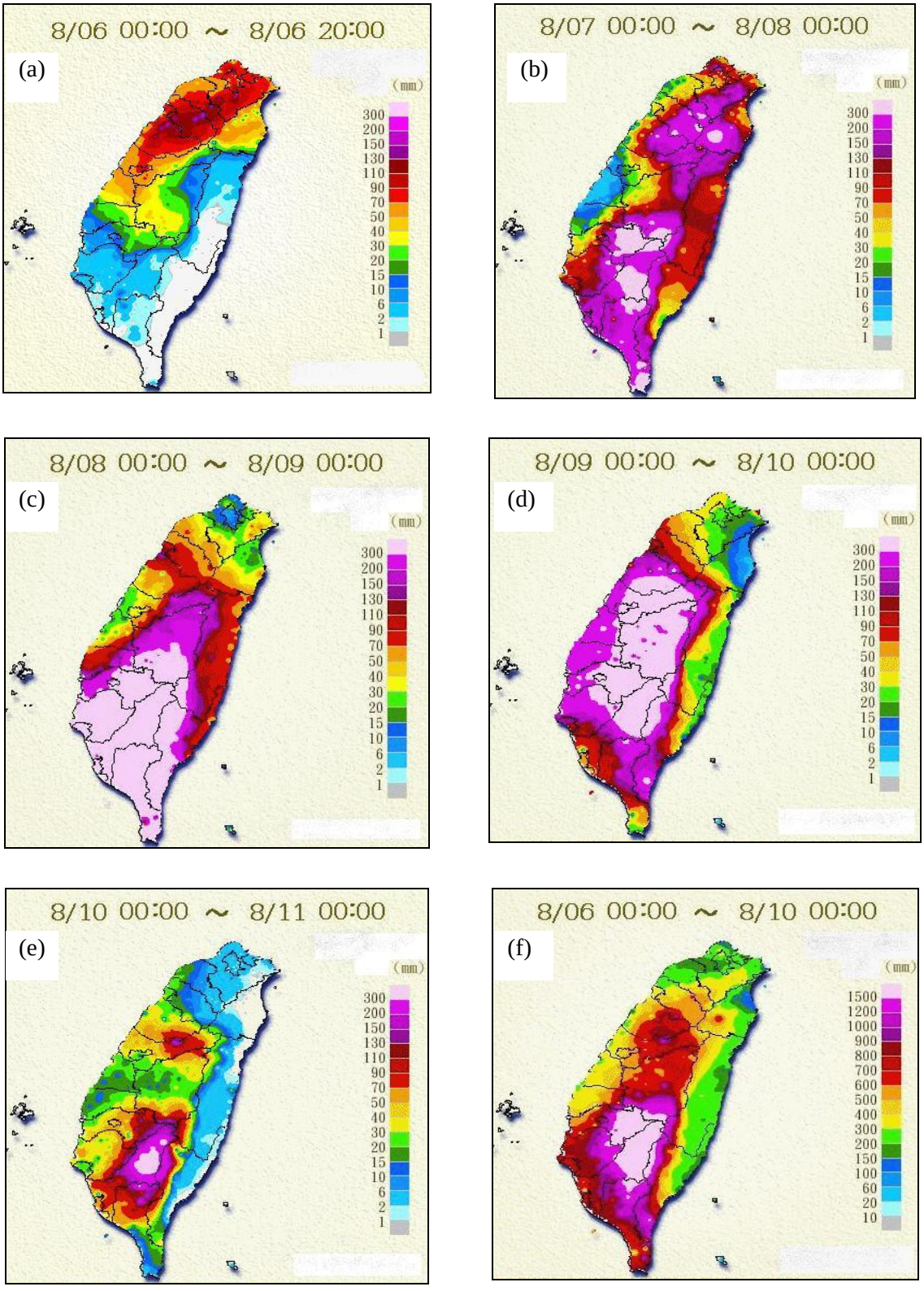

Figure 4.3 Observed accumulated rainfalls for the given periods in 2009. Note that (f) shows four-day accumulated rainfall, whereas the others present one-day accumulated rainfall, except for (a) [data from CWB]

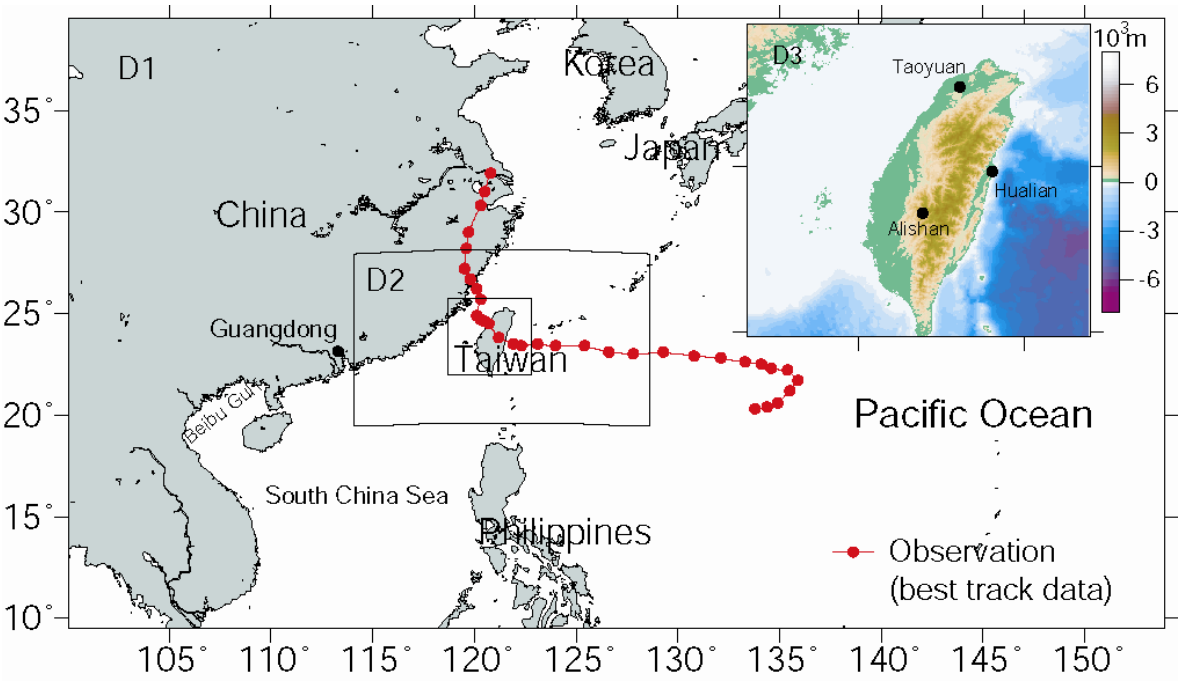

Figure 4.4 Domain configuration for MM5 simulations with the best track from JMA. Subplot shows the topography of Taiwan in Domain 3 depicting the Central Mountain Ridge (CMR) with the Alishan (Mount Ali)

The weather charts showing the meteorological conditions from 06:00 UTC 3 to 06:00 UTC 10 August 2009 are presented in Figure 4.1. This figure shows that an atmospheric low-pressure system (Morakot) with a minimum pressure of 994 hPa developed on the eastern side of the Philippines and was moving towards the east at 06:00 UTC 3 August. Another atmospheric low-pressure system, TC Goni, with a minimum pressure of 994 hPa developed in the SCS at 06:00 UTC 3 August. This storm moved towards the northwest and stayed in Beibu Gulf for nearly six days. In addition, there was a subtropical high system with maximum pressure of 1018 hPa toward the east of Japan near 160°E. This system was moving towards the southwest at 06:00 UTC 3 August. Subsequently, the subtropical high system changed direction from the southwest to the northwest at 06:00 UTC 4 August. The low-pressure system (Morakot) rapidly strengthened within two days and its central pressure dropped from 994 to 970 hPa at 06:00 UTC 5 August. The subtropical high system changed direction from the northwest to the northeast at 18:00 UTC 6 August. The other atmospheric low-pressure system, TC Etau, with a minimum pressure of 1002 hPa developed in the east of the Philippines at 06:00 UTC 6 August and moved towards the northwest, as mentioned above.

4.3 Numerical Models

The atmosphere - ocean coupled model consists of the following components: the MM5, a non-hydrostatic mesoscale model developed by Pennsylvania State University (PSU) and the National Center for Atmospheric Research (NCAR), was utilized for the atmosphere in this study. This model is based on a non-hydrostatic, compressible form of governing equations in spherical and sigma coordinates and includes physical processes such as precipitation physics, Planetary Boundary Layer (PBL) processes and atmospheric radiation processes that are incorporated by a number of physics parameterisations. MM5

also considers complex topographical effects during calculations. For more details on MM5, refer to Grell et al. (1995). The primitive-equation ocean model, POM (Mellor, 2004), for the ocean. The Princeton Ocean Model (POM), a simple-to-run yet powerful ocean modeling code that is able to simulate a wide-range of problems: circulation and mixing processes in rivers, estuaries, shelf and slope, lakes, semi-enclosed seas and open and global ocean. POM is a sigma coordinate, free surface ocean model with embedded turbulence and wave sub-models, and wet-dry capability.

4.3.1 Model setup

The atmosphere model MM5 in present study adopted an interactive grid nesting with three domains (Figure 4.4) that had horizontal resolutions of 27, 9 and 3 km, respectively. The three domains had 120×175, 100×163 and 136×136 grid points covering the regions at approximately: 100.07^{o} - 153.94^{o} E, 9.5^{o} - 39.54^{o} N for domain 1; 114.09^{o} - 128.59^{o} E, 19.45^{o} - 27.95^{o} N for domain 2; and 118.67^{o} - 122.79^{o} E, 21.95^{o} - 25.72^{o} N for domain 3, respectively (see Table 1). In addition, twenty three vertical sigma layers from the surface up to the 100 hPa level for three domains were set up with 60 s time steps. The MM5 computation was carried out for eight days from 00:00 UTC 3 to 00:00 UTC 11 August in 2009 with Real-time Global Sea Surface Temperature (RTG SST) data (Gemmill et al., 2007) for the lower surface boundary condition. The initial and lateral boundary conditions were imposed every six hours using NCEP FNL Operational Global Analysis data with 1°×1° latitude–longitude resolution (http://dss.ucar.edu/datasets/ds083.2/). The model topography for the chosen domain regions was obtained from the U.S. Geological Survey (USGS) topography data. Four-dimensional Data Assimilation (FDDA) was also applied to the first domain in wind, temperature and mixing ratio fields every six hours with the NCEP FNL data.

The POM simulation for the storm surge was also performed for the same period with onlydomain 1. The meteorological forcing (wind and pressure fields) were imposed from the MM5 results. The prescribed tidal forcing of 8 constituents (M2, S2, K1, O1, N2, K2, P1, and Q1) was applied at the lateral open ocean boundaries from the National Astronomical Observatory's ocean tide model [Matsumoto, 2000]. For storm surge simulations, the barotropic ocean states were considered such that the influences of temperature and salinity profiles in the ocean remained uniform. The bathymetry for storm surge simulations was taken from the GEBCO 30 arc-sec data.

During the simulations, the MM5 was performed independently without synchronous coupling with other models, while the POM was coupled synchronously in the domain 1 calculation with the external forcings from the MM5 output.

4.3.2 Verification by meteorological data

The Meteoric images of Typhoon Morakot from the Central Weather Bureau (CWB) are shown in Figure 4.2 and encompass the period from 08:30 UTC 5 to 08:30 UTC 10 August, 2009. These images depict characteristics demonstrating that the clouds of Typhoon Morakot on 7 August stayed over Taiwan for a long time, leaving on 9 August. The light clouds remained over Taiwan even until 10 August. These images also show that the clouds initially moved westward toward Taiwan after crossing it. Subsequently, it turned suddenly northward, as did its track.

Table 4. 1 Design of the microphysics scheme experiments performed in this study

Case	Domain		Range	Microphysics scheme	Planetary boundary layer (PBL) scheme	Cumulus parameterization	Bogus scheme
	No	Size					
E1	1	120×175	100.07° - 153.94°E 9.5° - 39.54°N	Reisner's mixed-phase	MRF	Grell	No
	2	100×163	114.09° - 128.59°E 19.45° - 27.95°N	Reisner's mixed-phase	MRF	Grell	No
	3	136×136	118.67° - 122.79°E 21.95° - 25.72°N	Reisner's mixed-phase with graupel (Reisner2)	MRF	None	No
E2	1	120×175	100.07° - 153.94°E 9.5° - 39.54°N	Reisner's mixed-phase with graupel (Reisner2)	MRF	Grell	No
	2	100×163	114.09° - 128.59°E 19.45° - 27.95°N	Reisner's mixed-phase with graupel (Reisner2)	MRF	Grell	No
	3	136×136	118.67° - 122.79°E 21.95° - 25.72°N	Reisner's mixed-phase with graupel (Reisner2)	MRF	None	No
E3	1	120×175	100.07° - 153.94°E 9.5° - 39.54°N	Schultz mixed-phase with graupel	MRF	Grell	No
	2	100×163	114.09° - 128.59°E 19.45° - 27.95°N	Schultz mixed-phase with graupel	MRF	Grell	No
	3	136×136	118.67° - 122.79°E 21.95° - 25.72°N	Schultz mixed-phase with graupel	MRF	None	No

Figure 4.3 shows the observed surface rainfall distribution for 4-day accumulated rainfall from 00:00 UTC 6 to 00:00 UTC 10 August (Figure 4.3f), as given by the CWB. This distribution exhibited two features: (1) the main precipitation distribution was elongated in the southwest-northeast direction and was organized into a convective line near southern

Taiwan; (2) the maximum accumulated rainfall occurred in the southern and northeastern regions of Taiwan. Some rain stations recorded enormous amounts of rain. For example, the station at Alishan recorded an accumulated rainfall of 3068 mm from 00:00 UTC 3 to 00:00 UTC 11 August (from CWB).

The ocean surface wind vector images during Typhoon Morakot are shown in the left column of Figure 4.6 Data for ocean surface winds having 10-m heights were retrieved using observational data from the NASA/JPL SeaWinds Scatterometer aboard the QuikSCAT. These data sets contain wind information for up to 22 hours prior to the update time (http://manati.orbit.nesdis.noaa.gov/datasets/QuikSCATData.php/).

The Observed sea levels data got from Japan Meteorological Agency at Yonaguni tidal stations during the Typhoon Morakot passage (Figure 4.12).

4.4 Numerical Experiments

4.4.1 Atmosphere model experimental designs

To investigate the characteristics of Typhoon Morakot in terms of its extremely heavy rainfall, intensity and track, a number of numerical experiments were performed. These can be categorized into three sets of experiments, as follows:

Microphysics scheme experiments

To improve our understanding of the microphysics processes that affected the behaviour of the typhoon track, intensity and rainfall simulation, three experiments with three different microphysics schemes were carried out with the Reisner's mixed-phase (Reisner et al., 1998), Reisner's mixed-phase with graupel, and Schultz mixed-phase schemes (Schultz, 1995). The parameterisations for planetary boundary layer (PBL) and cumulus were set constant to the Medium-Range Forecast (MRF) PBL scheme (Hong and Pan, 1996) and to the Grell cumulus parameterisation (Grell, 1993) for all experiments because of the grid resolutions of 27 km for domain 1, 9 km for domain 2 and 3 km for domain 1. The experiment configurations are shown in Table 1.

Terrain sensitivity experiments

To investigate the effect of the island terrain on the track, intensity and rainfall of Typhoon Morakot before and after the landfall on Taiwan, the following five numerical experiments were designed and carried out.

(1) The configuration, E1, shown in Table 1 was set as a control experiment (CTL).

(2) A fraction of 0.0001% elevation of the real island terrain (denoted as 0.00001) was retained. Compared with CTL, the island terrain was reduced to nearly 0 while leaving all other conditions unchanged.

(3) A fraction of 10% elevation of the real terrain (denoted as 0.1) was retained. Compared with CTL, no other changes were made except that the highest terrain elevation was reduced to nearly 400 m.

(4) A fraction of 30% elevation of the real terrain (denoted as 0.3) was retained. This was the same as for the 0.1 experiment, except the highest terrain elevation was nearly 1200 m in this case.

(5) A fraction of 65% elevation of the real island terrain (denoted as 0.65) was retained. This is the same as for the 0.1 experiment, except the highest terrain elevation was nearly 2500 m in this case.

(6) The real terrain was increased by 30% in elevation (denoted as 1.3). This is the same as for experiment 0.1, except the highest terrain elevation was increased to nearly 5000 m in this case.

Bogus scheme experiments

To investigate the effect of the bogus scheme on the typhoon track, intensity and rainfall, the following two numerical experiments were designed and conducted.

(1) The configuration, E1, was set as a control experiment (CTL).

(2) The every six-hour bogus scheme (B6) was utilized. No other changes were made from the CTL.

(3) The initial bogus scheme (Bi) was utilized. No other changes were made from the CTL.

For more details on the bogus and modified bogus schemes, refer to Lee et al. (2010).

4.4.2 Ocean model experimental designs

To investigate the effect of the bogus scheme on the storm surge simulation, three experiments (CTL, B6, B1) according to the bogus scheme experiments of MM5 experiments were designed and conducted. The POM simulation was also performed for the same period with only domain 1. The meteorological forcing (tidal, wind and pressure fields) were imposed from the MM5 results.

4.4.3 Results

Microphysics scheme

On 2 August, 2009, Typhoon Morakot formed in a large monsoon gyre over the WNP. It initially moved westward to Taiwan, then made landfall in Hualien county along the central east coast of Taiwan on the night of 7 August, passing over Taiwan nearly 24 hours later. After it crossed the island at a slow speed, it turned suddenly northward to make a second landfall on mainland China.

Figure 4.5 shows that the simulated rainfall from three microphysics scheme experiments. Generally, the simulations produced the correct precipitation distribution despite using different microphysics schemes. First, in all of the results the main precipitation event was elongated in the southwest-northeast direction and organized into a convective line near southern Taiwan, as observed (Figure 4.3). Second, the maximum simulated accumulated 192-h rainfalls in the microphysics scheme experiments occurred in two areas: (1) over southern Taiwan and (2) at the northeastern region. This feature was also quite similar to the observations (Figure 4.3). The maximum simulated accumulated (MSA) 192-h rainfall

shows that the MSA of the Schlutz mixed-phase scheme experiment was nearly 200 mm larger than for the Reisner's mixed-phase scheme and Reisner's with graupel (Reisner2) scheme experiments.

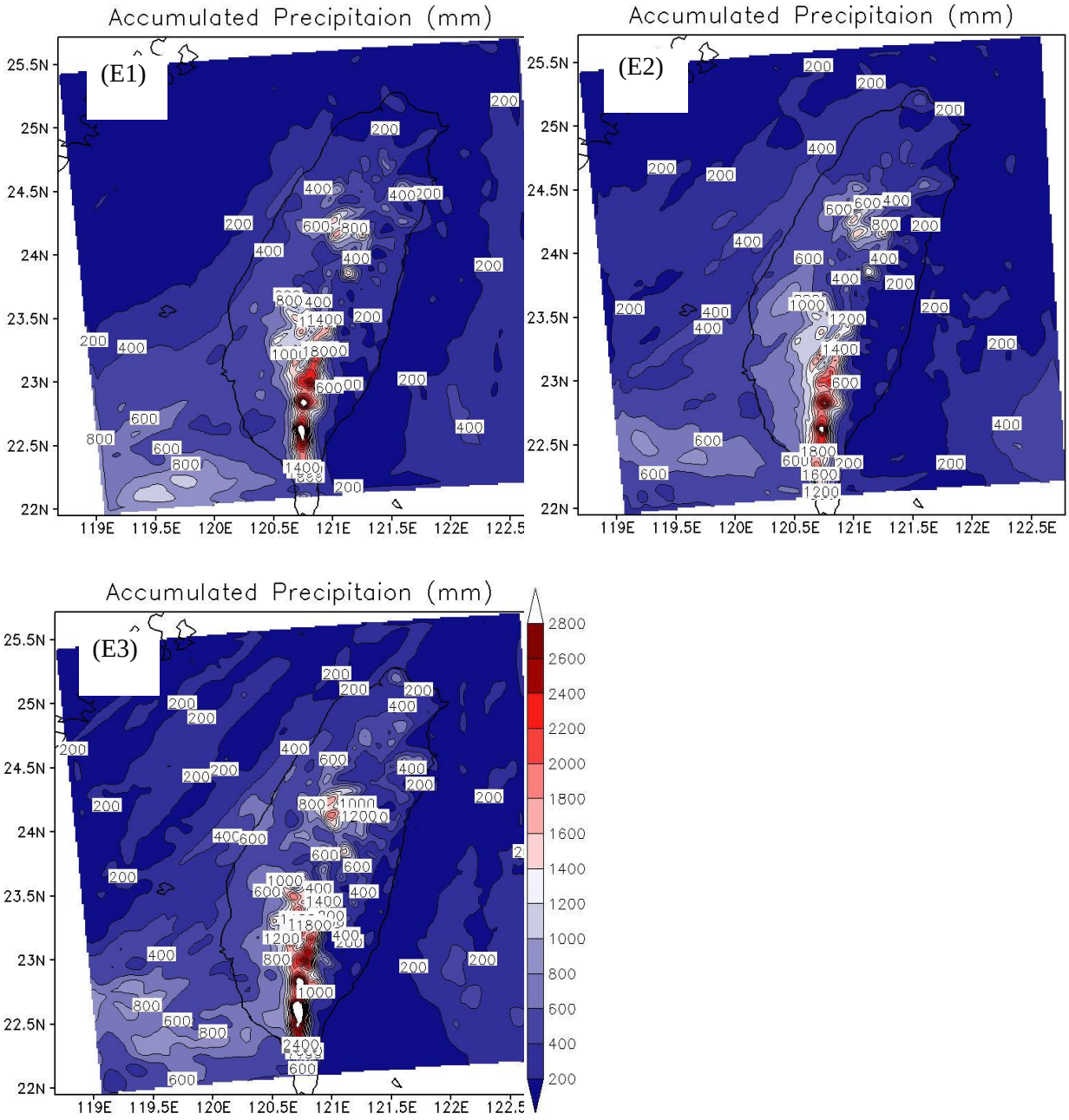

Figure 4. 5 Calculated accumulated rainfall during the simulation periods (192-h) from the microphysics scheme experiments, E1, E2, and E3 in Table 1

The wind velocities at the 10-m height level from the model were compared with QuikSCAT ocean surface winds (Figure 4.6). This comparison shows that the satellite data yielded more intense winds near the eyewall compared with simulation results, which might be attributed to the model resolution. On the other hand, the circulation and spatial distributions were in good agreement.

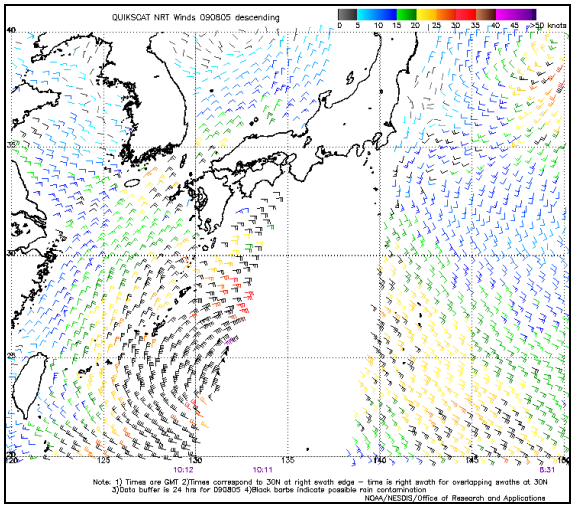
QUIKSCAT NRT Winds 090805 descending
0 5 10 15 20 25 30 35 40 45 >50 knots
Note. 1) Times are GMT 2)Times correspond to 30N at right swath edge – time is right swath for overlapping swaths at 30N
3)Data buffer is 24 hrs for 090805 4)Black barbs indicate possible rain contamination
NOAA/NESDIS/Office of Research and Applications

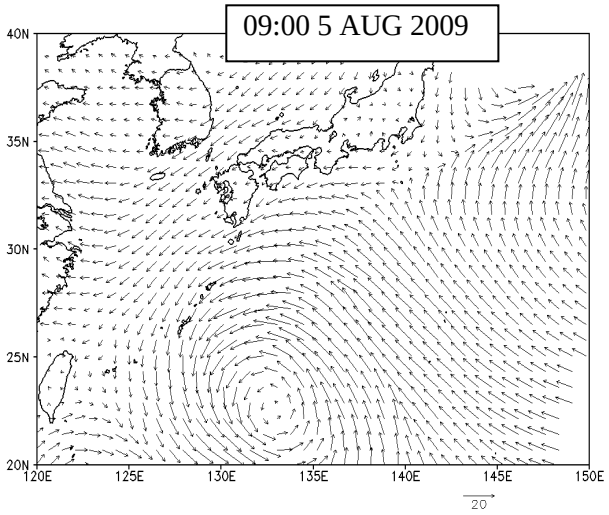
09:00 5 AUG 2009
40N
35N
30N
25N
20N
120E
125E
130E
135E
140E
145E
150E
20

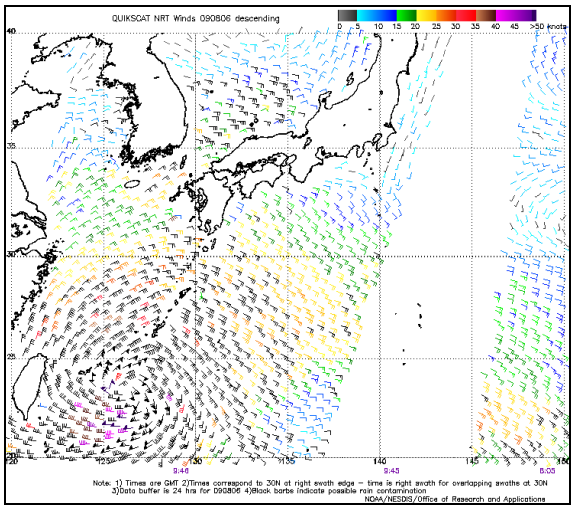
QUIKSCAT NRT Winds 090806 descending
0 5 10 15 20 25 30 35 40 45 >50 knots
Note. 1) Times are GMT 2)Times correspond to 30N at right swath edge – time is right swath for overlapping swaths at 30N
3)Data buffer is 24 hrs for 090806 4)Black barbs indicate possible rain contamination
NOAA/NESDIS/Office of Research and Applications

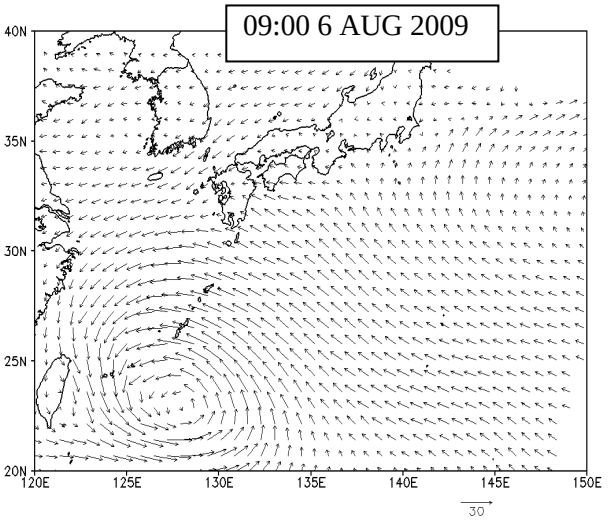
09:00 6 AUG 2009
40N
35N
30N
25N
20N
120E
125E
130E
135E
140E
145E
150E
30

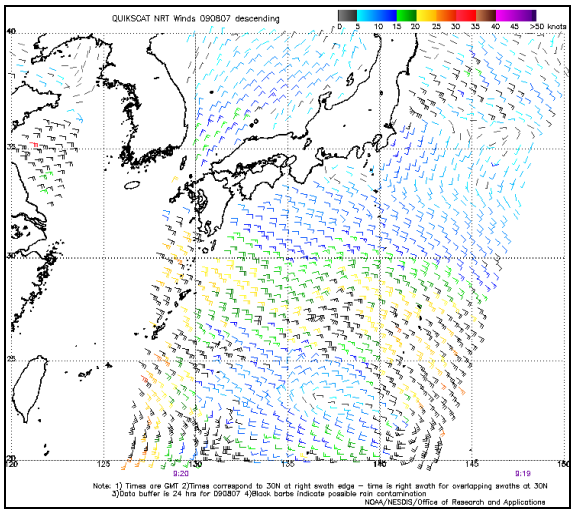
QUIKSCAT NRT Winds 090807 descending
0 5 10 15 20 25 30 35 40 45 >50 knots
Note. 1) Times are GMT 2)Times correspond to 30N at right swath edge – time is right swath for overlapping swaths at 30N
3)Data buffer is 24 hrs for 090807 4)Black barbs indicate possible rain contamination
NOAA/NESDIS/Office of Research and Applications

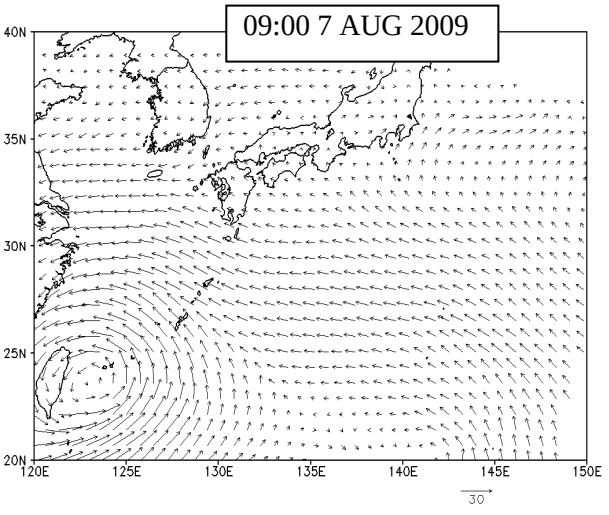
09:00 7 AUG 2009
40N
35N
30N
25N
20N
120E
125E
130E
135E
140E
145E
150E
30

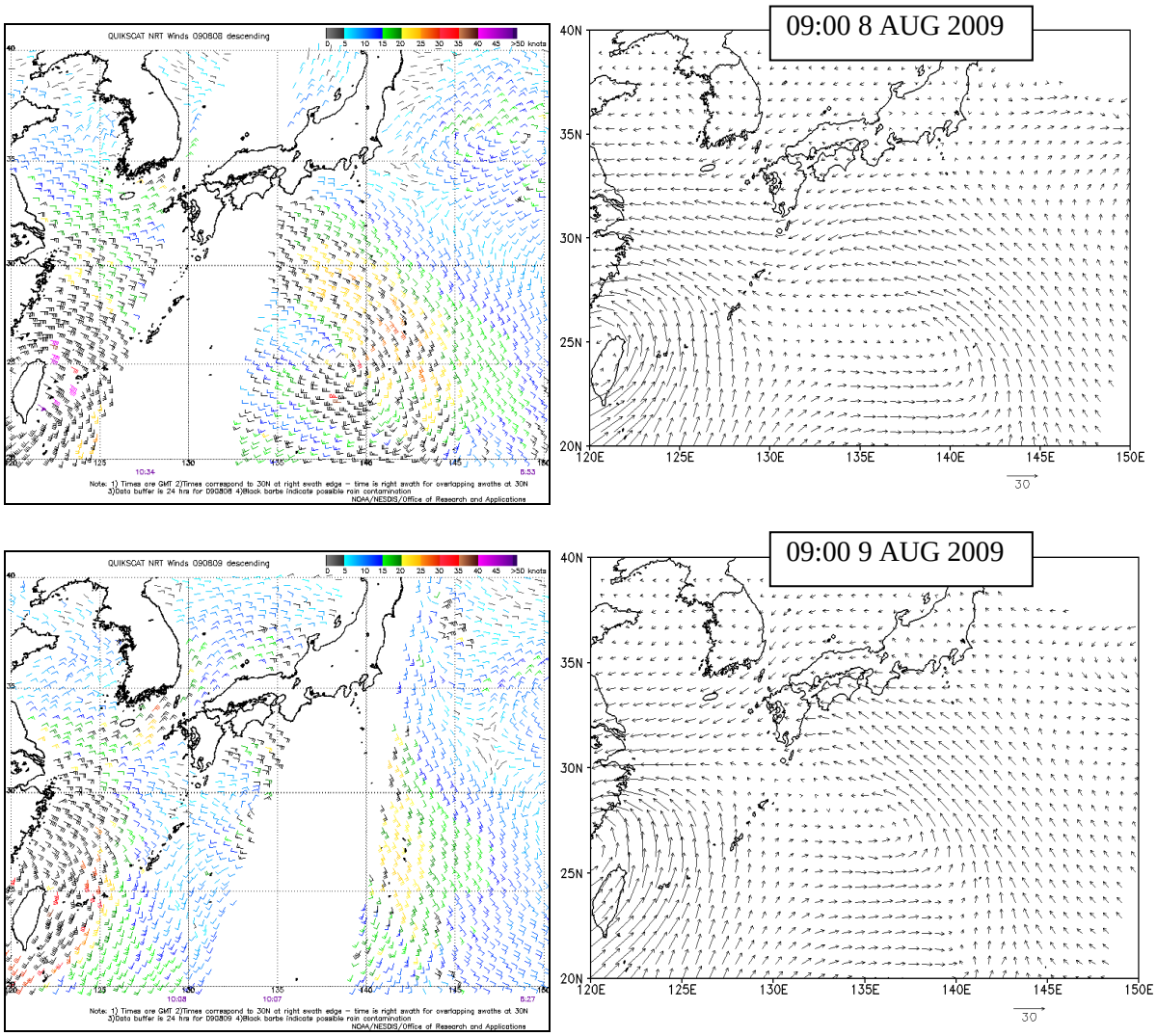

Figure 4.6 Comparison of 10-m height wind velocities between the observed ocean surface winds (left column) and CTL experiment result (right column) from 5 to 9 August 2009. The ocean surface winds were retrieved using observation data from NASA/JPL's SeaWinds Scatterometer aboard the QuikSCAT. The data images contain wind data up to 22 hours prior to the update time, while the calculated CTL wind velocities are snapshots at the given time

Terrain sensitivity

In the terrain sensitivity experiments, we set the E1 configuration in the microphysics scheme experiment as the control experiment (CTL).

Figure 4.7 shows the simulated rainfall from the five different terrain sensitivity experiments. The results show that the accumulated precipitation is reduced if the topography height is reduced. When the topography height was no more than 1,000 m, the maximum rainfall centre was in the west of Taiwan with a maximum accumulated precipitation of just 600 mm. While the topography height was more than 1,200 m, the maximum rainfall centre occurred over the southern and northeastern regions of Taiwan. If the topography height were increased, the maximum accumulated precipitation would be increased. When the topography height was more than 5,000 m, the maximum accumulated precipitation was more than 2,800 mm.

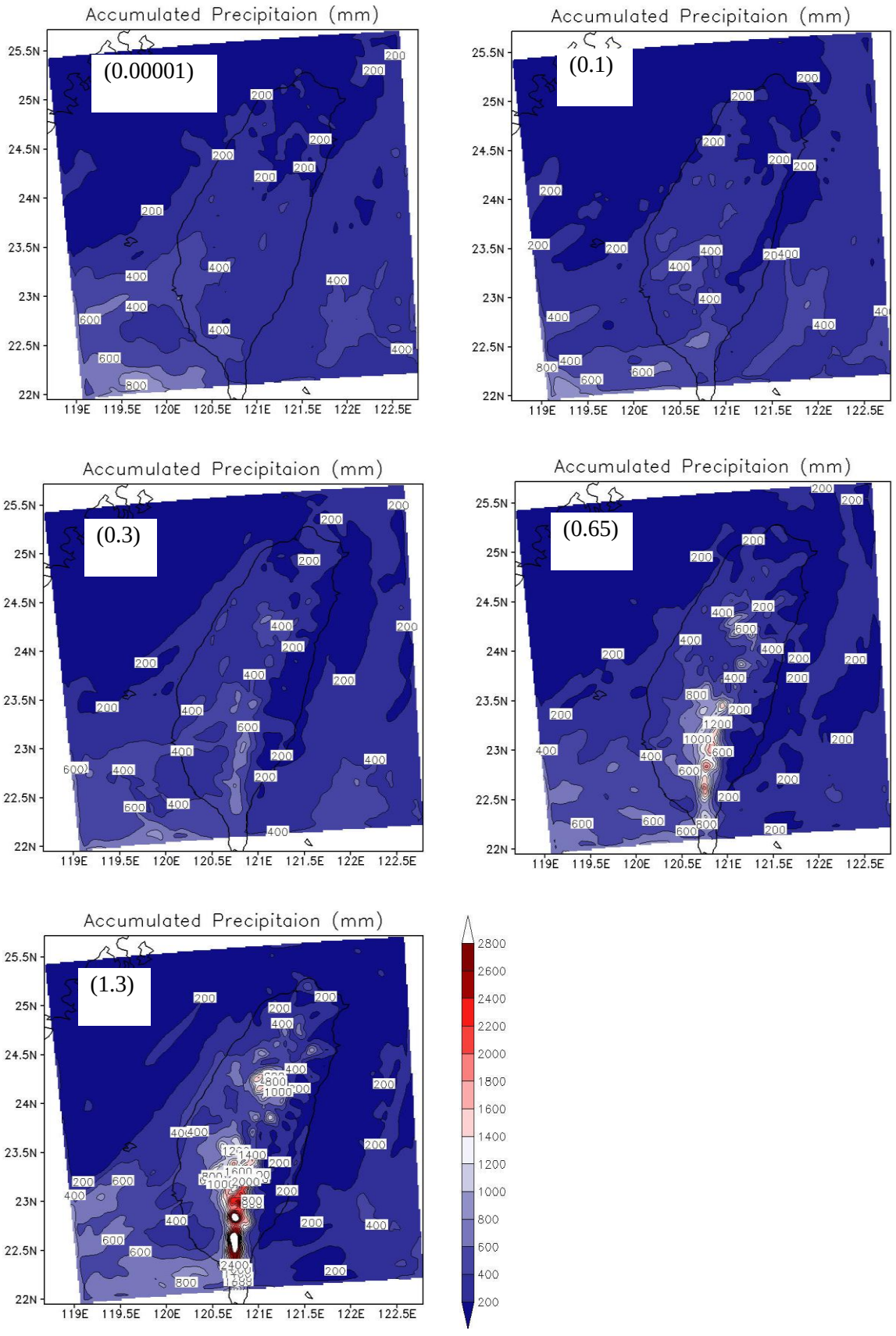

Figure 4. 7 Calculated accumulated rainfall amount during the simulation period (192-h) from the terrain sensitivity experiments, 0.00001, 0.1, 0.3, 0.65, and 1.3 indicating the terrain height ratios to the original elevation

(a) 00:00 UTC 7 August

(b) 00:00 UTC 7 August

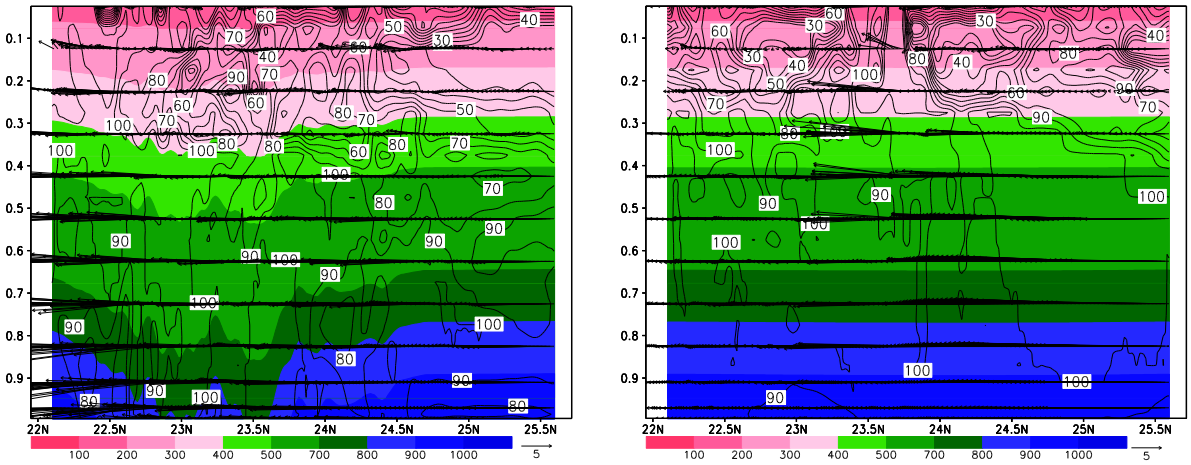

(c) 00:00 UTC 8 August

(d) 00:00 UTC 8 August

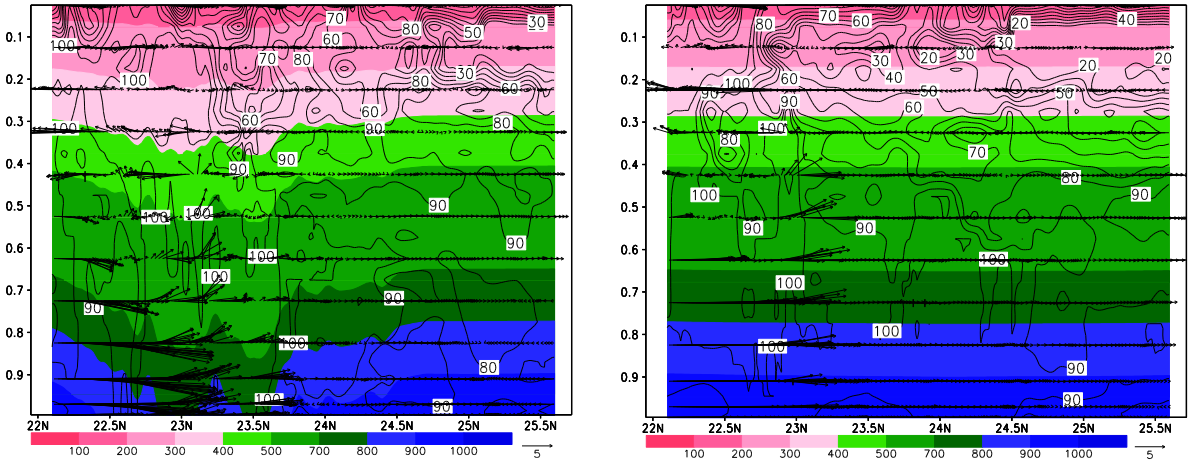

(e) 00:00 UTC 9 August

(f) 00:00 UTC 9 August

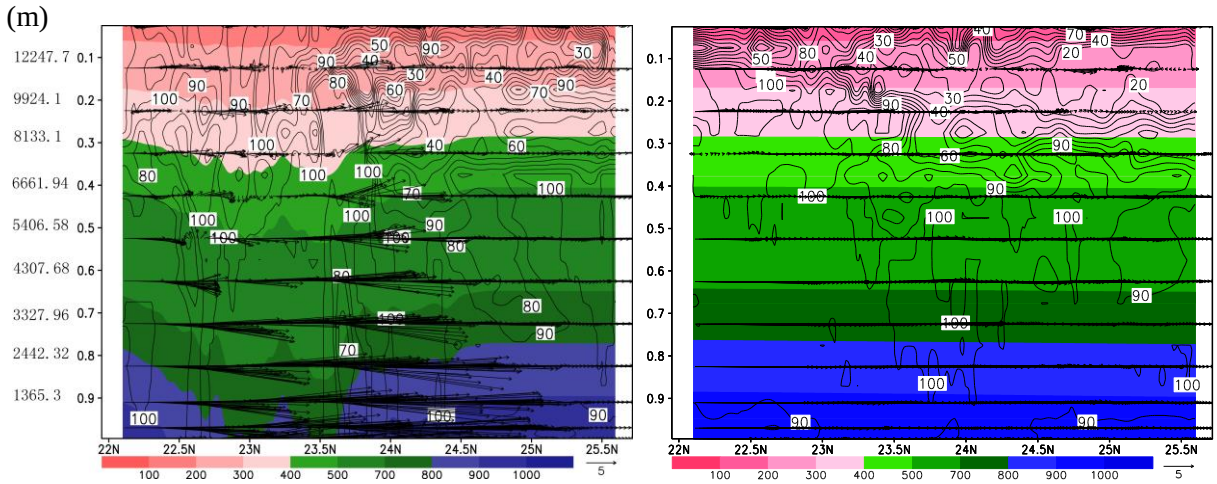

Figure 4. 8 Comparison of two-dimensional wind velocities (m/s), atmospheric pressures (shaded for every 100 hPa), and relative humidity (contour interval of 10%) at the given time in 2009 between the CTL experiment output (left column) and terrain sensitivity experiment 0.00001 (right column) of the meridional cross-section (from 21.95 °- 25.72 ℕ) at 120.8 ℈ approximately along the CMR where the Alishan is located.

Note that the vertical axis is in sigma coordinates. In the Figure e, the left axis is the average value of geopotential height of the cross-section at 120.8 ℃ which is according to the each sigma coordinate layers.

To highlight the importance of large-scale upslope motion in producing heavy rainfall, Figure 4.8 shows a comparison of the south–north vertical cross section of pressure, winds, and relative humidity (RH) fields cutting across Alishan along 120.8 ℃ at 97 h, 121 h and 145 h (equivalent to 00:00 UTC 8 and 9 August, which are the times when the modelled typhoons were located northeast of Taiwan, over Taiwan and northwest of Taiwan, respectively) between the CTL and experiment 0.00001. Figures 4.12a and 4.12c show significant northerly wind components throughout the troposphere to north, especially for the airflow below the 0.4 layer. The northerly wind components were about 6 m/s near the east of Taiwan CMR. As the airflow impinged upon the CMR, the entire nearly-saturated layers from the surface to the 0.5 layer were lifted above the mountains. The airflow then descended to the leeward side of the CMR. The entire troposphere along the cross-section under the influence of the typhoon had an RH close to 100%. This result is consistent with the observed foehn phenomenon and a mesolow over eastern Taiwan between Hualien and Taitung (Wu et al., 2002). If the terrain were reduced, the northerly winds would also be reduced (Figures 4.8b and 4.8d). The surface RH was only close to 90%.

Bogus scheme

Figure 4.9 compares the simulated tracks from the bogus scheme experiments and the observed best tracks. The results show that the track and intensity could be simulated very well using the every six-hour bogus scheme, except in the west of Taiwan. The track produced via the initial bogus scheme was similar to the CTL experiment, except at the initial time.

Figure 4.10 shows a comparison of the intensities of Typhoon Morakot between the simulations and the observation. The simulated intensity of the every six-hour bogus scheme experiment was similar to the observation, except for the minimum central sea-level pressure of 960 hPa. For the initial bogus scheme experiment, the intensity was similar to the CTL experiment, except at the initial time.

Figure 4.11 shows that the simulated rainfall of the bogus scheme experiments. In general, it was able to produce the correct precipitation distribution for the typhoon case very well, as for the CTL experiment. For the bogus scheme experiment, the MSA 192-h rainfall was nearly 2,600 mm, which is close to the observation. The MSA of the initial bogus scheme experiment was nearly 2,000 mm, which is similar to the CTL experiment.

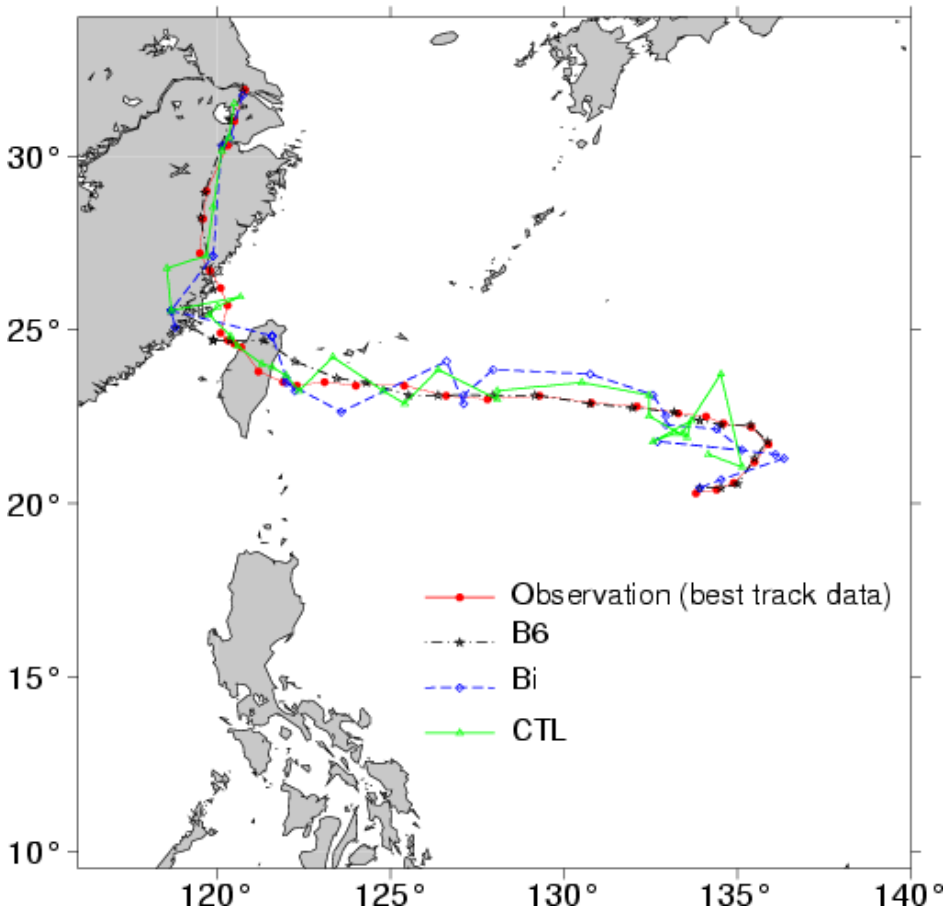

Figure 4. 9 Simulated tracks of Typhoon Morakot from the bogus scheme experiments together with the best track data

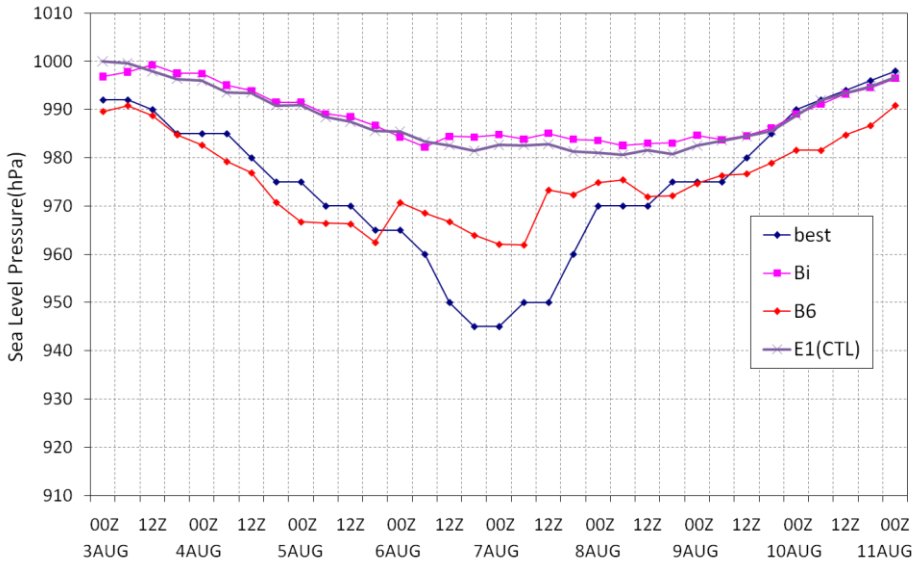

Figure 4. 10 Time variations of the simulated central sea level pressures from the bogus scheme experiments compared with the best track data

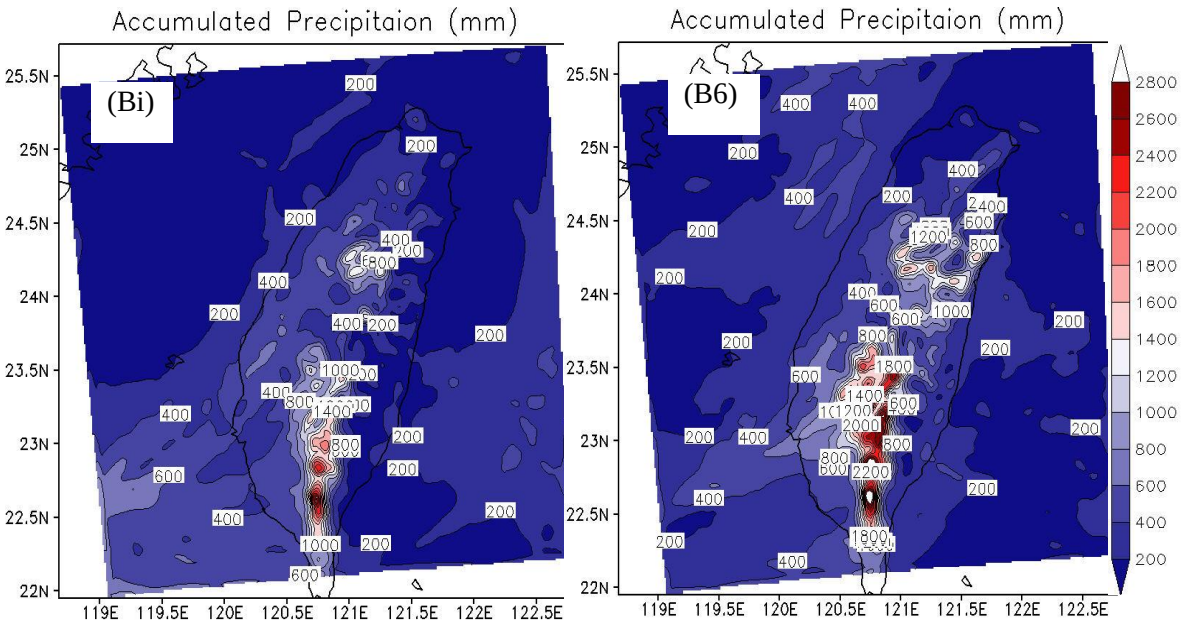

Figure 4. 11 Calculated accumulated rainfall amount during the simulation periods (192-h) from the bogus scheme experiments, Bi and B6

Tidal results

For the tidal simulation, three case studies (CTL, B6, B1) were performed with the astronomical tide and the meteorological forcings (tide, wind and pressure) that are considered.

Overall, the simulated astronomical tides agreed very well with the observed values (Figure 4.12). However, the observed sea levels show larger differences from the simulated during the Typhoon Morakot closing to Taiwan island (from 0:00 UTC 6 August to 12:00 UTC 9 August) compare with far from Taiwan island (from 0:00 UTC 4 August to 0:00 UTC 6 August and after 12:00 UTC 9 August). Compare the three case studies results, B6 case results depict overall improvements than other two case results.

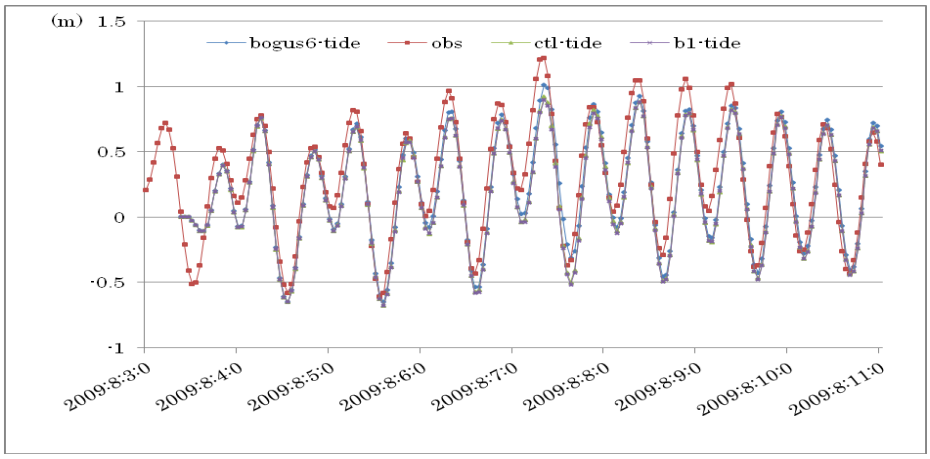

Figure 4. 12 Observed and calculated sea levels at Yonaguni tidal stations during the Typhoon Morakot passage.

4.5 Discussions and Conclusions

Typhoon Morakot had two special features: (1) the sudden change in its moving direction from westward to northward during its landfall over Taiwan and (2) its extremely heavy rainfall in Taiwan. The monsoon surge-induced sudden typhoon track change has been discussed by Carr and Elsberry (1995). The sudden northward-turning track of Typhoon Morakot is ascribed to the steering effect of the large-scale monsoon surge, as confirmed by Ge et al. (2010). On the other hand, as introduced in sub-Section 2, there was a subtropical high system in the east of Japan near 160 ℃E moving towards the southwest at 06:00 UTC 3 August. This then changed direction from the northwest to the northeast at 18:00 UTC 6 August. This might have played a significant role in affecting the track of Typhoon Morakot. On the other hand, while the subtropical high system was moving west, it affected the westward-moving Typhoon Morakot in its initial stage. Subsequently, Typhoon Morakot turned suddenly because the subtropical high system changed its direction from the northwest to the northeast. This affected Typhoon Morakot by causing it to cross over Taiwan at a slow speed, resulting in a long duration track over this region.

The other mechanisms that could affect the extremely heavy rainfall are the multiple typhoon interactions and orographic effect. Figure 4.1 shows that Typhoons Morakot, Goni, and Etau were independent in the lower troposphere. They formed a larger scale cyclonic circulation because of the south-westerly monsoon, and the monsoon gyre circulation enhanced the energy exchange of the three TCs. Morakot was capable of obtaining a positive vortex circulation and moisture supply from the other two typhoons. The strengthened south-westerly monsoon surge was capable of bringing excessive moisture into Taiwan. Then, the orographic effect of the Taiwan CMR could uplift the extremely large moisture flux over southern parts of the island, leading to the extremely heavy rainfall in Taiwan, as shown in Figure 4.8.

Typhoon Morakot is well simulated in this study by a non-hydrostatic mesoscale model, MM5. The simulations were based on three sets of numerical experiments: the microphysics scheme experiments, the terrain sensitivity experiments and the bogus scheme experiments. In the microphysics scheme experiments, three kinds of parameterizations were chosen; the Reisner's mixed-phase, the Reisner's mixed-phase with graupel (Reisner2), and Schultz mixed-phase schemes. The MSA 192-h rainfall of the Schlutz scheme experiment was nearly 200 mm larger than for the Reisner's mixed-phase and Reisner's with graupel (Reisner2) scheme experiments and was much closer to the observational data (Figure 4.7). Therefore, the Schultz mixed-phase scheme can simulate rainfall better than for the other two parameters in this study. In the terrain sensitivity experiments, the simulated rainfalls showed that the terrain elevation is important in determining heavy rainfall and its spatial distribution. If the terrain elevation increases, the rainfall amount also increases, and the heavy rainfall distribution moves southward in Taiwan. The effect of the terrain on the typhoon track is insignificant in Typhoon Morakot. In the bogus scheme experiments, the every six-hour bogus scheme (Lee et al., 2010) showed better and improved results in all aspects, including the rainfall (Figure 4.8), track , intensity and the seawater level of Typhoon Morakot.

From the results of numerical experiments, in addition to the observation data, it can be summarized that the special track of Typhoon Morakot was mainly affected by the synoptic-scale south-westerly monsoon gyre and the subtropical high system, which changed the moving direction of the system from northwest to northeast at about 18:00 UTC 6 August. The extremely heavy rainfall of Typhoon Morakot was mainly affected by

three factors: (1) interaction with the south-westerly monsoon gyre and the other two typhoons (Goni and Etau), taking more water vapour to the Taiwan region; (2) the unique track itself causing a slower and longer landfall duration over Taiwan; and (3) the orographic effect of the Taiwan CMR, the most significant factor for torrential rain, which uplifted the extremely large moisture flux over the southern part of the island.

In this study, we mainly focused on the relationship between the terrain of Taiwan, the microphysics parameterization, and the bogus scheme, as well as the characteristics of Typhoon Morakot, including its rainfall, track and intensity. The detailed interaction among the monsoon gyre, the subtropical high system and Typhoon Morakot necessitates further diagnoses. The relationship among the three Typhoons (Goni, Morakot, and Etau) also requires further careful examination. The simulations utilized here can be useful not only for reproduction but also for prediction, which can be a useful forcing for storm waves and storm surge calculations as well.

REFERENCES

Anthes, R. A.: A cumulus parameterization scheme utilizing a one-dimensional cloud model. *Mon. Wea. Rev.* 105, 270-286, 1977.

Anthes, R. A. and Chang, S .W.: Tropical cyclones: Their evolution, structure and effects, Meteorol. Monogr. Ser., Am. Meteorol. Soc., Boston, MA. 19, 41, 208, 1982.

Bayers, H. R.: *General Meteorology*, McGraw-Hill, 1–670, 1944.

Braun, S. A., and Tao, W. K.: Sensitivity of high-resolution simulations of Hurricane Bob (1991) to planetary boundary layer parameterizations. *Mon. Wea. Rev.* 128, 3941-3961, 2000.

Burk, S. D., and Thompson, W. T.: A vertically nested regional numerical weather prediction model with second-order closure physics. *Mon. Wea. Rev.* 117, 2305-2324, 1989.

Carr, L. E. and Elsberry, R. L.: Monsoonal Interactions Leading to Sudden Tropical Cyclone Track Changes. *Mon. Wea. Rev.* 123, 265-290, 1995.

Chiao, S. and Lin, Y.-L.: Numerical Modeling of an Orographically Enhanced Precipitation Event Associated with Tropical Storm Rachel over Taiwan. *Wea. Forecasting* 18, 325-344, 2003.

Frank, W. M.: The cumulus parameterization problem. *Mon. Wea. Rev.* 111, 1859-1871, 1983.

Ge, X., Li, T., Zhang, S. and Peng, M.: What causes the extremely heavy rainfall in Taiwan during Typhoon Morakot (2009)? *Atmos. Sci. Let.* 11, 46-50, 2010.

Gemmill, W., Katz, B. and Li, X.: Daily Real-Time Global Sea Surface Temperature - High Resolution Analysis at NOAA/NCEP. NOAA / NWS / NCEP / MMAB Office Note Nr.260, 39, 2007.

Gray, W. M.: Global view of the origin of tropical disturbances and storms, *Mon. Wea. Rev.* 96, 669–700, 1968.

Grell, G. A.: Prognostic Evaluation of Assumptions Used by Cumulus Parameterizations. *Mon. Wea. Rev.* 121, 764-787, 1993.

Grell, G. A., Dudhia, J. and Stauffer, D. R.: A description of the fifth-generation Penn State/NCAR Mesoscale Model (MM5). National Center for Atmospheric Research, NCAR Tech. Note, NCAR/TN-398 + STR, 1995.

Hong, S.-Y. and Pan, H.-L.: Nonlocal Boundary Layer Vertical Diffusion in a Medium-Range Forecast Model. *Mon. Wea. Rev.* 124, 2322-2339, 1996.

Hsiao, L.-F., Peng, M. S., Chen, D.S., Huang, K.N. and Yeh, T.C.: Sensitivity of Typhoon Track Predictions in a Regional Prediction System to Initial and Lateral Boundary Conditions. *J. Appl. Meteor. Climatol.* 48, 1913-1928. 2009.

Jian, G.-J. and Wu, C.C.: A Numerical Study of the Track Deflection of Supertyphoon Haitang (2005) Prior to Its Landfall in Taiwan. *Mon. Wea. Rev.* 136, 598-615, 2008.

Kim, K. O., T. Yamashita, and B. H. Choi.: Coupled process-based cyclone surge simulation for the Bay of Bengal, *Ocean Modelling*, 25(3-4), 132-143, 2008a.

Kim, K. O., H. S. Lee, T. Yamashita, and B. H. Choi.: Wave and storm surge simulations for Hurricane Katrina using coupled process based models, *KSCE Journal of Civil Engineering*, 12(1), 1-8, 2008b.

Kuo, H. L.: On formation and intensification of tropical cyclones through latent heat release by cumulus convection. *J. Atmos. Sci.* 22, 40-63, 1965.

Kuo, H. L.: Further studies of the parameterization of the influence of cumulus convection on large-scale flow. *J. Atmos. Sci.* 31, 1232-1240, 1974.

Kuo, H.-C., Williams, R. T., Chen, J.-H. and Chen, Y.-L.: Topographic Effects on Barotropic Vortex Motion: No Mean Flow. *J. Atmos. Sci.* 58, 1310-1327, 2001.

Kwon, H. Joe, S.-H. Won, M.-H. Ahn, A.-S. Suh, and H.-S. Chung.: GFDL-Type Typhoon Initialization in MM5. *Mon. Wea. Rev.* 130, 2966–2974, 2002.

Lee, H. S., Kim, K. O., Yamashita, T., Komaguchi, T. and Mishima, T.: Abnormal storm waves in the winter East/Japan Sea: generation process and hindcasting using an atmosphere-wind wave modelling system. *Nat. Hazards Earth Syst. Sci.* 10, 773-792, 2010.

Liu, Y., D. L. Zhang, and M. K. Yau.: A multiscale numerical study of Hurricane Andrew (1992). Part I: Explicit simulation and verification. *Mon. Wea. Rev.* 125, 3073-3093, 1997.

Lonfat, M., Marks, F. D. and Chen, S. S.: Precipitation Distribution in Tropical Cyclones Using the Tropical Rainfall Measuring Mission (TRMM) Microwave Imager: A Global Perspective. *Mon. Wea. Rev.* 132, 1645-1660, 2004.

Low-Nam, S. and Davis, C.: Development of a tropical cyclone bogussing scheme for the MM5 system, The Eleventh PSU/NCAR Mesoscale Model User's Workshop, Boulder, Colorado, 130–134, 2001.

Matsumoto, K., Takanezawa, T., and Ooe, M. Ocean Tide Models Developed by Assimilating TOPEX/POSEIDON Altimeter Data into Hydrodynamical Model: A Global Model and a Regional Model Around Japan, Journal of Oceanography, 56, 567-581, 2000.

McBride, J. L. and Zehr, R.: Observational analysis of tropical cyclone formation, Part II: Comparison of nondeveloping versus developing systems, *J. Atmos. Sci*. 38, 1132–1151, 1981.

Mellor, G. L.: Users guide for a three-dimensional, primitive equation, numerical ocean modelRep., 53 pp, Prog. in Atmos. And Ocean. Sci, 2004.

Ooyama, K.: Numerical simulation of the life cycle of tropical cyclones. *J. Atmos. Sci.* 26, 3-40, 1969.

Ooyama, K.: Conceptual evolution of the theory and modeling of the tropical cyclone. *J. Meteor. Soc. Japan.* 60, 369-379, 1982.

Pan, C. J., Krishna Reddy, K., Lai, H. C., Yang, S. S. and Wong, C. J.: Wind profiler observations on orographic effects of typhoon wind structure modification over Taiwan (120.38°E, 22.6°N). *Ann. Geophys.* 28, 141-147, 2010.

Pu, Z.-X. and Braun S. A.: Evaluation of bogus vortex techniques with four-dimensional variational data assimilation. *Mon. wea. Rev.* 129, 2023–2039, 2001.

Reisner, J., Rasmussen, R. M., and Bruintjes R. T.: Explicit forecasting of supercooled liquid water in winter storms using the MM5 mesoscale model. *Q. J. Roy. Meteor. Soc.* 124, 1071-1107, 1998.

Riehl, R. J.: On the formation of typhoons, *J. Meteor*., 5, 247–264, 1948.

Schultz, P.: An Explicit Cloud Physics Parameterization for Operational Numerical Weather Prediction. *Mon. Wea. Rev.* 123, 3331-3343, 1995.

Shabani, B., Nielsen, P. and Baldock, T. E.: Field Observations of Wind Stress Over Surf Zone, paper presented at The 21st International Offshore and Polar Engineering Conference, Maui, Hawaii, 2011.

Tolman, H. L.: User manual and system documentation of WAVEWATCH III version 3.14Rep., 194 pp, NOAA NCEP EMC MMAB, 2009.

Wang, Y.: An explicit simulation of tropical cyclones with a triply nested movable mesh primitive equation model. TCM3. Part II: Model refinements and sensitivity to cloud microphysics parameterization. *Mon. Wea. Rev.* 130, 3022-3036, 2002.

Wu, C.-C. and Kuo, Y.-H.: Typhoons Affecting Taiwan: Current Understanding and Future Challenges. *Bull. Amer. Meteor. Soc.* 80, 67-80, 1999.

Wu, C.-C., Yen, T.-H., Kuo, Y.-H. and Wang, W.: Rainfall Simulation Associated with Typhoon Herb (1996) near Taiwan. Part I: The Topographic Effect. *Wea. Forecasting* 17, 1001-1015,2002.

Yang, M. J., and R. A. Houze, Jr.: Sensitivity of squall-line rear inflow to ice microphysics and environmental humidity. *Mon. Wea. Rev.* 123, 3175-3193, 1995.

Yeh, T.-C. and Elsberry, R. L.: Interaction of Typhoons with the Taiwan Orography. Part I: Upstream Track Deflections. *Mon. Wea. Rev.* 121, 3193-3212, 1993a.

Yeh, T.-C. and Elsberry, R. L.: Interaction of Typhoons with the Taiwan Orography. Part II: Continuous and Discontinuous Tracks across the Island. *Mon. Wea. Rev.* 121, 3213-3233, 1993b.

Chapter 5

Atmosphere-Ocean- Groundwater Coupling Model System for Seawater Intrusion Simulation

Precipitation and seawater level are the two important factors to be considered in seawater intrusion simulation. However, these data are lacking in some regions of the world, it will limits the study on seawater intrusion. Considering the lack of availability of data on precipitation and seawater level, an atmosphere-ocean-groundwater coupling model system was constructed in this chapter. In the coupling model system, the atmosphere model (MM5) and the ocean model (POM) is used to simulate the precipitation and seawater level, respectively, while the SEAWAT model is used for groundwater model simulation. The system is used for seawater intrusion simulation in the Liaodong Bay coastal plain, China. The results show that the atmosphere-ocean-groundwater coupling model system provides a very reasonable result.

5.1 Introduction

Seawater intrusion is the movement of seawater into fresh water aquifers due to natural processes or human activities. In latest decades, there are some studies about seawater intrusion in the Liaodong Bay coastal plain. Li (2005) employed the software of Visual MODFLOW for the numerical study in the upper Neozoic groundwater quality of the Liaohe Oil Field which is located in the south of the lower Liaohe Plain. Xue (2005) conducted the simulation of groundwater level in the upper Neozoic using Visual MODFLOW in Panjin area. However, they did not consider the seawater intrusion into the Quaternary layer, groundwater density variable and the tidal effect. Ding (2011) constructed a three-dimensional model which considered groundwater density variable and seawater intrusion in Quaternary and Neozoic layers to simulate the seawater intrusion and analysis the tidal effects on it (see in chapter 3). In chapter 3 study, the precipitation and seawater level data were obtained from some observation station data. All of above simulation models are constrained due to lack of precipitation and seawater level data in some regions.

Nagai et al. (2005) developed a coupled water cycle models system to simulate mesoscale water and energy circulations. The coupled model consists of the atmosphere, land-surface, hydrology, ocean-wave, and ocean-current models. Calculations of models are carried out as parallel processes and a model coupling program (model coupler; Nagai et al. 2005, 2007) controls these processes and data exchanges among models using Message Passing Interface (MPI). The models system used the non-hydrostatic atmospheric dynamic model of Pennsylvania State University and National Center for Atmospheric Research (MM5; Grell *et al*., 1994; WRF, Skamarock *et al.*, 2008), detailed multi-layer land surface model (SOLVEG; Nagai 2002, 2003, 2005) and three-dimensional hydrology model (RIVERS; Tsuduki 2003) developed at Japan Atomic Energy Research Institute (JAERI), the third-generation ocean wind-wave model of NOAA, WAVEWATCH III (WW3; Tolman 2002), and the Princeton Ocean Model (POM; Mellor 1998).

Meanwhile, the SOLVEG model provides detailed calculations of surface water content, near-surface soil water content, and vertical fluxes of soil water to the hydrology model RIVERS. With these inputs, RIVERS calculates the river flow, deep layer soil water content, and three-dimensional movement of soil water, and the changes due to horizontal water movements are fed back to SOLVEG. These exchanges enable SOLVEG to consider the horizontal movement of soil water, which is not simulated in vertical one-dimensional

calculations. The hydrology model RIVERS is a grid type distributed runoff model. It consists of three-dimensional grid cells with five vertical layers and river channels. Horizontal and vertical water flows among connected grid cells and river channels are calculated from the GIS data (elevation, land-use, soil-type, etc.), and the water content of each grid cell is determined to keep the mass balance.

Walko et al., (2000) developed a coupled Atmosphere-Biophysics-Hydrology Models for Environmental Modeling which link the Regional Atmospheric Modeling System (RAMS), the Land Ecosystem-Atmosphere Feedback model (LEAF-2) and the land hydrology model (TOPMODEL). LEAF-2 is a prognostic model for the temperature and water content of soil, snow cover, vegetation, and canopy air, and includes turbulent and radiative exchanges between these components and with the atmosphere. Subdivision of a RAMS surface grid cell into multiple areas of distinct land-use types is allowed, with each subgrid area, or patch, containing its own LEAF-2 model, and each patch interacts with the overlying atmospheric column with a weight proportional to its fractional area in the grid cell. The TOPMODEL model is a land hydrology model that represents surface and subsurface downslope lateral transport of groundwater.

In these two coupled models system, there have not calculated saturated zone deep groundwater flow. Thus, these two coupled models system can not be used for seawater intrusion simulation.

Based on the above discussing, an atmosphere-ocean-groundwater coupling model system is constructed for seawater intrusion simulation, which especially can be used in the lack of precipitation and seawater level data regions area, and the coupling model system application to the case study for seawater intrusion simulation in Liaodong Bay coastal plain, China.

5.2 Atmosphere-Ocean-Groundwater Coupling Model System

The atmosphere-ocean-groundwater modeling system consists of three models consisting of non-hydrostatic mesoscale meteorological MM5 (Grell, 1995) model for atmosphere, a sigma-coordinate primitive equation ocean model-POM (Mellor, 2004), and a three-dimensional model SEAWAT (Guo and Langevin, 2002) model which considers variable density, transient ground-water flow in porous media for groundwater simulation.

In atmosphere-ocean coupling model, the calculation models are carried out as independent tasks for different processors and a model coupling program controls these processes and data exchanges among models using Message Passing Interface (MPI) in Program Multiple Data (PMD) as schematically shown in Figure 5.1. The coupling has flexibility to use different resolution of grid and time step for each model. The modification of each model code for this coupling is simple and easy with adding some data exchange routines and put some sentences in the original model code which call the coupling routines, and each model code keeps its original computing system.

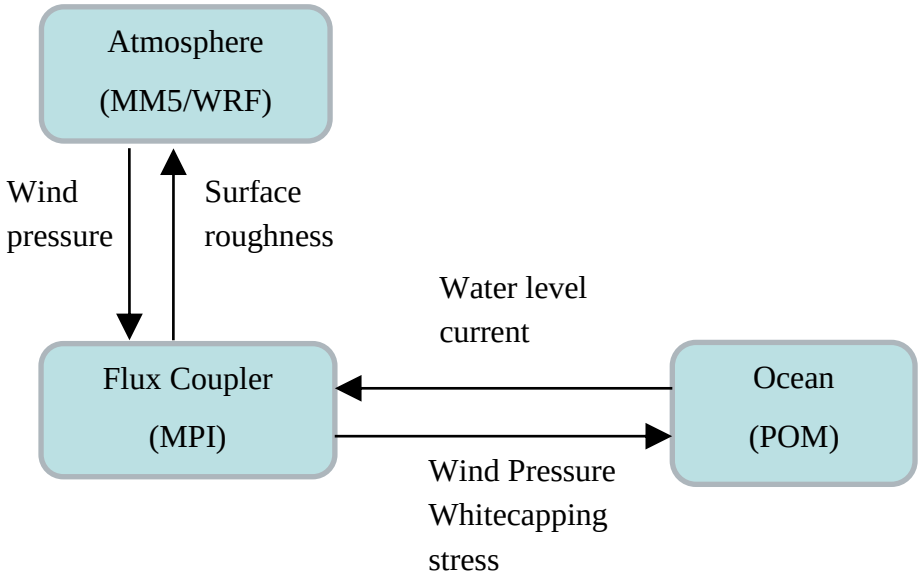

Figure 5. 1 Interactions in the atmosphere- ocean system

The interaction within atmosphere-ocean part has been developed in the first stage by Kim (2005) and modified by Lee (2007). The momentum exchanges in the atmosphere-ocean systems (Figure 5.1) are starting with MM5 or WRF model produced the surface wind and pressure and transferred to the coupler; the surface stress to generate current in POM model. POM calculates the surface current using the wind stress form MM5. It also simulates surface water elevation using sea surface pressure from MM5. This interaction is used to simulate typhoon, storm surge and specific phenomenon like long water waves generation. It can perform the wind, pressure, precipitation, seawater level. In most of simulations by atmosphere-ocean coupled model, the barotropic ocean states are considered such that the influences of temperature and salinity profiles in the ocean are remained uniform. Lee (2007) added a more detailed energy exchanges in the atmosphere-ocean interaction by considering the sea surface temperature and heat fluxes exchange between the ocean and atmosphere.

Details of each model can be obtained in the indicated references. The sea level pressure (SLP), precipitation, evaporation, heat flux, radiation and wind-induced surface stress affect the seawater level while the sea surface temperature (SST) affects the atmosphere condition. The governing equations (Eqs. 2.30, 2.31 and 2.32) for density-dependent groundwater flow and the solute-transport of the SEAWAT code show that $\overline{\rho}q_s$ and Z are very important effect on the seawater intrusion simulation. Respectively, the precipitation is one kind of entering water source ($\overline{\rho}q_s$) and seawater level is one kind of elevation (Z). In the atmosphere-ocean-groundwater modeling system, the precipitation results from MM5 model and seawater level results from POM model can be used for groundwater model SEAWAT to simulate groundwater flow, solute-transport. It can also be used for seawater intrusion simulation. Fig. 5.2 shows the modeling system with the exchanging physical parameters.

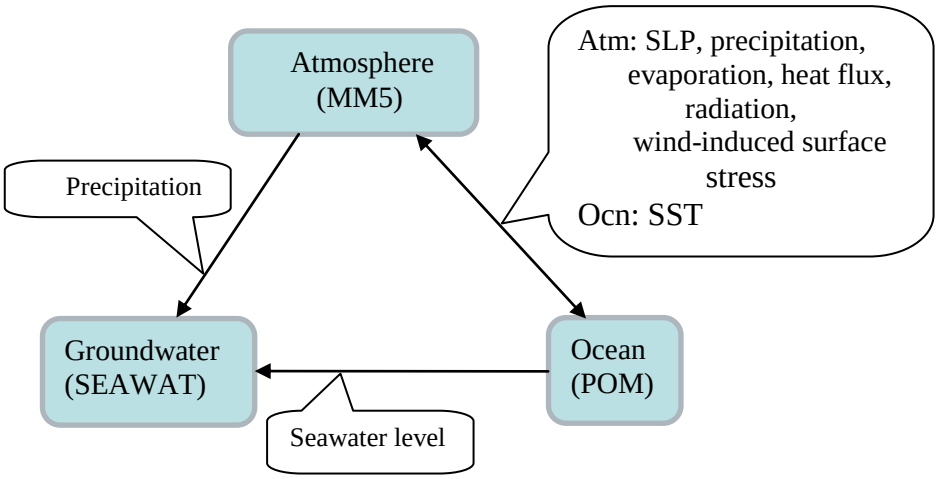

Figure 5. 2 An atmosphere-ocean-groundwater modeling system used in this study.

5.3 Experimental Set-up

5.3.1 Atmosphere model (MM5) set-up.

The present study adopted an interactive grid nesting with two domains (Figure 5.3) with horizontal resolutions of 27 and 9 km, respectively. The two domains have 80×75 and 64×64 grid points covering the regions at approximately: 107.38° - 135.591° E, 30.08° - 50.2656° N for domain 1; 119.47° - 126.679° E, 38.61° - 43.956° N for domain 2. In addition, twenty three vertical sigma layers from the surface up to the 100 hPa level for two domains are set up with 60 s time steps. The MM5 computation is carried out for twelve months from January to December in 2004.

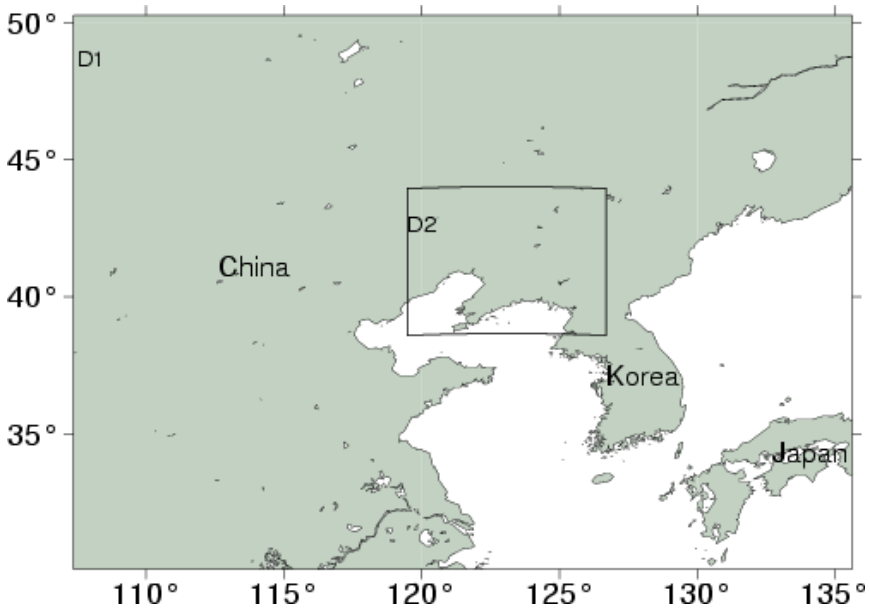

Figure 5. 3 The domain (D1 and D2) configuration for MM5 simulations.

In the case of precipitation simulation, the objective was to compare the freely available dataset (NCEP FNL and JMA JRA-25). The initial and lateral boundary conditions are

imposed every six hours using NCEP FNL Operational Global Analysis data with 1 °×1 ° latitude–longitude resolution (http://dss.ucar.edu/datasets/ds083.2/) and JRA-25 data with 1.25 °×1.25 ºresolution. The model topography for the chosen domain regions is obtained from the U.S. Geological Survey (USGS) topography data. Four-dimensional Data Assimilation (FDDA) was also applied to the two domains in wind, temperature and mixing ratio fields every six hours with the NCEP FNL data.

The microphysics schemes are carried out with mix phase. The parameterisations for planetary boundary layer (PBL) and cumulus are set constant to the Medium-Range Forecast (MRF) PBL scheme and to the Grell cumulus parameterisation for the simulation.

5.3.2 Ocean model (POM) set-up.

In seawater level simulations with POM in this study, only domain 2 case with horizontal resolutions of 9 km is used for the same periods with atmosphere model. The meteorological forcing (wind and pressure) forcing (momentum flux due to white capping and depth-induced wave breaking) are considered for external forcings as well as the prescribed tidal forcing of 8 constituents at lateral open ocean boundaries from the National Astronomical Observatory's ocean tide model. For all simulations, the barotropic ocean states are assumed such that the influences of temperature and salinity in the ocean were not considered. In addition, the bathymetry for domain 2 for POM simulations is taken from GEBCO-30 arc-sec data.

Because lack of available observation data, two years seawater level have been calculated. First, we calculate the seawater level in 1997 for twelve months from January to December and compare with the observation data from National Oceanographic Data Center (NODC). After that, the POM computation is carried out for twelve months from January to December in 2004 using the same parameters and initial conditions with 1997's case. All initial conditions are set to zero. The internal mode time step is ten second. The ratio between external and internal model time step is ten, the model grid is set the same with MM5 model while pressure and wind data are derived from the results of the atmosphere model.

5.3.3 Groundwater model (SEAWAT) set-up.

The model grid consists of the grid system of 60 columns and 60 rows with uniform spacing of 2.0 km (WE-direction) and 2.33 km (NS-direction), respectively. In the vertical direction, four layers (A1, A2, A3 and A4) are set up following the characteristics of the hydrostratigraphy of Liaodong Bay coastal plain.

Layer- A1 corresponds to the Holocene (Q_{4p}) and Upper Pleistocene (Q_{3y}) Quaternary aquifers. Layer- A2 corresponds to the Middle Pleistocene (Q2z) and Lower Pleistocene (Q_{1x}) Quaternary aquifers. Layer - A4 represents the Minhuazhen group aquifer that is a confining layer. Layer - A3 is an aquitard existing between A2 and A4 aquifers, which is also the confining bed between two aquifers (A2 and A4). In this model, the bottom boundary is set by the information from Guantao group aquifer and lower Neozoic aquifer. Model layer thicknesses are determined by the occurrence of sand and clay layers documented in well driller's reports archived by the Liao Ning hydrogeology and engineering geology exploration institute (Wang, 1992).

The precipitation data is derived from the atmosphere model (MM5) simulation results. All the precipitation are the same with 2004 in the prediction model. The seawater level results of ocean model (POM) simulation are used for the ocean boundary of groundwater model and the all boundary in groundwater prediction model is taken the same with the results in 2004. The parameter and others data are the same as with the previous study (see chapter 3, case 2).

The simulation time is considered from October, 2004 to April, 2009 with time step of quarter day. Prediction of the extent of seawater intrusion in coastal aquifers in Liaodong Bay coastal plain 40 years to come after April 2009 is carried out by running the calibrated computation 40-year forwards with all the conditions assumed to remain the same as those in 2004.

5.4 Simulation Results

5.4.1 Precipitation Simulation

Two background data of NCEP FNL and JMA JRA-25 were employed to simulate the precipitation from January to December, 2004. Two computational domains were set as shown in Figure 5.3. Overall, compare with the observation precipitation data from Tropical Rainfall Measuring Mission satellite (TRMM) data (Figure 5.4 left column), the results of this two case are good. The precipitation distribution figures of TRMM data show that in the east of domains area the rainfalls are higher than others area. It might be affected by the mountain in the east area. Which can be good performed in the two case simulations. In this study, five observation stations precipitation (Figure 5.5) data from the China Meteorological Data Sharing Service System (CMDSSS) were used to compare with calculation results (Figure 5.6). The results show that correlation of accumulated monthly rainfall between calculation and observation is good. Figure 5.6 show that the high rainfall season is from June to September which can be performed in the two calculation case studies. The correlation value is from 0.756 to 0.937 of the NCEP case study and 0.5296 to 0.9548 of the JRA-25 case study. Overall, the calculation precipitation results of NECP case study are better than JRA-25 case's results especially for the Jinzhou and Yingkou station results.

The spatial resolution of NCEP data and JRA-25 data are 1.0 degree and 1.25 degree, respectively. The difference resolution of temporal and spatial dimensions might be effect on the precipitation simulation results. Figure 5.7 shows the relative humidity results at Yingkou station of NECP background case and Right: JRA-25 background case in January and July, 2004. It is very clear present that, in the upper troposphere, the JRA results show the dry air mass clearly compare to that from NCEP data of the July and January case. It caused the small rainfall in Yingkou station of July, 2004 in JRA case study. On the other hand, the air mass of January case is drier than the July case.

Thus, the precipitation results of NECP case are used for seawater intrusion simulation which used the atmosphere-ocean-groundwater modeling system in Liaodong Bay plain.

TRMM

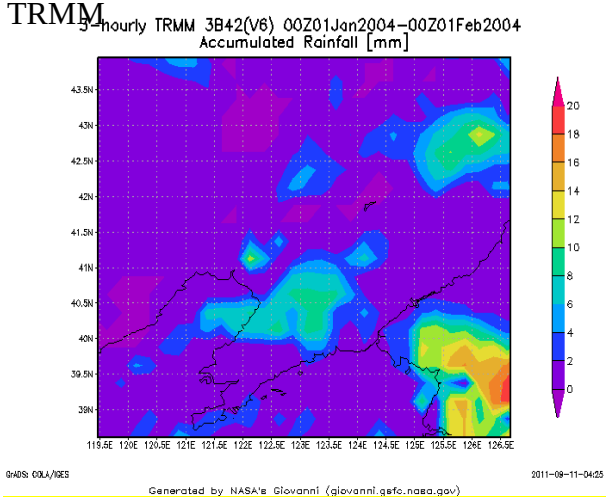

NCEP

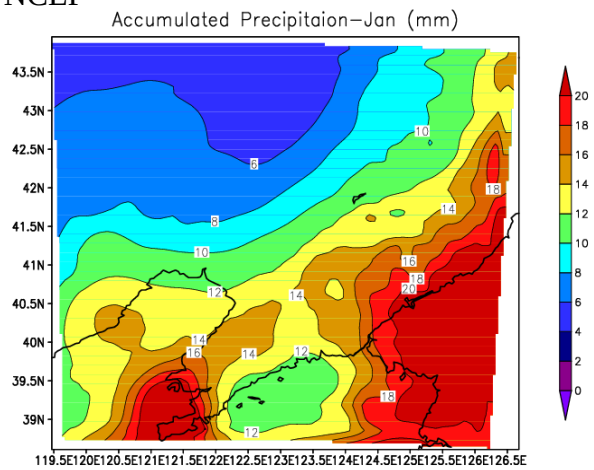

JRA-25

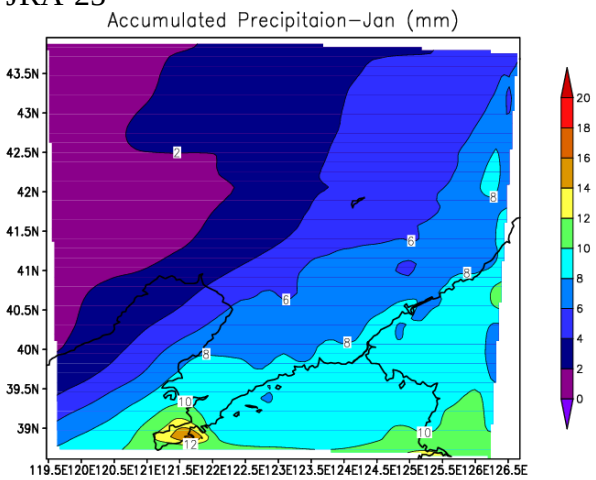

January (upper) / February (lower) 2004

TRMM

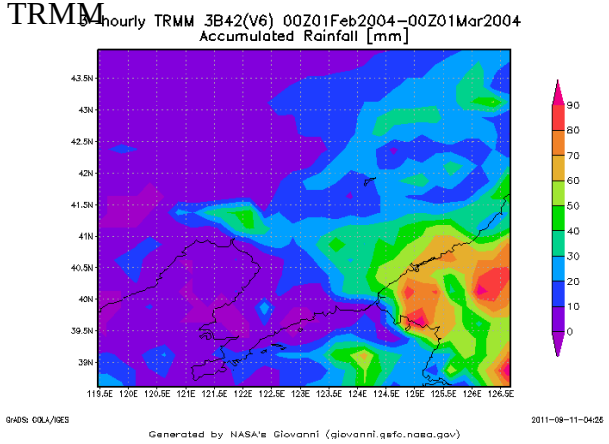

NCEP

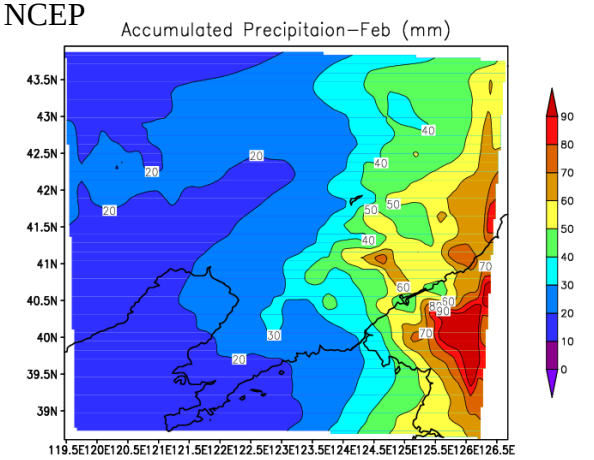

JRA-25

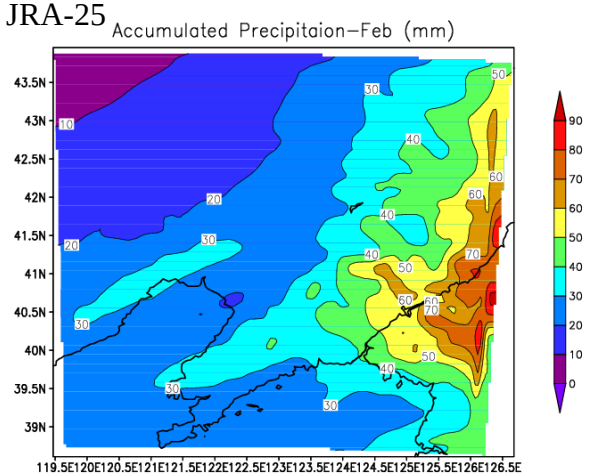

TRMM

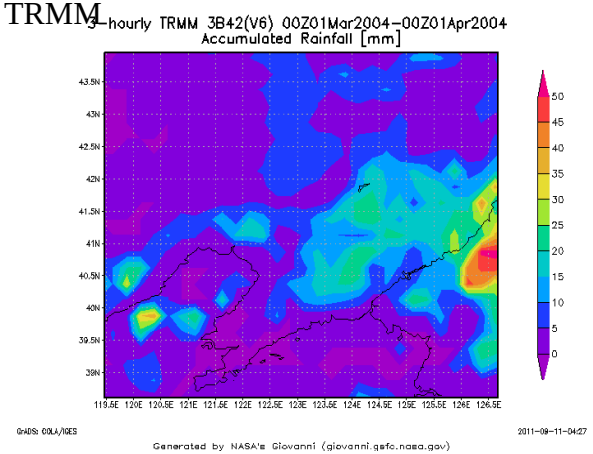

NCEP

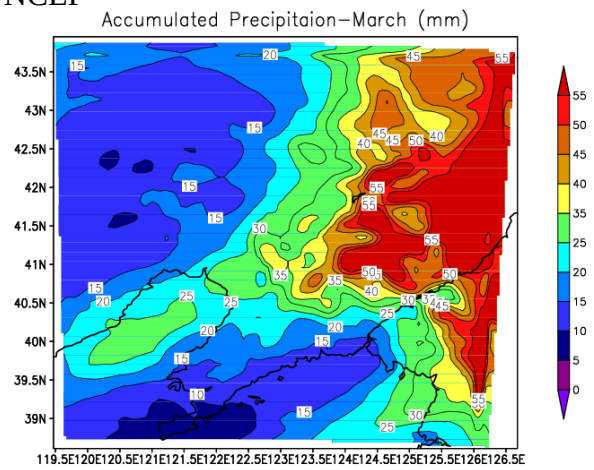

JRA-25

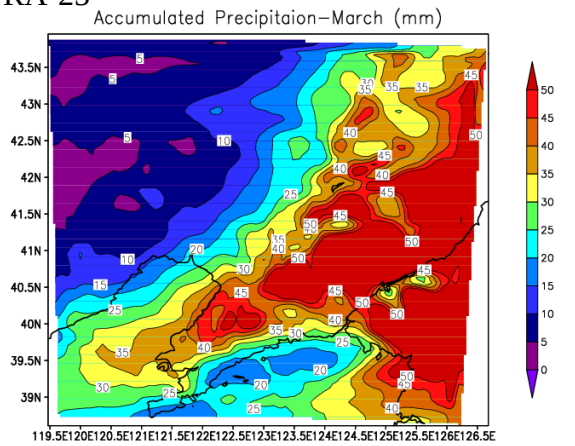

March (upper) / April.(lower) 2004

TRMM

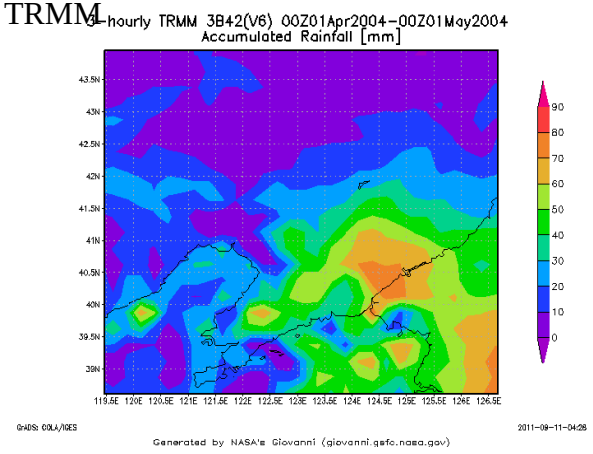

NCEP

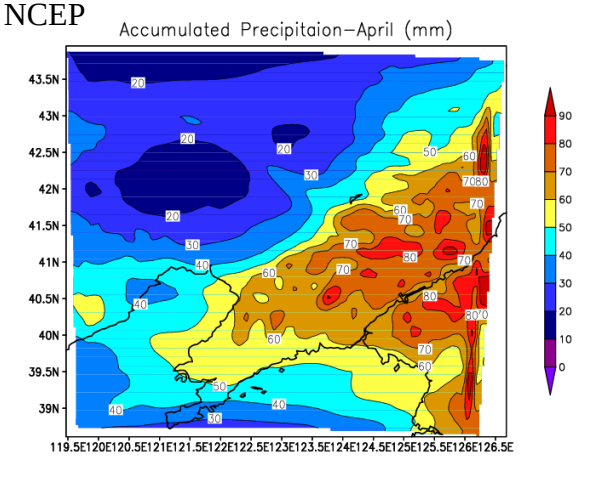

JRA-25

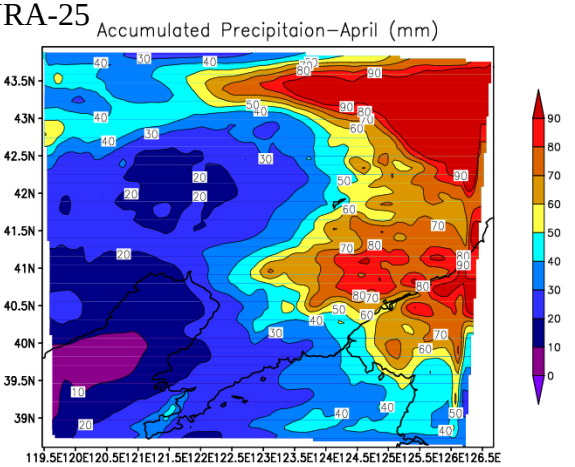

TRMM

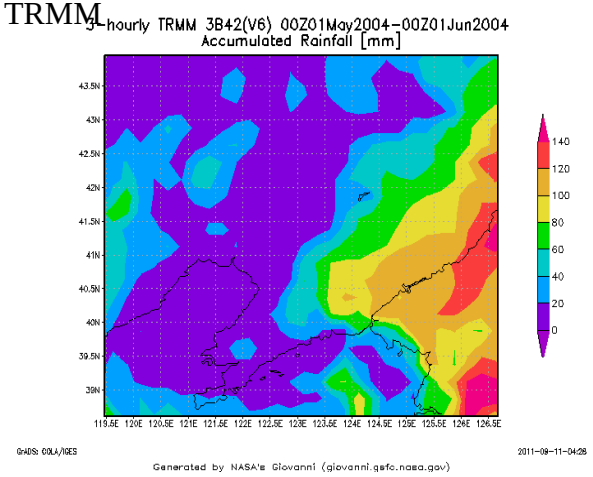

NCEP

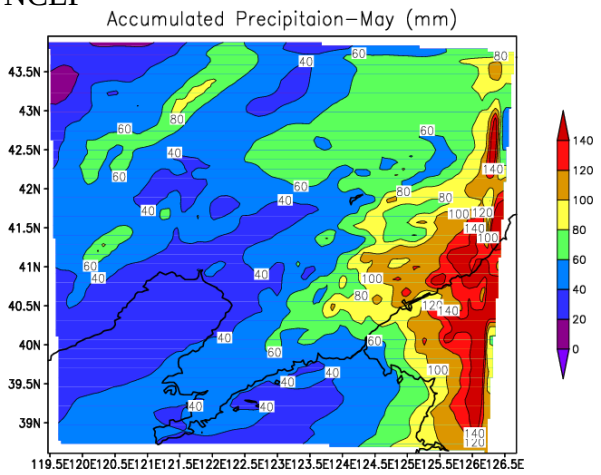

JRA-25

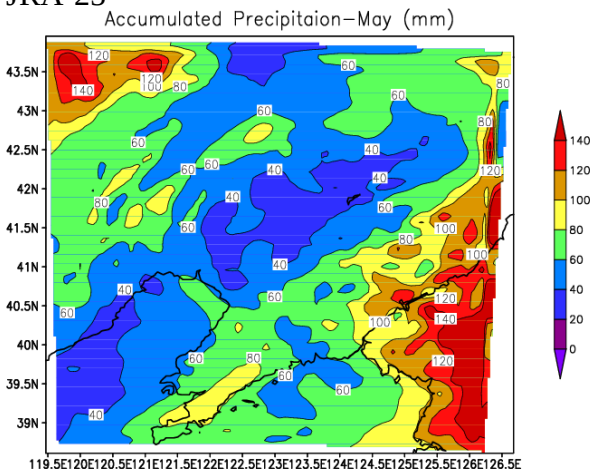

May (upper) / June.(lower) 2004

TRMM

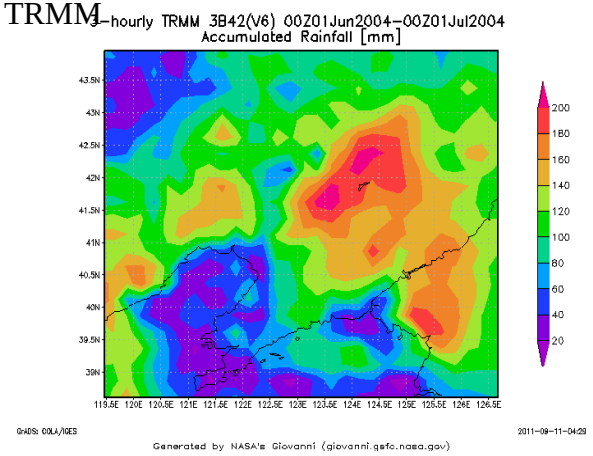

NCEP

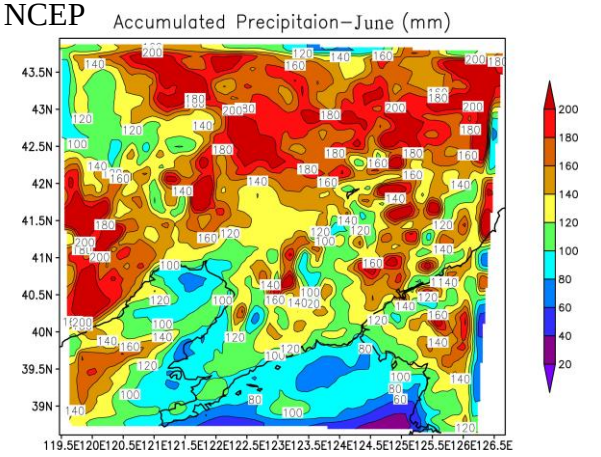

JRA-25

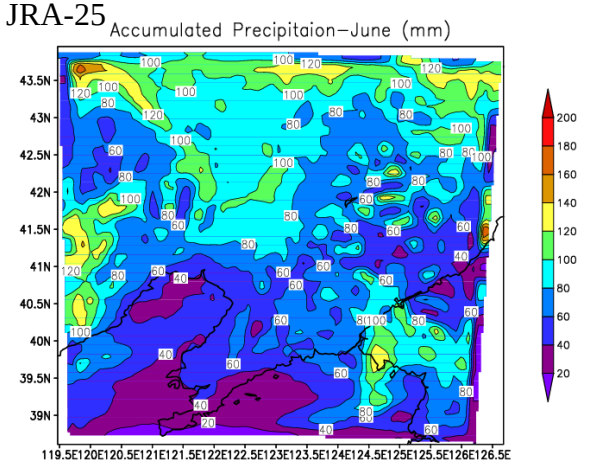

TRMM

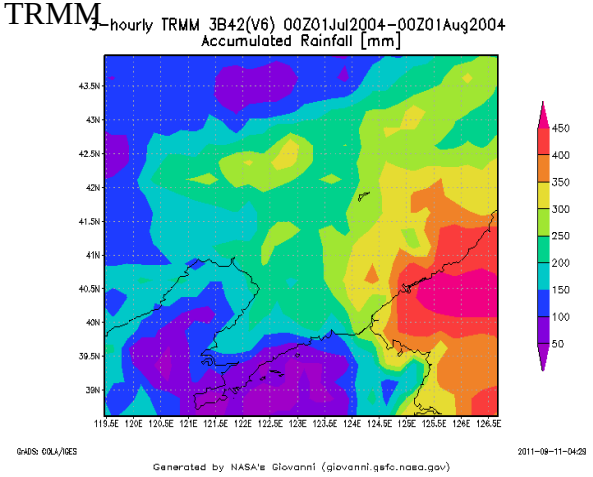

NCEP

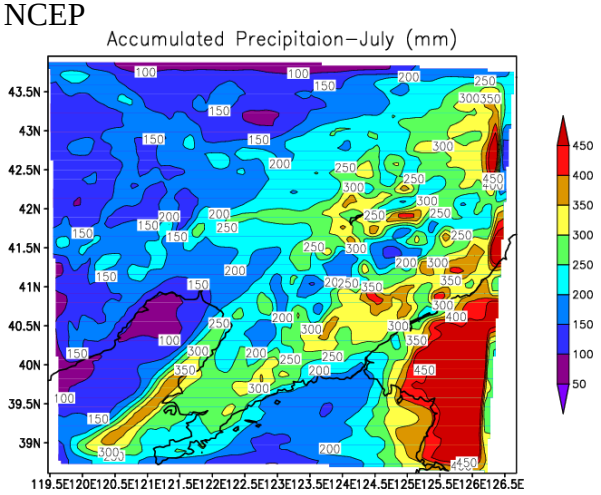

JRA-25

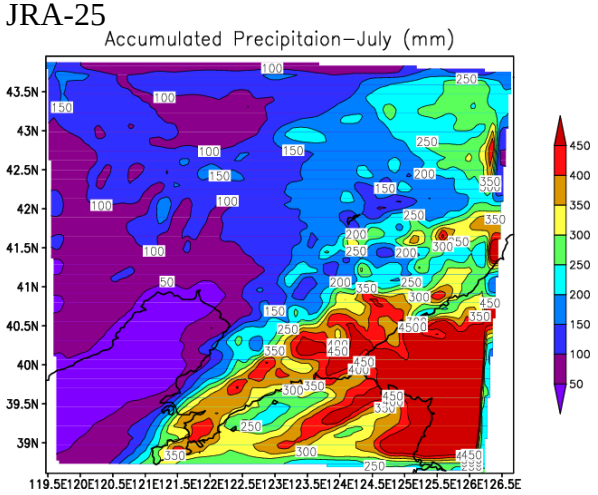

July (upper) / August(lower) 2004

TRMM

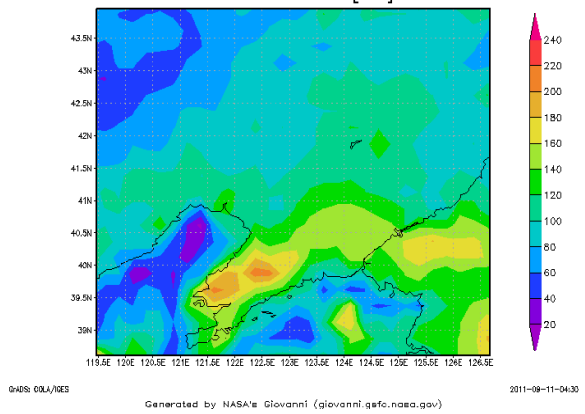

NCEP

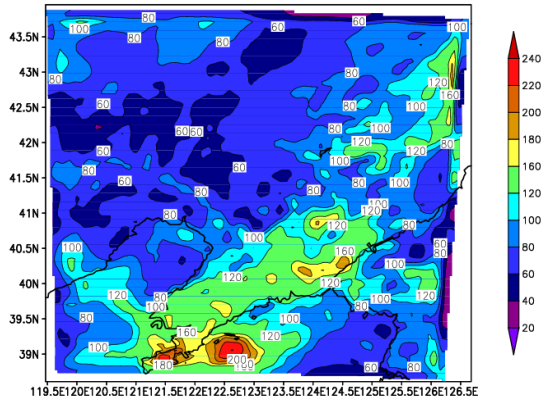

JRA-25

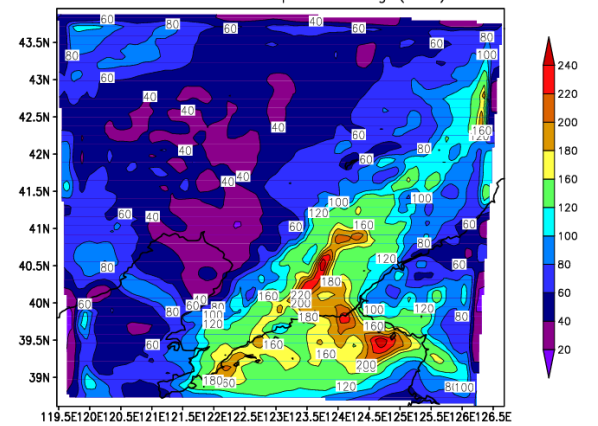

TRMM

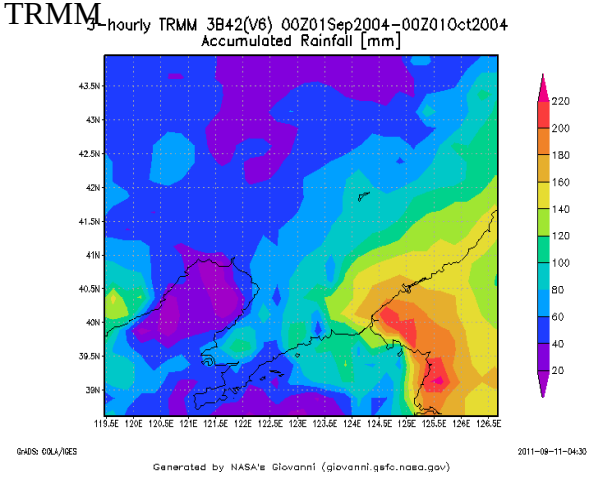

NCEP

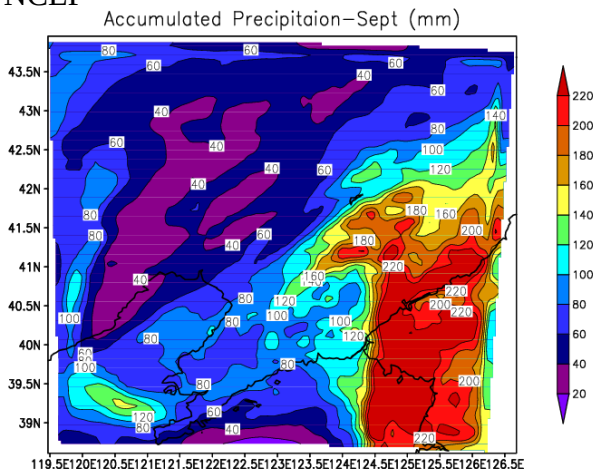

JRA-25

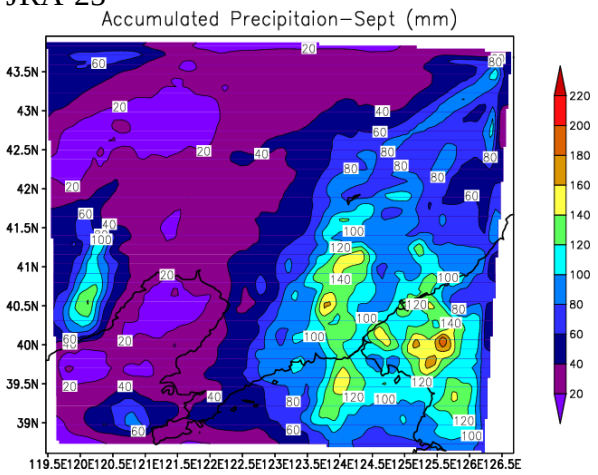

September / October (lower) 2004

TRMM

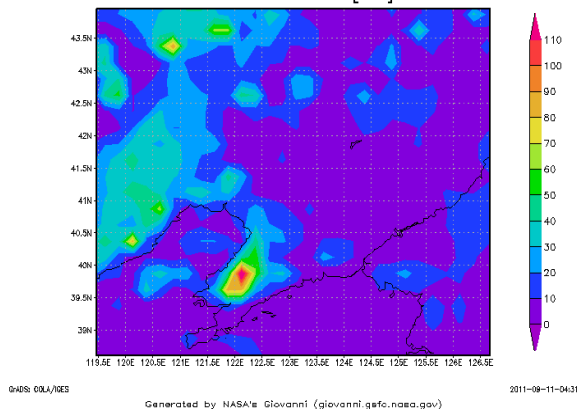

NCEP

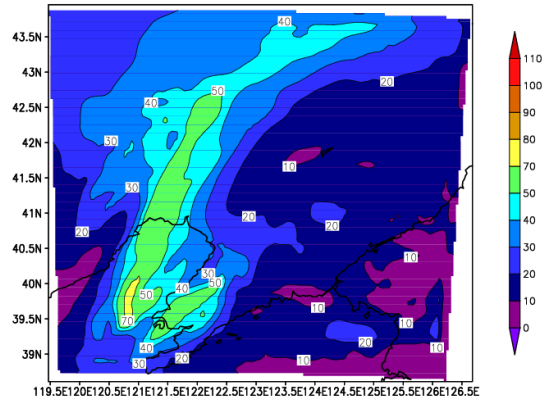

JRA-25

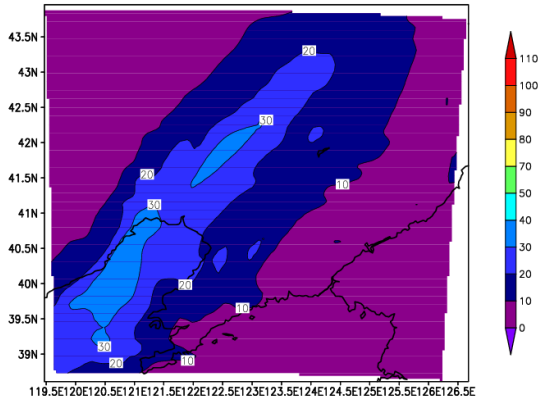

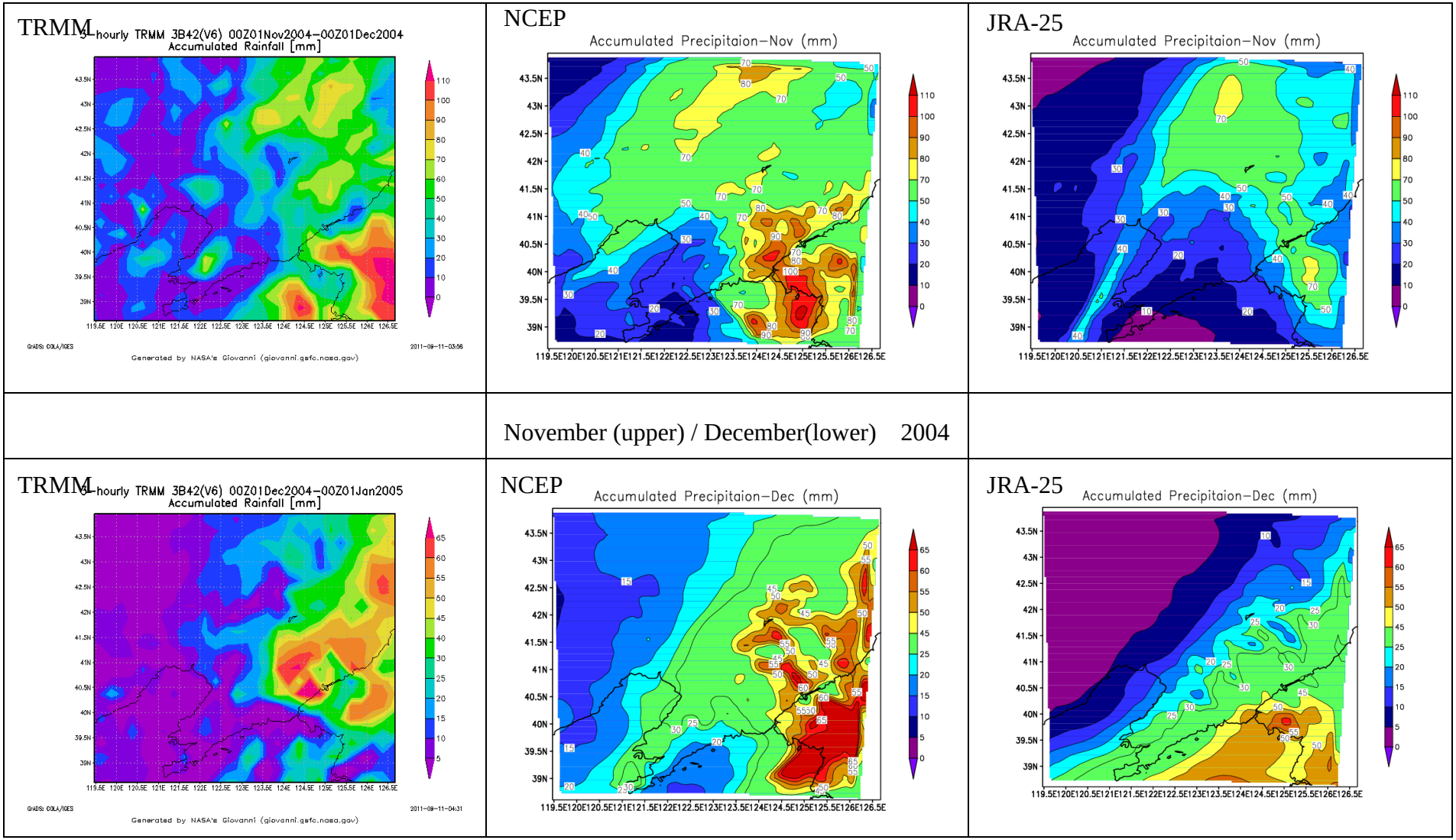

Figure 5. 4 The calculation and observation precipitation distribution results of domain 2 from January to December, 2004. (units in mm).

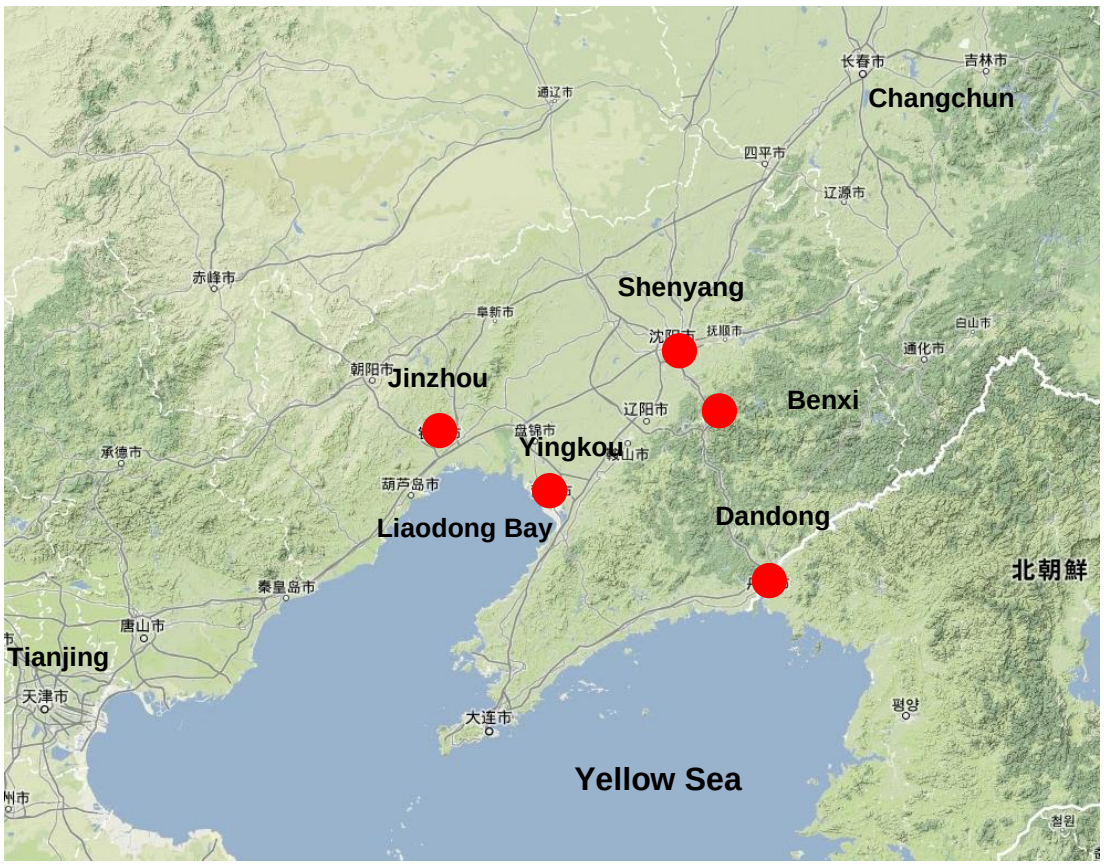

Figure 5. 5 The location of five observation stations of the China Meteorological Data Sharing Service System (CMDSSS)

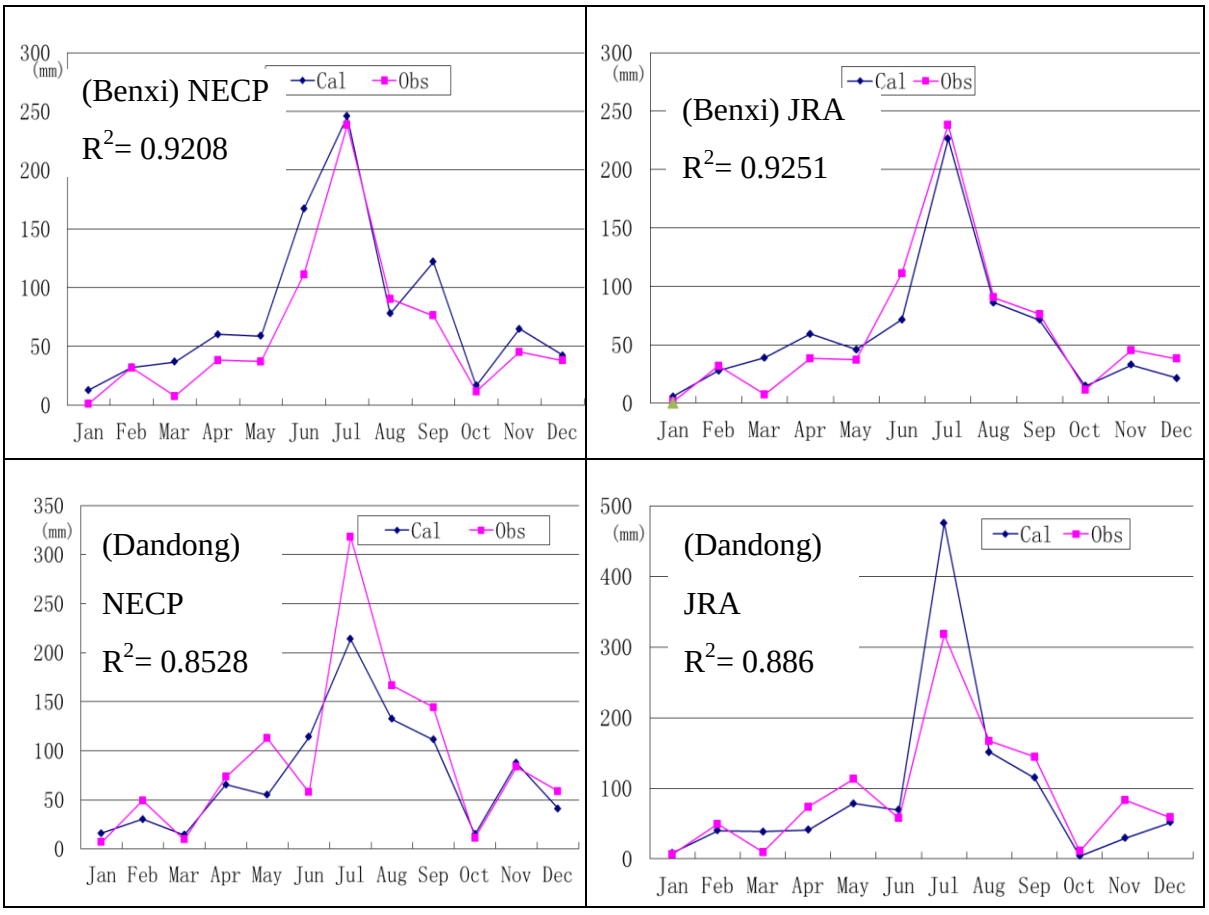

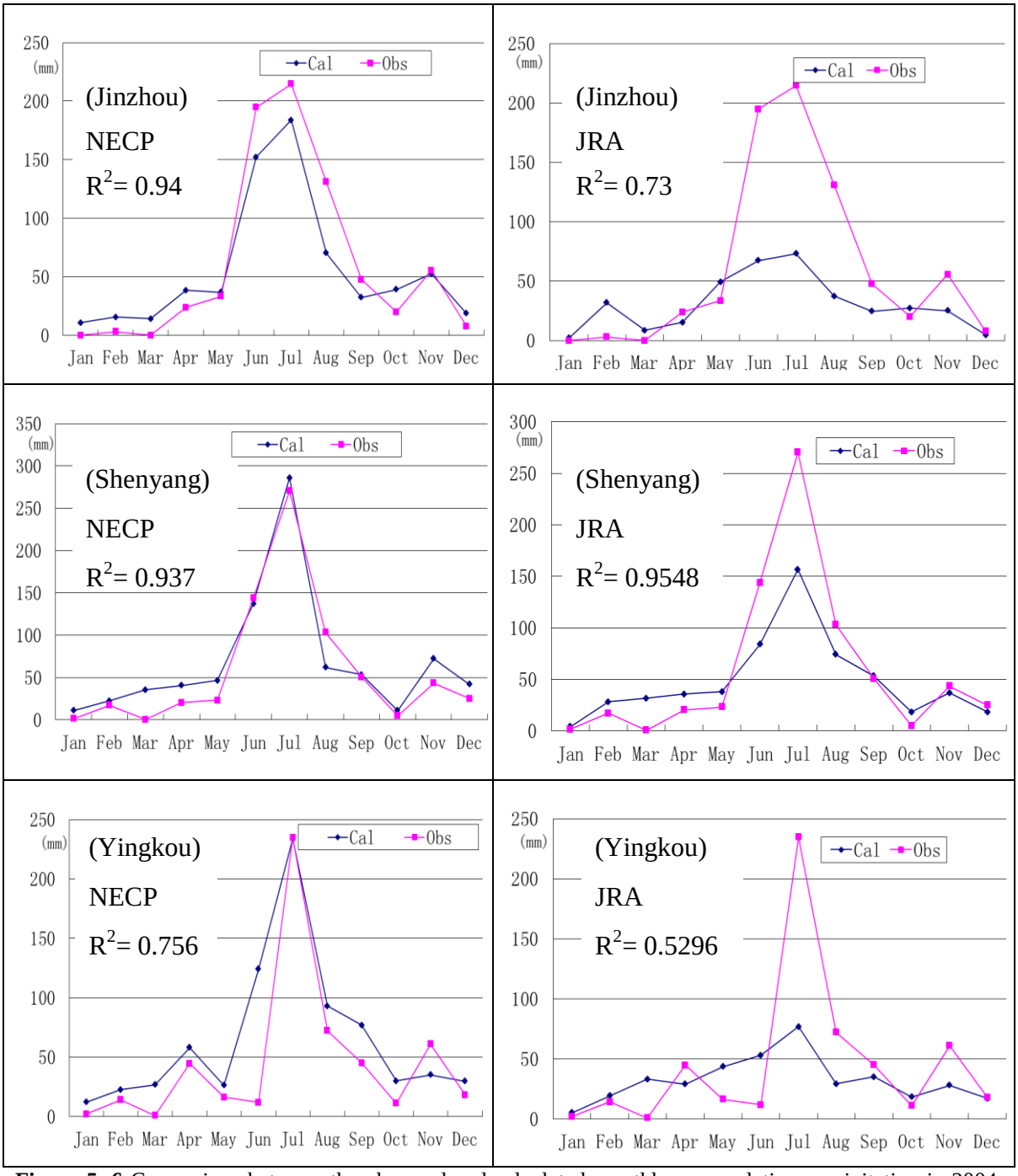

Figure 5. 6 Comparison between the observed and calculated monthly accumulation precipitation in 2004. Left: NECP background case and Right: JRA-25 background case. (unit: mm/month).

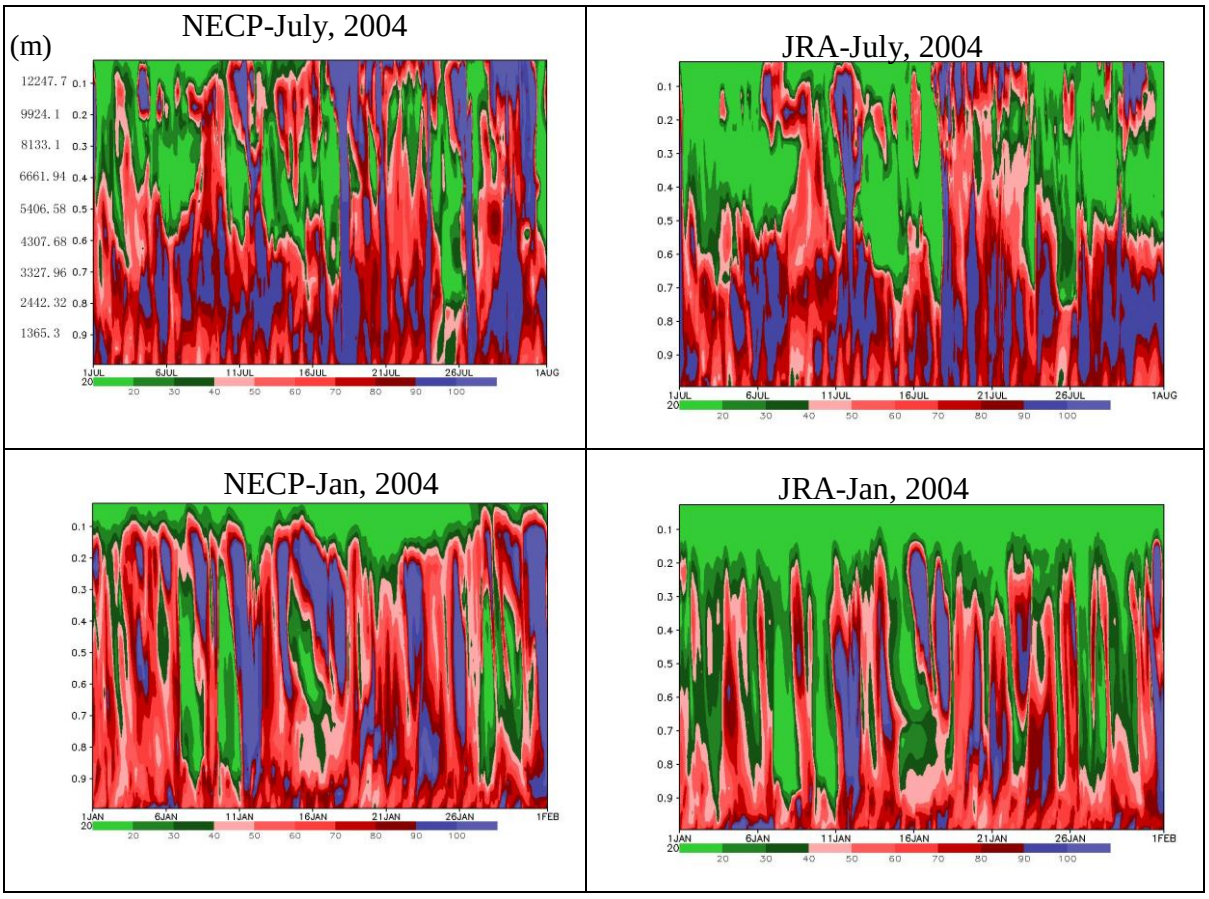

Figure 5. 7 Comparison the relative humidity results at Yingkou station NECP background case and Right: JRA-25 background case in January and July, 2004. The left axis is the average value of geopotential height at Yingkou station which is according to the each sigma coordinate layers.

5.4.2 Seawater level simulation

Two years (1997 and 2004) seawater levels have been calculated in this study. The seawater level of 1997 has been compared with observation data from National Oceanographic Data Center (NODC). Figure 5.8 show that the good match comparative results of the seawater level between the calculation result and observation (NODC) data at Laohutan station from January to December in 1997.

The seawater level of POM results at Yingkou station from January to December 2004 is presented in figure 5.9. The result shows that the tidal range at Yingkou station is 2.52 m while that in Liaodong bay is 2.7 m (Wan, 2003). It is shown that the simulated tidal range result is good. Because of the lack of observation data of NODC, comparison between the observation data and calculation results on the seawater level of 2004 is not considered.

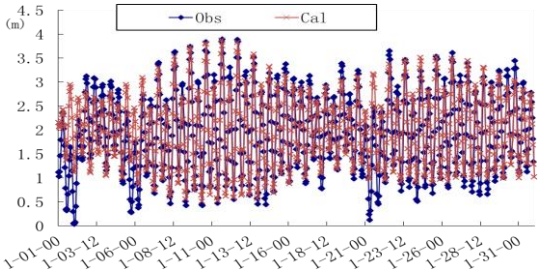
Obs
Cal
(m)

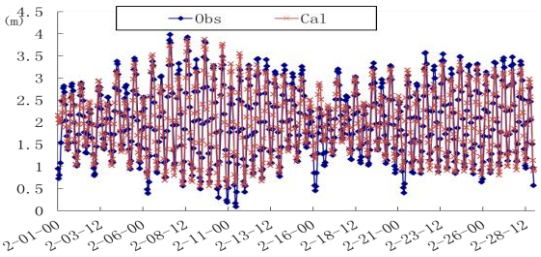
Obs
Cal
(m)

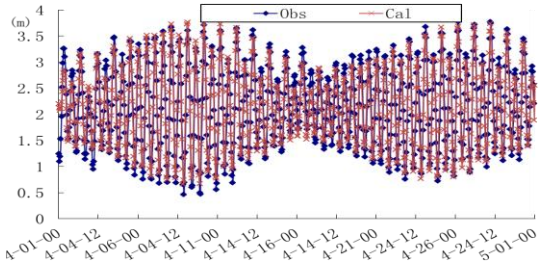
Obs
Cal
(m)

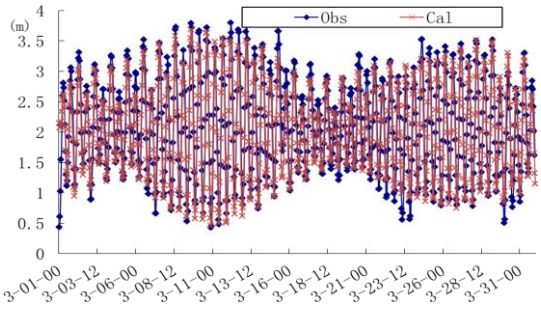
Obs
Cal
(m)

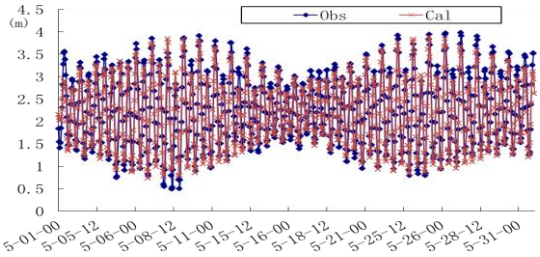
Obs
Cal
(m)

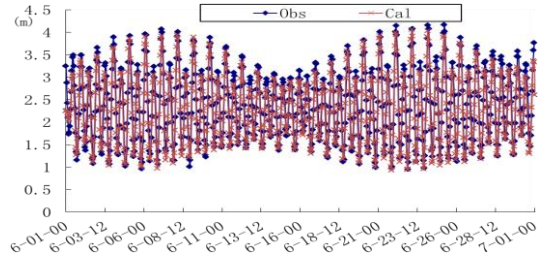
Obs
Cal
(m)

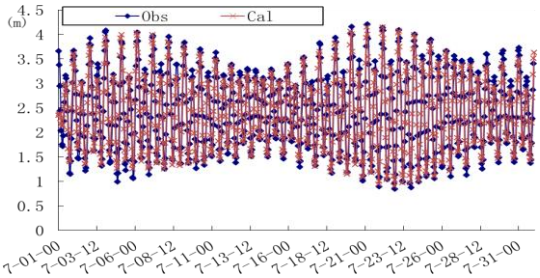
Obs
Cal
(m)

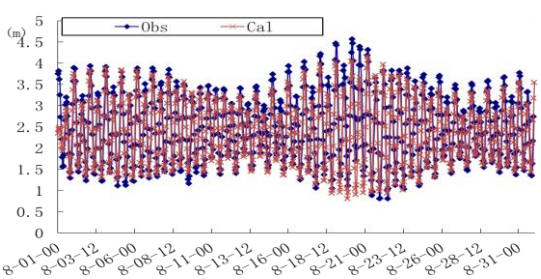
Obs
Cal
(m)

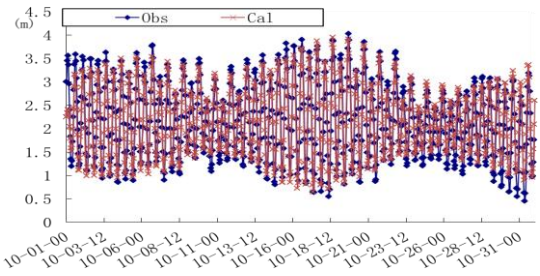
Obs
Cal
(m)

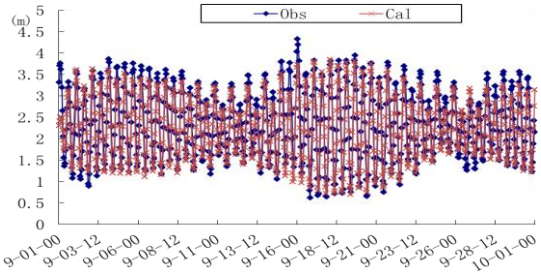
Obs
Cal
(m)

Obs
Cal
(m)

Obs
Cal
(m)

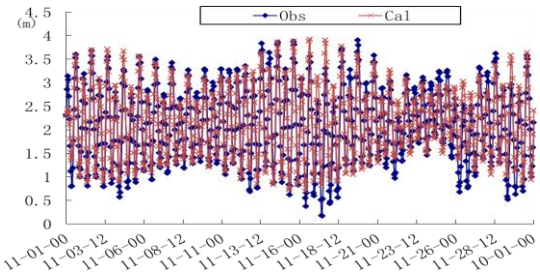

Figure 5. 8 Comparison of computed and observed seawater level (NODC) at the Laohutan station from January to December in 1997 (unit: m).

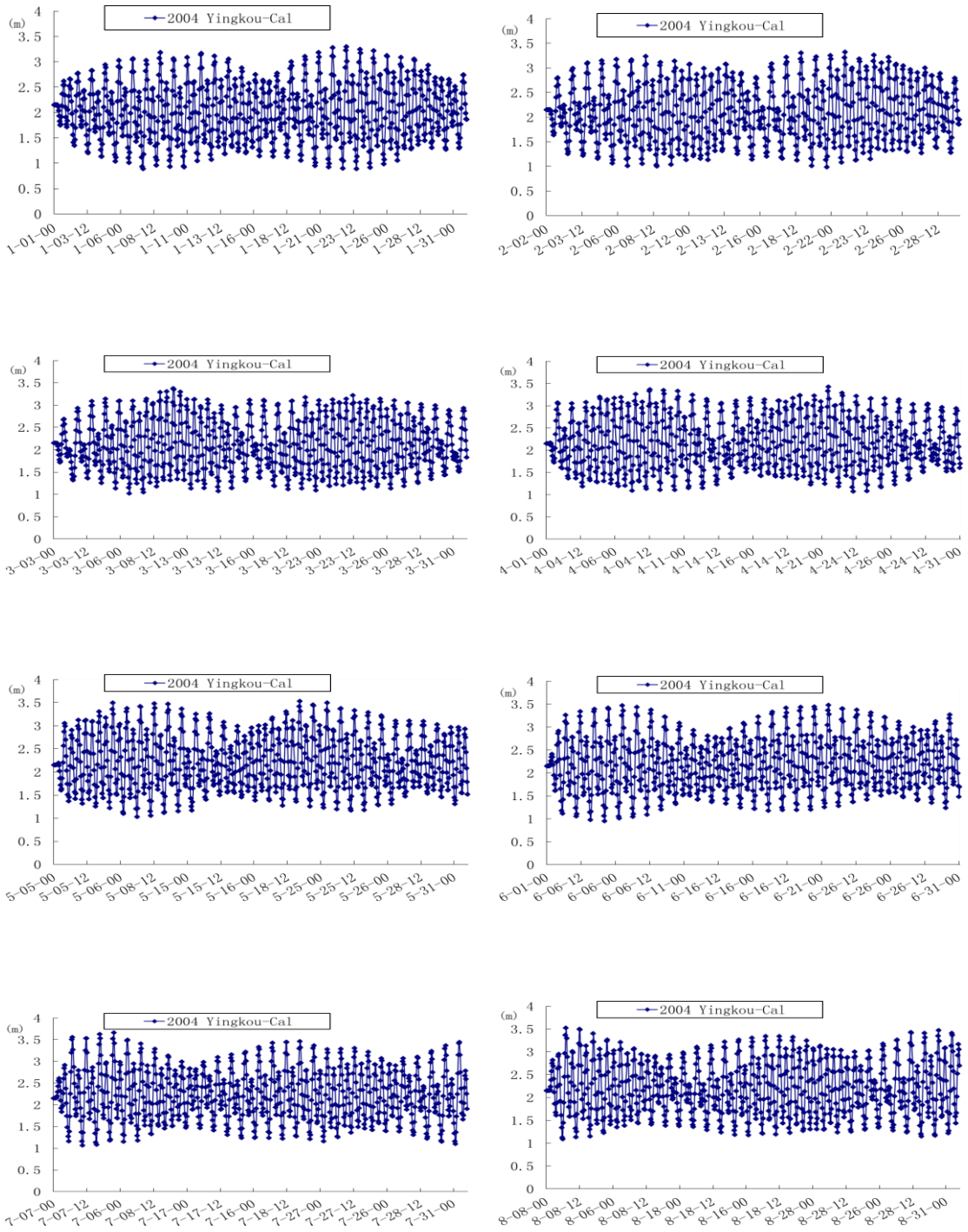

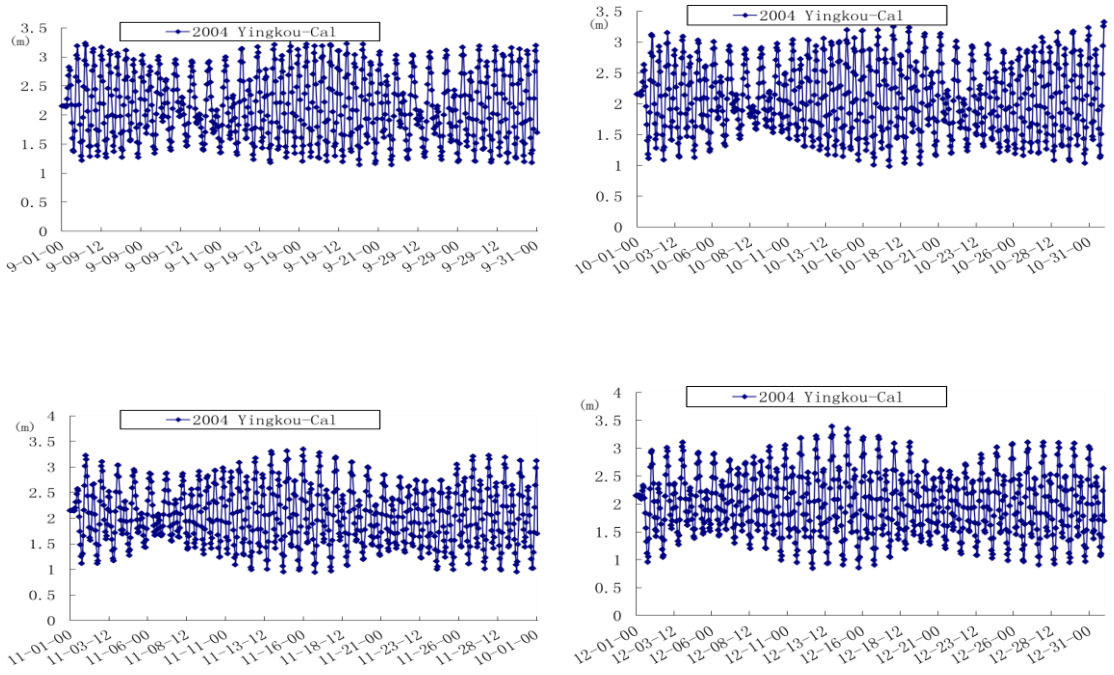

Figure 5. 9 The sea level changes computed by POM at the Yingkou station from January to December 2004. (unit: m).

5.4.3 Seawater intrusion simulation results

The results of the precipitation and seawater level simulation are then employed to simulate seawater intrusion simulation and prediction. This study uses hydraulic heads measured at 18 observation points in April 2009 to calibrate the model.

Model calibration

The model calibration was conducted by tuning conductivity and porosity. The model calibration is done using hydraulic heads measured at 18 observation points in April 2009. The final calibration is established by comparing the observed and calculated hydraulic heads. Figure 5.10 shows that showed a correlation coefficient at 0.982, a mean error of 0.881 m and a root mean square error value of 0.992 m. This indicates a reasonably good match between the observed and calculated heads. Residuals between the observed and calculated heads are also listed in Table 5.1.

Table 5.1 Observed and calculated heads with residuals at 18 observation points

Well ID	X-Model	Y-Model	Observed heads(m)	Calculated head(m)	Residuals (m)
1	117348.5	75583.85	2.8	3.58818	0.649896
2	107162	27707.29	4.1	3.00143	-1.25178

3	93919.55	59896.63	2.4	2.367115	-0.14747
4	96160.58	107569.5	3.5	4.440673	0.829527
5	70490.6	97586.69	3.7	2.932889	-0.90823
6	64989.89	85770.35	2.4	2.444758	-0.02712
7	41968.39	73342.82	2.6	3.451648	0.711563
8	44820.61	85159.16	3.7	3.381467	-0.491
9	31170.7	60304.1	2.5	4.019518	1.322999
10	129164.9	78843.53	-3.7	-2.80698	0.907314
11	105735.9	66823.46	-7.3	-8.83561	-1.57193
12	104106.1	79658.45	-6.5	-6.97839	-0.50136
13	95549.39	99216.53	-6.8	-5.51647	1.271788
14	70083.14	86177.81	-6.5	-7.18736	-0.6932
15	58877.98	80065.91	-9	-7.67849	1.309371
16	46246.72	65397.35	-8.3	-7.05218	1.24812
17	89844.95	38301.25	-6.6	-7.20372	-0.63111
18	91882.25	53988.46	-7.4	-8.84465	-1.48264

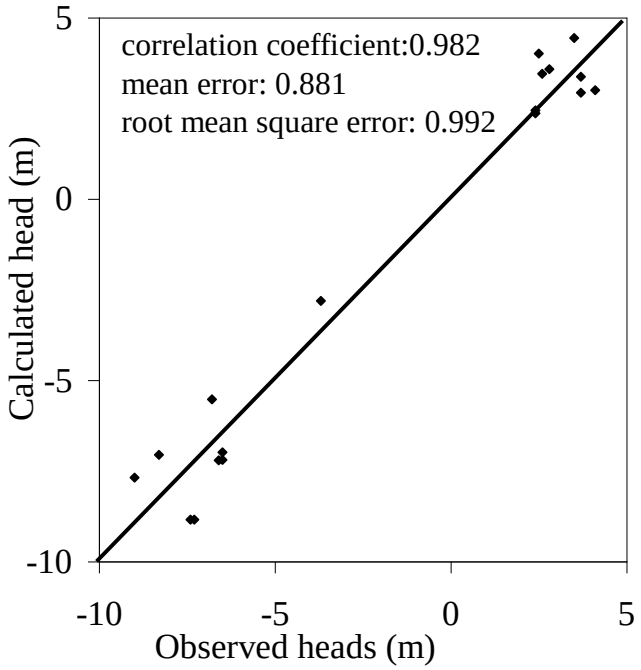

Figure 5. 10 Scatter diagram showing the relationship between the observed and calculated hydraulic for the computation of seawater intrusion in April, 2009.

Prediction of seawater intrusion.

After calibrating the simulated model, prediction was conducted for 40 years from April, 2009 to April, 2049 using the calibrated model.

Figure 5.11(A) and (B) shows that the extent of seawater intrusion on the coastal area is faster than in the north of the study area. Compared with the Figure 5.11(A), (B) and (C), it can be described that the seawater intrusion in Layer A2 becomes significantly faster than that in Layer A1 and A4. The maximum extent of seawater intrusion in Layers A2 will increase 9.8 km toward north in the west of research area. It shows that the tidal fluctuation has significant effects on the seawater intrusion in the upper layer. Compared with the previous study (Ding, 2011), the trend of seawater intrusion in layer A1, A2 and A4 is almost same. Therefore, the atmosphere–ocean-groundwater modeling system can be used in the seawater intrusion simulation.

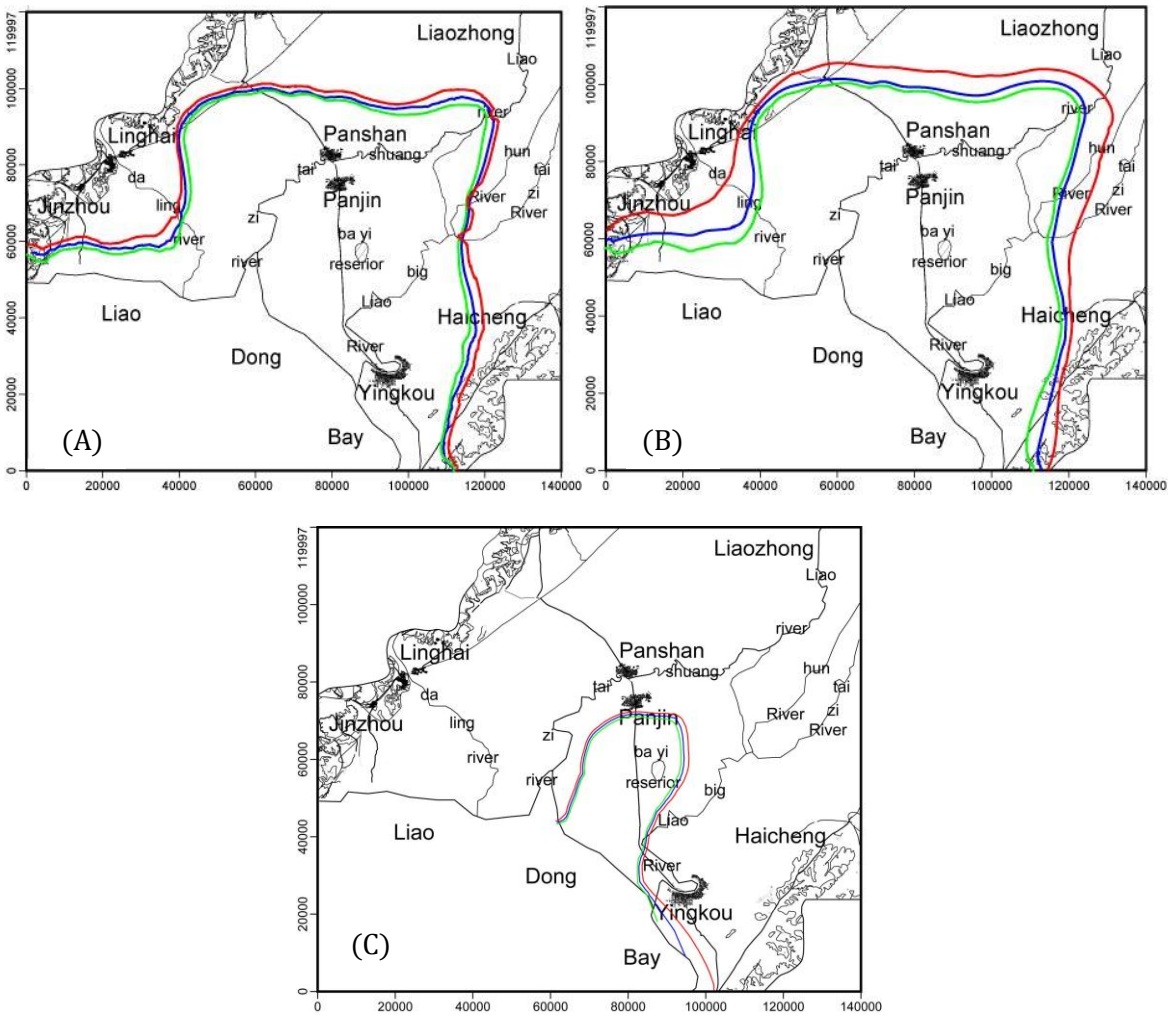

Figure 5. 11 Computed extent of seawater intrusion for (A) Layer A1, (B) Layer A2 and (C) Layer A4. Hind-cast result in April 2009 is shown by blue line, that in October 2004 by green line, and the predicted extent of seawater intrusion in April 2049 is shown by red.

5.5 Summary

In the developing country, the lacked of precipitation and seawater level data limits the seawater intrusion study. To solve this problem, an atmosphere–ocean-groundwater modeling system is constructed in this study. It can be used for precipitation, seawater level calculation and seawater intrusion simulation. It also can be used for groundwater simulation in regions with lack of data. A case study on seawater intrusion simulation is done in the Liaodong Bay coastal plain. The result of the atmosphere–ocean-groundwater modeling system provides a very reasonable result.

In this study, the atmosphere-ocean-groundwater modeling system considered the interaction within atmosphere-ocean part and considered the atmosphere-ocean effect on the groundwater part but not considered the groundwater effect on the atmosphere-ocean part. In the future study, it needs to improve the atmosphere-ocean-groundwater modeling system to considered the each other effect between atmosphere, ocean and groundwater part.

REFERENCES

Abd-Elhamid, H.F., and Javadi, A.A..: A density-dependant finite element model for analysis of saltwater intrusion in coastal aquifers. *Journal of Hydrology*, Vol. 401, pp. 259- 271, 2011.

Arlai, P., Koch, M., and Koontanakulvong, S.: Modeling flow and transport for sustainable yield estimation of groundwater resources in the Bangkok aquifer system. EGU General Assembly 2006, Vienna, Austria, 2006a.

Arlai, P., Koch M., Koontanakulvong, S. ,and Weerapol, B.: Numerical Modeling as a Tool to Investigate the Feasibility of Artificial Recharge to Prevent Possible Saltwater Intrusion into the Bangkok Coastal Aquifers System. Proceedings of Groundwater Hydraulics in omplex Environments, Toulouse, France, 2006b.

Arlai, P., Koch ,M. ,and Koontanakulvong, S.: Statistical and Stochastic Approaches to Assess Reasonable Calibrated Parameters in a Complex Multi-Aquifer System. Proceedings of CMWR XVI-Computational Methods in Water Resources, Copenhagen, Denmar, 2006c.

Arlai, P., Koch, M. ,and Koontanakulvong, S. Numerical.: Investigation of the Cradle of Saline Contamination and Effective Remediation Schemes for Amending Saline Water Pollution Problem in the Bangkok Coastal Aquifers System. 3rd APHW Conference, Bangkok, 2006d.

Ataie-Ashtiani, B., Volker, R.E., and Lockington, D.A.: Tidal effects on groundwater dynamics in unconfined aquifers. *Journal of Hydrological processes*, 15, 655–669, 2001.

Bakker, M., and Schaars, F.: T*he sea water intrusion (SWI) package manual, version 0.2*. University of Georgia, Athens, 2003.

Bhosale, D. and Kumar, C.: Simulation of Seawater Intrusion in Ernakulam Coast. proceeding of International Conference on Hydrology and Watershed Management, Hyderabad, pp. 390-399, 2002.

Bian, J. M., and Tang, J.: Groundwater resources optimal allocation countermeasures in the liaohe oil field area. Proceedings of the 34th Congress of International Association of Hydrogeologists, Bejing, China, October 9-13, 2006.

Bobba, A.G.: Mathematical models for saltwater intrusion in coastal aquifers. *Water Resources Management*, Vol. 7: pp. 3–37, 1993.

Chalikov, D.V. and Belevich, M.Y.: One-dimensional theory of the wave boundary layer. *Bound. Layer Meteor*., 63, 65-96, 1993.

Charnock, H: Wind stress on a water surface. *Quarterly Journal of Royal Meteorological Society*, 81, pp. 639-640, 1955.

Ding, F., Yamashita, T., Lee, H.S. and Pan, J.: Numerical study on seawater intrusion into groundwater in Liaodong Bay coastal plain, China. Proceedings of 2011 International Symposium on Water Resource and Environmental Protection (ISWREP 2011) conference, Chang An University, Xi'an, China, 2011.

Ding, F., Yamashita, T., Lee, H.S. and Haggag, M.: Numerical study of tidal effect on seawater intrusion into groundwater in Liaodong Bay coastal plain, China. Proceedings of the 6th International Conference on Asian and Pacific Coasts (APAC2011) conference, Hong Kong, China, 2011.

Dominick TF, Wilkins B, Roberts H.: Mathematical model for beach groundwater fluctuations. *Water Resources Research*, 7, 1971.

Dudhia, J.: A multi-layer soil temperature model for MM5. Preprints, The Sixth PSU/ NCAR Mesoscale Model User's Workshop, 22-24 July 1996, Boulder, Colorado, 49-50, 1996.

El-Bihery, M. A.: Groundwater flow modeling of Quaternary aquifer Ras Sudr, Egypt. *Environmental Geology*, Vol. 58, pp. 1095–1105, 2009.

Elhaggag, M.E.A.: *Regional environment simulator atmosphere ocean land surface hydrology coupled model*. PhD dissertation, Hiroshima University, Japan, 2009.

Evans, M.: *Nutrient Discharge to Cockburn Sound from a Subterranean Mixing Zone: a Comparison of Transport and Reaction Timescales*, Honours thesis, University of Western Australia, p.83, 2005.

Gerten, D., Schaphoff, S., Haberlandt, U., et al.: Terrestrial vegetation and water balance: Hydrological evaluation of a dynamic global vegetation model. *Journal of Hydrology*, 286, 249-270, 2004.

Giambastiani, B. M. S., Antonellini, M., Oude Essink, G. H. P., and Stuurman, R. J.: Saltwater intrusion in the unconfined coastal aquifer of Ravenna (Italy): A numerical model. *Journal of Hydrology*, Vol. 340, pp. 91-104, 2007.

Grell, G.A., Dudhia, J. and Stauffer, D.R.: *A description of the fifth-generation Penn State/ NCAR mesoscale model (MM5)*. NCAR Technical Note, NCAR/ TN-398+STR, 117 pp, 1995.

Guo, W. X., and Langevin, C. D.: User's guide to SEAWAT: a computer program for the simulation of three-dimensional variable-density ground-water flow, USGS Techniques of Water Resources Investigations, Book 6, chap A7, p. 77, 2002.

Harbaugh, A. W., Banta, E. R., Hill, M. C., and McDonald, M. G.: MODFLOW- 2000, the U.S. Geological Survey Modular Ground-Water Model—User Guide to Modularization Concepts and the Ground-Water Flow Processes, U.S. Geological Survey Open- File Report 00-92, 121p, 2000.

Hendri.: Environmental assessment studies on tropical forest carbon management and atmosphere-ocean coupled simulaton. PhD dissertation, Hiroshima University, Japan, 2011.

Huyakorn, P. S., Andersen, P. F., Mercer, J. W., and White, J. H. O.: Saltwater intrusion in aquifers: Development and testing of a three-dimensional finite element model. Water Resource Research, Vol. 23(2): 293–312, 1987.

HydroGeoLogic Inc.: MODHMS—MODFLOW-Based Hydrologic Modeling System: Documentation and User's Guide, Herndon, Virginia, 2002.

Kim, K.: Coastal ocean model with consideration of meterological-oceanographic mesoscale interaction. PhD dissertation, Kyoto University, Japan, 2005.

Kim, K.O. and Yamashita, T.: Wind-wave-surge coupled model: Application to storm surge simulation in the Bay of Bengal. *Proc. of Asian and Pacific Coasts 2005*, Jeju, Korea, pp. 603-606, 2005.

Kopsiaftis, G., Mantoglou, A., and Giannoulopoulos, P.: Variable density coastal aquifer models with application to an aquifer on Thira Island. *Desalination*, Vol. 237, pp. 65–80, 2009.

Langevin, C. D., and Guo, W. X.: MODFLOW/MT3DMS–Based Simulation of Variable-Density Ground Water Flow and Transport. *Ground water*, Vol. 44, No. 3, pp. 339–351, 2006.

Langevin, C.D., Thorne, D.T., Jr., Dausman, A.M., Sukop, M.C., and Guo, W. X.: SEAWAT Version 4: A Computer Program for Simulation of Multi-Species Solute and Heat Transport, U.S. Geological Survey Techniques and Methods Book 6, Chapter A22, 39 p, 2007.

Lee, H. S.: Regional Disaster events and environment simulations by atmosphere-ocean coupled model. PhD dissertation, Kyoto University, Japan, 2007.

Lee, H. S., T. Yamashita, and T. Komaguchi.: Reanalysis of past major storms in West Kyusyu and study of wind-induced current in Ariake Sea, *Journal of International Development and Cooperation*, 14(2), 19-36, 2008.

Lee, H. S., T. Yamashita, T. Komaguchi, and T. Mishima.: Reanalysis of Typhoon Meteorological Fields and Related Waves and Surges in the Seto Inland Sea, *Journal of Japan Society of Civil Engineers*, Ser. B2 (Coastal Engineering), 65(1), 441-445, 2009.

LeMone, M. A., and Coauthors.: Land–atmosphere interaction research, early results, and opportunities in the Walnut River watershed in southeast Kansas: CASES and ABLE. Bull. *Amer. Meteor. Soc.*, 81, 757–779, 2000.

Li, Y. M., Groundwater quality simulation and forecast in liaohe oil field, (in chinese), Msc Thesis, Jiling University, 86 p, 2005.

Lin, J., Snodsmith, J. B., Zheng, C. M., and Wu, J. F.: A modeling study of seawater intrusion in Alabama Gulf Coast, USA. *Environmental Geology*, 57: pp. 119–130, 2009.

Mao, X., Enot, P., Barry, D.A., Li, L., Binley, A., and Jeng, D. S.: Tidal influence on behaviour of a coastal aquifer adjacent to a low-relief estuary. *Journal of Hydrology*, 327, pp. 110-127, 2006.

Marshall, J., Adcroft, A., Hill, C., Perelman, L. and Heisey, C.: A finite-volume, incompressible navier-stokes model for studies of the ocean on parallel computers. *J. Geophys. Res*., 102(C3), 5753-5766, 1997a.

Marshall, J., Hill, C., Perelman, L. and Adcroft, A.: Hydrostatic, quasi-hydrostatic and non-hydrostatic ocean modeling. *J. Geophys. Res*., 102(C3), 5733-5752, 1997b.

McDonald, M. G., and Harbaugh, A. W.: *A modular three-dimensional finite-difference ground-water flow model*, U.S. Geological Survey Techniques of Water Resources Investigations, Book 6, chap A1, 588p, 1988.

Mellor, G.: *A three-dimensional, primitive equation, numerical ocean model. Program in Atmospheric and Oceanographic Sciences Report*. Princeton University, Princeton, 1998.

Mellor, G.L.: *Uses guide for a three-dimensional, primitive equation, numerical ocean model*. 56 pp, 2004.

Ministry of Health of the Heople's Republic of China, *Standards for drinking water quality*, GB 5749-2006, p. 9, 2006.

Moon, I.J.: "Impact of a coupled ocean wave-tide-circulation system on coastal modeling. *Ocean Modelling*. Vol. 8, pp. 203-236, 2005.

Nagai, H.: Validation and sensitivity analysis of new atmosphere-soil-vegetation model. *Journal of Applied Meteorology*, 41, 160-176, 2002.

Oude Essink, G. H. P.: MOC3D adapted to simulate 3D densitydependent groundwater flow. Proceedings of MODFLOW '98 conference at the international ground water modeling center, Colorado School of Mines, Golden, Colorado, vol 1, pp. 291–300, 1998.

Nagai, H. and Yamazawa, H.: Development of one-dimensional atmosphere-soil-vegetation model (in Japanese), *Japan Atomic Energy Research Institute Rep*. 99-124, 88 pp, 1999.

Nagai, H.: Validation and sensitivity analysis of a new atmosphere-soil-vegetation model. Part II: Impacts on in-canopy latent heat flux over a winter wheat field determined by detailed calculation of canopy radiation transmission and stomatal resistance. *Journal of Applied Meteorology*, 42, 434-451, 2003.

Nagai, H.: Incorporation of CO2 exchange processes into a multilayer atmosphere-soil-vegetation model. *Journal of Applied Meteorology*, 44, 1574-1592, 2005.

Oude Essink, G. H. P.: Saltwater Intrusion in 3D Large-Scale Aquifers: A Dutch Case. *Phys. Chem. Earth* (B), Vol. 26, No. 4, pp. 337-344, 200l.

Sorek, S., and Pinder, G. F.: Survey of computer codes and case histories. In: Bear J et al (ed) Seawater intrusion in coastal aquifers: concepts, methods, and practices, Kluwer Academic Publishers, Dordrecht, pp. 399–461, 1999.

Shabani, B., Nielsen, P. and Baldock, T. E.: Field Observations of Wind Stress Over Surf Zone. paper presented at The 21st International Offshore and Polar Engineering Conference, Maui, Hawaii, 2011.

Skamarock, W. C., J. B. Klemp, J. Dudhia, D. O. Gill, D. M. Barker, M. G. Duda, X.-Y. Huang, W. Wang, and J. G. Powers.: A Description of the Advanced Research WRF Version 3, NCAR/TN‐475+STR NCAR TECHNICAL NOTE, 113, 2008.

Tolman, H.L. and Chalikov, D.V.: Source terms in a third-generation wind-wave model. J. Phys. Oceanogr., 26, 2497-2518, 1996.

Tolman, H.L.: User manual and system documentation of Wave Watch III version 2.22, TN-No 222, NCEP MMAB, 133 pp, 2002.

Tsuboki, K. and Sakakibara, A.: Large-scale Parallel Computing of Cloud Resolving Storm Simulator, in High performance computing, edited by Hans, P. Z., Joe, K., Sato, M., Seo, Y. and Schimasaki, M., pp. 564, Springer, Berlin, 2002.

Tsuduki, K., and Matsunaga, T.: Importance of hydrological parameters in contaminant transport modeling in a terrestrial environment. Proceedings of the International Symposium on Environmental Modeling and Radioecology, Rokkasho, Japan, 2006.

Voss, C.: SUTRA: A Finite-Element Simulation Model for Saturated-Unsaturated Fluid-Density-Dependent Ground-Water Flow With Energy Transport or Chemically-Reactive Single-Species Solute Transport, Water Resources Investigation Report 84-4369, U.S. Geological Survey, 1984.

Wan, X.Q.: The preliminary study on the circulation characteristics and its variances in summertime and wintertime in Bohai Sea. Msc Thesis (in Chinese), Ocean University of China, p. 101, 2003.

Wang, W. D., Zhang, G. X., and Li, B. L.: *Report on Groundwater Management Simulation in Panjin City, Liaoning Province*, (in chinese), Liaoning hydrogeology and engineering geology exploration, 1992.

Walko, R. L.: Coupled Atmosphere–Biophysics–Hydrology Models for Environmental Modeling. *Journal of applied meteorology*, 2000.

Walko, R. L., W. R. Cotton, M. P. Meyers, and J. Y. Harrington.: New RAMS cloud microphysics parameterization. Part I: The single moment scheme. Atmos. Res., 38, 29–62, 1995.

Xue, X. D.: T*he research of the simulation with prediction of the groundwater level and the rational utilization of the water resource in panjin area*, (in chinese), Msc Thesis, Jiling University, 91p, 2005.

Yamashita, T., Kim, K., Lee, H.S., and Haggag, M.: Environment Simulator: Contribution to Coastal Engineering Problems (in Japanese), Annual Journal of Coastal Engineering, JSCE, 54, 1301-1305, 2007.

Yamashita, T.: Regional Environment Simulator and Its Applications to Environmental Impact Assessment. Presented in ISWREP, 2011.

Yamazawa, H and Nagai, H.: Development of one-dimensional atmosphere-bare soil model (in Japanese), *Japan Atomic Energy Research Institute Rep.*, 97-140, 56 pp, 1997.

Zheng, C. M. and Wang, P. P.: MT3DMS: Documentation and User's Guide. Contract Report SERDP-99-1, U.S. Army Engineer Research and Development Center, Vicksburg, MS, 1999

Chapter 6

Concluding Remarks

Numerical models and coupling mode system have been constructed in this study of which objective are simulate and predict the seawater intrusion condition of Liaodong bay coastal plain area, improve the numerical simulation method on seawater intrusion and the evaluation method of scheme choice for OAWR. Concluding remarks in this chapter summarize the section and conclusions and findings of the dissertation.

6.1 Conclusions

6.1.1 Numerical simulation of seawater intrusion in Liao Dng Bay coastal plain, China using SEAWAT model

Purposes of this study are simulate and predict the seawater intrusion condition of Liaodong bay coastal plain area, analysis the vertical grid effect on the seawater intrusion simulation and analysis the tidal effect on the seawater intrusion simulation.

The important results from this study present in the below.

- In the three vertical layer case 1, the maximum extent of seawater intrusion in Quaternary layer increased 7 km in the northwest of research area. In the southwest and northeast area, the extent of seawater intrusion increased smaller than other area. The seawater intrusion in Quaternary layer was significantly faster than that in upper Neozoic Layer. In the four vertical layer case 2, the maximum extent of seawater intrusion in Layers A1 will increase 4.3 km and Layers A2 will increase 6.2 km toward north in research area. In the southwest and northeast area, the extent of seawater intrusion increased smaller than other area. The seawater intrusion in Layer A2 was significantly faster than that in other two Layers.

- The results show that the results of four vertical layer case 2 can present the salt wedge at the bottom of and the top of the aquifer (quaternary aquifer) more better than three vertical layer case 1's. Thus, it can be advised to using more vertical grid layer in seawater intrusion simulation models if data enough.

- In the north, southwest and southeast of study area at the Quaternary layer, the seawater intrusion will increase 20 and 10 km and 3km in the Minhuazhen group layer if considering the tidal effect. Thus, the tidal fluctuation has significant effects on the seawater intrusion.

- The main numerical code SEAWAT can serve as an effective tool for simulating variable-density flow and transport under complex geometries and geological settings.

6.1.2 Atmosphere-ocean-groundwater simulation system for seawater intrusion

Purposes of this study are developed an atmosphere-ocean-groundwater coupling mode system to simulate the precipitation, seawater level, seawater intrusion， groundwater flow and groundwater quality, especially in the lack data region areas and countries.

The important results from this study present in the below.

- NCEP FNL and JMA JRA-25 data can be used for precipitation simulation in Liaodong Bay coastal plain. Compare with observation precipitation data of the China Meteorological Data Sharing Service System, the correlation value is from 0.756 to 0.937 of the NCEP case study and 0.5296 to 0.9548 of the JRA-25 case study. The calculation precipitation results of NECP case's study are better than JRA-25 case's results, especially at the Jinzhou and Yingkou station.

- The seawater level of POM results is good match with the observation data of National Oceanographic Data Center at Laohutan station in 1997. The tidal range at Yingkou station is 2.52 m in 2004, while the observation data in the Liaodong bay is 2.7 m. It is shown that the simulated tidal range result is good.

- The maximum extent of seawater intrusion in Layers A2 will increase 9.8 km toward north in the west of research area. Compared with the previous study, the trend of seawater intrusion in layer A1, A2 and A4 is almost same. Thus, the atmosphere-ocean-groundwater coupling model system can be used in the seawater intrusion simulation.

6.1.3 Numerical simulation of Typhoon Morakot by atmosphere-ocean coupled model

Purposes of this study are to study the atmosphere-ocean coupled model, and try to do the Typhoon Morakot case study to investigate the possible reasons for the unique track of Typhoon Morakot and the extremely heavy rainfall produced during its landfall in Taiwan. In particular, the effects of the terrain, microphysics parameterization and bogus scheme application were examined.

The important results from this study present in the below.

- The sudden northward-turning track of Typhoon Morakot is effect of the large-scale monsoon surge. On the other hand, there was a subtropical high system in the east of Japan near 160 ℉ moving towards the southwest at 06:00 UTC 3 August. This then changed direction from the northwest to the northeast at 18:00 UTC 6 August. This might have played a significant role in affecting the track of Typhoon Morakot.

- Typhoons Morakot, Goni, and Etau formed a larger scale cyclonic circulation because of the south-westerly monsoon, and the monsoon gyre circulation enhanced the energy exchange of the three TCs. Morakot obtain a positive vortex circulation and moisture supply from the other two typhoons. The strengthened south-westerly monsoon surge was capable of bringing excessive moisture into Taiwan. Then, the orographic effect of the Taiwan CMR could uplift the extremely large moisture flux over southern parts of the island, leading to the extremely heavy rainfall in Taiwan.

- The Schultz mixed-phase scheme can simulate rainfall better than for the other two parameters in this study. The terrain elevation is important in determining heavy rainfall and its spatial distribution. If the terrain elevation increases, the rainfall amount will increase. The effect of the terrain on the typhoon track is insignificant in Typhoon Morakot. In the bogus scheme experiments, the every six-hour bogus scheme show better and improve results in all aspects, including the rainfall track , intensity and the seawater level of Typhoon Morakot.

6.1.4 Scheme choice for optimal allocation of water resources

Scheme choice for Optimal Allocation of Water Resource (OAWR) is a fuzzy multiple attribute decision which is formed by the information from a lots of figures and fuzzy language in the evaluated factors.

Purposes of this study are establishes an evaluation system of schemes choice of OAWR which is based on the fuzzy language evaluation and the Generalized Induced Ordered Weighted Averaging (GIOWA) operator to do the Scheme choice for OAWR, which evaluation system can be used in the future OAWR study of Liaodong bay coastal plain area.

The important results from this study present in the below.

- The evaluating factors of the evaluation system are: (1) investment (Yuan), (2) daily water supplying (ton/day), (3) fee of contaminated water disposal (Yuan), (4) water conservation (fuzzy language), and (5) development of economy (fuzzy language). Analytic hierarchy process （AHP） method is used to determine the weighting vector.

- The case study of the north of Shen Yang city was conducted, and the result show that the evaluation system of the scheme choice for OAWR was feasible and useful. For the best scheme, its total investment is 9.6 hundred million yuan, its total fee of contaminated water disposal is 0.83 hundred million yuan. Its daily water supplying is 91.02 ten thousand ton/day that is enough for the next 20 years daily water supplying in the north of Shen Yang. Its water conservation and the development of economy are moderate.

6.2 Future development

In this study, the numerical models and coupling model system have been constructed to analysis the seawater intrusion into groundwater system in Liaodong Bay coastal plain, China. However it still has many possibilities of extension and parts to be improved. Future extensions include the following:

6.2.1 Improving the numerical models

In the further research, it is better to use vertical beach slope ocean boundary as the model ocean boundary and using the smaller grid size and non-uniform grid size to analysis the grid size effect on seawater intrusion simulation.

6.2.2 Coupling model system

In the coupling model system of this study, vegetation model and surface water model are not considered to coupling with atmosphere, ocean and groundwater models. Therefore for future plans, the land surface model (SOLVEG2) and surface water model (HSPF or SWAT) are useful to improve the representation of soil, land use type and surface water effect on the seawater intrusion which providing the boundary conditions for the coupling model system.

6.2.3 Water resources optimal allocation

To protect or reduce the groundwater resources in Liaodong Bay coastal plain, China, future study about the regional water resources assessment and optimal allocation should be done. Meantime, it is recommended that some protection schemes, such as operational controls (e.g., pumping and well-construction restrictions) and engineering works (e.g., artificial recharge schemes and cut-off wall schemes), should be established based on the regional water resources assessment and optimal allocation study.